

REPORT DOCUMENTATION PAGE

Public reporting burden for this collection of information is estimated to average 1 hour per response, including the time for reviewing instructions, sea the collection of information. Send comments regarding this burden estimate or any other aspect of this collection of information, including sugg Operations and Reports, 1215 Jefferson Davis Highway, Suite 1204, Arlington, VA 22202-4302, and to the Office of Management and Budget, Paper

AFRL-SR-BL-TR-00-

viewing
ormation

0715

1. AGENCY USE ONLY (Leave blank)		2. REPORT DATE December, 1998		3. REPORT NUMBER	
4. TITLE AND SUBTITLE 1998 Summer Research Program (SRP), Summer Research Extension Program (SREP), Final Report, Volume 2, Phillips Laboratory				5. FUNDING NUMBERS F49620-93-C-0063	
6. AUTHOR(S) Gary Moore					
7. PERFORMING ORGANIZATION NAME(S) AND ADDRESS(ES) Research & Development Laboratories (RDL) 5800 Uplander Way Culver City, CA 90230-6608				8. PERFORMING ORGANIZATION REPORT NUMBER	
9. SPONSORING/MONITORING AGENCY NAME(S) AND ADDRESS(ES) Air Force Office of Scientific Research (AFOSR) 801 N. Randolph St. Arlington, VA 22203-1977				10. SPONSORING/MONITORING AGENCY REPORT NUMBER	
11. SUPPLEMENTARY NOTES					
12a. DISTRIBUTION AVAILABILITY STATEMENT Approved for Public Release				12b. DISTRIBUTION CODE	
13. ABSTRACT (Maximum 200 words) The United States Air Force Summer Research Program (SRP) is designed to introduce university, college, and technical institute faculty members to Air Force research. This is accomplished by the faculty members, graduate students, and high school students being selected on a nationally advertised competitive basis during the summer intersession period to perform research at Air Force Research Laboratory (AFRL) Technical Directorates and Air Force Air Logistics Centers (ALC). AFOSR also offers its research associates (faculty only) an opportunity, under the Summer Research Extension Program (SREP), to continue their AFOSR-sponsored research at their home institutions through the award of research grants. This volume consists of a listing of the participants for the SREP and the technical report from each participant working at the AF Phillips Laboratory.					
14. SUBJECT TERMS Air Force Research, Air Force, Engineering, Laboratories, Reports, Summer, Universities, Faculty, Graduate Student, High School Student				15. NUMBER OF PAGES	
				16. PRICE CODE	
17. SECURITY CLASSIFICATION OF REPORT Unclassified	18. SECURITY CLASSIFICATION OF THIS PAGE Unclassified	19. SECURITY CLASSIFICATION OF ABSTRACT Unclassified	20. LIMITATION OF ABSTRACT UL		

GENERAL INSTRUCTIONS FOR COMPLETING SF 298

The Report Documentation Page (RDP) is used in announcing and cataloging reports. It is important that this information be consistent with the rest of the report, particularly the cover and title page. Instructions for filling in each block of the form follow. It is important to **stay within the lines** to meet **optical scanning requirements**.

Block 1. Agency Use Only (*Leave blank*).

Block 2. Report Date. Full publication date including day, month, and year, if available (e.g. 1 Jan 88). Must cite at least the year.

Block 3. Type of Report and Dates Covered. State whether report is interim, final, etc. If applicable, enter inclusive report dates (e.g. 10 Jun 87 - 30 Jun 88).

Block 4. Title and Subtitle. A title is taken from the part of the report that provides the most meaningful and complete information. When a report is prepared in more than one volume, repeat the primary title, add volume number, and include subtitle for the specific volume. On classified documents enter the title classification in parentheses.

Block 5. Funding Numbers. To include contract and grant numbers; may include program element number(s), project number(s), task number(s), and work unit number(s). Use the following labels:

C - Contract
G - Grant
PE - Program
Element

PR - Project
TA - Task
WU - Work Unit
Accession No.

Block 6. Author(s). Name(s) of person(s) responsible for writing the report, performing the research, or credited with the content of the report. If editor or compiler, this should follow the name(s).

Block 7. Performing Organization Name(s) and Address(es). Self-explanatory.

Block 8. Performing Organization Report Number. Enter the unique alphanumeric report number(s) assigned by the organization performing the report.

Block 9. Sponsoring/Monitoring Agency Name(s) and Address(es). Self-explanatory.

Block 10. Sponsoring/Monitoring Agency Report Number. (*If known*)

Block 11. Supplementary Notes. Enter information not included elsewhere such as: Prepared in cooperation with....; Trans. of....; To be published in.... When a report is revised, include a statement whether the new report supersedes or supplements the older report.

Block 12a. Distribution/Availability Statement. Denotes public availability or limitations. Cite any availability to the public. Enter additional limitations or special markings in all capitals (e.g. NOFORN, REL, ITAR).

DOD - See DoDD 5230.24, "Distribution Statements on Technical Documents."

DOE - See authorities.

NASA - See Handbook NHB 2200.2.

NTIS - Leave blank.

Block 12b. Distribution Code.

DOD - Leave blank.

DOE - Enter DOE distribution categories from the Standard Distribution for Unclassified Scientific and Technical Reports.
Leave blank.

NASA - Leave blank.

NTIS -

Block 13. Abstract. Include a brief (*Maximum 200 words*) factual summary of the most significant information contained in the report.

Block 14. Subject Terms. Keywords or phrases identifying major subjects in the report.

Block 15. Number of Pages. Enter the total number of pages.

Block 16. Price Code. Enter appropriate price code (*NTIS only*).

Blocks 17. - 19. Security Classifications. Self-explanatory. Enter U.S. Security Classification in accordance with U.S. Security Regulations (i.e., UNCLASSIFIED). If form contains classified information, stamp classification on the top and bottom of the page.

Block 20. Limitation of Abstract. This block must be completed to assign a limitation to the abstract. Enter either UL (unlimited) or SAR (same as report). An entry in this block is necessary if the abstract is to be limited. If blank, the abstract is assumed to be unlimited.

UNITED STATES AIR FORCE
SUMMER RESEARCH PROGRAM -- 1998
SUMMER RESEARCH EXTENSION PROGRAM FINAL REPORTS

VOLUME 2
PHILLIPS LABORATORY

RESEARCH & DEVELOPMENT LABORATORIES

5800 Uplander Way
Culver City, CA 90220-6608

Program Director, RDL
Gary Moore

Program Manager, AFOSR
Colonel Cerveny

Program Manager, RDL
Scott Licoscas

Program Administrator, RDL
Johnetta Thompson

Program Administrator, RDL
Rebecca Kelly-Clemmons

Submitted to:

AIR FORCE OFFICE OF SCIENTIFIC RESEARCH
Bolling Air Force Base
Washington, D.C.
December 1998

20010319 047

AQM01-06-1171

PREFACE

This volume is part of a four-volume set that summarizes the research of participants in the 1998 AFOSR Summer Research Extension Program (SREP). The current volume, Volume 1 of 5, presents the final reports of SREP participants at Armstrong Laboratory.

Reports presented in this volume are arranged alphabetically by author and are numbered consecutively -- e.g., 1-1, 1-2, 1-3; 2-1, 2-2, 2-3, with each series of reports preceded by a 35 page management summary. Reports in the five-volume set are organized as follows:

VOLUME	TITLE
1	Armstrong Research Laboratory
2	Phillips Research Laboratory
3	Rome Research Laboratory
4	Wright Research Laboratory
5	Air Logistics Center Arnold Engineering Development Center

1998 SREP Final Technical Report Table of Contents

Armstrong Research Laboratory

Volume 1

	Principle Investigator	Report Title University/Institution	Laboratory & Directorate
1	Dr. Gerald P. Chubb	Scoring Pilot Performance of Basic Flight Maneuvers Ohio University	AFRL/HEA
2	Dr. Brent D. Foy	Development & Validation of a Physiologically-Based Kinetic Model of Perfused Liver for water-soluble Compounds Wright State University	AFRL/HES
3	Dr. Charles Lance	Extension of Job Performance Measurement Technologies to Development of a Prototype Methodology for Assessing Work Team University of Georgia Research Foundation	AFRL/HEJ
4	Dr. David Woehr	Validation of the Multidimensional Work Ethic Profile (MWEP) as a Screening Tool for AF Enlisted Personnel Texas A & M University College Station	AFRL/HEJ

1998 SREP Final Technical Report Table of Contents

Phillips Research Laboratory

Volume 2

	Principle Investigator	Report Title University/Institution	Laboratory & Directorate
1	Dr. Mark J. Balas	Non-Linear Adaptive Control for a Precision Deployable Structure with White light University of Colorado at Boulder	AFRL/VSDD
2	Dr. Neb Duric	Image Recovery Using Phase Diversity University of New Mexico	AFRL/DEBS
3	Dr. George W. Hanson	Perturbation Analysis of the Natural Frequencies Targets in Inhomogeneous University of Wisconsin-Milwaukee	AFRL/DEHP
4	Dr. Brian D. Jeffs	Bayesian restoration of Space object Images from Adaptive Optics Data with unknown data Brigham Young University	AFRL/DES
5	Dr. Aravinda Kar	Effects of Vapor-Plasma Layer on Thick-Section Cutting and Calculation of Modes University of Central Florida	AFRL/DEOB
6	Dr. Donald J. Leo	Adaptive Vibration suppression for autonomous Control Systems University of Toledo	AFRL/VSDV
7	Dr. Hanli Liu	Continuous- Wave approach to 3-D imaging Through Turbid media w/a Single Planar Measurement University of Texas Arlington	AFRL/DEBS
8	Dr. Joshua C. Biefang	Optical Clocks Based on Diode Lasers University of New Mexico	AFRL/ DELO
9	Dr. Eric J. Paulson	Optimization 7 Analysis of a Waverider Vehicle For Global Spaceplane University of Colorado at Boulder	AFRL/PRR
10	Dr. Kenneth F. Stephens II	Simulation of an explosively Formed Fuse Using MACH 2 University of North Texas	AFRL/DEHE

1998 SREP Final Technical Report Table of Contents

Rome Research Laboratory

Volume 3

Principle Investigator	Report Title University/Institution	Laboratory & Directorate
1 Dr. Milica Barjaktarovic	Specification and Verification of SDN. 701 MSP Functions and Missi Crypto Wilkes University	AFRL/IFGB
2 Dr. Stella N. Batalama	Robust Spread Spectrum Communications: Adaptive Interference Mitigation SUNY Buffalo University	AFRL/IFGC
3 Dr. Nikolaos G. Bourbakis	Hierarchical-Adaptive Image Segmentation SUNY Binghamton University	AFRL/IRE
4 Dr. Venugopala R. Dasigi	Information Fusion w/Multiple Feature Extractors for automatic Text Sacred Heart University	AFRL/IRE
5 Dr. Richard R. Eckert	The Interactive Learning Wall: A PC-Based, Deployable Data Wall for Use in a College Classroom SUNY Binghamton University	AFRL/IFSA
6 Dr. Kuo-Chi Lin	Web-Based Distributed Simulation University of Central Florida	AFRL/IFSB
7 Dr. Dimitrios N. Pados	Adaptive Array Radars and Joint Space-Time Auxiliary Verctor Filtering	AFRL/SN
8 Dr. Brajendra N. Panda	Information Warfare" Design of an Efficient Log Management Method to Aid In Data University of North Dakota	AFRL/IFGB
9 Dr. Michael A Pittarelli	Complexity of Detecting and content-driven methods for resolving database SUNY of Tech Utica	AFRL/IFTB
10 Dr. Mark S. Schmalz	Errors Inherent in 3D Target Reconstruction from Multiple Airborne Images University of Florida	AFRL/IRE
11 Dr. Nong Ye	Model-based Assessment of Campaign Plan-Performance under Uncertainty Arizona State University	AFRL/IFSA
12 Mr. Parker Bradley	Development of User-Friendly CompEnvironment for Blind Source Separation Syracuse University	AFRL/IFGC

1998 SREP Final Technical Report Table of Contents

Wright Research Laboratory

Volume 4

Principle Investigator	Report Title University/Institution	Laboratory & Directorate
1 Dr. Brian P. Beecken	Development of a statistical Model predicting the impact of a scent Projector's Nonuniformity on a test Article's Image Bethel College	AFRL/MN
2 Dr. John H. Beggs	Implementation of an Optimization Algorithm in Electromagnetics for Radar absorbing Material Layers Mississippi State University	AFRL/VASD
3 Dr. Raj Bhatnagar	Analysis of Intra-Class Variability and synthetic Target Models Models for Use in ATR University of Cincinnati	AFRL/SN
4 Dr. Gregory Blaisdell	Validation of a Large Eddy Simulation Code & Development of Commuting Filters Purdue University	AFRL/VAAC
5 Dr. John Douglas	Roles of Matched Filtering and Coarse in Insect Visual Processing University of Arizona	AFRL/MN
6 Dr. William Hosford	Prediction of Compression Textures in Tantalum Using a Pencil-Glide Computer Mode Program University of Michigan	AFRL/MN
7 Dr. Yi Pan	Parallelization of Time-Dependent Maxwell Equations Using High Perform University of Dayton	AFRL/VASD
8 Dr. Kishore Pochiraju	A Hybrid Variational-Asymptotic Method for the Analysis of MicroMechanical Damage in Composites Stevens Institute of Technology	AFRL/MLBM
9 Dr. Yuri Shtessel	Continuous Sliding Mode Control Approach for Addressing Actuator Deflection and Deflection rate Saturation in Tailless Aircraft Control and Re-Configurable Flight Control University of Alabama In Huntsville	AFRL/VACD
10 Dr. Janusz Starzyk	Feature Selection for Automatic Target Recognition: Mutual Information & Statistical Techniques Ohio University	AFRL/SN

1998 SREP Final Technical Report Table of Contents

Volume 5

	Principle Investigator	Report Title University/Institution	Laboratory & Directorate
Arnold Engineering Development Center			
1	Dr. Frank Collins	Monte Carlo Computation of Species Separation by a Conical Skimmer in Hypersonic Transition Flow University of Tennessee Space Institute	AEDC
Air Logistics Centers			
2	Dr. Paul W. Whaley	Probabilistic Analysis of Residual Strength in Corroded and Uncorroded Aging Air Mineralization Oklahoma Christian University of Science & Art	OCALCTIE
3	Dr. Devendra Kumar	Further Development of a Simpler, Multiversion Control Protocol for Internet Databases University of Georgia	SAALC
4	Dr. Joe G. Chow	An Automated 3-D Surface Model Creation Module for Laser Scanned Point Data Florida International University	WRALC

1998 SUMMER RESEARCH EXTENSION PROGRAM (SREP) MANAGEMENT REPORT

1.0 BACKGROUND

Under the provisions of Air Force Office of Scientific Research (AFOSR) contract F49620-90-C-0076, September 1990, Research & Development Laboratories (RDL), an 8(a) contractor in Culver City, CA, manages AFOSR's Summer Research Program. This report is issued in partial fulfillment of that contract (CLIN 0003AC).

The Summer Research Extension Program (SREP) is one of four programs AFOSR manages under the Summer Research Program. The Summer Faculty Research Program (SFRP) and the Graduate Student Research Program (GSRP) place college-level research associates in Air Force research laboratories around the United States for 8 to 12 weeks of research with Air Force scientists. The High School Apprenticeship Program (HSAP) is the fourth element of the Summer Research Program, allowing promising mathematics and science students to spend two months of their summer vacations working at Air Force laboratories within commuting distance from their homes.

SFRP associates and exceptional GSRP associates are encouraged, at the end of their summer tours, to write proposals to extend their summer research during the following calendar year at their home institutions. AFOSR provides funds adequate to pay for SREP subcontracts. In addition, AFOSR has traditionally provided further funding, when available, to pay for additional SREP proposals, including those submitted by associates from Historically Black Colleges and Universities (HBCUs) and Minority Institutions (MIs). Finally, laboratories may transfer internal funds to AFOSR to fund additional SREPs. Ultimately the laboratories inform RDL of their SREP choices, RDL gets AFOSR approval, and RDL forwards a subcontract to the institution where the SREP associate is employed. The subcontract (see Appendix 1 for a sample) cites the SREP associate as the principal investigator and requires submission of a report at the end of the subcontract period.

Institutions are encouraged to share costs of the SREP research, and many do so. The most common cost-sharing arrangement is reduction in the overhead, fringes, or administrative charges institutions would normally add on to the principal investigator's or research associate's labor. Some institutions also provide other support (e.g., computer run time, administrative assistance, facilities and equipment or research assistants) at reduced or no cost.

When RDL receives the signed subcontract, we fund the effort initially by providing 90% of the subcontract amount to the institution (normally \$18,000 for a \$20,000 SREP). When we receive the end-of-research report, we evaluate it administratively and send a copy to the laboratory for a technical evaluation. When the laboratory notifies us the SREP report is acceptable, we release the remaining funds to the institution.

2.0 THE 1998 SREP PROGRAM

SELECTION DATA: A total of 490 faculty members (SFRP Associates) and 202 graduate students (GSRP associates) applied to participate in the 1998 Summer Research Program. From these applicants 188 SFRPs and 98 GSRPs were selected. The education level of those selected was as follows:

1997 SRP Associates, by Degree			
SFRP		GSRP	
PHD	MS	MS	BS
184	6	2	53

Of the participants in the 1997 Summer Research Program 90 percent of SFRPs and 13 percent of GSRPs submitted proposals for the SREP. One hundred and thirty-two proposals from SFRPs and seventeen from GSRPs were selected for funding, which equates to a selection rate of 54% of the SFRP proposals and of 34% for GSRP proposals.

1998 SREP: Proposals Submitted vs. Proposals Selected			
	Summer 1997 Participants	Submitted SREP Proposals	SREPs Funded
SFRP	188	132	20
GSRP	98	17	4
TOTAL	286	149	24

The funding was provided as follows:

Contractual slots funded by AFOSR	18
Laboratory funded	<u>22</u>
Total	40

Twelve HBCU/MI associates from the 1997 summer program submitted SREP proposals; six were selected (none were lab-funded; all were funded by additional AFOSR funds).

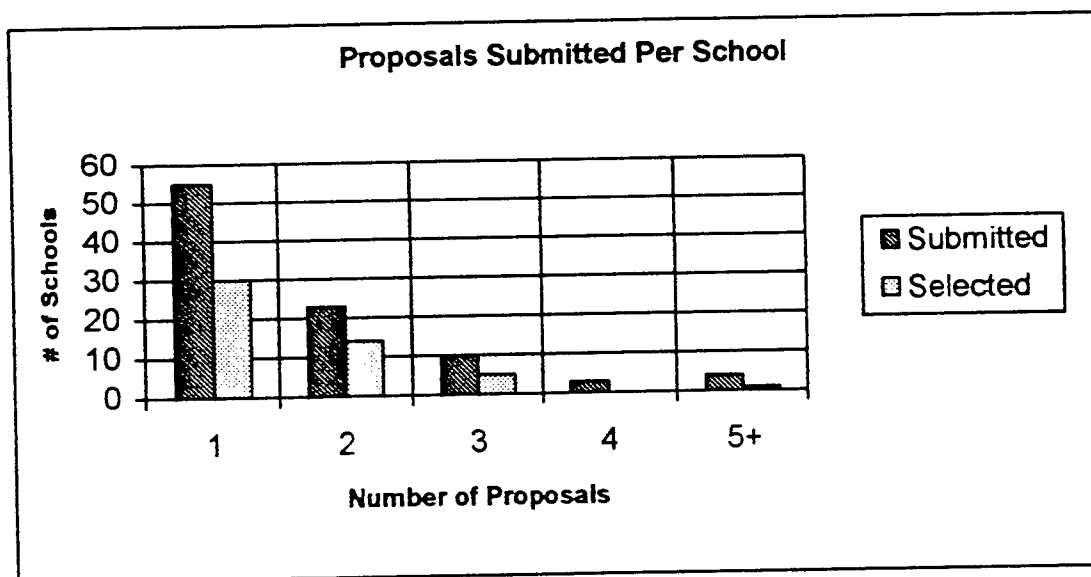
Proposals Submitted and Selected, by Laboratory		
	Applied	Selected
Armstrong Research Site	9	3
Air Logistic Centers	31	5
Arnold Engineering Development Center	2	1
Phillips Research Site	30	10
Rome Research Site	29	12
Wilford Hall Medical Center	1	0
Wright Research Site	47	9
TOTAL	149	40

Note: Armstrong Research Site funded 1 SREP; Phillips Research Site funded 6; Rome Research Site funded 9; Wright Research Site funded 6.

The 125 1997 Summer Research Program participants represented 60 institutions.

Institutions Represented on the 1997 SRP and 1998 SREP		
Number of schools represented in the Summer 97 Program	Number of schools represented in submitted proposals	Number of schools represented in Funded Proposals
125	110	55

Thirty schools had more than one participant submitting proposals.



The selection rate for the 65 schools submitting 1 proposal (68%) was better than those submitting 2 proposals (61%), 3 proposals (50%), 4 proposals (0%) or 5+ proposals (25%). The 4 schools that submitted 5+ proposals accounted for 30 (15%) of the 149 proposals submitted.

Of the 149 proposals submitted, 130 offered institution cost sharing. Of the funded proposals which offered cost sharing, the minimum cost share was \$3046.00, the maximum was \$39,261.00 with an average cost share of \$11,069.21.

Proposals and Institution Cost Sharing		
	Proposals Submitted	Proposals Funded
With cost sharing	117	32
Without cost sharing	32	8
Total	149	40

The SREP participants were residents of 31 different states. Number of states represented at each laboratory were:

States Represented, by Proposals Submitted/Selected per Laboratory		
	Proposals Submitted	Proposals Funded
Armstrong Laboratory	31	5
Air Logistic Centers	9	3
Arnold Engineering Development Center	2	1
Phillips Laboratory	30	10
Rome Laboratory	29	12
Wilford Hall Medical Center	1	0
Wright Laboratory	47	9

Nine of the 1997 SREP Principal Investigators also participated in the 1998 SREP.

ADMINISTRATIVE EVALUATION: The administrative quality of the SREP associates' final reports was satisfactory. Most complied with the formatting and other instructions provided to them by RDL. Thirty-seven final reports have been received and are included in this report. The subcontracts were funded by \$992,855.00 of Air Force money. Institution cost sharing totaled \$354,215.00.

TECHNICAL EVALUATION: The form used for the technical evaluation is provided as Appendix 2. Thirty-five evaluation reports were received. Participants by laboratory versus evaluations submitted is shown below:

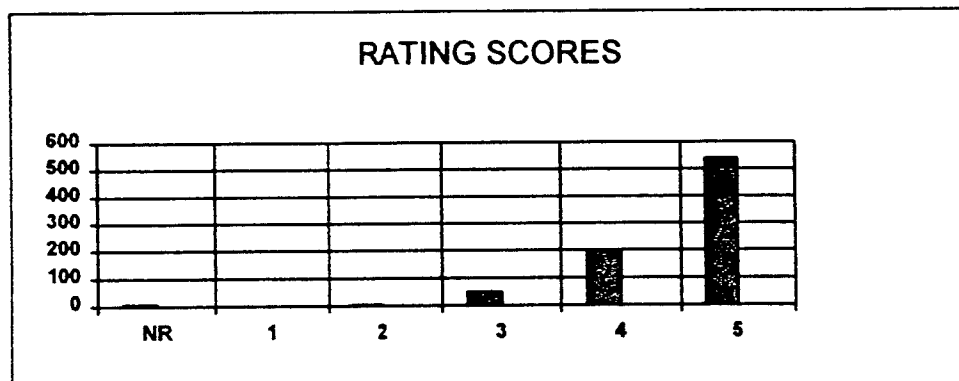
	Participants	Evaluations	Percent
Armstrong Laboratory	5	4	95.2
Air Logistic Centers	3	3	100
Arnold Engineering Development Center	1	1	100
Phillips Laboratory	10	10	100
Rome Laboratory	12	12	100
Wright Laboratory	9	5	91.9
Total	40	35	95.0

Notes:

- 1: Research on four of the final reports was incomplete as of press time so there aren't any technical evaluations on them to process, yet. Percent complete is based upon 20/21=95.2%
- 2: One technical evaluation was not completed because one of the final reports was incomplete as of press time. Percent complete is based upon 18/18=100%

The number of evaluations submitted for the 1998 SREP (95.0%) shows a marked improvement over the 1997 SREP submittals (65%).

PROGRAM EVALUATION: Each laboratory focal point evaluated ten areas (see Appendix 2) with a rating from one (lowest) to five (highest). The distribution of ratings was as follows:

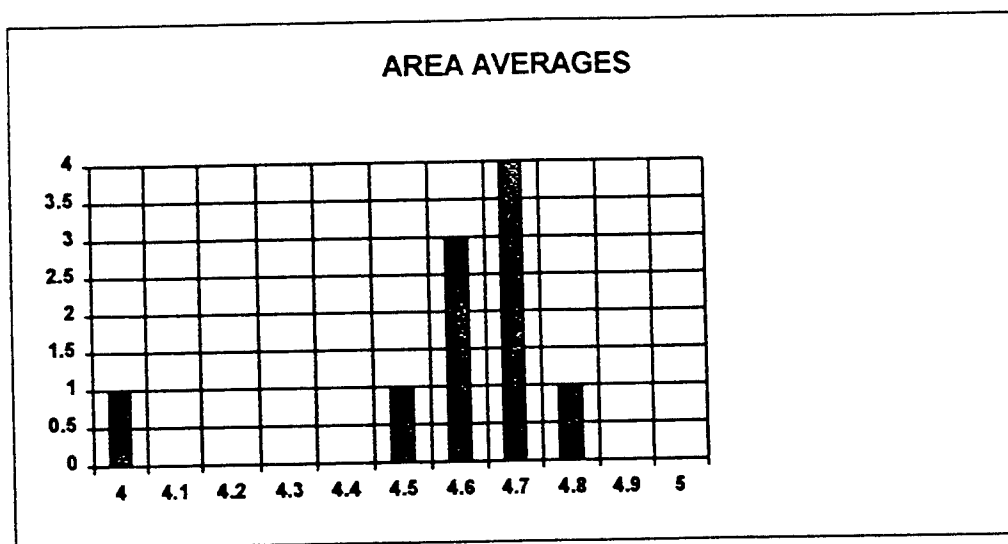


Rating	Not Rated	1	2	3	4	5
# Responses	7	1	7	62 (6%)	226 (25%)	617 (67%)

The 8 low ratings (one 1 and seven 2's) were for question 5 (one 2) "The USAF should continue to pursue the research in this SREP report" and question 10 (one 1 and six 2's) "The one-year period for complete SREP research is about right", in addition over 30% of the threes (20 of 62) were for question ten. The average rating by question was:

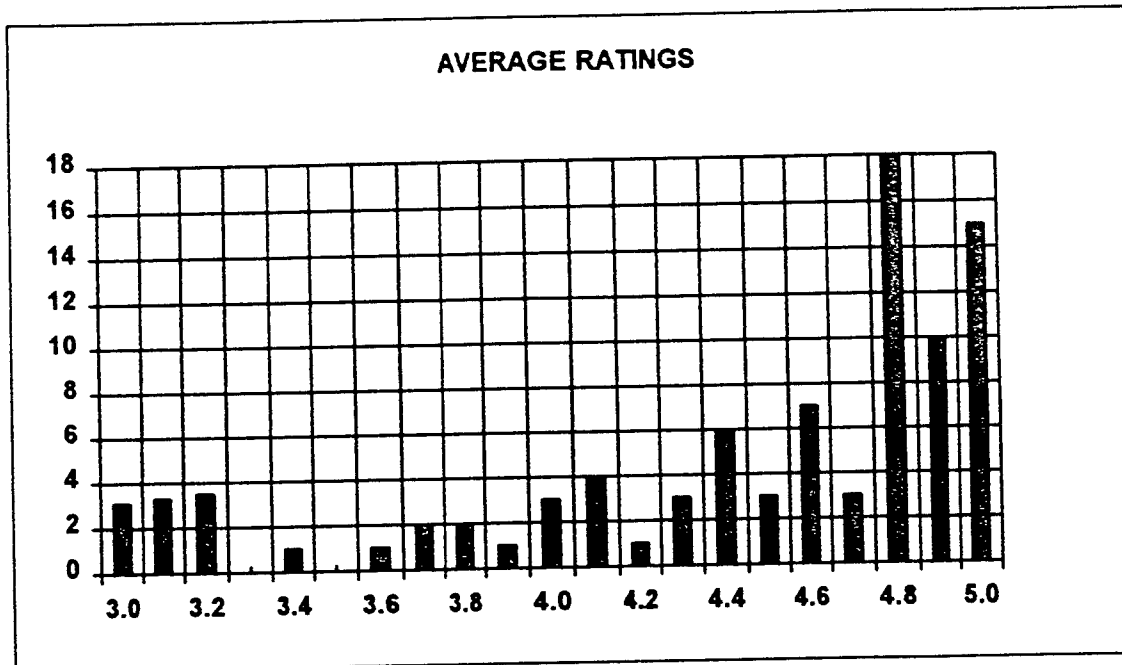
Question	1	2	3	4	5	6	7	8	9	10
Average	4.6	4.6	4.7	4.7	4.6	4.7	4.8	4.5	4.6	4.0

The distribution of the averages was:



Area 10 "the one-year period for complete SREP research is about right" had the lowest average rating (4.1). The overall average across all factors was 4.6 with a small sample standard deviation of 0.2. The average rating for area 10 (4.1) is approximately three sigma lower than the overall average (4.6) indicating that a significant number of the evaluators feel that a period of other than one year should be available for complete SREP research.

The average ratings ranged from 3.4 to 5.0. The overall average for those reports that were evaluated was 4.6. Since the distribution of the ratings is not a normal distribution the average of 4.6 is misleading. In fact over half of the reports received an average rating of 4.8 or higher. The distribution of the average report ratings is as shown:



It is clear from the high ratings that the laboratories place a high value on AFOSR's Summer Research Extension Programs.

3.0 SUBCONTRACTS SUMMARY

Table 1 provides a summary of the SREP subcontracts. The individual reports are published in volumes as shown:

<u>Laboratory</u>	<u>Volume</u>
Armstrong Research Site	1
Arnold Engineering Development Center	5
Air Logistic Centers	5
Phillips Research Site	2
Rome Research Site	3
Wright Research Site	4

SREP SUB-CONTRACT DATA

Report Author Author's University	Author's Degree	Sponsoring Lab	Performance Period	Contract Amount	Univ. Cost Share
Chubb, Gerald Industrial Engineering Ohio State University, Columbus, OH	PhD 98-0829	AL/HR	01/01/98 12/31/98 Scoring Pilot Performance of Basic Flight Manuevers	\$25000.00	\$0.00
Foy, Brent Medical Physics Wright State University, Dayton, OH	PhD 98-0828	AL/OE	01/01/98 12/31/98 Development & Validation of a Physiologically-Based Kinetic Model of Perfused	\$25000.00	\$11278.00
Lance, Charles Psychology Univ of Georgia Res Foundation, Athens, GA	PhD 98-0842	AL/HR	01/01/98 12/31/98 Extension of Job Performance Measurement Tech to the Development of a Prototype	\$24989.00	\$0.00
Woehr, David Department of Psychology Texas A & M Univ-College Station, College	PhD 98-0802	AL/HR	01/01/98 12/31/98 Validation of The Multidimensional work ethic profile (MWEF) as a screening too	\$25000.00	\$11508.00
Collins, Frank Mechanical Engineering Tennessee Univ Space Institute, Tullahoma, TN	PhD 98-0807	AEDC/E	01/01/98 12/31/98 Monte Carlo Computation of SpeciesSeparation by a Conical Skimmer in Hypersonic	\$25000.00	\$16104.00
Whaley, Paul Mechanical Engineering Oklahoma Christian Univ of Science & Art,	PhD 98-0820	ALC/OC	01/01/98 12/31/98 Probabilistic Analysis of Residual Strength in Corroded and Uncorroded Aging Air	\$23351.00	\$3046.00
Balas, Mark Applied Math Univ of Colorado at Boulder, Boulder, CO	PhD 98-0816	PL/SX	01/01/98 12/31/98 Non-Linear Adaptive Control for a Precision Deployable Structure with White light	\$25000.00	\$0.00
Duric, Neb Astrophysics University of New Mexico, Albuquerque, NM	PhD 98-0808	PL/LI	01/01/98 12/31/98 Image Recovery Using Phase Diversity	\$25000.00	\$5777.00
Hanson, George Electrical Engineering Univ of Wisconsin - Milwaukee, Milwaukee, WI	PhD 98-0811	PL/WS	01/01/98 12/31/98 Perturbation Analysis of the Natural Frequencies Targets in Inhomogeneous Media	\$25000.00	\$23250.00
Jeffs, Brian Electrical Engineering Brigham Young University, Provo, UT	PhD 98-0813	PL/LI	01/01/98 12/31/98 Bayesian Restoration of Space object Images From Adaptive Optics Data with unkno	\$25000.00	\$19177.00
Kar, Aravinda Engineering University of Central Florida, Orlando, FL	PhD 98-0812	PL/LI	01/01/98 12/31/98 Effects of Vapor-Plasma Layer on Thick-Section Cutting and Calculation of Modes	\$25000.00	\$5414.00
Leo, Donald Mechanical & Aerospace University of Toledo, Toledo, OH	PhD 98-0810	PL/VT	01/01/98 09/30/98 Adaptive vibration suppression for autonomous Control Systems	\$24964.00	\$9628.00
Liu, Hanli Physics Univ of Texas at Arlington, Arlington, TX	PhD 98-0814	PL/LI	01/01/98 12/31/98 Continuous-Wave Approach to 3-D Imaging through Turbid media w/a Single Planar M	\$25000.00	\$11000.00
Bienfang, Joshua Physics University of New Mexico, Albuquerque, NM	BS 98-0815	PL/LI	01/01/98 12/31/98 Optical Clocks Based on Diode Lasers	\$24994.00	\$0.00
Paulson, Eric Engineering/Physics Univ of Colorado at Boulder, Boulder, CO	BS 98-0837	PL/RK	01/01/98 12/31/98 Optimization & Analysis of a Waverider Vehicle for Global Spaceplane Trajectories	\$25000.00	\$7794.00

SREP SUB-CONTRACT DATA

Report Author Author's University	Author's Degree	Sponsoring Lab	Performance Period		Contract Amount	Univ. Cost Share
Stephens II , Kenneth	MA 98-0809	PL/WS	01/01/98	12/31/98	\$25000.00	\$16764.00
University of North Texas, Denton, TX						
Barjaktarovic , Milica	PhD 98-0824	RL/IW	01/01/98	12/31/98	\$24976.00	\$3158.00
Electrical Engineering Wilkes University, Wilkes Barre, PA						
Batalama , Stella	PhD 98-0823	RL/C3	01/01/98	12/31/98	\$25000.00	\$5600.00
EE SUNY Buffalo, Buffalo, NY						
Bourbakis , Nikolaos	PhD 98-0832	RL/IR	01/01/98	12/31/98	\$25000.00	\$22723.00
Computer Science & Engr SUNY Binghamton, Binghamton, NY						
Dasigi , Venugopala	PhD 98-0830	RL/C3	01/01/98	12/31/98	\$25000.00	\$4000.00
Computer Science Southern Polytechnic State Univ, Marietta, GA						
Eckert , Richard	PhD 98-0825	RL/C3	01/01/98	12/31/98	\$25000.00	\$39261.00
Physics SUNY Binghamton, Binghamton, NY						
Lin , Kuo-Chi	PhD 98-0822	RL/IR	01/01/98	12/31/98	\$25000.00	\$0.00
Aerospace Engineering University of Central Florida, Orlando, FL						
Pados , Dimitrios	PhD 98-0818	RL/OC	01/01/98	12/31/98	\$25000.00	\$5600.00
Dept. of Electrical /Computer Eng. State Univ. of New York Buffalo, Buffalo, NY						
Panda , Brajendra	PhD 98-0821	RL/CA	01/01/98	12/31/98	\$25000.00	\$7113.00
Computer Science University of North Dakota, Grand Forks, ND						
Pittarelli , Michael	PhD 98-0827	RL/C3	01/01/98	12/31/98	\$24998.00	\$0.00
Systems Science SUNY OF Tech Utica, Utica, NY						
Schmalz , Mark	PhD 98-0831	RL/IR	01/01/98	12/31/98	\$24619.00	\$0.00
Dept of Computer & Info Science University of Florida, Gainesville, FL						
Ye , Nong	PhD 98-0826	RL/CA	01/01/98	12/31/98	\$25000.00	\$5000.00
Industrial Engineering Arizona State University, Tempe, AZ						
Bradley , Parker	BS 98-0834	RL/IR	01/01/98	12/31/98	\$25000.00	\$0.00
Physics Syracuse University, Syracuse, NY						
Kumar , Devendra	PhD 98-0805	ALC/SA	01/01/98	12/31/98	\$25000.00	\$11362.00
Computer Science CUNY-City College, New York, NY						
Chow , Joe	PhD 98-0806	ALC/W	01/01/98	12/31/98	\$25000.00	\$5360.00
Mechanical Engineering Florida International Univ, Miami, FL						

SREP SUB-CONTRACT DATA

Report Author Author's University	Author's Degree	Sponsoring Lab	Performance Period	Contract Amount	Univ. Cost Share
Beecken, Brian Physics Bethel College, St. Paul, MN	PhD 98-0804	WL/MN	01/01/98 12/31/98	\$19986.00	\$3997.00
Beggs, John Electrical Engineering Mississippi State University, Mississippi State,	PhD 98-0817	WL/FI	01/01/98 12/31/98	\$25000.00	\$25174.00
Bhatnagar, Raj Computer Science University of Cincinnati, Cincinnati, OH	PhD 98-0819	WL/AA	01/01/98 09/30/98	\$25000.00	\$17488.00
Blaisdell, Gregory Mechanical Engineering Purdue University, West Lafayette, IN	PhD 98-0839	WL/FI	01/01/98 12/31/98	\$25000.00	\$11844.00
Douglass, John Zoology University of Arizona, Tucson, AZ	PhD 98-0803	WL/MN	01/01/98 12/31/98	\$25000.00	\$3719.00
Hosford, William Metallurgy Univ of Michigan, Ann Arbor, MI	PHD 98-0840	WL/MN	01/01/98 12/31/98	\$25000.00	\$5000.00
Pan, Yi Computer Science University of Dayton, Dayton, OH	PhD 98-0838	WL/FI	01/01/98 12/31/98	\$25000.00	\$9486.00
Pochiraju, Kishore Mechanical Engineering Stevens Inst of Technology, Hoboken, NJ	PhD 98-0833	WL/ML	01/01/98 12/31/98	\$25000.00	\$9625.00
Shtessel, Yuri Electrical Engineering Univ of Alabama at Huntsville, Huntsville, AL	PhD 98-0841	WL/FI	01/01/98 12/31/98	\$25000.00	\$4969.00
Starzyk, Janusz Electrical Engineering Ohio University, Athens, OH	PhD 98-0801	WL/AA	01/01/98 12/31/98	\$24978.00	\$12996.00

APPENDIX 1:

SAMPLE SREP SUBCONTRACT

**AIR FORCE OFFICE OF SCIENTIFIC RESEARCH
1998 SUMMER RESEARCH EXTENSION PROGRAM
SUBCONTRACT 98-0812**

BETWEEN

**Research & Development Laboratories
5800 Uplander Way
Culver City, CA 90230-6608**

AND

**University of Central Florida
Office of Sponsored Research/ Admin#423
4000 Central Florida Blvd.
Orlando, FL 32816-0150**

REFERENCE: Summer Research Extension Program Proposal 97-0018
Start Date: 01/01/98 End Date: 12/31/98
Proposal Amount: \$25000.0
Proposal Title:
Effects of Vapor-Plasma Layer on Thick-Section Cutting and Calculation of
Modes

(1) PRINCIPAL INVESTIGATOR:

**DR Aravinda Kar
CREOL
University of Central Florida
Orlando, FL 32816-2700**

(2) UNITED STATES AFOSR CONTRACT NUMBER: F49620-93-C-0063

**(3) CATALOG OF FEDERAL DOMESTIC ASSISTANCE NUMBER (CFDA): 12.800
PROJECT TITLE: AIR FORCE DEFENCE RESEARCH SOURCES PROGRAM**

(4) ATTACHMENTS

- 1 REPORT OF INVENTIONS AND SUBCONTRACT**
- 2 CONTRACT CLAUSES**
- 3 FINAL REPORT INSTRUCTIONS**

***** SIGN SREP SUBCONTRACT AND RETURN TO RDL *****

1. BACKGROUND: Research & Development Laboratories (RDL) is under contract (F49620-93-C-0063) to the United States Air Force to administer the Summer Research Program (SRP), sponsored by the Air Force Office of Scientific Research (AFOSR), Bolling Air Force Base, D.C. Under the SRP, a selected number of college faculty members and graduate students spend part of the summer conducting research in Air Force laboratories. After completion of the summer tour participants may submit, through their home institutions, proposals for follow-on research. The follow-on research is known as the Summer Research Extension Program (SREP). Approximately 61 SREP proposals annually will be selected by the Air Force for funding of up to \$25,000; shared funding by the academic institution is encouraged. SREP efforts selected for funding are administered by RDL through subcontracts with the institutions. This subcontract represents an agreement between RDL and the institution herein designated in Section 5 below.
2. RDL PAYMENTS: RDL will provide the following payments to SREP institutions:
 - 80 percent of the negotiated SREP dollar amount at the start of the SREP research period.
 - The remainder of the funds within 30 days after receipt at RDL of the acceptable written final report for the SREP research.
3. INSTITUTION'S RESPONSIBILITIES: As a subcontractor to RDL, the institution designated on the title page will:

- a. Assure that the research performed and the resources utilized adhere to those defined in the SREP proposal.
- b. Provide the level and amounts of institutional support specified in the SREP proposal..
- c. Notify RDL as soon as possible, but not later than 30 days, of any changes in 3a or 3b above, or any change to the assignment or amount of participation of the Principal Investigator designated on the title page.
- d. Assure that the research is completed and the final report is delivered to RDL not later than twelve months from the effective date of this subcontract, but no later than December 31, 1998. The effective date of the subcontract is one week after the date that the institution's contracting representative signs this subcontract, but no later than January 15, 1998.
- e. Assure that the final report is submitted in accordance with Attachment 3.
- f. Agree that any release of information relating to this subcontract (news releases, articles, manuscripts, brochures, advertisements, still and motion pictures, speeches, trade associations meetings, symposia, etc.) will include a statement that the project or effort depicted was or is sponsored by: Air Force Office of Scientific Research, Bolling AFB, D.C.
- g. Notify RDL of inventions or patents claimed as the result of this research as specified in Attachment 1.
- h. RDL is required by the prime contract to flow down patent rights and technical data requirements to this subcontract. Attachment 2 to this subcontract

contains a list of contract clauses incorporated by reference in the prime contract.

4. All notices to RDL shall be addressed to:

RDL AFOSR Program Office
5800 Uplander Way
Culver City, CA 90230-6609

5. By their signatures below, the parties agree to provisions of this subcontract.

Abe Sopher
RDL Contracts Manager

Signature of Institution Contracting Official

Typed/Printed Name

Date

Title

Institution

Date/Phone

ATTACHMENT 2
CONTRACT CLAUSES

This contract incorporates by reference the following clauses of the Federal Acquisition Regulations (FAR), with the same force and effect as if they were given in full text. Upon request, the Contracting Officer or RDL will make their full text available (FAR 52.252-2).

FAR CLAUSES

TITLE AND DATE

52.202-1

DEFINITIONS

52.203-3

GRATUITIES

52.203-5

COVENANT AGAINST CONTINGENT FEES

52.203-6

RESTRICTIONS ON SUBCONTRACTOR
SALES TO THE GOVERNMENT

52.203-7

ANTI-KICKBACK PROCEDURES

52.203-8

CANCELLATION, RECISSION, AND
RECOVERY OF FUNDS FOR ILLEGAL OR IMPROPER
ACTIVITY

52.203-10

PRICE OR FEE ADJUSTMENT FOR ILLEGAL
OR IMPROPER ACTIVITY

52.203-12

LIMITATION ON PAYMENTS TO INFLUENCE
CERTAIN FEDERAL TRANSACTIONS

52.204-2

SECURITY REQUIREMENTS

52.209-6

PROTECTING THE GOVERNMENT'S
INTEREST WHEN SUBCONTRACTING WITH
CONTRACTORS DEBARRED, SUSPENDED, OR
PROPOSED FOR DEBARMENT

52.212-8

DEFENSE PRIORITY AND ALLOCATION
REQUIREMENTS

52.215-2

AUDIT AND RECORDS - NEGOTIATION

52.215-10

PRICE REDUCTION FOR DEFECTIVE COST
OR PRICING DATA

52.215-12	SUBCONTRACTOR COST OR PRICING DATA
52.215-14	INTEGRITY OF UNIT PRICES
52.215-8	ORDER OF PRECEDENCE
52.215-18	REVERSION OR ADJUSTMENT OF PLANS FOR POSTRETIREMENT BENEFITS OTHER THAN PENSIONS
52.222-3	CONVICT LABOR
52.222-26	EQUAL OPPORTUNITY
52.222-35	AFFIRMATIVE ACTION FOR SPECIAL DISABLED AND VIETNAM ERA VETERANS
52.222-36	AFFIRMATIVE ACTION FOR HANDICAPPED WORKERS
52.222-37	EMPLOYMENT REPORTS ON SPECIAL DISABLED VETERAN AND VETERANS OF THE VIETNAM ERA
52.223-2	CLEAN AIR AND WATER
52.223-6	DRUG-FREE WORKPLACE
52.224-1	PRIVACY ACT NOTIFICATION
52.224-2	PRIVACY ACT
52.225-13	RESTRICTIONS ON CONTRACTING WITH SANCTIONED PERSONS
52.227-1	ALT. I - AUTHORIZATION AND CONSENT
52.227-2	NOTICE AND ASSISTANCE REGARDING PATIENT AND COPYRIGHT INFRINGEMENT

52.227-10	FILING OF PATENT APPLICATIONS - CLASSIFIED SUBJECT MATTER
52.227-11	PATENT RIGHTS - RETENTION BY THE CONTRACTOR (SHORT FORM)
52.228-7	INSURANCE - LIABILITY TO THIRD PERSONS
52.230-5	COST ACCOUNTING STANDARDS - EDUCATIONAL INSTRUCTIONS
52.232-23	ALT. I - ASSIGNMENT OF CLAIMS
52.233-1	DISPUTES
52.233-3	ALT. I - PROTEST AFTER AWARD
52.237-3	CONTINUITY OF SERVICES
52.246-25	LIMITATION OF LIABILITY - SERVICES
52.247-63	PREFERENCE FOR U.S. - FLAG AIR CARRIERS
52.249-5	TERMINATION FOR CONVENIENCE OF THE GOVERNMENT (EDUCATIONAL AND OTHER NONPROFIT INSTITUTIONS)
52.249-14	EXCUSABLE DELAYS
52.251-1	GOVERNMENT SUPPLY SOURCES

DOD FAR CLAUSES**DESCRIPTION**

252.203-7001	SPECIAL PROHIBITION ON EMPLOYMENT
252.215-7000	PRICING ADJUSTMENTS
252.233-7004	DRUG FREE WORKPLACE (APPLIES TO SUBCONTRACTS WHERE THERE IS ACCESS TO CLASSIFIED INFORMATION)
252.225-7001	BUY AMERICAN ACT AND BALANCE OF PAYMENTS PROGRAM
252.225-7002	QUALIFYING COUNTRY SOURCES AS SUBCONTRACTS
252.227-7013	RIGHTS IN TECHNICAL DATA - NONCOMMERCIAL ITEMS
252.227-7030	TECHNICAL DATA - WITHHOLDING PAYMENT
252.227-7037	VALIDATION OF RESTRICTIVE MARKINGS ON TECHNICAL DATA
252.231-7000	SUPPLEMENTAL COST PRINCIPLES
252.232-7006	REDUCTIONS OR SUSPENSION OF CONTRACT PAYMENTS UPON FINDING OF FRAUD

APPENDIX 2:

SAMPLE TECHNICAL EVALUATION FORM

**SUMMER RESEARCH EXTENSION PROGRAM
TECHNICAL EVALUATION**

SREP No: 98-0810
Principal Investigator: DR Donald Leo
University of Toledo

Circle the rating level number, 1 (low) through 5 (high),
you feel best evaluate each statement and return the
completed form to RDL by fax or mail to:

RDL
Attn: SREP Tech Evals
5800 Uplander Way
Culver City, CA 90230-6608
(310) 216-5940 or (800) 677-1363

- | | |
|--|-----------|
| 1. This SREP report has a high level of technical merit. | 1 2 3 4 5 |
| 2. The SREP program is important to accomplishing the lab's mission. | 1 2 3 4 5 |
| 3. This SREP report accomplished what the associate's proposal promised. | 1 2 3 4 5 |
| 4. This SREP report addresses area(s) important to the USAF. | 1 2 3 4 5 |
| 5. The USAF should continue to pursue the research in this SREP report. | 1 2 3 4 5 |
| 6. The USAF should maintain research relationships with this SREP associate. | 1 2 3 4 5 |
| 7. The money spent on this SREP effort was well worth it. | 1 2 3 4 5 |
| 8. This SREP report is well organized and well written. | 1 2 3 4 5 |
| 9. I'll be eager to be a focal point for summer and SREP associates in the future. | 1 2 3 4 5 |
| 10. The one-year period for complete SREP research is about right. | 1 2 3 4 5 |

11. If you could change any one thing about the SREP program, what would you change:

12. What do you definitely NOT change about the SREP program?

PLEASE USE THE BACK FOR ANY OTHER COMMENTS

Laboratory Phillips Laboratory
Lab Focal Point Capt Jeanne Sullivan
Office Symbol AFRL/VSDV

Phone: (505) 846-2069

**STABLE CONTROLLER DESIGN FOR DEPLOYABLE PRECISION STRUCTURES
USING PERTURBATION THEORY**

Mark J. Balas
Professor
and
Robert J. Fuentes
Research Assistant
Department of Aerospace Engineering

University of Colorado at Boulder
Campus Box 429
Boulder, CO 80309-0429

Final Report for:
Summer Research Extension Program
Phillips Laboratory Site

April 1999

STABLE CONTROLLER DESIGN FOR DEPLOYABLE PRECISION STRUCTURES USING PERTURBATION THEORY

ROBERT J. FUENTES
MARK J. BALAS

*Center for Aerospace Structures
University of Colorado at Boulder
Boulder, CO 80309-0429*

ABSTRACT

Perturbation methods for linear operators are commonly used in the analysis of systems that tend to deviate linearly from a given reference model. The construction of an operator with a first order perturbation is investigated and the resulting eigenvalue series is constructed. It is shown that a simplified perturbation series can be obtained for matrix operators with special structure. The given theory is applied to a reduced order model (ROM) control scenario and an algorithm for computing an $O(\epsilon^3)$ eigenvalue approximation is described.

STABLE CONTROLLER DESIGN FOR DEPLOYABLE PRECISION STRUCTURES USING PERTURBATION THEORY

Robert J. Fuentes
Mark J. Balas

INTRODUCTION

Modern modeling of large dimensional physical systems primarily employs matrix methods, often via finite elements, system identification, or partial differential equations. The introduction of control to these types of systems is constrained by the reality of implementation, however, and an adequate model reduction is often needed. It has been shown that the combination of a residual mode filter (RMF) and a reduced order model (ROM) controller can ensure stability in many high order linear systems, but proper execution of this approach requires information that links the eigenvalues of the open loop to those of the closed loop system.¹ An eigenvalue perturbation method has previously been proposed for matrix operators with no multiplicities.³ In this paper, we have expanded this technique to consider any diagonalizable matrices derived from physical systems and also provide proof of the order of approximation.

Perturbation methods are particularly useful when the eigenvalues of a matrix, A^0 , are precisely known and those of the combination $A^0 + \varepsilon \Delta A$ are not. The eigenvalues of $A^0 + \varepsilon \Delta A$ are continuous functions of the real parameter ε , therefore an approximation of the perturbed spectrum can be constructed with the assumption that ε is small enough. A number of major contributions to this field were pioneered by T. Kato, where the subsequent derivations become special cases.⁴

The following definitions lay the groundwork for the construction of an eigenvalue perturbation series. The type of structure imparted upon a matrix operator of interest is illustrated and the corresponding eigenvalue series is given. An example of the application of this method to the control design of a spectral system is explained. A proof and the numerical algorithm for this approach are given in the appendices.

OPERATOR PERTURBATIONS

Let $A(\varepsilon)$ be a matrix operator with a first order perturbation,

$$\begin{aligned} A(\varepsilon) &= A^0 + \varepsilon \Delta A \\ A^0 &\in \mathbb{R}^{L \times L} \text{ (diagonalizable)} \\ \varepsilon &\in \mathbb{R}, \Delta A \in \mathbb{R}^{L \times L} \end{aligned} \quad (1)$$

the resolvent of $A(\varepsilon)$ is defined by the following inverse:

$$R(\lambda, A(\varepsilon)) \equiv [A(\varepsilon) - \lambda I]^{-1} \quad (2)$$

and is analytic everywhere except at the eigenvalues of $A(\varepsilon)$. It has been shown that the resolvent can be written in series form,

$$\begin{aligned} R(\lambda, A(\varepsilon)) &= R(\lambda, A^0) + \sum_{n=1}^{\infty} R^{(n)}(\lambda) \varepsilon^n \\ R^{(n)}(\lambda) &\equiv R(\lambda, A^0) [-\Delta A R(\lambda, A^0)]^n \end{aligned} \quad (3)$$

and the series is convergent if the following inequality holds.³

$$0 \leq \|\Delta A R(\lambda, A^0)\| |\varepsilon| < 1$$

The spectral factorization of A^0 can be expressed as a sum of S orthogonal eigen-projections, P_l .

$$A^0 = U \bar{\Lambda} U^{-1} = \sum_{k=1}^L \bar{\lambda}_k P_k' = \sum_{l=1}^S \lambda_l P_l^0 = \sum_{l=1}^S \lambda_l U E_l U^{-1} \quad (4)$$

$$E_l \equiv \begin{bmatrix} 0 & 0 & \cdot & 0 \\ 0 & I_{m \times m} & \cdot & 0 \\ \cdot & \cdot & \cdot & \cdot \\ 0 & 0 & \cdot & 0 \end{bmatrix}$$

Note that $S < N$ if any of the eigenvalues in $\bar{\Lambda}$ are repeated. The multiplicity of the l^{th} eigenvalue is computed by taking the trace of the l^{th} factor in equation (4) and corresponds to the rank of the associated matrix E_l .

$$\text{Tr}[U E_l U^{-1}] = \text{Tr}[E_l U^{-1} U] = \text{Tr}[E_l] = m_l$$

Similarly, the resolvent can be written as a sum of projections:

$$R(\lambda, A^0) = \sum_{l=1}^S \frac{P_l}{\lambda_l - \lambda} \quad (5)$$

and the reduced resolvent, $S_n(\lambda)$, is defined as the complement of the n^{th} projection.

$$S_n(\lambda) \equiv \sum_{\substack{l=1 \\ l \neq n}}^S \frac{P_l}{\lambda_l - \lambda} \quad (6)$$

Each of these eigen-projections can be recovered from an integration of the resolvent around a closed curve in the complex plane.

$$P_l = \frac{-1}{2\pi j} \oint_{\Gamma_l} R(\lambda, A^0) d\lambda \quad (7)$$

OPERATOR PARTITIONING

Assume that the linear operator $A(\varepsilon)$ can be partitioned in the following manner:

$$\begin{aligned} A(\varepsilon) &= \begin{bmatrix} A^{1,1} & \varepsilon \Delta A^{1,2} \\ \varepsilon \Delta A^{2,1} & A^{2,2} \end{bmatrix} \\ &= \begin{bmatrix} A^{1,1} & 0 \\ 0 & A^{2,2} \end{bmatrix} + \varepsilon \begin{bmatrix} 0 & \Delta A^{1,2} \\ \Delta A^{2,1} & 0 \end{bmatrix} \\ &= A^0 + \varepsilon \Delta A \end{aligned} \quad (8)$$

$A^0 \in X_{\text{BD}}$ (Block Diagonal)

$\Delta A \in X_{\text{OD}}$ (Block Off-Diagonal)

The first factor, A^0 , is an element in the space of block diagonal matrices. The perturbing matrix, ΔA , is a member of the complementary block off-diagonal space. In fact, matrix multiplication of these operators can be interpreted as mappings between these spaces.

It is said that A and B are partitioned when A is a complement matrix of B . (A and B do not overlap) If $A \in X_{\text{BD}}$; $B \in X_{\text{OD}}$, then the following relations hold:

$$(1.) A^n \in X_{BD} \quad \forall n = 1, 2, \dots$$

$$(2.) B^n \in \begin{cases} X_{BD} & \text{for } n \text{ even} \\ X_{OD} & \text{for } n \text{ odd} \end{cases}$$

$$(3.) \begin{Bmatrix} A \cdot B \\ B \cdot A \end{Bmatrix} \in X_{OD}$$

EIGENVALUE PERTURBATIONS

The k^{th} projection acting on an operator, $A(\epsilon)$, can be written as the corresponding eigenvalue scaling that projection.

$$A(\epsilon) P_k(\epsilon) = P_k(\epsilon) A(\epsilon) = \lambda_k(\epsilon) P_k(\epsilon) \quad (9)$$

$P_k(\epsilon)$ is determined from integrating the resolvent, $R(\lambda, A(\epsilon))$, around the k^{th} eigenvalue and results in an infinite series in ϵ .

$$\begin{aligned} P_k(\epsilon) &= \frac{-1}{2\pi j} \oint_{\Gamma_k} R(\lambda, A(\epsilon)) d\lambda \\ &= \frac{-1}{2\pi j} \oint_{\Gamma_k} R(\lambda, A^0) d\lambda + \sum_{n=1}^{\infty} \epsilon^n \frac{(-1)}{2\pi j} \oint_{\Gamma_k} R^n(\lambda) d\lambda \\ &= P_k^0 + \sum_{n=1}^{\infty} P_k^{(n)} \epsilon^n \end{aligned} \quad (10)$$

By taking the trace of equation (9), the k^{th} eigenvalue series is recovered.

$$\begin{aligned} \lambda_k(\epsilon) &= \frac{1}{m_k} \text{Tr}[A(\epsilon) P_k(\epsilon)] \\ &= \lambda_k^0 + \sum_{n=1}^{\infty} \lambda_k^{(n)} \epsilon^n \end{aligned} \quad (11)$$

where λ^0 represents an eigenvalue of A^0 . If $A(\epsilon)$ is partitioned into the form given in (8), the previous equation is simplified to an even series.

$$\lambda_k(\epsilon) = \lambda_k^0 + \lambda_k^{(2)} \epsilon^2 + \lambda_k^{(4)} \epsilon^4 + \dots = \lambda_k^0 + \sum_{n=1}^{\infty} \lambda_k^{(2n)} \epsilon^{2n} \quad (12)$$

Proof of this result is given in Appendix A.

DETERMINATION OF INSTABILITY IN LINEARLY PERTURBED SYSTEMS

At this point, the application of this method to the state space control problem is considered.¹ Given a linear plant governed by the following vector differential equation,

$$\begin{aligned} \dot{\underline{x}} &= A \underline{x} + B \underline{u} \\ \underline{y} &= C \underline{x} + D \underline{u} \end{aligned} \quad (13)$$

$\underline{x} \equiv$ plant state vector
 $\underline{u} \equiv$ control input vector

$\underline{y} \equiv$ output observation vector

the objective is to command the plant to follow a desired output through the use of M actuator inputs and P sensor outputs. Matrix operators B and C will have the finite rank of M and P, respectively, with the linear differential operator, A , possibly of infinite dimension.

Using ROM methodology, it is possible to transform the plant to a modal coordinate system and separate (13) into two sets of decoupled state equations. Assuming the feed-through term, D , is zero:

$$\dot{\underline{x}}_N = A_N \underline{x}_N + B_N \underline{u} \quad (14a)$$

$$\underline{y}_N = C_N \underline{x}_N$$

$$\dot{\underline{x}}_R = A_R \underline{x}_R + B_R \underline{u} \quad (14b)$$

$$\underline{y}_R = C_R \underline{x}_R$$

$$\underline{y} = \underline{y}_N + \underline{y}_R$$

The preliminary control design for the entire plant is based upon the dynamics of (14a). A finite number of modes are chosen for A_N , which is an operator of dimension N. Equation (14b) consists of modes that are not of immediate consideration and are open loop stable. ($\text{Re}(\lambda(A_R)) < 0$) ROM Nth order state estimation and feedback is characterized by the following equations:

$$\dot{\hat{\underline{x}}}_N = A_N \hat{\underline{x}}_N + B_N \underline{u} + K_N (\underline{y} - \hat{\underline{y}}_N)$$

$$\hat{\underline{y}}_N = C_N \hat{\underline{x}}_N$$

$$\underline{u} = G_N \hat{\underline{x}}_N$$

Defining the error between estimated and actual states by the vector \underline{e}_N , the differential equation governing error progression becomes the difference between the dynamic state equations:

$$\underline{e}_N = \hat{\underline{x}}_N - \underline{x}_N$$

$$\dot{\underline{e}}_N = (A_N - K_N C_N) \underline{e}_N + K_N C_R \underline{x}_R \quad (15)$$

Since the implementation of a ROM controller alone cannot guarantee stability for the closed loop system, additional control designs may be needed in order to rectify any induced instabilities.

Writing equations (14a), (14b), and (15) in matrix form, the sources of instability in the closed loop can be determined.

$$\begin{bmatrix} \dot{\underline{x}}_N \\ \dot{\underline{e}}_N \\ \dot{\underline{x}}_R \end{bmatrix} = \underbrace{\begin{bmatrix} A_N + B_N G_N & B_N G_N & 0 \\ 0 & A_N - K_N C_N & K_N C_R \\ \mathbf{B}_R \mathbf{G}_N & \mathbf{B}_R \mathbf{G}_N & A_R \end{bmatrix}}_{A_c} \begin{bmatrix} \underline{x}_N \\ \underline{e}_N \\ \underline{x}_R \end{bmatrix} \quad (16)$$

Cross-coupling terms in (16), illustrated in bold, characterize the introduction of the unwanted effects of ROM estimator feedback. One technique to resolve this problem involves the addition of an RMF design to the closed loop system.¹ Knowledge of the destabilized open loop eigenvalues of A_R is required, however, for proper implementation of this method. Previous work offers a limited perturbation approach to this problem.³

Partitioning equation (16) according to the method outlined previously, the matrix A_c can be considered to be the sum of a stable, linear operator, A^0 , and a perturbing operator, ΔA .

$$A(\varepsilon) \equiv \begin{bmatrix} A_N + B_N G_N & B_N G_N & 0 \\ 0 & A_N - K_N C_N & 0 \\ 0 & 0 & A_R \end{bmatrix} + \varepsilon \begin{bmatrix} 0 & 0 & 0 \\ 0 & 0 & K_N C_R \\ B_R G_N & B_R G_N & 0 \end{bmatrix} \quad (17)$$

$$= A^0 + \varepsilon \Delta A$$

Our objective is to find out which eigenvalues of A^0 are driven unstable by ΔA through the computation of the first few non-zero terms of the perturbation series (12). Taking $\varepsilon = 1$ would give equation (16), but convergence of the eigenvalue series solely rests upon the condition that $\|\Delta A R(\lambda, A^0)\| < 1$. Therefore, it is possible that (12) is divergent for arbitrary $\|\Delta A R(\lambda, A^0)\| \neq 1$ and may have asymptotic properties.

An example of implementation of this perturbation scheme is given for a simple Euler-Bernoulli beam with pinned ends:

$$m z_{,tt}(x,t) - 2\xi z_{,txx}(x,t) + EI z_{,xxxx}(x,t) = u(t) \delta(x - 0.1 \cdot l) \quad (18)$$

$$\text{B.C.} \quad \begin{aligned} z(0, t) &= z(l, t) = 0 \\ z_{,xx}(0, t) &= z_{,xx}(l, t) = 0 \end{aligned}$$

All of the constants in (18) are normalized with the exception of the damping ratio. ($|\xi| = 5.0 \cdot 10^{-6}$) Actuation of the beam occurs at the point $x = 0.1$. Observations of the beam displacement, $y(t)$, are taken at $x = 0.9$.

$$y(t) = \int_0^l z(x, t) \delta(x - 0.9 \cdot l) dx = z(0.9 \cdot l, t)$$

A temporal ordinary differential equation can be constructed as follows:

$$\ddot{z}_k(t) = -(k\pi)^4 z_k(t) - 2\xi(k\pi)^2 \dot{z}_k(t) + \phi_k(0.1) u(t)$$

The spatial eigenfunctions, ϕ_k , transform the input, $u(t)$, into the modal system of equations. Control is introduced to dampen the first few modes, where $k = 1, 2$, and 3 . There exist an infinite number of residual modes ($k \geq 4$), but for computational purposes only the next 12 are considered. Putting the equations derived from (13) in the form given in (17), we can calculate an estimate of the residual eigenvalue resulting from the control design:

$$\lambda_k(\varepsilon)|_{\varepsilon=1} \cong \lambda_k^0 + \lambda_k^{(2)}$$

The results of this $O(\varepsilon^3)$ approximation are illustrated in Figure 1. From this graph, it can be determined that modes $n = 5, 7$ are driven unstable. Using these modes in an RMF control design, exponential stability for the entire system can be achieved.

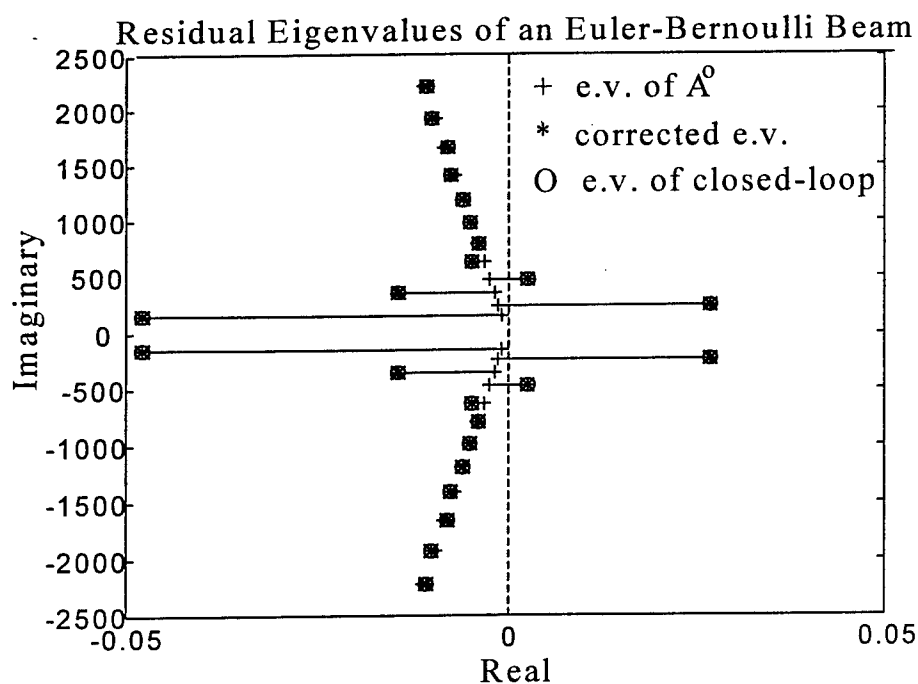


FIGURE 1.

CONCLUSIONS

A generalized perturbation approach has been developed for use in structural control applications. Given a block diagonal linear operator with a first order perturbation in partitioned form, it has been shown that there exists a corresponding even perturbation series. An algorithm is outlined to find the $O(\epsilon^3)$ eigenvalue correction for diagonalizable block diagonal operators. Application of this technique to a simple structural model illustrates that this method is a viable approach to ROM-RMF control design. This procedure can be successfully applied to a variety of realistic structural models, including those based on a finite element design or a system identification model.

ACKNOWLEDGMENTS

This research was supported by the Air Force Office of Scientific Research Summer Research Extension Program and the National Science Foundation. Any opinions, findings, and conclusions stated in this publication are those of the authors and do not necessarily reflect the views of AFOSR or NSF.

APPENDIX A

Equation (12) is derived from (11) as follows:
Let $A(\epsilon) = A^0 + \epsilon \Delta A$, where $A^0 \in X_{BD}$ and $\Delta A \in X_{OD}$.

$$\lambda_k(\epsilon) = \frac{1}{m_k} \text{Tr}[A(\epsilon) P_k(\epsilon)] \quad (A1)$$

$$\begin{aligned}
&= \frac{1}{m_k} \text{Tr}[(A(\varepsilon) - \lambda_k^0 I) P_k(\varepsilon) + \lambda_k^0 P_k(\varepsilon)] \\
&= \lambda_k^0 + \frac{1}{m_k} \text{Tr}[(A(\varepsilon) - \lambda_k^0 I) P_k(\varepsilon)] \\
\lambda_k(\varepsilon) - \lambda_k^0 &= \frac{1}{m_k} \text{Tr}[(A(\varepsilon) - \lambda_k^0 I) P_k(\varepsilon)]
\end{aligned}$$

Rewriting part of the previous result:

$$\begin{aligned}
(A(\varepsilon) - \lambda_k^0 I) P_k(\varepsilon) &= \frac{-1}{2\pi j} \oint_{\Gamma_k} (A(\varepsilon) - \lambda_k^0 I) R(\lambda, A(\varepsilon)) d\lambda \\
&= \frac{-1}{2\pi j} \oint_{\Gamma_k} (A(\varepsilon) - \lambda I + \lambda I - \lambda_k^0 I) R(\lambda, A(\varepsilon)) d\lambda \\
&= \frac{-1}{2\pi j} \oint_{\Gamma_k} (A(\varepsilon) - \lambda I) R(\lambda, A(\varepsilon)) d\lambda + \frac{-1}{2\pi j} \oint_{\Gamma_k} (\lambda - \lambda_k^0) R(\lambda, A(\varepsilon)) d\lambda
\end{aligned} \tag{A2}$$

The first integral in (A2) is analytic since $(A(\varepsilon) - \lambda I) \cdot R(\lambda, A(\varepsilon)) = I$. Therefore:

$$\lambda(\varepsilon) - \lambda_k^0 = \frac{-1}{2\pi j m_k} \text{Tr} \left[\oint_{\Gamma_k} (\lambda - \lambda_k^0) R(\lambda, A(\varepsilon)) d\lambda \right] \tag{A3}$$

A series form is desired for (A3). Rewriting the kernel of this equation:

$$(\lambda - \lambda_k^0) R(\lambda, A(\varepsilon)) = (\lambda - \lambda_k^0) R(\lambda, A^0) + \sum_{n=1}^{\infty} (\lambda - \lambda_k^0) R^{(n)}(\lambda) \varepsilon^n \tag{A4}$$

Integrating the first term in the right hand side of the equation, we find that this is completely analytic inside Γ_k .

$$\begin{aligned}
\oint_{\Gamma_k} (\lambda - \lambda_k^0) R(\lambda, A^0) d\lambda &= \oint_{\Gamma_k} (\lambda - \lambda_k^0) \sum_l \frac{P_l^0}{\lambda_l^0 - \lambda} d\lambda \\
&= \oint_{\Gamma_k} (\lambda - \lambda_k^0) \left[\frac{P_k^0}{\lambda_k^0 - \lambda} + S_k^0(\lambda) \right] d\lambda = 0
\end{aligned}$$

From equation (A4):

$$\begin{aligned}
\lambda(\varepsilon) - \lambda_k^0 &= \frac{-1}{2\pi j m_k} \text{Tr} \left[\oint_{\Gamma_k} \sum_{n=1}^{\infty} (\lambda - \lambda_k^0) R^{(n)}(\lambda) \varepsilon^n d\lambda \right] \\
&= \frac{-1}{2\pi j m_k} \text{Tr} \left[\oint_{\Gamma_k} \sum_{n=1}^{\infty} (-1)^n (\lambda - \lambda_k^0) \cdot R(\lambda, A^0) [\Delta A R(\lambda, A^0)]^n \varepsilon^n d\lambda \right]
\end{aligned} \tag{A5}$$

Using the cyclic permutation property of the trace operator:

$$\text{Tr} \left[\frac{d}{d\lambda} [\Delta A R(\lambda, A^0)]^n \right] = n \cdot \text{Tr} [R(\lambda, A^0) [\Delta A R(\lambda, A^0)]^n] \tag{A6}$$

Substitution of (A6) into equation (A5) yields a form that can be integrated by parts:

$$\begin{aligned}\lambda(\varepsilon) - \lambda_k^0 &= \frac{-1}{2\pi j m_k} \text{Tr} \left[\oint_{\Gamma_k} \sum_{n=1}^{\infty} \frac{(-1)^n}{n} (\lambda - \lambda_k^0) \cdot \frac{d}{d\lambda} [\Delta A R(\lambda, A^0)]^n \varepsilon^n d\lambda \right] \\ &= \frac{-1}{2\pi j m_k} \text{Tr} \left[\oint_{\Gamma_k} \frac{d}{d\lambda} \left[\sum_{n=1}^{\infty} \frac{(-1)^n}{n} (\lambda - \lambda_k^0) [\Delta A R(\lambda, A^0)]^n \varepsilon^n \right] d\lambda - \oint_{\Gamma_k} \sum_{n=1}^{\infty} \frac{(-1)^n}{n} [\Delta A R(\lambda, A^0)]^n \varepsilon^n d\lambda \right]\end{aligned}\quad (\text{A7})$$

The first term in (A7) can be evaluated about the circle centered at λ^0 . Making the substitution: $\lambda = \lambda_k^0 + r e^{j\theta}$, this integral is zero:

$$\oint_{\Gamma_k} \frac{d}{d\lambda} \left[\sum_{n=1}^{\infty} \frac{(-1)^n}{n} (\lambda - \lambda_k^0) [\Delta A R(\lambda, A^0)]^n \varepsilon^n \right] d\lambda = \sum_{n=1}^{\infty} \frac{(-1)^n r e^{j\theta}}{n} [\Delta A R(\lambda_k^0 + r e^{j\theta}, A^0)]^n \varepsilon^n \Big|_0^{2\pi} = 0$$

The remaining non-zero term in (A7) gives a series in ε . By equation (10), it is seen that the remainder of (A7) can be rewritten:

$$\begin{aligned}\lambda_k(\varepsilon) - \lambda_k^0 &= \frac{1}{2\pi j m_k} \text{Tr} \left[\oint_{\Gamma_k} \sum_{n=1}^{\infty} (-\Delta A R(\lambda, A^0)) \cdot \frac{(-1)^{n-1}}{n} [\Delta A R(\lambda, A^0)]^{n-1} \varepsilon^n d\lambda \right] \\ &= \frac{1}{m_k} \text{Tr} \left[\Delta A \cdot \sum_{n=1}^{\infty} \frac{\varepsilon^n}{n} \cdot \left(\frac{-1}{2\pi j} \oint_{\Gamma_k} \frac{(-1)^{n-1} R(\lambda, A^0) [\Delta A R(\lambda, A^0)]^{n-1} d\lambda}{R^{(n-1)}(\lambda)} \right) \right] \\ &= \frac{1}{m_k} \text{Tr} \left[\Delta A \cdot \sum_{n=1}^{\infty} \frac{\varepsilon^n P_k^{(n-1)}}{n} \right]\end{aligned}$$

For each coefficient, $\lambda_k^{(n)}$, in this expansion:

$$\lambda_k^{(n)} = \frac{1}{m_k n} \text{Tr} [\Delta A P_k^{(n-1)}] \quad (\text{A8})$$

Integrating $P^{(n-1)}$ yields an expansion in terms of the reduced resolvent, $S(\lambda_k)$, and the projection, P^0 .

$$\lambda_k^{(n)} = \frac{1}{m_k n} \text{Tr} \left[\sum_{\substack{l_1 + \dots + l_n = n-1 \\ l_i \geq 0}} \Delta A S_k^{(l_1)}(\lambda_k) \Delta A S_k^{(l_2)}(\lambda_k) \dots \Delta A S_k^{(l_n)}(\lambda_k) \right]$$

where $S^{(0)} \equiv P^0$ and $S^{(i)} \equiv S^i$ for $i \geq 1$.

Writing the previous equation in terms of an ordered multiplication:

$$\lambda_k^{(n)} = \frac{1}{m_k n} \text{Tr} \left[\sum_{\substack{l_1 + \dots + l_n = n-1 \\ l_i \geq 0}} \prod_{r=1}^n [\Delta A S_k^{(l_r)}(\lambda_k)] \right] \quad (\text{A9})$$

Since $\Delta A \in X_{OD}$ and $S^{(i)} \in X_{BD}$ for all $j \geq 0$ by definition (1.) of the third section, then $\Delta A S^{(i)} \in X_{OD}$ by definition (3.). Therefore, equation (A9) is the sum of a multiplication of n block off-diagonal matrices that are contained in either X_{OD} or X_{BD} , depending on whether n is

odd or even. The trace of a block off diagonal matrix is zero, therefore the only non-zero coefficients in (11) are even. Q.E.D.

APPENDIX B

Assume all of the eigenvalues of the diagonalizable block diagonal matrix, $A^0 \in \mathbb{R}^{L \times L}$, and the corresponding right and left eigenvector matrices, U and U^{-1} are given. An algorithm for computing the first two non-zero terms in the eigenvalue perturbation series is outlined below.

- 1.) Diagonalize A^0 , where the eigenvalues in $\bar{\Lambda}^{i,i}$ are ordered $\text{Re}(\bar{\lambda}^{i,i}_1) \geq \text{Re}(\bar{\lambda}^{i,i}_2) \geq \dots \geq \text{Re}(\bar{\lambda}^{i,i}_L)$:

$$A^0 = \begin{bmatrix} A^{1,1} & 0 \\ 0 & A^{2,2} \end{bmatrix} \\ = \begin{bmatrix} U^{1,1} & 0 \\ 0 & U^{2,2} \end{bmatrix} \cdot \begin{bmatrix} \bar{\Lambda}^{1,1} & 0 \\ 0 & \bar{\Lambda}^{2,2} \end{bmatrix} \cdot \begin{bmatrix} (U^{1,1})^{-1} & 0 \\ 0 & (U^{2,2})^{-1} \end{bmatrix}$$

- 2.) Form the eigen-projections $P^{i,i}_k$ from P'_k for each distinct eigenvalue:

$$A^0 = \begin{bmatrix} \sum_{k=1}^{N1} \bar{\lambda}_k^{1,1} P'_k & 0 \\ 0 & \sum_{k=1}^{N2} \bar{\lambda}_k^{2,2} P'_k \end{bmatrix}$$

$N(1) = \#$ of eigenvalues in $\bar{\Lambda}^{1,1}$

$N(2) = \#$ of e.v. in $\bar{\Lambda}^{2,2}$.

For $i = 1$ to 2,

$k = 1$

$L = N(i)$

$P' = 0^{L \times L}$

$P' = \text{Col}_1(U^{i,i}) \otimes \text{Row}_1((U^{i,i})^{-1}) **$

$m(k, i) = 1$

For $j = 2$ to L ,

$P_{\text{temp}} = \text{Col}_j(U^{i,i}) \otimes \text{Row}_j((U^{i,i})^{-1})$

If $\bar{\lambda}^{i,i}_{j-1} = \bar{\lambda}^{i,i}_j$,

$P' = P' + P_{\text{temp}}$

$m(k, i) = m(k, i) + 1$

Else,

$P^{i,i}_k = P'$

$\bar{\lambda}^{i,i}_k = \bar{\lambda}^{i,i}_{j-1}$

$k = k + 1$

$m(k, i) = 1$

$P' = P_{\text{temp}}$

End If

End

$$\begin{aligned} P^{i,i}_k &= P' \\ \lambda^{i,i}_k &= \bar{\lambda}^{i,i}_L \\ S(i) &= k \end{aligned}$$

End

** \otimes denotes an outer-product.

3.) Compute reduced resolvents, correcting coefficients, $\lambda^{(2)}_k$, and eigenvalue estimates:

For $k = 1$ to $S(1)$,

$$\begin{aligned} S_k^{1,1} &= \sum_{j=1}^{S(1)} \frac{P_j^{1,1}}{\lambda_k^{2,2} - \lambda_j^{1,1}} \\ (\lambda_k^{1,1})^{(2)} &= \frac{1}{m(k,1)} \text{Tr} [\Delta A^{1,2} S_k^{2,2} \Delta A^{2,1} P_k^{1,1}] \\ \lambda_k^{1,1}(\varepsilon) &= \lambda_k^{1,1} + (\lambda_k^{1,1})^{(2)} \varepsilon^2 \end{aligned}$$

End

For $k = 1$ to $S(2)$,

$$\begin{aligned} S_k^{2,2} &= \sum_{j=1}^{S(2)} \frac{P_j^{2,2}}{\lambda_k^{1,1} - \lambda_j^{2,2}} \\ (\lambda_k^{2,2})^{(2)} &= \frac{1}{m(k,2)} \text{Tr} [\Delta A^{2,1} S_k^{1,1} \Delta A^{1,2} P_k^{2,2}] \\ \lambda_k^{2,2}(\varepsilon) &= \lambda_k^{2,2} + (\lambda_k^{2,2})^{(2)} \varepsilon^2 \end{aligned}$$

End

REFERENCES

1. M. Balas, Finite-Dimensional Controllers for Linear Distributed Parameter Systems: Exponential Stability Using Residual Mode Filters, *J. Math. Anal. Appl.*, Vol. 133, No.2, 1988.
2. M. Balas et. al., Low Order Control of Large Aerospace Structures Using Residual Mode Filters, CU-CSSC-88-05, 1988.
3. A. Gooyabadi, Doctoral Thesis, University of Colorado at Boulder, Boulder, CO, 1992.
4. T. Kato, Perturbation Theory for Linear Operators, Springer-Verlag, New York, 1980 Reprint.
5. B. Reisenauer and M. Balas, Master's Thesis, CSI Compensation for Reduced-Order Model Based Control of a Flexible Robot Manipulator, 1990.

Dr. Neb Duric's report was not available at the time of publication.

PERTURBATION ANALYSIS OF THE NATURAL FREQUENCIES OF TARGETS
IN INHOMOGENEOUS MEDIA

George W. Hanson
Associate Professor
Department of Electrical Engineering and Computer Science

University of Wisconsin-Milwaukee
3200 North Cramer Street
Milwaukee, Wisconsin 53211

Final Report for:
Summer Faculty Research Extension Program
Phillips Laboratory
Kirtland Air Force Base

Sponsored by:
Air Force Office of Scientific Research
Bolling Air Force Base, DC

and

Phillips Laboratory
Kirtland Air Force Base

December 1998

PERTURBATION ANALYSIS OF THE NATURAL FREQUENCIES OF TARGETS IN INHOMOGENEOUS MEDIA

George W. Hanson
Associate Professor
Department of Electrical Engineering and Computer Science
University of Wisconsin-Milwaukee

Abstract

An accurate electromagnetic formulation to determine the natural frequencies of a target residing in an inhomogeneous environment was developed. This formulation is applicable to a simplified model of an aircraft over a realistic earth or ocean, where both environments are considered as being large-scale planarly inhomogeneous. Although such configurations can be modeled by purely numerical procedures, the formulation presented here provides a simple, quasi-analytical perturbation formula which is easy to apply and interpret. Results are presented to validate the theory, and further application of the method to a wider class of target geometries is discussed.

ELECTROMAGNETIC MODELING OF COMPLEX DIELECTRIC/METALLIC MINES IN A LAYERED EARTH

George W. Hanson
Associate Professor
Department of Electrical Engineering and Computer Science
University of Wisconsin-Milwaukee

Contents

Abstract.....	4
I. Introduction and Problem Significance.....	4
II. Background Theory.....	7
III. Formulation of Electromagnetic Model and Perturbation Formula	9
i. Perturbation Theory	12
ii. Scaling Relations	16
IV Results and Discussion	18
VI. References	20

I. Introduction and Problem Significance

The electromagnetic interaction of a target and the background environment in which it resides is an important problem in the area of target detection and discrimination. All targets have some natural characteristic features which are associated with the target's size, shape, and material composition. One such natural characteristic is the set of complex natural frequencies (damped resonances) which can be used as an aid to target detection and discrimination schemes, and in the interpretation of electromagnetic interaction data. These natural frequencies are manifested in the electromagnetic return signal in a radar system, and form the basis of the singularity expansion method (SEM) conceptualized by Carl Baum [1]. An important attribute of the natural frequencies is that they are aspect independent, which is a very convenient property for a target discrimination scheme.

When a target is immersed in an inhomogeneous environment, such as an aircraft flying low over the ground or water, the target's natural frequencies are modified from their free-space values by the presence of the inhomogeneities. For a target essentially in free-space, such as an aircraft at sufficient elevation, some set of the natural frequencies can be used to identify the target. For targets not isolated in free-space, an extremely large number of possible environments exist in which the target may reside. Since it would be impractical to numerically study the effect of each separate environment on some target of interest, simple formulas which describe the target-environment interaction are desirable. In this way, the effect of different environments on the natural frequencies of a target can be analyzed. Aside from specific numerical results, qualitative results provided by these simple formulas are of use in studying in some general manner the interaction of a target and its background environment. For instance, does the presence of a secondary planar layer beyond the primary air/ground (or air/ocean) interface significantly affect the target's natural frequencies? For what range of separations between the target and the air/ground (air/ocean) interface can the target be considered as residing in free-space, and for which separations does the interface play a significant role? Investigation of these types of questions can be pursued with the aid of the proposed simple analytical formulas in an efficient manner.

In this report I describe an exact integral equation formulation for the determination of the natural

frequencies of a target embedded in an inhomogeneous environment. This leads, using appropriate approximations, to a simple analytical formula [2] which describes the influence of the background environment on a target's natural frequencies. The formula will be applied to several configurations of simple targets embedded in inhomogeneous planar environments. These formulas, while not eliminating the need for numerically obtained full-wave solutions, will provide significant physical insight into the target-environment interaction problem, in a similar manner for which related perturbation formulas have been used for targets over a perfect ground plane [3]. The latter formulas can be shown to be special cases of the more general formula presented here.

II. Background Theory

Traditionally, natural frequencies have been computed for finite-sized objects in free-space. Recently there has been some attention devoted to the determination of the natural frequencies of an object in the presence of a layered medium [8],[9]. Such efforts have been directed towards accounting for realistic environments such as an air-sea or air-ground interface in target detection and identification schemes.

Early in the development of SEM it was shown that for an integral equation (IE) treatment of finite-sized objects in free-space, the operator inverse to the integral operator is a meromorphic function in the complex frequency plane [10], leading to the occurrence of only pole-singularities in the current density response of the object (perhaps with the addition of an entire function term depending on the chosen time-space origin for the problem [11]). With this in mind, some early work on the natural frequencies of thin-wire scatterers in free-space was described in [12]. A short time later the natural system frequencies of coupled wires were studied [13],[14]. It was found that the natural system frequencies of the two-wire configuration exhibited some interesting characteristics as wire separation was varied. In particular, for certain configurations the natural frequencies of two identical coupled wires tended to spiral about the natural frequency of the isolated wire as spacing between the wires was varied over some intermediate distance. As separation was further increased, the system resonances moved off towards the origin in the complex frequency plane, and other system modes moved in to take their place, again spiraling around the dominant isolated natural frequency.

Since the natural frequencies of a coupled system are rigorously obtained from a complicated (usually integral) system of equations, simple approximate formulas which describe the natural system resonance behavior as a function of body separation are of interest. For intermediate separations, perturbation formulas have been obtained which relate the natural system frequencies of two or more objects to the natural frequencies of the same objects when isolated. Two related classes of perturbation solution have been obtained, both based upon the exact integral-operator description of the coupled system. The first method yields a quasi-analytic formula for the system frequencies of an object and a mirror object, separated by some intermediate distance. The resulting formula involves a numerically computed coefficient which only depends upon the isolated object's characteristics, multiplied by an exponential term which is a function of the separation between the objects [3]. The second method is more numerical in nature, yet represents a considerable simplification of the exact IEs and is applicable to a more general system of coupled bodies [15]. The formulation described in [15] was subsequently applied to a variety of coupled objects [16]-[18]. For the case of large separation between coupled objects, the system frequencies tend towards the origin in the complex frequency plane. An asymptotic formulation for this situation is described in [4].

Although the previously described perturbation formulations have been developed for the natural frequencies of two or more coupled objects, the described spiraling behavior is not limited to coupling between finite-sized objects in homogeneous space. For instance, in [8] it was observed that the lowest-order natural frequency of a wire ring over a lossy dielectric half-space exhibited a similar behavior, as spacing between the wire and material interface was varied. Similar findings were reported in [9] for a straight wire embedded in a lossy ground in the vicinity of the air-ground interface, and early work in [19] describes results for a wire above a lossy ground. This report details a perturbation formula for the natural frequencies of an target over multi-layered media. This perturbation formula is based on an exact integral equation formulation. Subsequent approximations are then made to yield a useful formula which relates the natural frequencies of an object over a multi-layered medium to the natural frequencies of an object when in free-space.

It should be noted that for a finite-sized object embedded in a laterally infinite layered environment, the operator inverse to the integral operator is not a meromorphic function in the complex frequency plane [20]. Branch-point singularities also exist, which are associated with the

propagation of surface waves in the layered medium. Although an SEM expansion for the current density response then includes branch-cut as well as pole singularity terms, the natural frequencies of such objects are still very important, and associated pole singularities may be expected to dominant the response for a wide variety of environments.

III. Formulation of Electromagnetic Model and Perturbation Formula

Consider a target in the presence of a planarly layered medium, as depicted in Fig. 1. For a specified impressed field an integral equation (IE) can be formed which leads to the determination of the current induced on/in the object. For generality, the object will be considered to either have a perfectly conducting surface, leading to a surface IE, or be composed of a lossy dielectric ($\epsilon = \epsilon_2$), leading most simply to a volume IE. In either case, an electric field integral equation (EFIE) can be formed as

$$\langle \vec{Z}(\vec{r}|\vec{r}',s) ; \vec{J}(\vec{r}',s) \rangle = \vec{E}^{(inc)}(\vec{r},s) \quad (1)$$

where the bracket notation indicates a real inner product over common spatial coordinates. For perfectly conducting objects the surface IE is enforced over the surface of the body, whereas for dielectric objects the volume IE is enforced over the volume of the body.

The kernel for either IE can be written as

$$\begin{aligned} \vec{Z}(\vec{r}|\vec{r}',s) &= s\mu_0 \vec{I}_{(s)}(\vec{r}) \cdot \left[\vec{G}^h(\vec{r}|\vec{r}',s) + \vec{G}^s(\vec{r}|\vec{r}',s) \right] \cdot \vec{I}_{(s)}(\vec{r}') \\ &= \vec{Z}^h(\vec{r}|\vec{r}',s) + \vec{Z}^s(\vec{r}|\vec{r}',s) \end{aligned} \quad (2)$$

where \vec{Z}^h is the homogeneous space kernel (principal part of \vec{Z}), and \vec{Z}^s is the scattered kernel which accounts for the material layering. In (2), $\vec{I}_{(s)}$ distinguishes between surface and volume formulations, where for the surface IE

$$\vec{I}_s(\vec{r}) = \vec{I}_t(\vec{r}) = \vec{I} - \vec{I}_s(\vec{r}) \vec{I}_s(\vec{r}) \quad (3)$$

is the transverse dyadic at \vec{r} on S, where $\vec{I}_s(\vec{r})$ is the unit normal to S at \vec{r} , with $\vec{I} = \vec{I}_x \vec{I}_x + \vec{I}_y \vec{I}_y + \vec{I}_z \vec{I}_z$ being the identity dyadic. The transverse dyadic is used to enforce the tangential boundary condition for the electric field at the surface of a perfectly conducting object. For the lossy dielectric object, $\vec{I}_p(\vec{r}) = \vec{I}$. The Green's functions are defined by

$$\begin{aligned} (\vec{r}|\vec{r}',s) = PV \left[\vec{I} - \gamma^{-2} \nabla \nabla \right] \cdot \vec{g}^h(\vec{r}|\vec{r}',s) + \gamma^{-2} \vec{L}(\vec{r}) \delta(\vec{r} - \vec{r}') \\ + \gamma^{-2} \left(\frac{\epsilon_2}{\epsilon_c} - 1 \right)^{-1} \vec{I} \delta(\vec{r} - \vec{r}') \end{aligned} \quad (4)$$

$$\vec{G}^s(\vec{r}|\vec{r}',s) = \left[\vec{I} - \gamma^{-2} \nabla \nabla \right] \cdot \vec{g}^s(\vec{r}|\vec{r}',s) \quad (5)$$

where the last term in (4) only occurs for the volume IE. For a perfectly conducting object (surface IE), the last term in (4) is omitted. In (4), \vec{L} is a depolarizing dyadic [21], the contribution from which is removed by the transverse dyad for the surface IE, but remains for the volume IE. The PV notation indicates that the corresponding term be integrated in a principal value sense by removing from the integration a small patch (surface IE) or small volume (volume IE) centered at $\vec{r} = \vec{r}'$.

In (4),(5), the potential Green's terms are

$$\begin{aligned} \vec{g}^h(\vec{r}|\vec{r}',s) = \vec{I} \frac{e^{-\gamma R}}{4\pi R} \\ = \int_{-\infty}^{\infty} \int \frac{\vec{I}}{2(2\pi)^2 p} e^{-p(z-z')} e^{j\vec{\lambda} \cdot (\vec{r} - \vec{r}')} d^2\lambda \end{aligned} \quad (6)$$

for a homogeneous space in either spatial or spectral form, and

$$\vec{g}^s(\vec{r}|\vec{r}',s) = \int_{-\infty}^{\infty} \int \frac{\vec{F}(\lambda,s)}{2(2\pi)^2 p} e^{-p(z+z')} e^{j\vec{\lambda} \cdot (\vec{r} - \vec{r}')} d^2\lambda \quad (7)$$

for the scattered part. In the above, $\gamma = s\sqrt{\mu_0\epsilon_c}$, $R = |\vec{r} - \vec{r}'|$, $\vec{\lambda} = \vec{I}_x k_x + \vec{I}_y k_y$, $d^2\lambda = dk_x dk_y$, $\lambda^2 = k_x^2 + k_y^2$, and $p = \sqrt{\lambda^2 + \gamma^2}$. The wavenumber parameter $p(\lambda)$ is multivalued, necessitating the definition of an

appropriate branch cut in the complex λ -plane. Unless otherwise specified, we'll consider the permittivity parameter to be generally complex, i.e., $\epsilon = \epsilon^{re} + \sigma/s$, with (ϵ^{re}, σ) the real-valued permittivity and conductivity, respectively.

In the scattered Greens' function, $\tilde{F}(\lambda, s)$ is an amplitude dyadic which is obtained by matching boundary conditions at the layering interfaces. For the configuration depicted in Fig. 1, this term can be expressed as

$$\tilde{F}(\lambda, s) = (\bar{I}_x \bar{I}_x + \bar{I}_y \bar{I}_y) R_t(\lambda, s) + \bar{I}_z \bar{I}_z R_n(\lambda, s) + \bar{I}_z (\bar{I}_x j k_x + \bar{I}_y j k_y) R_c(\lambda, s) \quad (8)$$

where R_t, R_n, R_c are given in [22] for the tri-layered environment shown. Note that the presence of additional layering below the object, i.e., more than three layers, only affects the coefficients R_t, R_n, R_c , and not the general form of (8).

Associated with (1) are natural mode solutions which exist in the absence of an excitation [1]. These modes (natural frequencies and corresponding natural current distributions) satisfy the homogeneous form of (1),

$$\langle \tilde{Z}(\vec{r}|\vec{r}', s_\alpha) ; \vec{J}_\alpha(\vec{r}') \rangle = \vec{0} \quad (9)$$

where s_α is the natural frequency, and \vec{J}_α is the associated natural current distribution (surface or volume). Equation (9) can be cast as a scalar relation by dot multiplication on the left by the natural mode current, leading to

$$\langle \vec{J}_\alpha(\vec{r}) ; \tilde{Z}(\vec{r}|\vec{r}', s_\alpha) ; \vec{J}_\alpha(\vec{r}') \rangle = 0. \quad (10)$$

It is convenient to define a local coordinate system centered at some appropriate point in V as shown in Fig. 2, such that $\vec{r} = \vec{r}_c + \vec{r}_1$. For simplicity, assume $\vec{r}_c = \bar{I}_z \frac{b}{2}$. The integral relation (10) can

be expressed in terms of the local coordinate system as

$$\langle \vec{J}_\alpha(\vec{r}_1) ; \tilde{Z}(\vec{r}_1|\vec{r}_1, s_\alpha, b) ; \vec{J}_\alpha(\vec{r}_1) \rangle = 0. \quad (11)$$

In (11), the spectral forms for the Green's functions have become

$$\begin{aligned}\bar{g}^h(\bar{r}_1|\bar{r}'_1,s) &= \int \int_{-\infty}^{\infty} \frac{\bar{I}}{2(2\pi)^2 p} e^{-p(z_1-z'_1)} e^{j\bar{\lambda} \cdot (\bar{r}_1 - \bar{r}'_1)} d^2\lambda \\ \bar{g}^s(\bar{r}_1|\bar{r}'_1,s,b) &= \int \int_{-\infty}^{\infty} \frac{\bar{F}(\lambda,s)}{2(2\pi)^2 p} e^{-p b} e^{-p(z_1+z'_1)} e^{j\bar{\lambda} \cdot (\bar{r}_1 - \bar{r}'_1)} d^2\lambda\end{aligned}\quad (12)$$

with an associated change of coordinates in (4), (5).

i. Perturbation Theory

In this section we will consider the case when the material layering has a sufficiently small effect on the object's natural frequency that it may be treated as a perturbation of the homogeneous space result. First, define the appropriate relationship for the situation $\epsilon_f = \epsilon_s = \epsilon_c$ (object in homogeneous space), such that $\vec{Z}^s = \vec{0}$, and (11) becomes

$$\left\langle \bar{J}_\alpha^h(\bar{r}_1); \bar{Z}^h(\bar{r}_1|\bar{r}_1, s_\alpha^h); \bar{J}_\alpha^h(\bar{r}_1) \right\rangle = 0. \quad (13)$$

For later purposes, define the special case of the homogeneous space being free-space as

$$\left\langle \bar{J}_\alpha^0(\bar{r}_1); \bar{Z}^0(\bar{r}_1|\bar{r}_1, s_\alpha^0); \bar{J}_\alpha^0(\bar{r}_1) \right\rangle = 0. \quad (14)$$

Returning to (11), under certain conditions, $\|\bar{g}^s\| \ll \|\bar{g}^h\|$ (for some appropriately defined norm), and \vec{Z}^s can be treated as a small perturbation of \vec{Z}^h in (2). One such situation would be 'b' large (large separation between the object and the nearest material interface), but this is not necessary if the material parameters of the layers differ only slightly from the material parameters of the half-space in which the object resides. If we can assume $s_\alpha \approx s_\alpha^h + \Delta s_\alpha$, where s_α^h is the α th natural frequency of the object when in a homogeneous space characterized by (μ_0, ϵ_c) and Δs_α represents a small perturbation, then we may expect that the natural mode currents may be expressed as $\bar{J}_\alpha \approx \bar{J}_\alpha^h + \Delta \bar{J}_\alpha$.

With the above assumption, expand the kernel in a Taylor's series about s_α^h

$$\tilde{Z}(\vec{r}_1'|\vec{r}_1', s_\alpha) \approx \tilde{Z}(\vec{r}_1|\vec{r}_1', s_\alpha^h) + \frac{\partial}{\partial s} \tilde{Z}(\vec{r}_1|\vec{r}_1', s_\alpha^h) \Delta s_\alpha + O(\Delta s_\alpha^2) \quad (15)$$

where $O(\Delta s_\alpha^2)$ indicates terms which are at least quadratically small. It is understood in the second term that $s = s_\alpha^h$ is substituted after the frequency derivative is evaluated. Insertion of the two-term approximation for $(\tilde{J}_\alpha, s_\alpha)$ into (11) and retaining the first non-vanishing term leads to the perturbation equation

$$\left\langle \tilde{J}_\alpha^h(\vec{r}_1); \frac{\partial}{\partial s} \tilde{Z}^h(\vec{r}_1|\vec{r}_1', s_\alpha^h) \Delta s_\alpha + \tilde{Z}^s(\vec{r}_1|\vec{r}_1', s_\alpha^h, b); \tilde{J}_\alpha^h(\vec{r}_1) \right\rangle = 0. \quad (16)$$

The above can be solved for the first-order perturbation in natural frequency due to the planar layering as

$$\Delta s_\alpha = - \frac{\left\langle \tilde{J}_\alpha^h(\vec{r}_1); \tilde{Z}^s(\vec{r}_1|\vec{r}_1', s_\alpha^h, b); \tilde{J}_\alpha^h(\vec{r}_1) \right\rangle}{\left\langle \tilde{J}_\alpha^h(\vec{r}_1); \frac{\partial}{\partial s} \tilde{Z}^h(\vec{r}_1|\vec{r}_1', s_\alpha^h); \tilde{J}_\alpha^h(\vec{r}_1) \right\rangle}. \quad (17)$$

While (17) may be computationally accurate under the assumption $\|\tilde{g}^s\| \ll \|\tilde{g}^h\|$, and represents an efficient formulation compared to the exact expression (10), in its present form it does not provide much physical insight into the effect of planar layering on the natural frequencies of an object. Accordingly, further restrictions may be stated to simplify (17). Let us assume that the separation 'b' between the object and the nearest interface is sufficiently large relative to dimensions of the object. For this case (12) can be reorganized as

$$\tilde{g}^s(\vec{r}_1|\vec{r}_1', s, b) = \int \int_{-\infty}^{\infty} \left\{ \frac{\tilde{F}(\lambda, s)}{2(2\pi)^2 p} e^{-p(z_1 + z_1')} e^{j\vec{\lambda} \cdot (\vec{r}_1 - \vec{r}_1')} \right\} e^{-p b} d^2 \lambda \quad (18)$$

where the term in brackets is slowly varying compared to $e^{-p b}$ for 'b' large. The largest contribution to the integral will come from the point in the k_x - k_y plane where the phase of the rapidly varying

exponential is stationary, i.e.,

$$\begin{aligned}\frac{\partial}{\partial k_x}(pb) &= 0 \\ \frac{\partial}{\partial k_y}(pb) &= 0\end{aligned}\tag{19}$$

leading to $k_{x0} = k_{y0} = 0$ ($\lambda = 0$). Replacing the slowly varying part of the integrand with its value at $\lambda = 0$, results in

$$\tilde{g}^s(\vec{r}_1|\vec{r}'_1, s, b) \approx \frac{\tilde{F}(0, s)}{2(2\pi)^2 \gamma} e^{-\gamma(z_1 + z'_1)} \int_{-\infty}^{\infty} \int_{-\infty}^{\infty} e^{-\sqrt{k_x^2 + k_y^2 + \gamma^2} b} d^2\lambda.\tag{20}$$

Converting the integral to polar form

$$\begin{aligned}\int_{-\infty}^{\infty} \int_{-\infty}^{\infty} e^{-\sqrt{k_x^2 + k_y^2 + \gamma^2} b} d^2\lambda &= \int_0^{\infty} \int_0^{2\pi} e^{-\sqrt{\lambda^2 + \gamma^2} b} \lambda d\theta d\lambda \\ &= 2\pi \int_0^{\infty} e^{-\sqrt{\lambda^2 + \gamma^2} b} \lambda d\lambda\end{aligned}\tag{21}$$

the last integral can be easily evaluated in closed form to yield

$$I = 2\pi \left(\frac{\gamma}{b} - \frac{1}{b^2} \right) e^{-\gamma b}.\tag{22}$$

Retaining the leading term for 'b' large results in

$$\tilde{g}^s(\vec{r}_1|\vec{r}'_1, s, b) \approx \tilde{F}(0, s) \frac{e^{-\gamma b}}{4\pi b} e^{-\gamma(z_1 + z'_1)}.\tag{23}$$

With $\lambda = 0$, the amplitude coefficient for the scattered term becomes

$$\tilde{F}(0, s) = (\vec{1}_x \vec{1}_x + \vec{1}_y \vec{1}_y) R_t(0, s) + \vec{1}_z \vec{1}_z R_n(0, s)\tag{24}$$

where the contribution from the coupling term associated with R_c in (8) has vanished.

The IE kernel for the scattered term in (17) then becomes

$$\begin{aligned}\bar{r}_1|\bar{r}'_1, s, b) &= s\mu_0 \frac{e^{-\gamma b}}{4\pi b} \bar{\mathbf{I}}_{(s)} \cdot \left\{ \bar{\mathbf{I}} - \gamma^{-1} \bar{\mathbf{I}}_z \bar{\mathbf{I}}_z \frac{\partial^2}{\partial z_1^2} \right\} \cdot \bar{\mathbf{F}}(0, s) e^{-\gamma(z_1+z'_1)} \cdot \bar{\mathbf{I}}_{(s)} \\ &= s\mu_0 \frac{e^{-\gamma b}}{4\pi b} e^{-\gamma(z_1+z'_1)} \bar{\mathbf{I}}_{(s)} \cdot \left[(\bar{\mathbf{I}}_x \bar{\mathbf{I}}_x + \bar{\mathbf{I}}_y \bar{\mathbf{I}}_y) R_t(0, s) \right] \cdot \bar{\mathbf{I}}_{(s)}.\end{aligned}\quad (25)$$

Defining

$$\bar{\mathbf{I}}_{z_i} \equiv \bar{\mathbf{I}}_x \bar{\mathbf{I}}_x + \bar{\mathbf{I}}_y \bar{\mathbf{I}}_y \quad (26)$$

leads to

$$\Delta s_\alpha = -s_\alpha^h \mu_0 \frac{e^{-\gamma_\alpha^h b}}{4\pi b} R_t(0, s_\alpha^h) \frac{\left\langle \bar{\mathbf{J}}_\alpha^h(\bar{\mathbf{r}}_1); e^{-\gamma_\alpha^h(z_1+z'_1)} \bar{\mathbf{I}}_{z_i}; \bar{\mathbf{J}}_\alpha^h(\bar{\mathbf{r}}_1) \right\rangle}{\left\langle \bar{\mathbf{J}}_\alpha^h(\bar{\mathbf{r}}_1); \frac{\partial}{\partial s} \bar{\mathbf{Z}}^h(\bar{\mathbf{r}}_1|\bar{\mathbf{r}}'_1, s_\alpha^h); \bar{\mathbf{J}}_\alpha^h(\bar{\mathbf{r}}_1) \right\rangle} \quad (27)$$

where $\gamma_\alpha^h = \gamma_\alpha(s_\alpha^h) = s_\alpha^h \sqrt{\mu_0 \epsilon_c}$ is the propagation constant in the cover evaluated at the natural frequency of the object when in a homogeneous space. Note that the dyadic triple dot product in (25) becomes $\bar{\mathbf{I}}_{z_i}$ for both the surface and volume IE formulation. For the volume IE, this follows simply from the fact that $\bar{\mathbf{I}}_{\nu}(\bar{\mathbf{r}}) = \bar{\mathbf{I}}$. For the surface IE, the knowledge that the natural mode currents are tangential reduces the triple dot product accordingly. Defining

$$v_\alpha^h(s_\alpha^h) \equiv \frac{\left\langle \bar{\mathbf{J}}_\alpha^h(\bar{\mathbf{r}}_1); e^{-\gamma_\alpha^h(z_1+z'_1)} \bar{\mathbf{I}}_{z_i}; \bar{\mathbf{J}}_\alpha^h(\bar{\mathbf{r}}_1) \right\rangle}{\left\langle \bar{\mathbf{J}}_\alpha^h(\bar{\mathbf{r}}_1); \frac{\partial}{\partial s} \bar{\mathbf{Z}}^h(\bar{\mathbf{r}}_1|\bar{\mathbf{r}}'_1, s_\alpha^h); \bar{\mathbf{J}}_\alpha^h(\bar{\mathbf{r}}_1) \right\rangle} \quad (28)$$

which is exactly the same coefficient utilized in [3] (although there the homogeneous space was specifically free-space), the perturbation formula becomes

$$\Delta s_\alpha = -s_\alpha^h \mu_0 \frac{e^{-\gamma_\alpha^h b}}{4\pi b} R_t(0, s_\alpha^h) v_\alpha^h(s_\alpha^h). \quad (29)$$

This formula is identical to that obtained in [3] (Eq. (34) of [3]), except for the multiplicative term R_t , and the fact that the perturbation term is evaluated at s_α^h rather than s_α^0 . If $\epsilon_c = \epsilon_0, \epsilon_f = \epsilon_s = -j\infty$, implementing free-space over a perfectly conducting ground plane, $R_t = -1$, and (29) reduces to the result in [3] for the antisymmetric mode of two coupled objects in free-space, as expected. For the case of a perfect magnetic conductor, $R_t = 1$, and (29) reduces to the solution for the symmetric mode of two coupled objects in a homogeneous space.

ii. Scaling Relations

The perturbation formula (29) involves the natural frequencies s_α^0 of an object embedded in a homogeneous space characterized by (μ_0, ϵ_c) . As detailed in [23]-[25], scaling relations exist which relate the natural modes of an object in a lossy, homogeneous environment to those of the same object when in free-space. The relevant scaling relationship for natural frequency is

$$s_\alpha^h = -\frac{\sigma_c}{2\epsilon_c^{re}} + \sqrt{\left(\frac{\sigma_c}{2\epsilon_c^{re}}\right)^2 + \frac{\epsilon_0}{\epsilon_c^{re}}(s_\alpha^0)^2} \quad (30)$$

where $(\sigma_c, \epsilon_c^{re})$ are real-valued parameters of the homogeneous space, which are written in terms of a single complex (effective) permittivity as $\epsilon_c = \epsilon_c^{re} + \sigma_c/s$. Note that in the case of a lossless homogeneous space, the scaling relationship becomes simply $s_\alpha^h = s_\alpha^0/\sqrt{\epsilon_{cr}}$, with ϵ_{cr} being the relative permittivity, $\epsilon_{cr} = \epsilon_c^{re}/\epsilon_0$. The scaling relationship (30) comes from equality of the propagation constants, $\gamma_\alpha^h(s_\alpha^h) = \gamma_\alpha^0(s_\alpha^0)$. The natural modes scale as

$$\bar{J}_\alpha^h = \bar{J}_\alpha^0 \quad (31)$$

and the coefficient (28) scales as [25]

$$v_{\alpha}^h(s_{\alpha}^h) = \left(\frac{2\sigma_c + 2s_{\alpha}^h \epsilon_c^{re}}{\sigma_c + 2s_{\alpha}^h \epsilon_c^{re}} \right) v_{\alpha}^0(s_{\alpha}^0). \quad (32)$$

With the above, (29) becomes

$$\Delta s_{\alpha} = -s_{\alpha}^h \left(\frac{2\sigma_c + 2s_{\alpha}^h \epsilon_c^{re}}{\sigma_c + 2s_{\alpha}^h \epsilon_c^{re}} \right) \mu_0 \frac{e^{-\gamma_{\alpha}^0 b}}{4\pi b} R_t(0, s_{\alpha}^h) v_{\alpha}^0(s_{\alpha}^0). \quad (33)$$

Since

$$\Delta s_{\alpha}^0 \equiv s_{\alpha}^0 \mu_0 \frac{e^{-\gamma_{\alpha}^0 b}}{4\pi b} v_{\alpha}^0(s_{\alpha}^0) \quad (34)$$

is the perturbation for the antisymmetric mode of two coupled objects in free-space as obtained in [3], (33) can be written as

$$\Delta s_{\alpha} = -\frac{s_{\alpha}^h}{s_{\alpha}^0} \left(\frac{2\sigma_c + 2s_{\alpha}^h \epsilon_c^{re}}{\sigma_c + 2s_{\alpha}^h \epsilon_c^{re}} \right) R_t(0, s_{\alpha}^h) \Delta s_{\alpha}^0 \quad (35)$$

where s_{α}^h is given by (30). This formula reduces to the correct result for the special case of an object in free-space over a perfectly conducting ground plane ($R_t = -1, \sigma_c = 0, \epsilon_c^{re} = \epsilon_0, s_{\alpha}^h = s_{\alpha}^0$), and gives no perturbation in the absence of planar layers ($\epsilon_f = \epsilon_s = \epsilon_c$), for which $R_t = 0$. Equation (35) provides the perturbation of the natural frequency of an object embedded in a half-space characterized by (μ_0, ϵ_c) over a planarly layered medium in terms of the perturbation of the same object in free-space over a perfect ground plane, for which perturbation formulas have been derived. Equivalently, the perturbation may be directly computed from (29).

The reflection coefficient for the tri-layered environment depicted in Fig. 1 is [22]

$$R_t = R_{fc} + \frac{T_{cf} R_{sf} T_{fc}}{1 - R_{cf} R_{sf} e^{-2p_f t}} e^{-2p_f t} \quad (36)$$

where $R_{\alpha\beta} = \frac{P_\beta - P_\alpha}{P_\beta + P_\alpha}$, $T_{\alpha\beta} = \frac{2P_\alpha}{N_{\beta\alpha}^2(P_\alpha + P_\beta)}$, $P_\beta^2 = \lambda^2 + s^2\mu_0\epsilon_\beta$, and $N_{\alpha\beta}^2 = \frac{\epsilon_\alpha}{\epsilon_\beta}$. For the special case of a two

half-spaces ($\epsilon_f = \epsilon_s$ or $t=0$), R_t becomes

$$R_t = \frac{P_c - P_s}{P_c + P_s} \quad (37)$$

which for $\lambda=0$ is

$$R_t = \frac{\sqrt{\epsilon_c} - \sqrt{\epsilon_s}}{\sqrt{\epsilon_c} + \sqrt{\epsilon_s}} \quad (38)$$

a familiar interfacial reflection coefficient.

IV. Results and Discussion

As a check on the accuracy of perturbation formula (35), the example of a straight wire of length L in the vicinity of the interface between two differing media will be considered. Results are provided for a wire in air above a lossless and lossy half-space, and for a wire embedded in a lossy half-space near the interface with air. In all cases, numerical values of $\gamma_{1,1}^0$ and $\nu_{1,1}^0$ are obtained from tables in [3], leading to the coefficient (34). The subscript $\alpha=1,1$ indicates the lowest order mode in the first layer of the complex plane [12], which is the dominant natural frequency. In the following all results correspond to $\alpha=1,1$, the perturbation of the dominant natural frequency of the isolated wire.

The first example is depicted in the insert of Fig. 3(a), which shows a wire in air ($\epsilon_{cr}=1, \sigma_c=0$) over a lossless dielectric half-space ($\epsilon_{sr}=15, \sigma_s=0$). Since the wire is in air, $s^h = s^0$, and the perturbation formula becomes simply $\Delta s_{1,1} = -R_t(0, s_{1,1}^0) \Delta s_{1,1}^0$ with R_t computed from (38). Results of the perturbation formula are shown in Fig. 3(a), where the separation parameter is varied from $b/L=0.5$ to 3.0. Results from an integral equation solution [19] are shown in Fig. 3(b), where generally good agreement is found between the two methods for the range of b/L values examined in [19].

The second example is depicted in the insert of Fig. 4(a), which shows a wire in air ($\epsilon_{cr}=1, \sigma_c=0$) over a lossy dielectric half-space ($\epsilon_{sr}=15, \sigma_s L=120 S$). The perturbation formula is the same as for the geometry considered in Fig. 3, although the substrate permittivity is now complex-valued in the coefficient R_t . Results of the perturbation formula are shown in Fig. 4(a), where the separation parameter is again varied from $b/L=0.5$ to 3.0 . Results from an integral equation solution [19] are shown in Fig. 4(b). Agreement between the two methods is again fairly good.

The geometry for the last example is depicted in the insert of Fig. 5(a). For this situation, the wire ($L=.825$ cm.) is in a lossy ground near the interface with an air half-space. The permittivity of the ground is $\epsilon_c=(5.9-j1.5)\epsilon_0$ from Fig. 3 of [9], leading to ($\epsilon_{cr}=5.9, \sigma_c=5.45 \cdot 10^{-3}$ S/m) at $f=65.35$ MHz. The wire is inclined at a 45° angle to the planar interface, and separation between the end of the wire nearest to the interface and the interface is varied over the range specified in [9], i.e., from $d=0.1L$ to $3L$. Fig. 5(a) shows the perturbation formula results, while Fig. 5(b) shows the IE results from [9]. Note that, consistent with [9], results are plotted as complex frequency, related to the Laplace variable as $s=j2\pi f$. Good agreement is found between the two methods except for small d/L values, which is expected.

A final result concerns the perturbation of the natural frequencies for a dielectric rectangle (sides a, b , height d) of permittivity $\epsilon=20\epsilon_0$ immersed in a region $\epsilon=4\epsilon_0$ near an interface with free space. Figure 6 shows the spiraling behavior, where the circles show the exact IE solution and the triangles show the perturbation solution (17). Equation 17 was used for the perturbation solution since approximate evaluation of the Sommerfeld integrals in (17) leads to zero perturbation. This arises since the dominant mode has an odd field variation, the spatial integrals of which lead to zero perturbation. For modes with an even variation the simpler formula may be used.

V. Future work

Given that the perturbation method is accurate for simple targets, the focus future work should be on applying this technique to more complicated targets, both metallic and dielectric. General classes of targets such as wire models of aircraft could be considered from both an integral equation

and perturbation formulation. Identifying the types of targets for which the observed spiral-like target-environment interaction occurs would be of interest. Another important consideration which should be addressed is the categorization of environments which significantly affect the natural frequencies of targets. Combinations of permittivity and conductivity profiles could be studied to ascertain their effect on the natural frequencies of a target class.

V. References

- [1] C.E. Baum, "On the singularity expansion method for the solution of electromagnetic interaction problems," *Interaction Note 88*, Dec. 1971.
- [2] G.W. Hanson and C.E. Baum, "Perturbation formula for the Natural Frequencies of an Object in the Presence of a Layered Medium," *Interaction Note*, Sept. 1997.
- [3] C.E. Baum, T.H. Shumpert, and L.S. Riggs, "Perturbation of the SEM-pole parameters of an object by a mirror object," *Electromagnetics*, vol. 8, pp. 169-186, 1989. Also, C.E. Baum, T.H. Shumpert, and L.S. Riggs, "Perturbation of the SEM-pole parameters of an object by a mirror object," *Sensor and Simulation Note 309*, Sept. 1987.
- [4] G.W. Hanson and C.E. Baum, Asymptotic analysis of the natural system modes of coupled bodies in the large separation, low-frequency regime, *Interaction Note 528*, July 1997.
- [5] G.W. Hanson and C.E. Baum, "Perturbation formula for the Natural Frequencies of an Object in the Presence of a Layered Medium," submitted to *Electromagnetics*.
- [6] G.W. Hanson and C.E. Baum, "Perturbation Formula for the Internal Resonances of a Dielectric Object Embedded in a Low-Impedance Medium," *Interaction Note 520*, Aug. 1996.
- [7] M. C. Worthy, "Exact Pole Locations of Dielectric Geometrical Objects in Various Dielectric Medium," AFOSR Final Report, 1996.
- [8] E.J. Rothwell and M.J. Cloud, "On the natural frequencies of an annular ring above a conducting half space," *J. Electromagnetic waves and applications*, vol. 10, pp. 155-179, 1996.
- [9] S. Vitebskiy and L. Carin, "Resonances of perfectly conducting wires and bodies of revolution buried in a lossy dispersive half-space," *IEEE Trans. Antennas Propagat.*, vol. 44, pp. 1575-1583, Dec. 1996.

- [10] L. Marin and R.W. Latham, "Analytical properties of the field scattered by a perfectly conducting, finite body," *Interaction Note 92*, Jan. 1972.
- [11] C.E. Baum, "Representation of surface current density and far scattering in EEM and SEM with entire functions," *Interaction Note 486*, Feb. 1992.
- [12] F.M. Tesche, "On the analysis of scattering and antenna problems using the singularity expansion technique," *IEEE Trans. Antennas Propagat.*, vol. AP-21, pp. 53-62, Jan. 1973. Also, F.M. Tesche, "On the singularity expansion method as applied to electromagnetic scattering from thin-wires," *Interaction Note 102*, April 1972.
- [13] K.R. Umashankar, T.H. Shumpert, and D.R. Wilton, "Scattering by a thin wire parallel to a ground plane using the singularity expansion method," *IEEE Trans. Antennas Propagat.*, vol. AP-23, pp. 178-184, Mar. 1975.
- [14] T.H. Shumpert and D.J. Galloway, "Finite length cylindrical scatterer near perfectly conducting ground. A transmission line mode approximation," *IEEE Trans. Antennas Propagat.*, vol. AP-26, pp. 145-151, Jan. 1978.
- [15] C.I. Chuang and D.P. Nyquist, "Perturbational formulation for nearly degenerate coupling," *1984 National Radio Science Meeting*, Boulder, CO., Jan. 1984.
- [16] J.E. Ross, E.J. Rothwell, D.P. Nyquist, and K.M. Chen, "Approximate integral-operator methods for estimating the natural frequencies of coupled objects," *Radio Science*, vol. 29, pp. 677-684, 1994.
- [17] Y. Yuan and D.P. Nyquist, "Full-wave perturbation theory based upon electric field integral equation for coupled microstrip transmission lines," *IEEE Trans. Microwave Theory Tech.*, vol. 38, pp. 1576-1584, Nov. 1990.
- [18] G.W. Hanson and D.P. Nyquist, "Full-wave perturbation theory for the analysis of coupled microstrip resonant structures," *IEEE Trans. Microwave Theory Tech.*, vol. 40, pp. 1774-1779, Sept. 1992.
- [19] L.S. Riggs and T.H. Shumpert, "Trajectories of the singularities of a thin wire scatterer parallel to a lossy ground," *IEEE Trans. Antennas Propagat.*, vol. AP-27, pp. 864-868, Nov. 1979.
- [20] G.W. Hanson, "SEM formulation for a dielectric object embedded in a layered medium: general considerations and specialization to a low wave-impedance surround," *Progress in Electromagnetics Research Symposium*, Schlumberger-Doll Research, Cambridge, MA, July 1997.

- [21] A.D. Yaghjian, "Electric dyadic Green's functions in the source region," *Proc. IEEE*, vol. 68, pp. 248-263, Feb. 1980.
- [22] J.S. Bagby and D.P. Nyquist, "Dyadic Green's functions for integrated electronic and optical circuits," *IEEE Trans. Microwave Theory Tech.*, vol. MTT-35, pp. 206-210, Feb. 1987.
- [23] K.R. Umashankar and D.R. Wilton, "Transient characterization of circular loop using singularity expansion method," *Interaction Note 259*, Aug. 1974
- [24] D.V. Giri and F.M. Tesche, "On the singularity expansion method for analysis of antennas in conducting media," *Electromagnetics*, pp. 455-471, 1981.
- [25] C.E. Baum, "The SEM representation of scattering from perfectly conducting targets in simple lossy media" *Interaction Note 492*, April 1993.

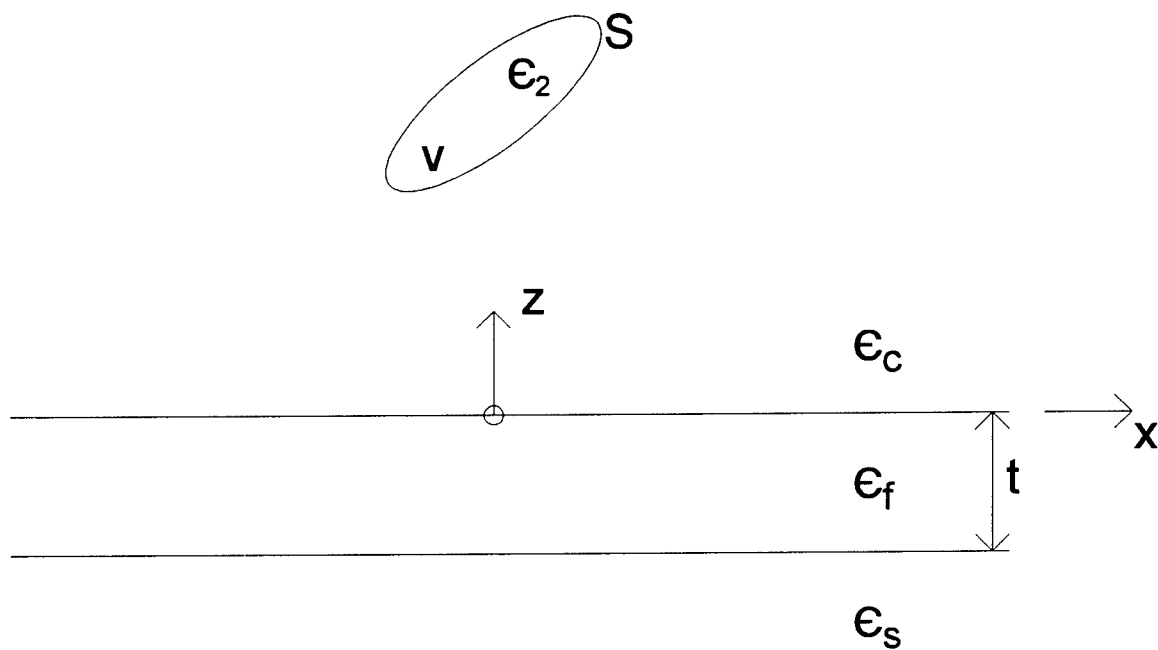


Fig. 1. A target in the vicinity of a layered medium.

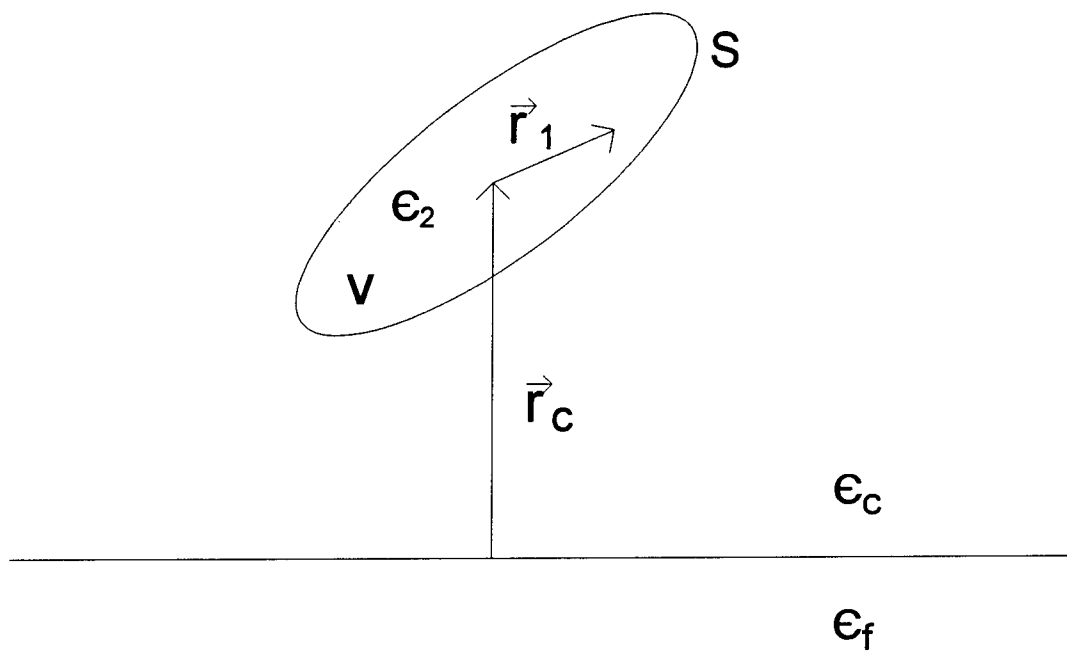


Fig. 2. Local coordinate system used in development of perturbation formula.

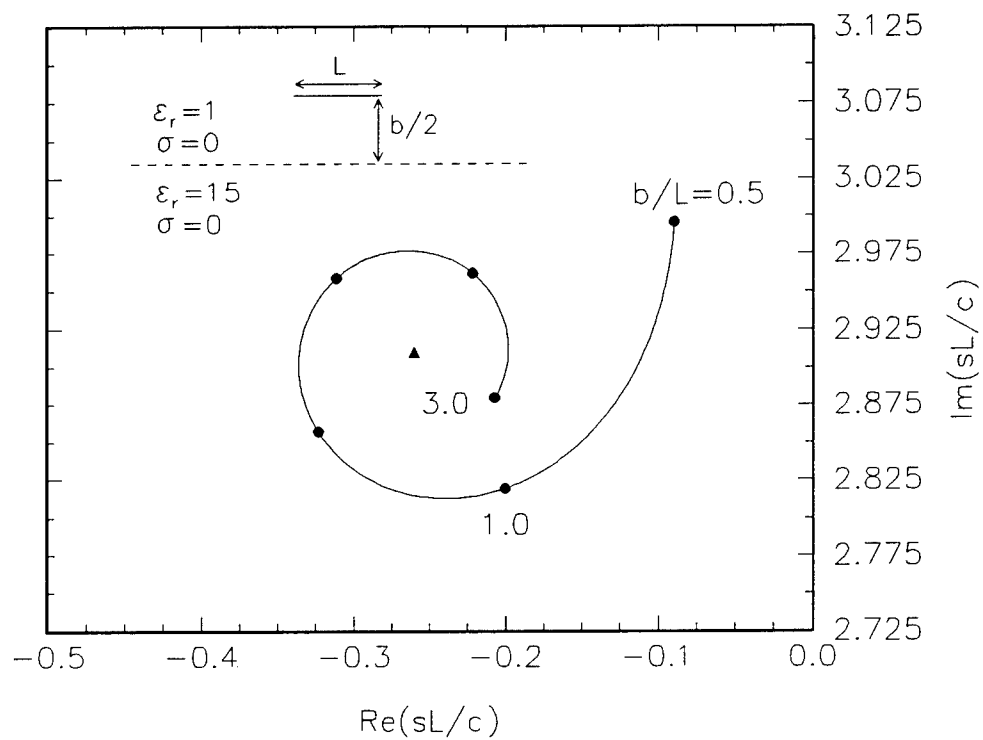


Fig. 3(a). Results of perturbation formula (35) for the natural frequencies of a wire in air above a lossless dielectric half-space. Triangle denotes the natural frequency for a wire in free-space.

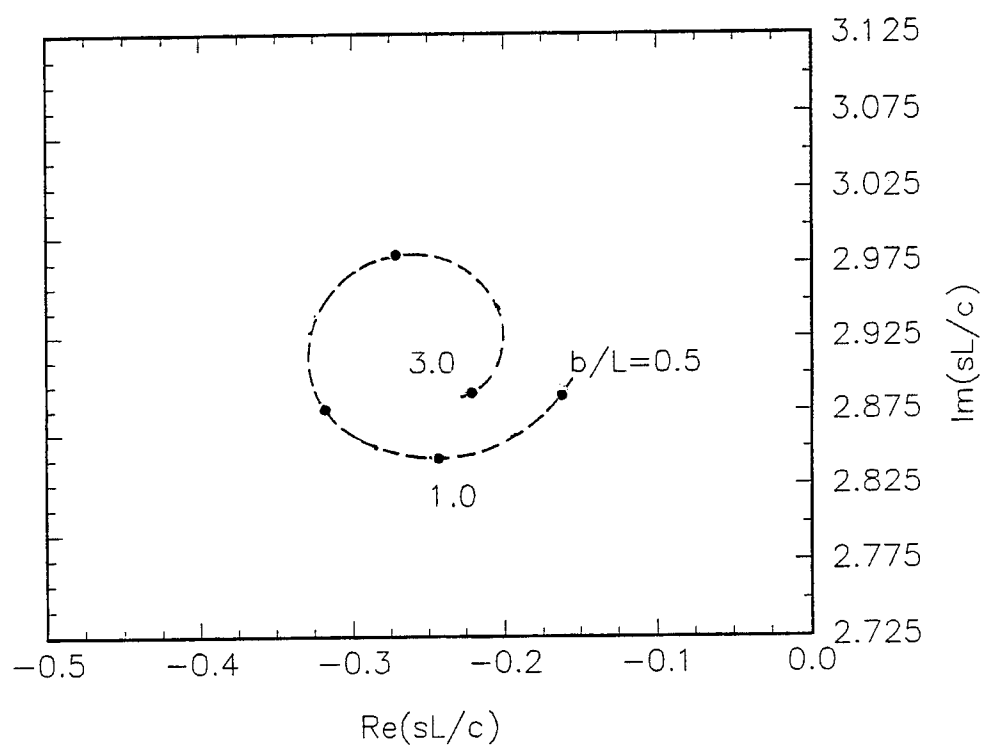


Fig. 3(b). IE results [15] for the natural frequencies of a wire in air above a lossless dielectric half-space.

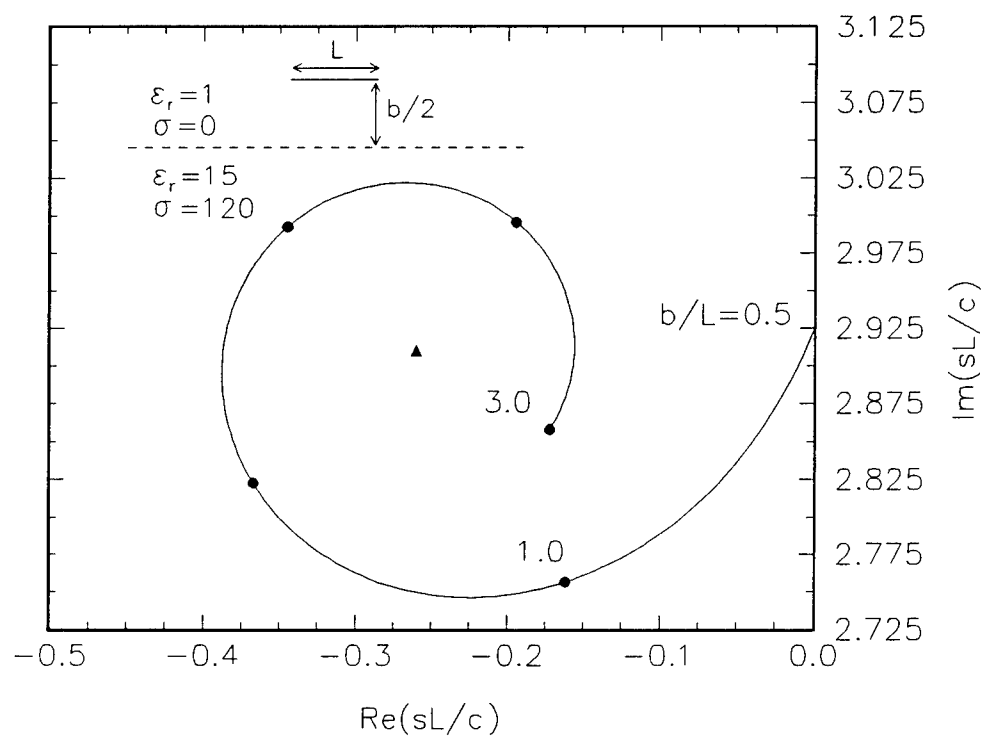


Fig. 4(a). Results of perturbation formula (35) for the natural frequencies of a wire in air above a lossy dielectric half-space. Triangle denotes the natural frequency for a wire in free-space.

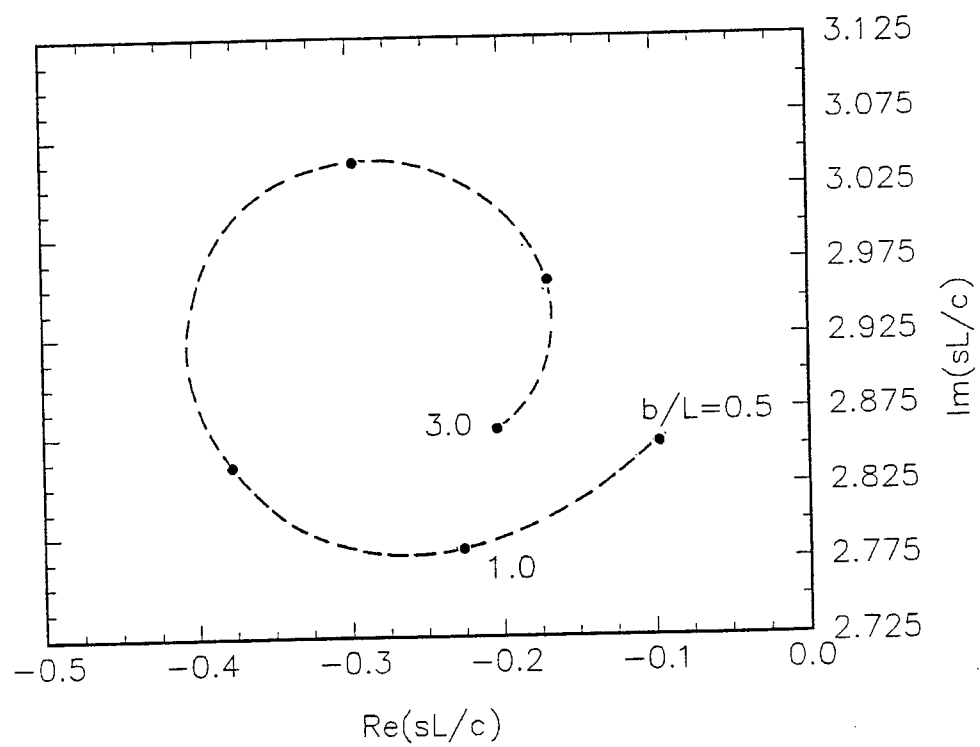


Fig. 4(b). IE results [15] for the natural frequencies of a wire in air above a lossy dielectric half-space.

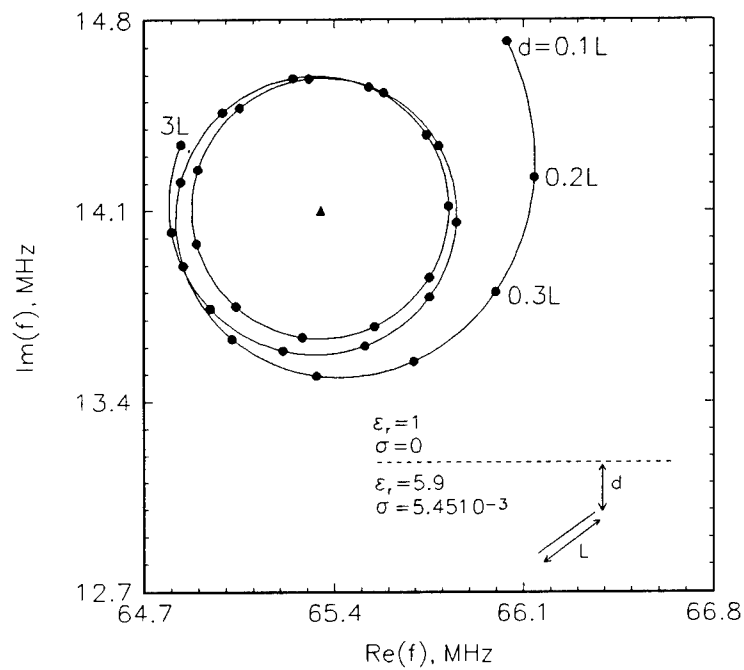


Fig. 5(a). Results of perturbation formula (35) for the natural frequencies of an inclined wire (45 degrees) in a lossy ground below an air half-space. Triangle denotes the natural frequency for a wire in a homogeneous-space (lossy ground).

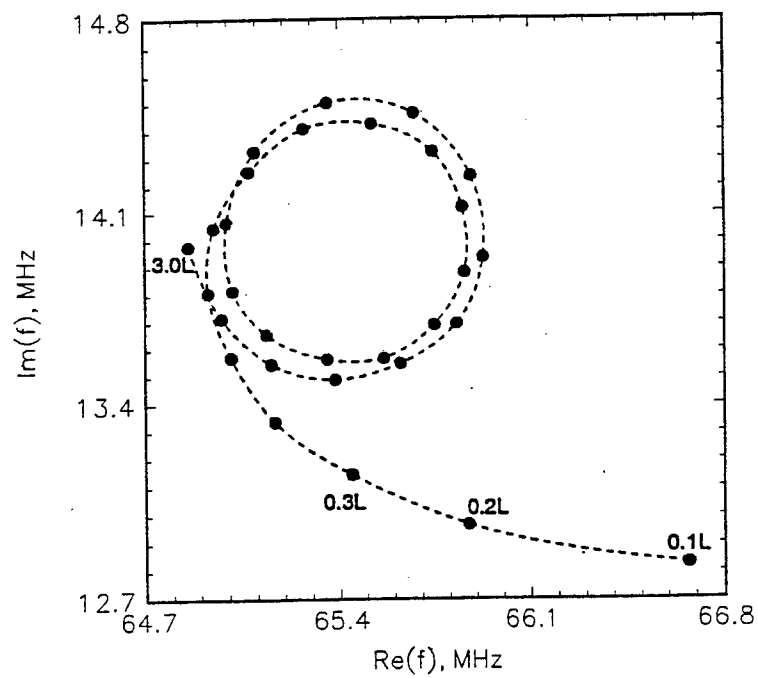


Fig. 5(b). IE results [3] for the natural frequencies of an inclined wire (45 degrees) in a lossy ground below an air half-space.

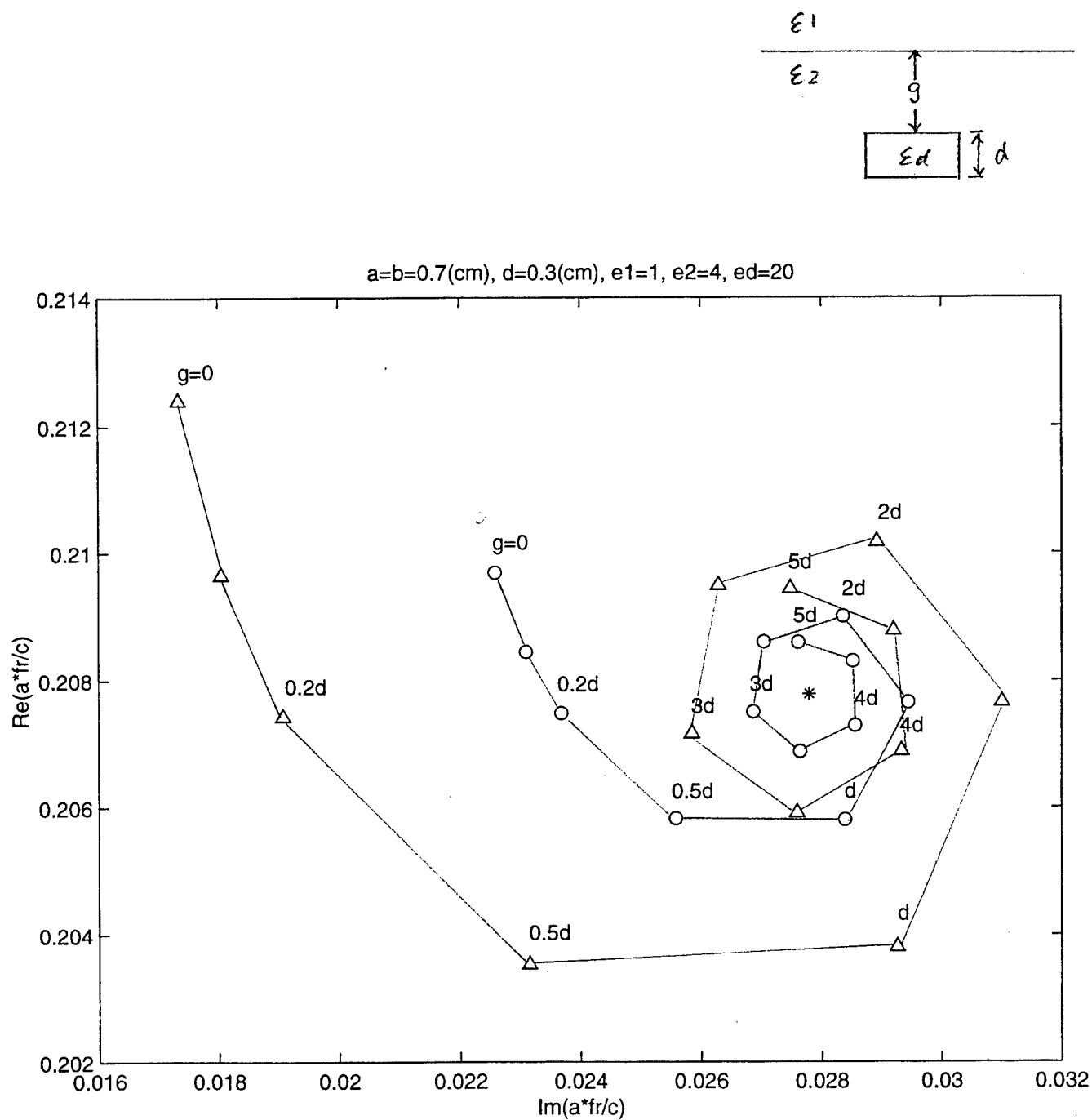


Fig. 6. IE results for the natural frequencies of a rectangular dielectric object near the air-ground interface..

BAYESIAN RESTORATION OF SPACE OBJECT IMAGES FROM ADAPTIVE OPTICS DATA WITH UNKNOWN RESIDUAL BLUR

Brian D. Jeffs
Associate Professor
Department of Electrical and Computer Engineering

Brigham Young University
459 CB, Provo, UT 84602, USA.
E-mail: bjeffs@ee.byu.edu

Final Report for the
Summer Research Extension Program
Subcontract No. 98-0813, Contract No. F49620-93-C-0063

Sponsored by:
Air Force Office of Scientific Research
Bolling Air Force Base, DC

and

AFRL

December 1998

BAYESIAN RESTORATION OF SPACE OBJECT IMAGES FROM ADAPTIVE OPTICS DATA WITH UNKNOWN RESIDUAL BLUR

Brian D. Jeffs
Associate Professor
Department of Electrical and Computer Engineering
Brigham Young University

Abstract

The focus of this research program is algorithm development for blind image restoration of multiframe adaptive optics (AO) telescope images. Methods of primary interest are those algorithms capable of removing residual blur in multiframe space objects image sequences acquired using the Starfire Optical Range ground based 1.5m and 3.5 m AO telescope systems located at Kirtland Air Force Base, NM. This report presents a "blind" method based on Bayesian maximum a posteriori (MAP) estimation theory for restoring images corrupted by noise and blurred by one or more unknown point-spread-functions (psf). In the problem formulation, both the true image and the unknown blur psf's are represented by the generalized Gaussian Markov random field (GGMRF) model. The GGMRF probability density function provides a natural mechanism for expressing available prior information about the image and blur. Incorporating such prior knowledge in the deconvolution optimization is crucial for the success of blind restoration algorithms. The reported work includes a preliminary algorithm performance demonstration using examples from AO images collected at the Starfire Optical Range, USAF Phillips Laboratory. Results from both real and synthetic data indicate significant resolution enhancement when applied to partially corrected AO images. New algorithms for estimating GGMRF model parameters are also presented and Evaluated. In addition to the GGMRF MAP restoration approach, this report discusses studies in deterministic, or algebraic methods which can sometimes lead to closed form solutions rather than the iterative algorithms mentioned above. New techniques drawn from the literature on blind channel equalization for digital communications are evaluated for adaptation to the blind restoration problem.

Contents

1	Introduction	4
1.1	Background	4
1.2	Problem Statement	5
2	The GGMRF MAP Restoration Method	6
2.1	Formulation	6
2.2	GGMRF Image Prior pdf Models	6
2.3	Blind Multiframe GGMRF Restoration Solution	9
2.4	A Steepest Descent Algorithm	9
3	Experimental Results for GGMRF Restoration	11
3.1	Results Using Synthetic AO Space Object Data	11
3.2	Restoration Using Real AO Satellite Data	12
4	GGMRF Shape parameter Estimation	12
5	GGMRF Neighborhood Influence parameter Estimation	17
6	Deterministic Methods for Blind Restoration of AO Images	25
6.1	Homomorphic Blind Star Image Restoration	26
6.2	Direct Multiframe Solution	27
6.3	Cross Relationship Multiframe Blur Estimation	30
6.4	Cross Relationship Metric used in Iterative Bayesian Restoration	31
6.4.1	The Composite GGMRF - Cross Relation Blur Model	32
6.4.2	Solution for GGMRF Blur and Object Models	33
6.4.3	Steepest Descent Algorithm	33
7	Additional Accomplishments Supported by the SREP Grant	34
8	Conclusions	35

BAYESIAN RESTORATION OF SPACE OBJECT IMAGES FROM ADAPTIVE OPTICS DATA WITH UNKNOWN RESIDUAL BLUR ¹

Brian D. Jeffs

1 Introduction

1.1 Background

This document is the final report of progress made during calendar year 1998 under the AFOSR Summer Research Extension Program, Subcontract No. 98-0813. Participants include Dr. Brian D. Jeffs of Brigham Young University as principal investigator, and graduate students Sheila Hong, Miguel Apezteguia, and Brent Chipman. This work was accomplished in collaboration with Dr. Robert Q. Fugate and Dr. Julian C. Christou of the Starfire Optical Range, Air Force Research Laboratories, Kirtland Air Force Base, New Mexico.

The focus of this research program is algorithm development for blind image restoration of multiframe adaptive optics (AO) telescope images. In particular, methods of primary interest are those algorithms capable of removing residual blur in space objects images acquired using the SOR ground based 1.5m and 3.5m AO telescope systems.

AO systems can remove much of the atmospheric-turbulence-induced blur in astronomical and orbiting space objects imagery, but there is typically some adaptation error [1] [2] [3] [4]. Thus, a residual time-varying blur below the theoretical aperture cutoff resolution limit remains. Though the general structure of this residual blur is known [5] [6], the detail is not, and varies significantly over a period of milliseconds.

It is often impractical to acquire an accurate sample of the true residual psf by observing a nearby star. This residual blur is spatially varying, so a natural guide star may not be in the same isoplanatic patch as the object, and in the case of tracking orbiting space objects, no natural reference stars which follow the object are available. When observing bright objects, it is possible to acquire a sequence of high SNR, closely spaced (in time) frames with significant blur variation from frame to frame. This scenario is ideally suited to multiframe blind deconvolution methods which exploit the blur diversity to solve the difficult blind problem.

As is usually the case, the blind restoration problem addressed here is complicated by the ill-posed nature of the associated inverse problem [7], and by the fact that the blur psf, H , and the true object image, F can only be identified in combination ($H * F$) unless distinguishing prior information is available. This solution ambiguity is due to the commutative property of convolution which will yield the same observation regardless of whether a given observed image feature arises from H or F . Therefore, the blind restoration problem is hopeless without a well formed method of expressing and imposing prior information on the solution. A number of authors have successfully applied various "hard" and "soft" constraints on the object and blur solutions as a means of incorporating prior information into the blind multiframe solution [2] [3] [1] [4] [8] [9] [10] [6].

The availability of multiple observations with different but unknown blur psf's, H_i , can be a great aid in estimating F . The multiple frame observation reduces convolutional ambiguity because any image component that is not common to all frames cannot be a component of the F . The method presented below will be developed to exploit this fact, and will be applicable for both single and multiple frame cases.

¹Sponsored by the Air Force Office of Scientific Research, Bolling Air Force Base, DC. The author acknowledges the contributions to this work from Dr. Julian C. Christou and Dr. Robert Fugate, Starfire Optical Range, Air Force Research Laboratory. Also, Ms. Sheila Hong contributed much to this work while a graduate student at Brigham Young University.

This report describes a new “blind” image restoration Method, developed during the SFRP program, which is based on Bayesian maximum a posteriori (MAP) estimation theory. Though this new algorithm may be used in a wide variety of blind deconvolution problems, we are particularly interested in high resolution restoration of multiframe (AO) space objects images. A major advantage of the MAP method is that it provides a natural (rather than ad-hoc) mechanism for incorporating prior information about the image and blur. Use of this prior knowledge is crucial for the success of blind algorithms. In the new method, this information is expressed in the form of image probability density functions (pdf), which serve as a regularizing terms in the associated inverse problem. These statistical models are used to represent prior information as a probabilistic preference on the structures of both the true image, F , and the blurring psf, H , without explicitly describing any fixed image features. We will show that adopting appropriate image and blur pdf models serves as a powerful discriminating constraint that leads to realistic estimates for both H and F .

The new algorithm uses the generalized Gaussian Markov random field as a prior image model (GGMRF) [11] because of its ability to represent a wide range of practical image types [12] [13]. With appropriate parameter settings, the GGMRF can accurately model both structured, hard edged fields typical of the true image for man-made artificial satellites, and smooth, “low pass” or “band limited” images typical of blurring psf’s.

This report also discusses our recent work on deterministic, or algebraic methods of blind image restoration. These new techniques are drawn from the literature on blind channel equalization for digital communications [14, 15, 16, 17, 18, 19, 20, 21, 22], and were evaluated for adaptation to the blind image restoration problem. Three methods were developed to the simulation stage: 1) Homomorphic blind star image restoration, which uses an extremely fast closed form computation to recover blurred points, 2) Direct multiframe solution, which finds the linear algebraic nullspace of the observed data frames, from which the true image is found by subspace matching, and 3) An algebraic cross relationship algorithm which enables estimating the unknown blurs without having to solve for the object image. Adaptation of this method to GGMRF MAP algorithm discussed above was also investigated. A major focus of this present study is to evaluate how effectively these algorithms can be adapted to the blind AO multiframe image restoration problem.

1.2 Problem Statement

We adopt the following linear image observation model

$$G_i = H_i * F + \eta_i, \quad i = 1 \cdots M \quad (1)$$

where G_i is the i^{th} observed image frame, η_i is additive noise, H_i is the unknown AO residual blur point spread function for the i^{th} frame, F is the true object image, and ‘*’ denotes 2-D convolution. G_i , H_i , F , and η_i are all assumed to be realizations of 2-D random fields, but F remains constant between observation frames. It will also be convenient in our analysis to use the vector-matrix forms of equation (1). In this notation G_i , H_i , and F may be in column scanned vector form (\mathbf{g}_i , \mathbf{h}_i and \mathbf{f} respectively), or represented as large Toeplitz-Block-Toeplitz convolution matrices (\mathbf{G}_i , \mathbf{H}_i and \mathbf{F}) [23]. For example, equation (1) can be written as

$$\mathbf{g}_i = \mathbf{H}_i \mathbf{f} + \eta_i, \quad i = 1 \cdots M, \quad \text{or} \quad (2)$$

$$\mathbf{g}_i = \mathbf{F} \mathbf{h}_i + \eta_i, \quad i = 1 \cdots M \quad (3)$$

When it is necessary to represent the entire set of observed image frames as a single entity, equation (2) is represented with the following notation

$$\begin{aligned} \bar{\mathbf{g}} &= \mathcal{H} \mathbf{f} + \bar{\eta}, \quad \text{where} \\ \bar{\mathbf{g}} &= [\mathbf{g}_1, \mathbf{g}_2, \cdots, \mathbf{g}_M]^T, \quad \bar{\eta} = [\eta_1, \eta_2, \cdots, \eta_M]^T, \end{aligned} \quad (4)$$

$$\mathcal{H} = \begin{bmatrix} \mathbf{H}_1 \\ \vdots \\ \mathbf{H}_M \end{bmatrix}.$$

With the mathematical notation established, we are now ready to express a statement of the problem: “Given observations $\bar{\mathbf{g}}$, with \mathcal{H} unknown, estimate \mathbf{f} .” In the following section, the theory behind GGMRF MAP blind restoration is developed, a solution is derived, and an algorithm to compute the solution is presented. Experimental examples of GGMRF blind restoration are presented in Section 3. Sections 4 and 5 introduce new methods for estimating the GGMRF model parameters in order to improve restoration performance. Section 6 presents our work on deterministic methods for blind image restoration, while Section 7 lists other accomplishments which were supported by the SREP grant. Overall conclusions are presented in Section 8. Sections 3, 4, and 5 present research and results that have not previously appeared in an AFOSR SRRP report or document.

2 The GGMRF MAP Restoration Method

2.1 Formulation

Assuming \mathbf{f} and \mathcal{H} are statistically independent (a reasonable assumption in practice), the blind MAP restoration problem may be stated as

$$\begin{aligned} \hat{\mathbf{f}}, \hat{\mathcal{H}} &= \arg \max_{\mathbf{f}, \mathcal{H}} p_{f,h|g}(\mathbf{f}, \mathcal{H} | \bar{\mathbf{g}}) \\ &= \arg \max_{\mathbf{f}, \mathcal{H}} p_{g|f,h}(\bar{\mathbf{g}} | \mathbf{f}, \mathcal{H}) p_f(\mathbf{f}) p_h(\mathcal{H}) \end{aligned} \quad (5)$$

Assuming the noise is zero mean, white Gaussian, the noise density is given by

$$p_\eta(\bar{\eta}) = \frac{1}{\sqrt{2\pi}^{MN} \sigma_\eta} e^{-\frac{1}{2\sigma_\eta^2} \bar{\eta}^t \bar{\eta}} \quad (6)$$

where N is the total number of pixels in the image field. The following development could also be easily adapted to a Poisson distribution noise model. This approach is favored by some authors in Adaptive Optics restoration because it more accurately characterizes photon noise in short exposure images [8]. Assuming that the noise is statistically independent from both the true image and the blur, the conditional probability of $\bar{\mathbf{g}}$ given \mathbf{f} and \mathcal{H} can be trivially shown to be

$$\begin{aligned} p_{g|f,h}(\bar{\mathbf{g}} | \mathbf{f}, \mathcal{H}) &= p_\eta(\bar{\mathbf{g}} - \mathcal{H}\mathbf{f}) \\ &= \frac{1}{\sqrt{2\pi}^{MN} \sigma_\eta} e^{-\frac{1}{2\sigma_\eta^2} (\bar{\mathbf{g}} - \mathcal{H}\mathbf{f})^t (\bar{\mathbf{g}} - \mathcal{H}\mathbf{f})} \end{aligned} \quad (7)$$

pdf models for the image and blur are introduced in the following section.

2.2 GGMRF Image Prior pdf Models

The image is modeled as a generalized Gaussian Markov random field (GGMRF), with joint pdf given by the Gibbs distribution [11]

$$p_f(\mathbf{f}) = \frac{1}{Z_f} \exp \left\{ -\beta \left[\sum_{\langle s,t \rangle \in \mathcal{C}_f} b_{s,t} |f_s - f_t|^p + \sum_{s \in S_f} a_s |f_s|^p \right] \right\} \quad (8)$$

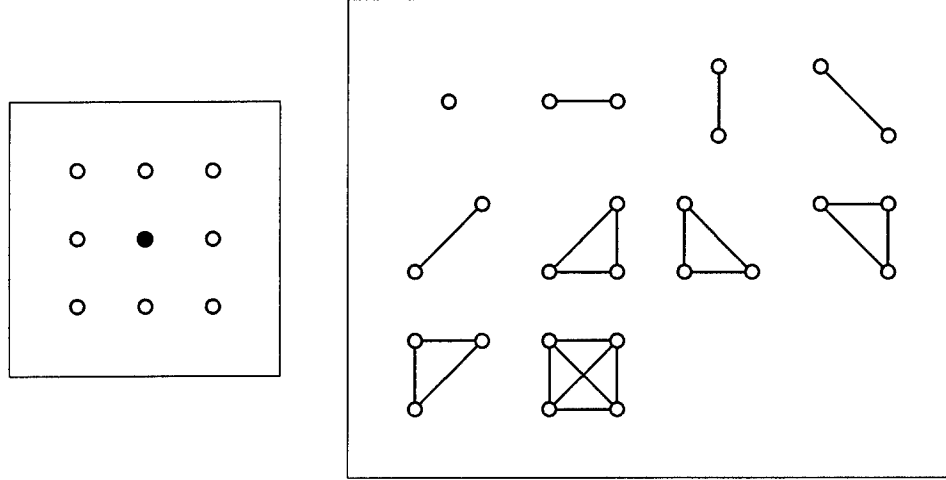


Figure 1: Neighborhoods and cliques. a) [left] A second order neighborhood. b) [right] The cliques associated with a second order neighborhood.

where \mathcal{C}_f is the set of all cliques of pixels invoked by the specified neighborhood system, p is the GGMRF shape parameter, S_f is the set of all pixels in the image lattice, f_s denotes the s^{th} pixel in \mathbf{f} , and $b_{s,t}$ and a_s are neighborhood influence. β is the scale parameter (controlling variance) and Z_f is the partition function, which is simply the scale constant required to insure the pdf integrates to 1.0. The neighborhood clique system is a critical part of defining a Markov random field, and it controls local pixel interactions. Figure 1a illustrates all the neighbors for a single pixel (the center darkened dot) in a second order neighborhood. A clique is defined as any set of pixels which are all mutual neighbors. Figure 1b shows all possible geometric configurations of cliques permitted in a second order neighborhood. \mathcal{C}_f contains all such cliques over the entire image, i.e. the union (non repeating) over all pixels of the set of cliques containing each pixel. A first order neighborhood is defined as containing only left, right, up and down neighbors. The circles in Figure 1a located diagonally from the center dot would be excluded from a first order neighborhood. Likewise, only the first four cliques shown in Figure 1b would be defined in a first order neighborhood.

The GGMRF model is a particularly flexible and useful for image restoration problems because it is capable of representing a wide variety of statistical image classes using just a few parameters. Equation (8) can be viewed as a definition for a random texture field. Parameters p , $b_{s,t}$ and a_s control the structure of this texture. p is known as the shape parameter, and controls the “edginess,” or transition structure in the image. $b_{s,t}$ and a_s jointly control the correlation structure between neighboring pixels. With appropriate value selections, the model can be parameterized to generate fields that look like the detail in any desired visual texture, such as gravel, cork, grass, clouds, sand, waves, natural animal coat coloring, or geometric blocky structures. Figure 2 shows an example of how shape parameter p affects this texture field. The images shown were generated as synthetic Markov random fields using Chen’s algorithm to express the model of equation (8) [24]. A first order uniform (i.e. $b_{s,t} = 1.0$) neighborhood was used in each example, and only p was varied. We propose that Figure 2a, with $p = 0.5$, is a better statistical match for the blocky geometric structures of man-made objects, like satellites, than are the

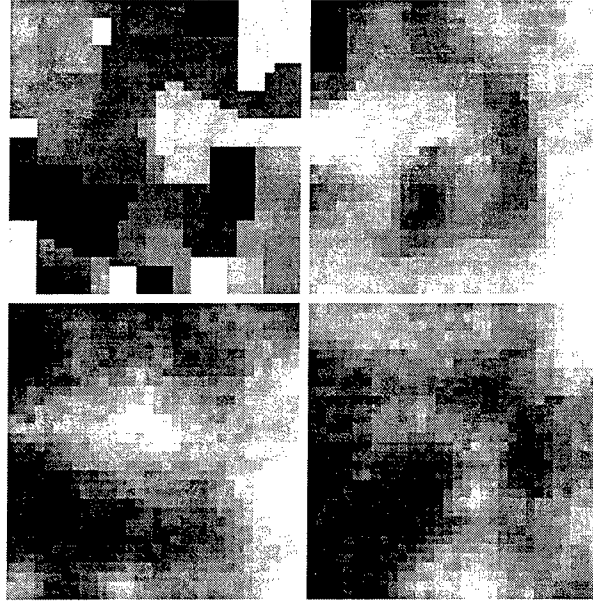


Figure 2: Synthetic GGMRF images. a) [top left] $p = 0.5$, b) [top right] $p = 1.0$, c) [bot. left] $p = 2.0$, d) [bot. right] $p = 3.0$.

other three fields. Thus the GGMRF model with p values near 0.5 can serve as a powerful image prior to influence as restoration solution away from overly smoothed results typical of many other algorithms. This regularization is accomplished without detailed geometric descriptions of unknown object, but with a simple statistical preference for the desired texture-like pixel relationships.

For $.5 < p < 1.5$ (approximately) a MAP restoration using this GGMRF image prior preserves edge detail and regional structure found in most images of interest. The structural information contained in $p_f(\mathbf{f})$ is key to overcoming the convolutional ambiguity between \mathbf{f} and \mathbf{H} in blind restoration. Further, due to the Markov properties inherent in Gibbs distributions, the pdf of any single pixel depends only on the value of its neighbors as defined in the clique system, \mathcal{C} . This greatly simplifies the MAP optimization algorithm because updates need only consider local neighbor data rather than the entire image at each iteration.

The appropriate blur pdf model is application dependent, and two different approaches will be discussed in the following sections. Our notions of what a blur field should look like are conveyed by specifying a few neighbor potential weights, the GGMRF shape parameter (q will be used to distinguish it from the object shaper parameter, p) and a mean value, μ_h . This in turn defines a texture class used to penalize the optimization objective function if a candidate blur differs significantly from the model.

The GGMRF blur model is given by

$$p_h(\mathcal{H}) = \frac{1}{Z_h} \exp \left\{ -\alpha \left[\sum_{\langle s,t \rangle \in \mathcal{C}_h} c_{s,t} |(h_s - \mu_{h,s}) - (h_t - \mu_{h,t})|^q + \sum_{s \in S_h} d_s |h_s - \mu_{h,s}|^q \right] \right\} \quad (9)$$

where \mathcal{C}_h is the set of all cliques of pixels invoked by the specified neighborhood system, q is the GGMRF shape parameter, S_h is the set of all points in blur the lattice over all frames (set of every pixel in every frame), and $c_{s,t}$ and d_s are potential weights. Equation (9) is flexible enough to not only represent a wide variety of blur types, but to also quantify the degree of uncertainty in the model relative to observation \mathbf{g} . Including a mean in the $p_h(\mathcal{H})$ model (which was not needed in $p_f(\mathbf{f})$) allows us to incorporate prior information from previous experiments. For example, in astronomical imaging, isolated stars in a nearby

field, or even from frames acquired on different experiments, can be averaged to serve as the reference mean. An analytic model can also be used as a mean. The Lorentzian function model may be used for residual AO blur [5] [6], or a simple Gaussian function for atmospheric turbulence.

The GGMRF scale parameter, α , controls variance, and can be adjusted to match the degree of confidence in the GGMRF model as a whole. If the mean is a very good estimate of the actual blur, we set the scale parameter high (for low variance), and keep d_s fairly large (positive) relative to $c_{s,t}$. If the mean estimate is very poor, d_s is kept small, or zero, and all μ_h terms are dropped from equation (9). The model can then still impose the desired texture structure in \mathcal{H} . If the blur is known to be spectrally band limited (e.g. bounded by the pupil cut off frequency), then the corresponding values of $b_{s,t}$ are large (relative to a_s), nearly uniform, and are all positive. It has been shown that for $1.75 < q < 3.0$ and \mathcal{C}_h corresponding to a first or second order uniformly weighted neighborhood, this model produces a random field with smoothed structures typical of many blur operators [13] [12].

2.3 Blind Multiframe GGMRF Restoration Solution

Substituting equations (9),(8) and (7) into (5), and performing a little algebra yields

$$\begin{aligned} \hat{\mathbf{f}}, \hat{\mathcal{H}} = & \arg \min_{\mathbf{f}, \mathcal{H}} \sum_{i=1}^M \|\mathbf{g}_i - \mathbf{H}_i \mathbf{f}\|^2 + \gamma \left[\sum_{\langle s,t \rangle \in \mathcal{C}_f} b_{s,t} |f_s - f_t|^p + \sum_{s \in S_f} a_s |f_s|^p \right] \\ & + \lambda \left[\sum_{\langle s,t \rangle \in \mathcal{C}_h} c_{s,t} |(h_s - \mu_{h,s}) - (h_t - \mu_{h,t})|^q + \sum_{s \in S_h} d_s |h_s - \mu_{h,s}|^q \right] \end{aligned} \quad (10)$$

where we have taken the logarithm of the r.h.s. (which does not change the maximization due to monotonicity) and have dropped additive constants. γ and λ control the relative influence, as regularizing terms, that the image and blur pdf's have respectively on the solution.

If the neighborhood clique system, \mathcal{C}_h does not include cliques that cross frame boundaries, then the \mathbf{H}_i are mutually independent, and equation (10) simplifies slightly to

$$\begin{aligned} \hat{\mathbf{f}}, \hat{\mathcal{H}} = & \arg \min_{\mathbf{f}, \mathcal{H}} \sum_{i=1}^M \left(\|\mathbf{g}_i - \mathbf{H}_i \mathbf{f}\|^2 + \lambda \left[\sum_{\langle s,t \rangle \in \mathcal{C}_{h,i}} c_{s,t} |(h_s - \mu_{h,s}) - (h_t - \mu_{h,t})|^q + \sum_{s \in S_{h,i}} d_s |h_s - \mu_{h,s}|^q \right] \right) \\ & + \gamma \left[\sum_{\langle s,t \rangle \in \mathcal{C}_f} b_{s,t} |f_s - f_t|^p + \sum_{s \in S_f} a_s |f_s|^p \right] \end{aligned} \quad (11)$$

where now $\mathcal{C}_{h,i}$ and $S_{h,i}$ contain only cliques and pixels in the single frame, \mathbf{H}_i . The theoretical values γ and λ are functions of p , q , and the SNR, though exact expressions for are difficult to derive. Therefore, these parameters are usually manually adjusted for most desirable results. The following proportionality relationships give some guidance on how to set γ and λ .

$$\gamma \propto 2\beta\sigma_\eta^2, \quad \lambda \propto 2\alpha\sigma_\eta^2 \quad (12)$$

Examples of restorations using the above formulation are presented in Section 3.

2.4 A Steepest Descent Algorithm

For certain choices of the GGMRF parameters, equations (10) and (11) represent optimizations of convex functionals, and can therefore be solved using the relatively efficient gradient descent techniques. Sufficient conditions for the model parameters to insure convex optimization are: $q, p > 1$, $a_s, d_s \geq 0 \forall s$, and $b_{s,t}, c_{s,t} \geq 0 \forall s, t$. If $p = 2$, then a necessary and sufficient condition for the image prior term to be

convex is that $\mathbf{B} = \{B_{st}\}$ be a non-negative definite matrix with elements related to equation (8) by $B_{st} = -b_{s,t}$, $a_s = \sum_{t \in \delta_s} B_{st}$, and $B_{st} = 0$ for $s \notin \delta_s$. δ_s is the set of neighboring pixels in all cliques containing f_s . Similar constraints hold for $c_{s,t}$ and d_s if $q = 2$.

These conditions are not overly restrictive. We have found that with $p = 1.1$ and $q \geq 2$ the image model preserves edge features, and the blur model imposes sufficient smoothness to separate \mathbf{f} from \mathcal{H} . In order to simplify gradient computation, the objective function of equation (11) can be expressed as

$$\begin{aligned} J(\mathbf{f}, \mathcal{H}) &= (\bar{\mathbf{g}} - \mathcal{H}\mathbf{f})^T (\bar{\mathbf{g}} - \mathcal{H}\mathbf{f}) + \gamma \text{Trace}\{\text{Diag}\{\sum_{t \in \delta_f} b_t |\mathbf{f} - \mathbf{P}_t \mathbf{f}|^p\}\} \\ &\quad + \lambda \text{Trace}\{\text{Diag}\{d |\mathbf{h} - \mu_h|^q + \sum_{t \in \delta_h} c_t |(\mathbf{h} - \mu_h) - \mathbf{P}_t (\mathbf{h} - \mu_h)|^q\}\} \end{aligned} \quad (13)$$

where $|\cdot|^p$ indicates element-wise exponentiation of the magnitude and $\text{Diag}\{\cdot\}$ forms a diagonal matrix from a vector. We have assumed $a_s = 0$ (a common choice [11]), and that $b_{s,t}$, $c_{s,t}$, and d_s are constant with respect to s . This assumption restricts the model to homogeneous (spatially stationary) random fields. \mathbf{P}_t is a permutation matrix which shifts \mathbf{f} to align f_t with f_s . δ_f and δ_h are sets of indices used to select shifts consistent with the neighborhood structures of \mathcal{C}_f and \mathcal{C}_h respectively. Since the field is stationary, these sets are independent of s . For example, in the case of a first order neighborhood, δ_f would contain four indices to select up, down, left, and right neighbors. Neglecting edge effects, an example of \mathbf{P}_t where $t = \text{"nearest neighbor down"}$ would be as follows:

$$\mathbf{P}_t = \begin{bmatrix} 0 & 1 & 0 & \cdots & 0 \\ & \ddots & \ddots & & \\ 0 & \cdots & 0 & 1 & 0 \\ 0 & \cdots & & 0 & 1 \\ 0 & \cdots & & & 0 \end{bmatrix} \quad \text{when } t \text{ is the index for 1 row down.} \quad (14)$$

The derivative of equation (13) with respect to \mathbf{f} is readily computed. However, to compute the derivative with respect to the i^{th} frame blur, \mathbf{h}_i , the first term of (13) is replaced with the equivalent expression $\sum_{i=1}^M M(\bar{\mathbf{g}} - \mathbf{F}\mathbf{h}_i)^T (\bar{\mathbf{g}} - \mathbf{F}\mathbf{h}_i)$, where \mathbf{F} is the block Toeplitz convolution matrix formed from \mathbf{f} .

$$\begin{aligned} \frac{d}{d\mathbf{f}} J(\mathbf{f}, \mathcal{H}) &= -2 \sum_{i=1}^M \mathbf{H}_i^T (\mathbf{g}_i - \mathbf{H}_i \mathbf{f}) + \alpha p \sum_{t \in \delta_f} b_t \mathbf{Q}_t^T |\mathbf{Q}_t \mathbf{f}|^{p-1} \odot \text{sign}\{\mathbf{Q}_t \mathbf{f}\} \\ \frac{d}{d\mathbf{h}_i} J(\mathbf{f}, \mathcal{H}) &= -2 \mathbf{F}^T (\mathbf{g}_i - \mathbf{F} \mathbf{h}_i) + \lambda q \sum_{t \in \delta_h} c_t \mathbf{Q}_t^T |\mathbf{Q}_t (\mathbf{h}_i - \mu_h)|^{q-1} \odot \text{sign}\{\mathbf{Q}_t (\mathbf{h}_i - \mu_h)\} \\ &\quad + \lambda q d |\mathbf{h}_i - \mu_h|^{q-1} \odot \text{sign}\{\mathbf{h}_i - \mu_h\} \end{aligned} \quad (15) \quad (16)$$

where $\mathbf{Q}_t = \mathbf{I} - \mathbf{P}_t$, \odot is the Schur matrix product, and $\text{sign}\{\cdot\}$ is the signum function.

Having used matrix-vector notation to facilitate evaluating the gradients, we now note that the conventional matrix vector products in equations (15) and (16) involve huge matrices, and are extremely computationally inefficient. Fortunately, each product corresponds to either 2-D convolution or 2-D deterministic correlation in the image domain, which can be computed directly with far lower computational burden. A simple and efficient iterative steepest descent algorithm based on the gradient expressions given above is

$$\mathbf{F}^{k+1} = \mathbf{F}^k + \alpha \sum_{i=1}^M \mathbf{H}_i^k \star (\mathbf{G}_i - \mathbf{H}_i^k \star \mathbf{F}^k) - \alpha \gamma p \sum_{t \in \delta_f} b_t \mathbf{Q}_t \star |\mathbf{Q}_t \star \mathbf{F}^k|^{p-1} \odot \text{sign}\{\mathbf{Q}_t \star \mathbf{F}^k\} \quad (17)$$

$$\begin{aligned}
H_i^{k+1} = & H_i^k + \alpha F^k \star (G_i - F^k \star H_i^k) - \alpha \lambda q \sum_{t \in \delta_h} c_t Q_t \star |Q_t \star (H_i^k - \mu_h)|^{q-1} \odot \text{sign}\{Q_t \star (H_i^k - \mu_h)\} \\
& - \alpha d |H_i^k - \mu_h|^{q-1} \odot \text{sign}\{H_i^k - \mu_h\}
\end{aligned} \tag{18}$$

where all upper case variables represent 2-D images (rather than the column scanned images), superscripts, k , indicate the iteration number, ‘ \star ’ represents 2-D deterministic correlation, ‘ \odot ’ indicates 2-D convolution, and α is the iteration step size.

The convolutions and correlations in equations (17) and (18) involving F and H_i can be computed efficiently in the frequency domain using a 2-D FFT based algorithm. Since Q_t was formed as the sum of permutation and identity matrices, it is seen that convolutions and correlations involving Q_t are computationally trivial, involving just a simple shift and add, i.e.

$$\begin{aligned}
Q_t \star F &= F[m, n] - F[m - m_t, n - n_t], \quad [m - m_t, n - n_t] \in \{\text{the region of support for } F\} \\
Q_t \star F &= F[m, n] - F[m + m_t, n + n_t], \quad [m + m_t, n + n_t] \in \{\text{the region of support for } F\}
\end{aligned} \tag{19}$$

where m_t and n_t are the row and column distances to the neighbor indexed by t . Restorations results using this algorithm are presented in the following section.

3 Experimental Results for GGMRF Restoration

In this section we present a variety of results for blind image restoration using the GGMRF MAP algorithm described above. All of the observation data used in the examples presented below, whether real data, or synthesized blurred image frames, have a random multiframe residual blur that is representative of a partially adapted AO telescope system. The algorithm of equation (18) was tried with a variety of parameter settings for α , γ , λ , p , and q in order to find the best performing points to achieve the results presented below.

3.1 Results Using Synthetic AO Space Object Data

Natural (i.e non-man-made) space objects, including asteroids, planets, galaxies, comets and nebulae, are often imaged by AO systems, and are candidates for blind restoration. These objects exhibit a wide variety of edge activity (i.e. predominance of sharp edge boundaries), smoothness, and texture-like features. This section presents some experiments which show the performance of blind Bayesian restoration on these objects using the GGMRF model. Experiments have been processed for a wide range of parameter settings and operational conditions on synthetically generated image data.

In each of the examples to follow, the simulated AO observation data was synthesized by corrupting an actual high resolution image (recorded by a near fly-by of a NASA spacecraft) with three different realizations of a random blur. This blur consisted of an elliptical Lorentzian central peak surrounded by a low-frequency Gaussian random field mottled halo pattern. This model has been shown to be an excellent representation of the residual blur observed at the Starfire Optical Range 3.5m and 1.5m AO telescopes [5, 6]. In each example three observed frames were processed, and the blur psf’s were treated as unknown by the GGMRF MAP algorithm, so fully blind multiframe restoration could be evaluated. All images are normalized in amplitude so that $\sum_{i,j} x(i, j) = 1$ in order to reduce variability between images in the required algorithm parameter settings.

Figure 3 presents an example of blind GGMRF restoration for the asteroid Ida. This object is well modeled with the GGMRF for $p \approx 1.1$ because of its abundance of sharp edges and well defined regions (craters) that are relative constant valued. Figures 3 (d), (e), and (f) show the reconstruction for three different settings of the regularization parameter γ . It is instructive to see that when γ is too large (e), the solution is over-regularized and loses all but the largest details. Also, with too little emphasis on the image prior model, a Maximum Likelihood-like solution is achieved with significant noise amplification

(Figure (f)). Figure 3 (d) represents the best parameter settings achieved. Note the significant recovery of crater detail.

Figure 4 presents a three-frame blind restoration example for an image of the planet Saturn. The peak SNR was 40 dB and again the synthetic blur psf's simulated AO residual blur. Note that the restoration recovers much of the ring detail and the gas cloud bands. As with the asteroid image, the Saturn image is also a good candidate for blind GGMRF restoration because of the sharp edge detail in the image, which differs significantly from the smooth, low-pass blur function. This permits a small value of $p = 1.5$ to be used for the object, with a large value of $q = 2.5$ for the blur model. This distinction between p and q is key to overcoming the convolutional ambiguity between object and blur. Other experiments with 50 dB and 30 dB peak SNR show comparable improvement in the restored image over the observation.

Figure 5 presents a third example of blind GGMRF restoration, this time processing a telescopic image of the Andromeda Galaxy. In this case, the object of interest is nebulous, and low-pass in nature, as is the blur operator. $p = 2.0$ was deemed to be a good shape parameter value for the object model, and again $q = 2.5$ was used to model the blur. Figure 5(d) shows that the method fails under these circumstances. Because the object and blur models were so similar it was not possible to resolve the convolutional ambiguity, and much of the object detail was included as part of the blur estimate.

Additional restoration examples and a more extensive list of the algorithm parameter settings can be found in [25].

3.2 Restoration Using Real AO Satellite Data

The section presents some blind restoration results using real AO data, collected at the Starfire Optical Range (SOR) of the Air Force Research Laboratory. The SOR AO system includes a 1.5 meter telescope with a (approximately) 200 cell fully adaptive deformable mirror and a Shack-Hartmann wavefront detector of corresponding size in a closed loop control configuration.

The data presented here is from a pass of a METEOR-1 satellite, collected in July or 1995. Partial AO correction was obtained using the object image itself at the wavefront detector, without the use of a guide star. Figure 6 is a sketch of the configuration of the METEOR-1 satellite class.

In the results that follow, only the GGMRF portion of the blur model was used, i.e. $\vartheta = 0$. Experiments to evaluate performance with the cross relation term included are under way. Figure 7 shows the data set used to compute the restoration.

Each of the 10 frames shown is the average (without alignment correction) of 16 consecutive frames of the original data. collected with a frame exposure time of 5 ms. This averaging increases SNR, albeit at the expense of the desired blur diversity.

Figure 8 presents the steepest descent restoration achieved using GGMRF models for object and blur. Note that the solar panels are clearly resolved, and that shadowing at the junction of the lower panel and main body is evident. Figure 8b shows the result that would be obtained with no object regularization, i.e. without the GGMRF image prior term. This result is equivalent to the commonly used Maximum Likelihood solution. It is apparent that without the image prior model, the solution converges to an overly thinned, unrealistic region of support. Figure 8a is consistent with phase diversity processing of this data reported by Paxman et al [4], and with results using the algorithm of Jefferies and Christou [1] [2].

4 GGMRF Shape parameter Estimation

The GGMRF pdf model of equation (8) includes three parameter sets (p , $b_{s,t} \forall (s,t)$, and $a_s \forall s$) which affect the texture structure of the underlying random field, and consequently its effectiveness as a prior model in MAP restoration. It is important to choose parameter values which are representative of the class of image being restored, or the solution will be biased away from reality. Settings of p control the "edginess" of the image, while $b_{s,t}$ influences the correlation structure and patterning. a_s affects the

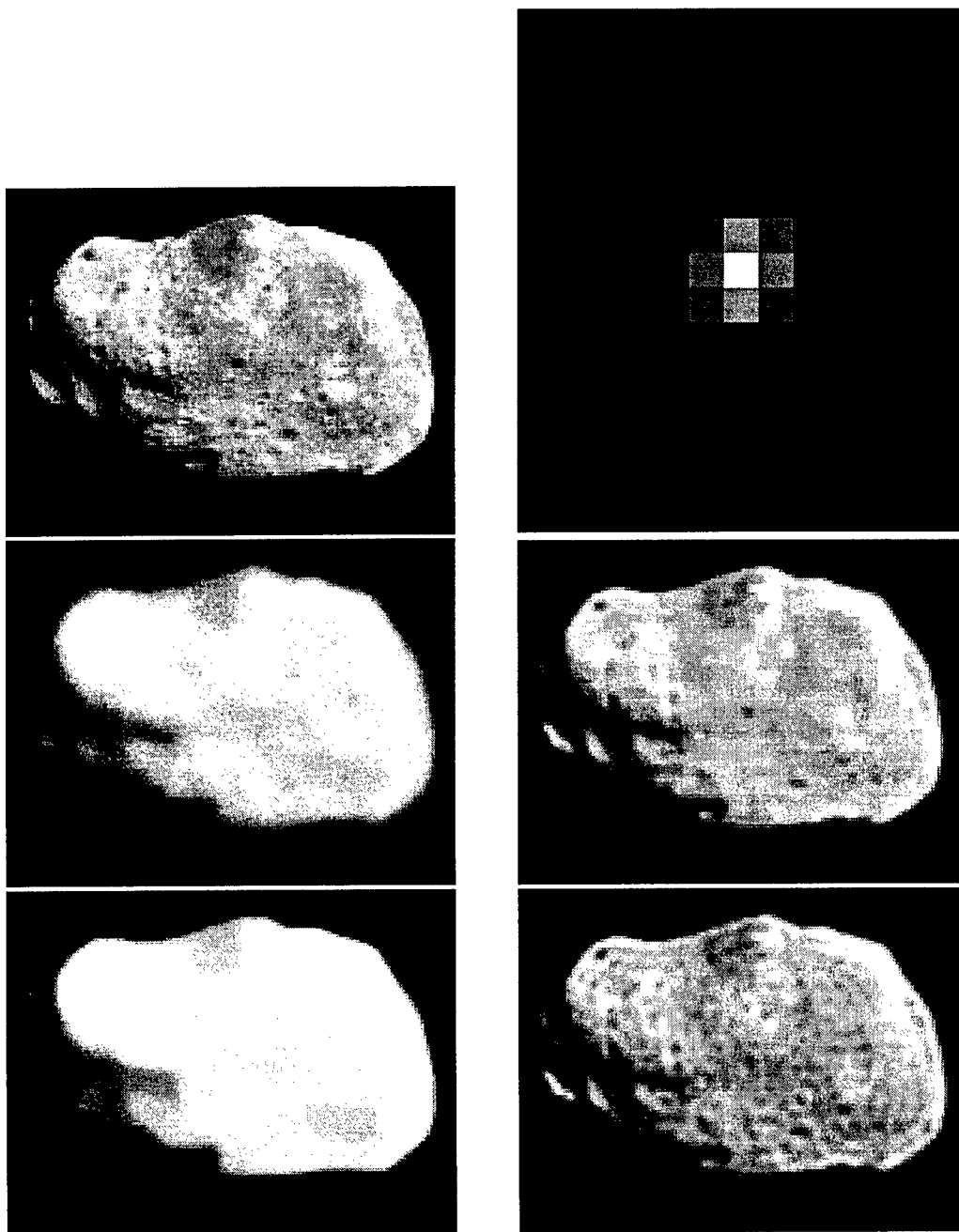


Figure 3: **Ida Image.** a)[Top Left] Original image, size 115×150 , b)[Top Right] True blur psf for frame one of three frames, c)[Middle Left] Observed image that correspond to frame one of three blur frames, corrupted by Lorentzian blur and 40 dB peak SNR, d)[Middle Right] Restoration with $p = 1.1$, $\gamma = 5 \times 10^{-4}$ and $\lambda = 2.1 \times 10^{-5}$, e)[Bottom Left] Restoration with $p = 1.1$, $\gamma = 3 \times 10^{-3}$ and $\lambda = 2.1 \times 10^{-5}$, f)[Bottom Right] Restoration with $p = 1.1$, $\gamma = 0$ and $\lambda = 1.6 \times 10^{-5}$.

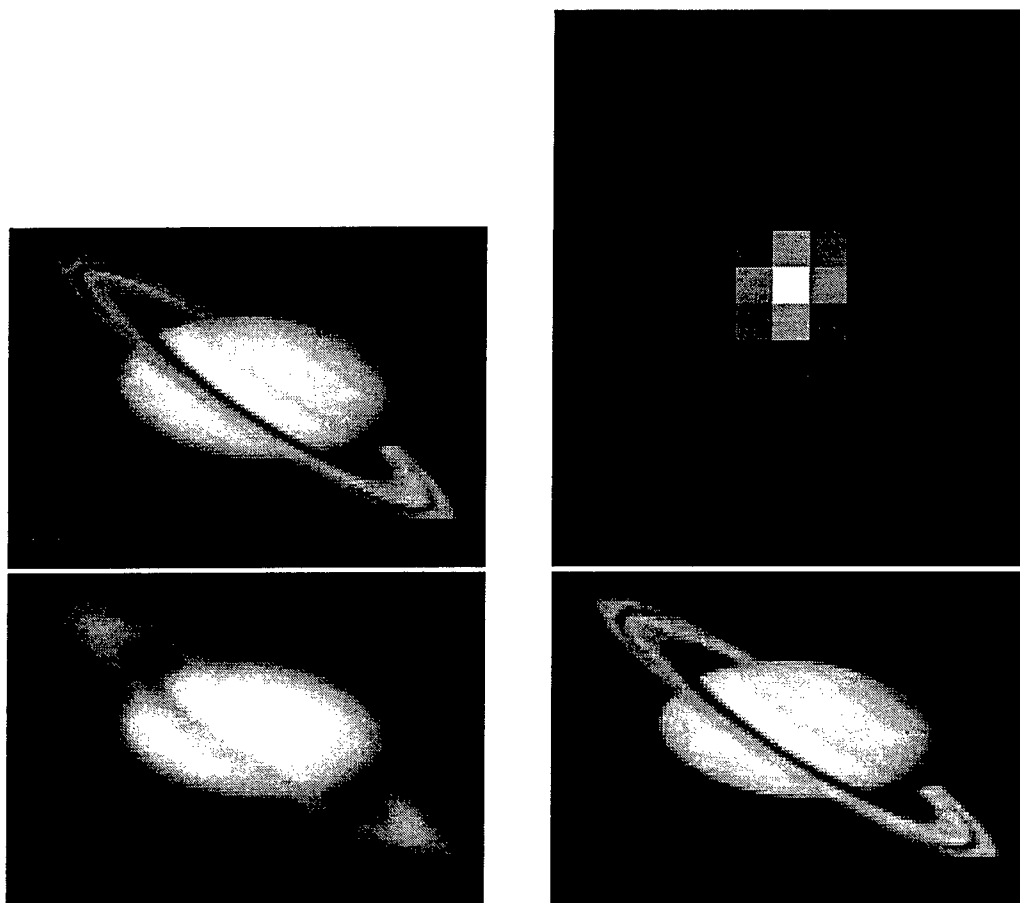


Figure 4: **Saturn Image.** a)[Top Left] Original image, size 90×128 , b)[Top Right] True blur psf for frame one of three frames, c)[Bottom Left] Observed image, corrupted by Lorentzian blur and 40 dB peak SNR, d)[Bottom right] Restoration with $p = 1.5$, $\gamma = 0.01$ and $\lambda = 1.1 \times 10^{-5}$.

overall variance level, but is usually set to zero in MAP image restoration applications because the fidelity term, $p_{g|f,h}(\bar{g}|\mathbf{f}, \mathcal{H})$, has a greater impact on the signal level of the solution. In this section and the one following we discuss methods of estimating p and $b_{s,t}$ from a library of uncorrupted images similar to the one being restored.

In the previous section it was assumed that the value of the GGMRF shape parameter, p , was known or could be chosen by the operator to represent an image of interest. We have found by experimentation that p values in the general range of 0.7 to 1.5 work well for restoring man-made-object images, like artificial satellites. This approach to setting p is however unsatisfying because it does not answer the question of what the best parameter fit would be for a given image class, nor do we know how much restoration performance could be improved with an “optimal” parameter match. In this section we address these issues, introduce a method for estimating p , and compute p estimates for a variety of satellite images.

Shape parameter estimation for the GGMRF model is crucial for higher quality image restoration. The value of p ranges widely when modeling a representative selection of images and texture fields. Though it is difficult to obtain good ‘ p ’ estimates from a degraded image, it is often possible to find an ensemble of images similar to the desired true image [12] [13]. Estimates of p from this ensemble can then be

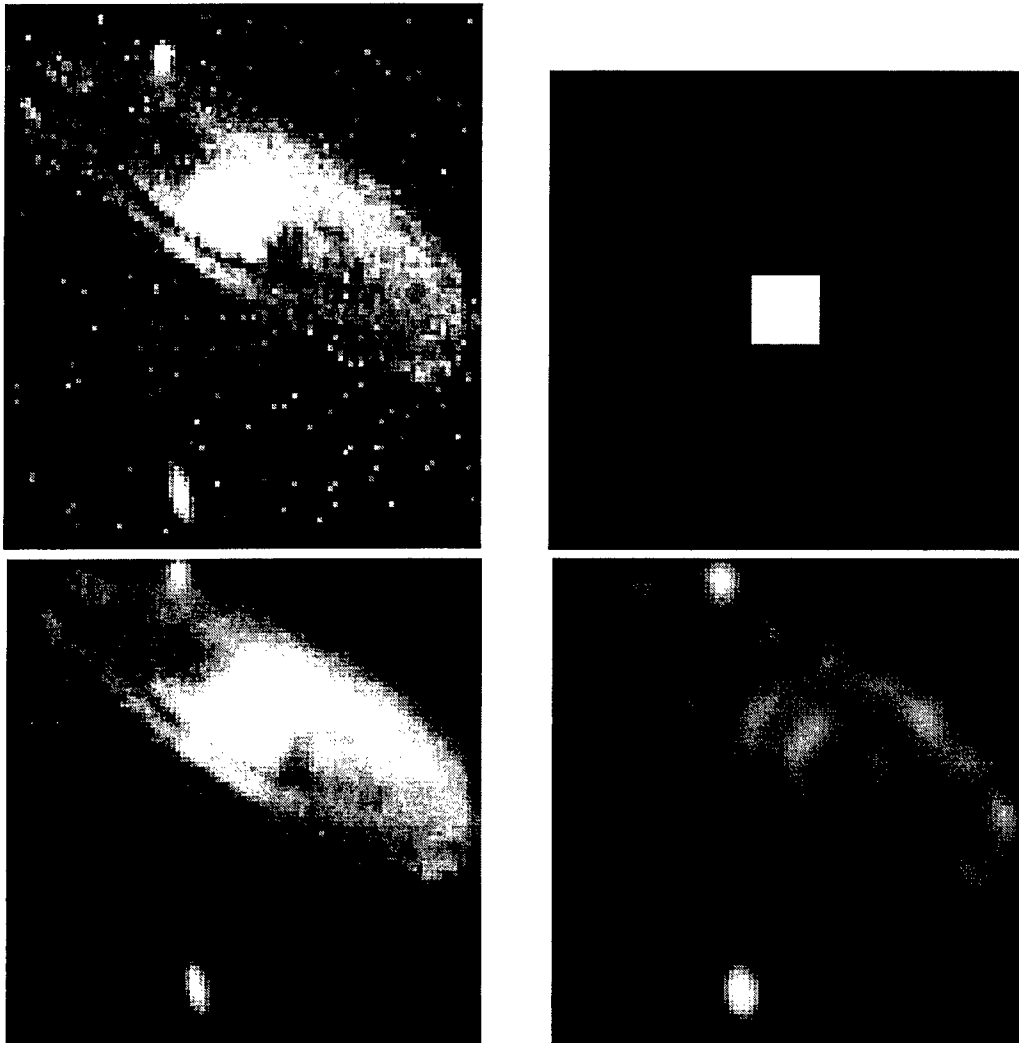


Figure 5: **Spiral Image.** a)[Top Left] Original image, size 108×96 , b)[Top Right] True blur psf for frame one of three frames, c)[Bottom Left] Observed image, corrupted by Lorentzian blur and 40 dB peak SNR, d)[Bottom Right] Restoration with $p = 2.0$, $\gamma = 0.31$ and $\lambda = 1 \times 10^{-6}$.

used in restoring the degraded image.

A simple estimation of p based on sample kurtosis can be obtained using a neighbor difference image, d , with pixels defined as $d_{s,a} = f_s - f_a$ where f_a is the one directional (e.g. right) nearest neighbor of f_s . We have shown that the exact relationship between kurtosis and the GG shape parameter p is

$$\beta_2 = \frac{\Gamma(5/p)\Gamma(1/p)}{[\Gamma(3/p)]^2} \quad (20)$$

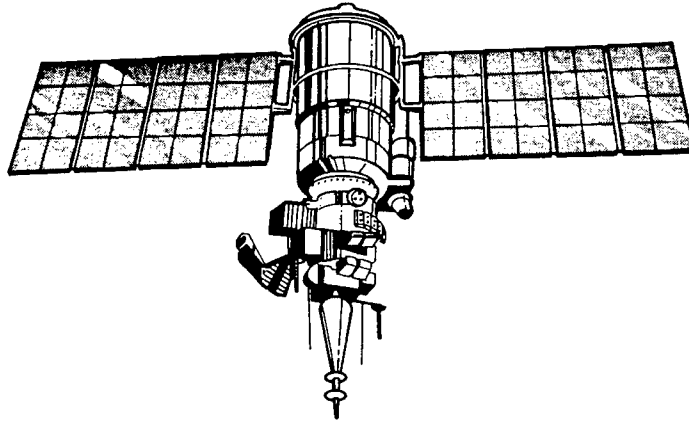


Figure 6: Diagram of the METEOR-1 satellite class. Drawing courtesy of USAF Phillips Laboratory [26].

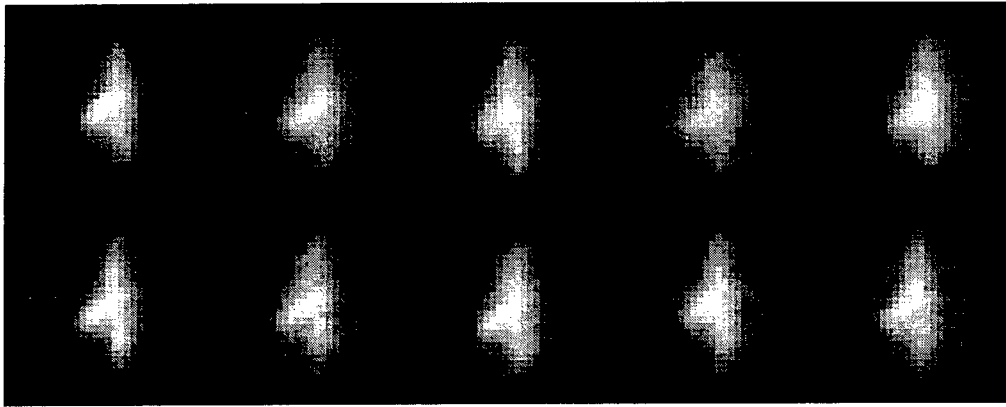


Figure 7: Observed data for catalog number 4419, METEOR-1 satellite. Each of the 10 frames consists of the average over 16 sequential original 5 ms exposure frames. Frames are 32×32 pixels. Note the shift in alignment and blur extent from frame to frame.

Sample kurtosis can be computed as

$$\hat{\beta}_2 = \frac{|S| \sum_{s \in S} (d_{s,a} - \bar{d})^4}{\left[\sum_{s \in S} (d_{s,a} - \bar{d})^2 \right]^2} \quad (21)$$

where $|S|$ is the total number of pixels on the lattice set, S , and $\bar{d} = \frac{1}{|S|} \sum_{s \in S} d_{s,a}$.

A look-up table approximation of equation (20) can be computed. By sampling equation (20) for a number of values of p , and then using cubic spline interpolation between the nearest table entries, we can approximate the inverse function for (20) and compute the value of p that corresponds to \hat{p} . This is the “inverse kurtosis method [13].”

An ensemble of unblurred spacecraft images was collected to estimate p values for GGMRF blind restoration. A total of 21 different images with widely ranging structures, including Cassini, Mir, Mariner,

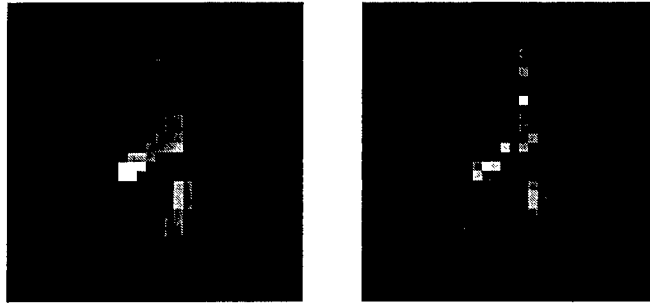


Figure 8: Restoration of the data in Figure 7. A logarithmic grayscale is used to emphasize low level detail. 6,000 iterations of the steepest descent algorithm were used, with $p = 1.1$, $q = 2.5$, first order GGMRF object model, and second order blur model. a) [left] Solution with $\gamma = .4$. b) [right] Solution with $\gamma = 0$, i.e. using no image prior model. This is equivalent to the Maximum likelihood solution, and is seen in this example to overly thin the solution.

Pioneer, etc, have been chosen to form the spacecraft database. In order to reduce bias in p value estimates that results from large blank areas in the images, a mask was computed automatically for each image to exclude much of the background when applying the inverse kurtosis estimator. The p value estimations without masks will produce values that are much smaller than the true p values because the sample Kurtosis is biased low by zero valued $d_{s,a}$ terms in the sum.

Table 1 lists the estimated p values associated with the twenty-one spacecraft images at two resolution scales. Figures 9 and 10 are examples of images and masks used for this estimation. The high resolution image in Figure 9 is a 270×200 pixels. The low resolution image is obtained by low pass filtering and decimating the high resolution image by 4 in each direction. The high resolution image in Figure 10 is a 400×230 pixels, while the resolution image is decimated by 8 in each direction. The low resolution images in each case are representative of the resolution scale for low level orbiting space objects as seen in an AO telescope image.

Over the tabulated trials, the estimated p values range mainly from 0.63 to 1.00 for high resolution and from 0.93 to 1.5 for low resolution. This result shows that as resolution increases, the p value generally decreases. One of the sufficient conditions for the model parameters to insure convex optimization in blind GGMRF restoration is that p be greater than 1. We note that for the low resolution images, which more closely represent the scale of the Starfire Optical Range AO images, there are a number of spacecraft with p values just greater than 1.0. This observation justifies our previous trial-and-error selection of $p = 1.1$. In practice, we recommend that for spacecraft images $p \approx 1.1$ to 1.2 for the GGMRF shape parameter to preserve edge features, rather than using table values less than 1.0.

5 GGMRF Neighborhood Influence parameter Estimation

For the results presented in Section 3 the neighborhood influence parameters, $b_{s,t}$, were arbitrarily set to a first order neighborhood with uniform (all equal) weighting. Though uniform weights performed acceptably and imposed the desired correlation structure on the solution image, this ad-hoc method of parameter setting is unsatisfying. Using values of $b_{s,t}$ estimated from a library of uncorrupted images similar to the blurred image of interest is expected to produce improved restorations.

In this section we demonstrate the effectiveness of the coding method for GGMRF neighborhood influence parameter estimation. We will show that the maximum likelihood (ML) coding estimator for Gauss Markov random fields (GMRF) works surprising well when applied to GGMRF images. This is true even though the method is not a true ML estimator in the GGMRF case. The conditional density function for a Gauss Markov random field can be expressed in a form similar to the GGMRF model of

<i>Name</i>	<i>p estimate</i>	
	<i>High Res.</i>	<i>Low Res.</i>
STS	0.66	1.01
Cassini 1	0.70	1.16
Cassini 2	0.63	0.96
Cassini 3	0.70	1.3
Cassini 4	1.06	1.61
Cassini	1.41	1.99
Mir 1	0.74	1.03
Mir 2	1.04	1.53
Mir 3	1.03	1.95
Mariner 5	0.89	1.34
Mariner 9	0.64	0.93
Mariner 4	0.97	1.06
Mariner 6,7	0.90	1.08
Mariner 2	0.98	1.76
Mariner 10	0.77	1.43
Voyager	0.77	1.24
Voyager	0.89	1.08
Ranger 3	0.85	1.06
Seasat	0.96	1.10
Explorer 1	0.97	1.76
Pioneer 10	0.50	0.93

Table 1: **Estimated p value** from 21 spacecraft images at two resolution scales.

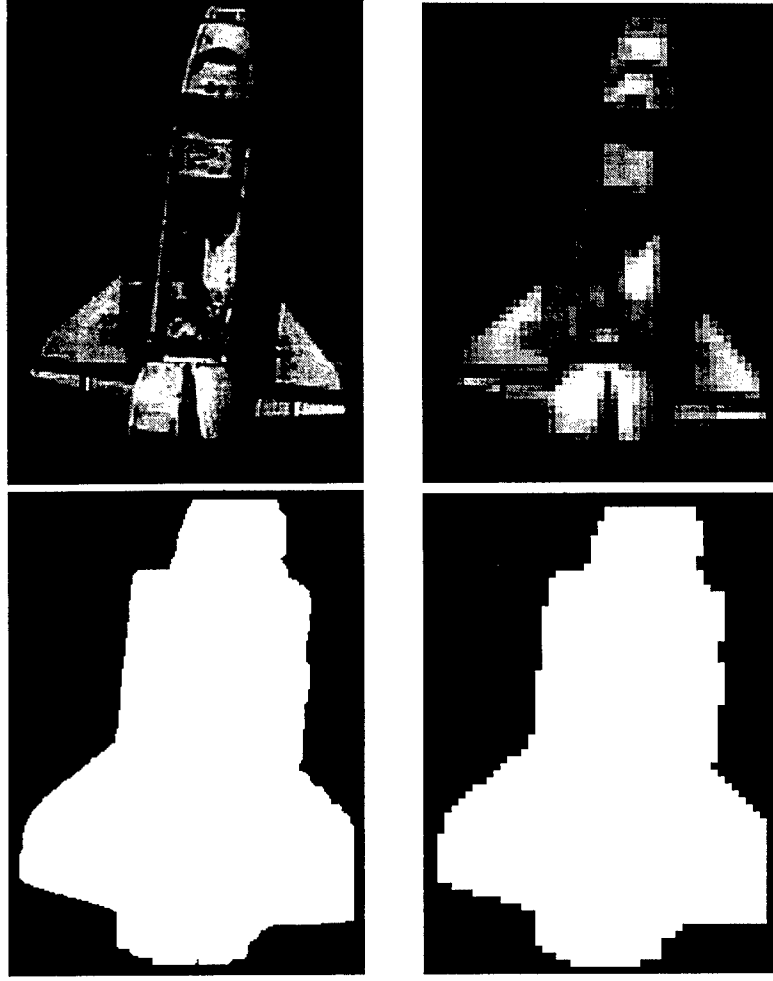


Figure 9: **Space Shuttle (STS) image** a)[Top Left] High resolution photograph b)[Top Right] Low resolution photograph, more representative of AO telescope system pixel resolution c)[Bottom Left] Mask for High resolution. Only pixel in the white region are used for p estimation. d)[Bottom right] Mask for Low resolution

equation (8),

$$p(f_s | f_t, \forall t \in \delta_s) = \frac{1}{Z_f} \exp \left\{ \sum_{t \in \delta_s} b_{s,t} |f_s - f_t|^2 \right\}, \quad (22)$$

where δ_s is the neighborhood of s .

It can be shown [25] that this representation is equivalent to a form used by Kayshap, Chellappa and others [27]

$$p(f_s | f_t, \forall t \in \delta_s) = \frac{1}{\sqrt{2\pi\sigma^2}} \exp \left\{ -\frac{1}{2\sigma^2} \left[f_s - \sum_{t \in \delta_s} \theta_t f_t \right]^2 \right\}. \quad (23)$$

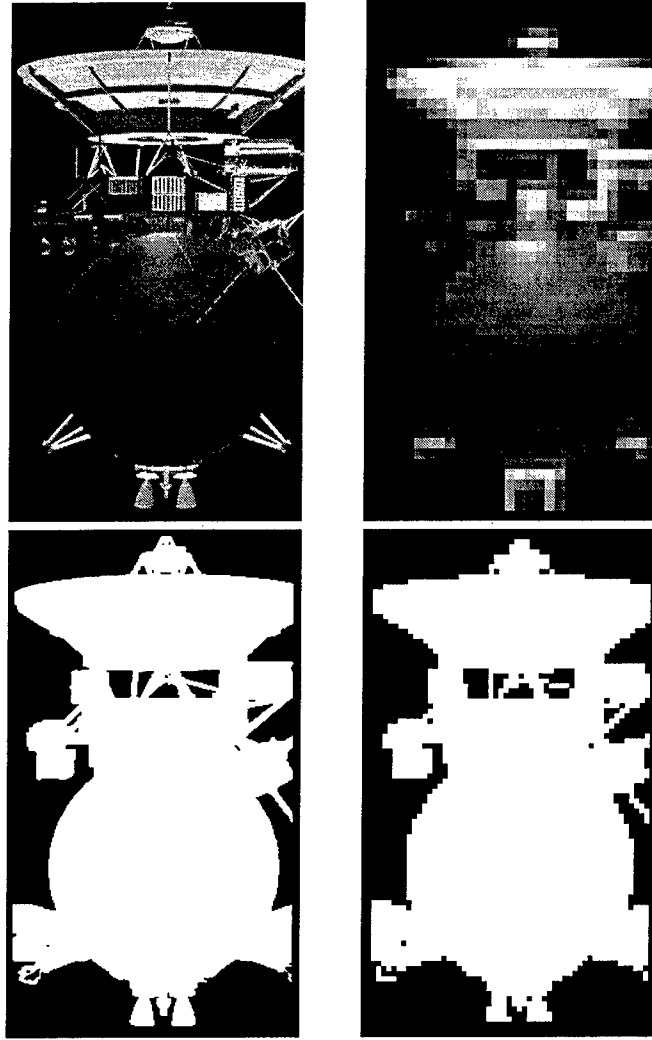


Figure 10: **Cassini image** a)[Top Left] High resolution photograph b)[Top Right] Low resolution photograph, more representative of AO telescope system pixel resolution c)[Bottom Left] Mask for High resolution Only pixel in the white region are used for p estimation. d)[Bottom right] Mask for Low resolution

The advantage of equation (23) is that well known techniques are available for estimating θ_t . The relationship between θ_t and our neighborhood influence parameters, $b_{s,t}$, is $\theta_t = \frac{b_{s,t}}{\sum_{t' \in \delta_s'} b_{s,t'}}$. Thus, given a method to estimate θ_t , we can use it to estimate $b_{s,t}$ in a GMRF.

The coding method was introduced by Besag [28], and later updated by Kashyap and Chellappa [27]. We adopt the Chellappa notation in this discussion. The main idea of the coding method is to separate the lattice set S into several disjoint sets, $S^{(k)}$, called codings, such that no two sites in one $S^{(k)}$ are neighbors, and where $S = S^{(1)} \cup S^{(2)} \cup \dots \cup S^{(k)}$. $\mathbf{f}^{(k)}$ is then the image consisting of only pixels from \mathbf{f} drawn from the lattice sites belonging to coding $S^{(k)}$. Figure 11 shows the codings for a first-order system.

1	2	1	2	1
2	1	2	1	2
1	2	1	2	1
2	1	2	1	2
1	2	1	2	1

Figure 11: Coding for the Four-neighborhood (First-order) System. All pixels designated with the same number belong to a single coding.

Within a single coding no pixels are neighbors, thus by the Markovian property their conditional distributions are independent. The joint density of \mathbf{f} on a coding may therefore be written in product form, which greatly simplifies solving for the maximum likelihood estimator of θ . The joint density on a coding is

$$p(\mathbf{f}^{(k)} | \theta) = \prod_{s \in S^k} p(f_s^{(k)} | f_t, \forall t \in \delta_s, \theta), \quad (24)$$

where all $f_s^{(k)}$ on coding $S^{(k)}$ are mutually independent, and $\theta = [\theta_1, \theta_2, \dots, \theta_{|S|}]^T$. Maximizing equation (24) with respect to θ gives the ML coding estimate, $\hat{\theta}^k$. The arithmetic average of the estimate over all codings yields the final value of $\hat{\theta}$.

For a sample image, \mathbf{f} , drawn from a first order zero mean GMRF, the coding estimate of $\hat{\theta}^k$ is the solution, with respect to θ , of the linear system

$$\begin{aligned} \Lambda \theta &= \chi, \text{ where} \\ \Lambda &= \begin{bmatrix} \sum_s f_{s+r_1}^2 & \sum_s f_{s+r_1} f_{s+r_2} \sum_s f_{s+r_1} f_{s+r_3} & \sum_s f_{s+r_1} f_{s+r_4} \\ \sum_s f_{s+r_2} f_{s+r_1} & \sum_s f_{s+r_2}^2 \sum_s f_{s+r_2} f_{s+r_3} & \sum_s f_{s+r_2} f_{s+r_4} \\ \sum_s f_{s+r_3} f_{s+r_1} & \sum_s f_{s+r_3} f_{s+r_2} \sum_s f_{s+r_3}^2 & \sum_s f_{s+r_3} f_{s+r_4} \\ \sum_s f_{s+r_4} f_{s+r_1} & \sum_s f_{s+r_4} f_{s+r_2} \sum_s f_{s+r_4} f_{s+r_3} & \sum_s f_{s+r_4}^2 \end{bmatrix}, \\ \theta &= [\theta_1, \theta_2, \theta_3, \theta_4]^T, \\ \chi &= \begin{bmatrix} \sum_s f_{s+r_1} f_s \\ \sum_s f_{s+r_2} f_s \\ \sum_s f_{s+r_3} f_s \\ \sum_s f_{s+r_4} f_s \end{bmatrix}, \end{aligned} \quad (25)$$

and where $f_s \in S^{(k)}$.

In this equation we have used a relative position index, r_n , to neighbor pixel $t = s + r_n$. Note that f_{s+r_n} , $n = \{1, 2, 3, 4\}$ is not in coding $S^{(k)}$. For a first-order neighborhood, $r_n = \{r_0 = (0, 0), r_1 = (0, 1), r_2 = (0, -1), r_3 = (-1, 0), r_4 = (1, 0)\}$. This is illustrated in Figure 12.

ML estimation of $b_{s,t}$ for a GGMRF with $p \neq 2$ is an unsolved problem because the partition function, Z_f , depends on these parameters in an unknown way that cannot easily be evaluated. Lacking a direct

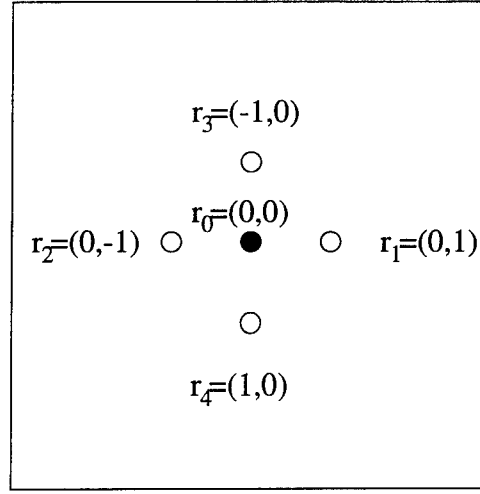


Figure 12: First-Order Neighborhood System For the Coding Method.

solution, we hypothesize that the ML coding estimator for neighborhood influence parameters in a GMRF is an acceptable approximation for the corresponding parameters in a GGMRF for $p \approx 2$. The remainder of this section presents an experimental evaluation of this hypothesis. It is shown that for $0.8 \leq p \leq 2.6$, the first-order GMRF coding estimate of equation (25) provides surprisingly accurate estimates of $b_{s,t}$ for a GGMRF.

The experimental procedure used to evaluate the coding method for GGMRF parameter estimation involved generating a variety of synthetic GGMRF random fields with known shape and neighborhood influence parameters. Estimator results were then compared with the known values. Seven different shape parameter values, $p = 0.8, 1.1, 1.4, 1.8, 2.0, 2.2$, and 2.6 , (covering the range of values that we have commonly used in restoration applications), and four sets of neighborhood influence parameters were used in all possible combinations to generate the test image set. Chen's algorithm was used for image synthesis [24]. For notational convenience we define an augmented influence parameter matrix

$$\mathcal{B} = \begin{bmatrix} \theta_1, r_1 \\ \theta_2, r_2 \\ \theta_3, r_3 \\ \theta_4, r_4 \end{bmatrix}. \quad (26)$$

where θ_n indicates the n^{th} neighborhood influence parameter, and r_n is the corresponding relative position index to designate the neighbor pixel location associated with that parameter. Figure 13 shows an example of the four different images generated using different influence parameters ($\mathcal{B}_1 \cdots \mathcal{B}_4$) as defined in Table 2 while p is fixed at 1.1.

Table 2 also presents the estimation results for the $p = 1.1$ case. Note that even though p is much different than the GMRF value of $p = 2.0$ for which the coding method was designed, each estimated influence parameter (weight) was correct to within 0.02. This was the maximum estimation error over all trials, for all combinations of p and \mathcal{B} . These results demonstrate that the proposed coding method, though designed for GMRF images, is an excellent neighborhood influence parameter estimator for GGMRF images. The $p = 1.1$ case was presented here as an example, but the other experiments documented in [25] also support the conclusion that the coding method is an excellent estimator for GGMRF neighborhood influence parameters regardless of the value of p .

True Weight Matrix \mathcal{B}	Estimated Weight Matrix $\hat{\mathcal{B}}$
$\mathcal{B}_1 = \begin{bmatrix} 0.250, & (1, 0) \\ 0.250, & (-1, 0) \\ 0.250, & (0, 1) \\ 0.250, & (0, -1) \end{bmatrix}$	$\begin{bmatrix} 0.270, & (1, 0) \\ 0.251, & (-1, 0) \\ 0.247, & (0, 1) \\ 0.258, & (0, -1) \end{bmatrix}$
$\mathcal{B}_2 = \begin{bmatrix} 0.250, & (1, 0) \\ 0.250, & (-1, 0) \\ -.250, & (0, 1) \\ -.250, & (0, -1) \end{bmatrix}$	$\begin{bmatrix} 0.258, & (1, 0) \\ 0.258, & (-1, 0) \\ -.264, & (0, 1) \\ -.263, & (0, -1) \end{bmatrix}$
$\mathcal{B}_3 = \begin{bmatrix} 0.083 & (1, 0) \\ 0.083, & (-1, 0) \\ 0.417, & (0, 1) \\ 0.417, & (0, -1) \end{bmatrix}$	$\begin{bmatrix} 0.080, & (1, 0) \\ 0.075, & (-1, 0) \\ 0.425, & (0, 1) \\ 0.432, & (0, -1) \end{bmatrix}$
$\mathcal{B}_4 = \begin{bmatrix} 0.000, & (1, 0) \\ 0.000, & (-1, 0) \\ 0.500, & (0, 1) \\ 0.500, & (0, -1) \end{bmatrix}$	$\begin{bmatrix} -.006, & (1, 0) \\ -.005, & (-1, 0) \\ 0.486, & (0, 1) \\ 0.500, & (0, -1) \end{bmatrix}$

Table 2: GGMRF Neighborhood Influence Parameter Estimation, $p = 1.1$.

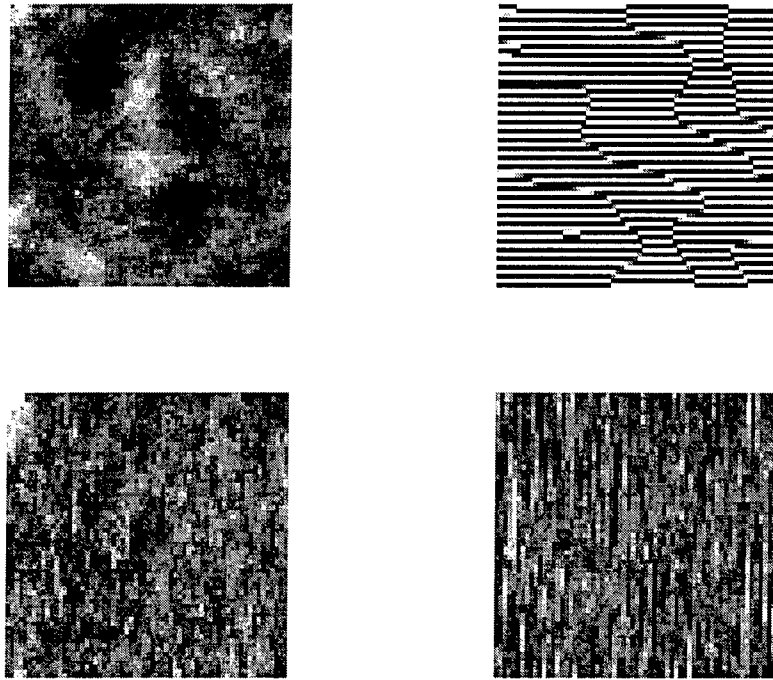


Figure 13: Synthetic GGMRF Images for Shape Parameter $p = 1.1$. a)[Top Left] true neighborhood influence matrix, \mathcal{B}_1 , b)[Top Right] \mathcal{B}_2 , c)[Bottom Left] \mathcal{B}_3 , d)[bottom Right] \mathcal{B}_4 .

The purpose of the next two experiments is to evaluate the neighborhood influence parameter estimation technique when applied to space object images. In effect, we are here assuming space object images can be modeled as GGMRF's, and we wish to evaluate the effectiveness of using estimated neighborhood influence parameters in GGMRF blind restoration.

First, the coding method for GGMRF neighborhood influence parameter estimation was applied to simulated adaptive optics (AO) images. The asteroid Ida and planet Saturn images from Section 3.1 were tested, along with a synthetic satellite image. Table 3 shows the figure numbers, names, image sizes, and the estimated GGMRF neighborhood influence parameters.

Although it is not possible to evaluate the accuracy of the estimates in Table 3 (in fact, the test images are not GGMRF's, and true \mathcal{B} values are not known), we can evaluate the effectiveness of the GGMRF model and parameter estimator for the purpose of restoring these images.

An example is presented here demonstrating use of estimated neighborhood influence parameters in restoring the asteroid Ida image obtained by a spacecraft close fly-by. The original image is shown in Figure 15a. Three distinct AO residual blurs were synthesized using randomized realizations of Drummond's Lorentzian model [5], and then used to blur Figure 15a. Figure 15b shows one of the three observed frames, generated by convolving the original image with one frame of the blur model. Figure 15c is the GGMRF restoration result obtained with a first-order uniform neighborhood model for \mathbf{f} , $p = 1.1$, a second order model for \mathbf{H} , and $q = 3.0$. Note the significant recovery of detail in Figure 15c as compared to 15b. The original asteroid image was processed using the coding method to estimate neighborhood influence parameters. The computed values shown in Table 3, for Ida were used. The restoration using these parameter values, shown in Figure 15d, recovers slightly more detail than the restoration using a uniform neighborhood influence parameter.

Figure Number	Name	size	Estimated Parameter \mathcal{B}
Figure 3a	Ida	115×150	$\begin{bmatrix} 0.3385, & (1, 0) \\ 0.3385, & (-1, 0) \\ 0.1638, & (0, 1) \\ 0.1638, & (0, -1) \end{bmatrix}$
Figure 14a	Satellite	200×220	$\begin{bmatrix} 0.3084, & (1, 0) \\ 0.3084, & (-1, 0) \\ 0.1955, & (0, 1) \\ 0.1955, & (0, -1) \end{bmatrix}$
Figure 4a	Saturn	90×128	$\begin{bmatrix} 0.5365, & (1, 0) \\ 0.5365, & (-1, 0) \\ -.0346, & (0, 1) \\ -.0346, & (0, -1) \end{bmatrix}$

Table 3: Restoration Parameter

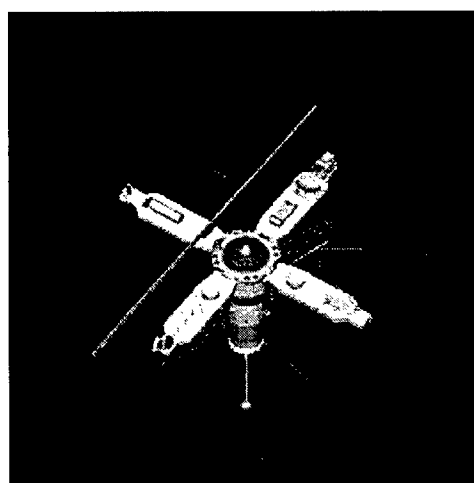


Figure 14: **Synthetic Satellite Image.** This image was used to compute neighborhood influence parameters as shown in Table 3

6 Deterministic Methods for Blind Restoration of AO Images

During the 1998 SREP effort, research in blind restoration evolved into a new parallel path of study beyond the Bayesian GGMRF approach. This section discusses some of our recent work in deterministic,

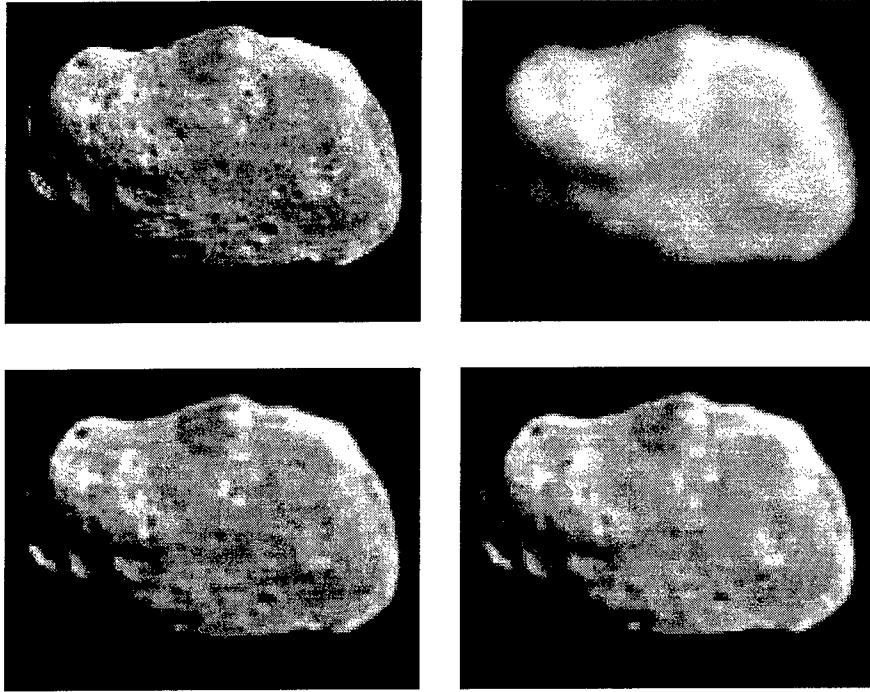


Figure 15: Restoration Results Using Estimated Neighborhood Influence Parameters and Uniform Neighborhood Influence Parameters. a)[Top Left] Original 115×150 pixel image, b)[Top Right] Single frame of AO residual blur image, c)[Bottom Left] Restoration using estimated neighborhood influence parameter, with $p = 1.1$, $\gamma = 4 \times 10^{-4}$ and $\lambda = 1.5 \times 10^{-5}$, d)[Bottom Right] Restoration using uniform neighborhood influence parameter, $p = 1.1$, $\gamma = 5 \times 10^{-4}$ and $\lambda = 2.1 \times 10^{-5}$.

rather than statistical methods. The emphasis of this research has shifted to considering deterministic, or algebraic methods which can sometimes lead to closed form solutions rather than iterative algorithms. Many such techniques have been introduced over the past few years in the literature on blind channel equalization for digital communications [14, 15, 16, 17, 18, 19, 20, 21, 22]. A major focus of this present study is to evaluate how effectively these algorithms can be adapted to the blind AO multiframe image restoration problem.

Three methods were developed to the simulation stage: 1) Homomorphic blind star image restoration, which uses an extremely fast closed form computation to recover blurred points, 2) Direct multiframe solution, which finds the linear algebraic nullspace of the observed data frames, from which the true image is found by subspace matching, and 3) An algebraic cross relationship algorithm which enables estimating the unknown blurs without having to solve for the object image. Adaptation of this method to a previous iterative Bayesian algorithm was also investigated.

6.1 Homomorphic Blind Star Image Restoration

This method of deterministic blind restoration is based on filtering the homomorphic transform known as the 2-D complex cepstrum [29, 30]. This approach relies on a property of the cepstrum that in the transform domain, convolutional terms are mapped to additive terms. For example, as shown in equation

(27), the cepstral transforms, \hat{H}_i and \hat{F} are added to form \hat{G}_i , rather than convolved as in equation (1).

$$\begin{aligned} G_i &= H_i * F \\ \hat{G}_i &\equiv \mathcal{F}^{-1}\{\log\{\mathcal{F}\{G_i\}\}\} \\ &= \hat{H}_i + \hat{F} \end{aligned} \quad (27)$$

where $\mathcal{F}\{\}$ indicates the Fourier transform.

If \hat{H}_i and \hat{F} have non-overlapping regions of support, a simple masking operation can be used to select the desired components, and form an estimate of F using the inverse cepstrum transform as in equation (28). W is a masking window with entries of "1" or "0" used to select the desired components.

$$\bar{F} = \mathcal{F}^{-1}\{\exp\{\mathcal{F}\{W \cdot \hat{G}_i\}\}\} \quad (28)$$

Clearly this method will only work if \hat{H}_i and \hat{F} are essentially non-overlapping in the transform index, quefrency. In the case of point-like star images, we have found that \hat{F} dominates the high "quefrency" terms, while \hat{H}_i , which is low-pass in nature, resides in the low "quefrency" region. Thus W need only block the low terms to form an estimate of F . This method is related to techniques used in pitch period estimation for speech coding [29].

Figure 16 illustrates application of this technique to star image restoration. A single synthetic star image was blurred and noise corrupted to simulate an AO frame. The processing of equations (27) and (28) were then applied to restore the image. Note that in the result, most of the original stars were recovered with high resolution, but that additional noisy "star" artifacts also appear.

Advantages of this method are principally related to its simplicity. The closed form solution does not require iteration, and using FFT code for the transforms makes it extremely efficient. A 256 by 256 pixel image can be processed in seconds on a modest p.c. Additionally, the resultant image is high resolution, with no blurring components. The biggest disadvantages of the approach is its sensitivity to noise. As seen in Figure 16, noise produces false star artifacts. Also, there is at present no obvious method for jointly processing multiple frames, each with distinct blur, in order to reduce noise effects. Simply averaging a series of restored frames does reduce noise, but blurs the stars due to jitter in the estimated star positions.

Future work will attempt to generalize the homomorphic method for multiframe data, and to reduce artifacts. With the existing limitations, this method appears to be primarily useful as a fast computation initialization for other iterative blind restoration algorithms.

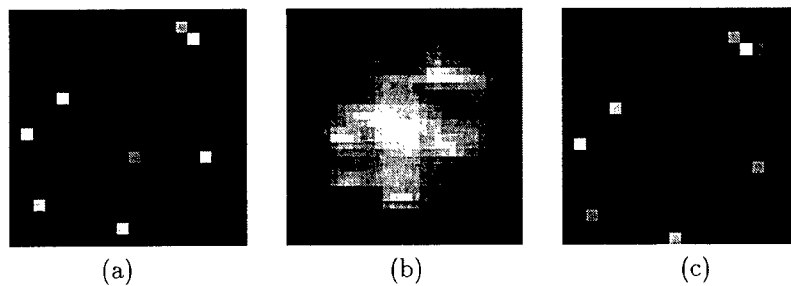


Figure 16: A Single frame example of homomorphic blind star image restoration. a) The original (synthetic) star image. b) Blurred and noise corrupted image. c) The restored image.

6.2 Direct Multiframe Solution

In recent years there have been a number of articles in the digital communication literature that propose deterministic and subspace decomposition methods for solving the blind channel equalization problem

[14, 15, 16, 17, 18, 19]. For a typical scenario, there are multiple sensors which receive a desired coded signal over radio frequency (r.f.) channels with unknown propagation distortion. These channels are represented for each sensor as FIR convolutional filters with distinct, impulse responses corresponding to the unknown r.f. multipath distortion. The objective is to equalize, or remove the effect of channel distortions to enable accurate decoding of the desired signal.

The channel equalization problem is structurally similar to multiframe blind image restoration. The true image, \mathbf{f} , corresponds to the coded signal, the observed image frames, \mathbf{g}_i , correspond to the receiver sensor signals, and the unknown blurs, \mathbf{H}_i , corresponds to the unknown radio frequency channel responses.

The potential advantage of these new methods is that they may yield more accurate solutions than existing image restoration algorithms, and may do so using closed form solutions rather than the iterative, slowly convergent optimization algorithms typically used. Additionally, these methods are direct estimators of \mathbf{f} , and do not require a joint estimate of blurs \mathbf{H}_i . This drastically reduces the degrees of freedom in the estimation problem, and therefore may reduce estimator error.

The focus of this present research topic is to generalize and exploit some of these channel equalization methods for use in multiframe blind image restoration. A few authors have proposed adaptations of blind channel equalization for image restoration [22, 31]. It is our opinion that these methods, as presented, have computational resource requirements that make their use for AO image restoration impractical. The Emphasis of our research will be to exploit underlying principles of blind equalization methods in a more computationally tractable form. This may involve a hybrid of iterative optimization and closed form solution techniques. Also, in the case of point source images like star fields, it is expected that the underlying special data structure may be exploited to reduce memory size and computational load.

It has been shown that if the \mathbf{H}_i have no common factors, and the signal, \mathbf{f} has sufficient modes, then \mathbf{f} can be uniquely determined in the absence of noise with no knowledge of \mathbf{H}_i [21, 14]. Typically, this translates to requiring that three or more frames with sufficiently distinct blurs be available. As an initial study of this property, we have used the method of Liu and Xu for blind recovery of point source images. The Liu - Xu method begins by forming a block Hankel matrix from the observed images

$$\mathbf{G}_{(K)} = \begin{bmatrix} \bar{\mathbf{g}}_1 & \cdots & \bar{\mathbf{g}}_{N-K+1} \\ \vdots & & \vdots \\ \bar{\mathbf{g}}_K & \cdots & \bar{\mathbf{g}}_N \end{bmatrix}, \quad \text{where} \quad (29)$$

$$\bar{\mathbf{g}}_k = [\mathbf{g}_1(k), \dots, \mathbf{g}_M(k)]^T.$$

Here index k selects a particular pixel across all M frames, N is the total number of pixels in G_i , L is the number of pixels in H_i , and K is the smoothing factor chosen by the analyst.

A singular value decomposition is then used to compute \mathbf{V}_o , the nullspace matrix for $\mathbf{G}_{(K)}$. The nullspace matrix for \mathbf{f} is then constructed as

$$\mathbf{V} = \begin{bmatrix} \mathbf{V}_o & \mathbf{0} & \cdots & \mathbf{0} \\ \mathbf{0} & \mathbf{V}_o & \mathbf{0} & \vdots \\ \mathbf{0} & \mathbf{0} & \cdots & \mathbf{V}_o \end{bmatrix} \quad (30)$$

where $\mathbf{0}$ is an $(N - 2L - 2K - 1) \times 1$ vector. \mathbf{f} is then found simply as the non-trivial solution to $\mathbf{V}\mathbf{f} = \mathbf{0}$. Figures 17 and 18 illustrate how this algorithm works for a 1-D point source (star) image. Figure 17a shows plots for the six frames of observed data, while 17b shows the six corresponding psf's. Note that each PSF is a Gaussian function with randomly selected variance (width) and mean (shift position) values. Figure 18a shows the true image, with four distinct point (star) sources, and 18b shows the reconstructed \mathbf{f} computed from the data of Figure 17a alone, with no knowledge of the blur psf's. All four of the point sources were correctly located.

It is noteworthy in the example shown that the solution is obtained with a completely closed form computation, and without any estimate of the blur psf's being formed. These initial tests were restricted

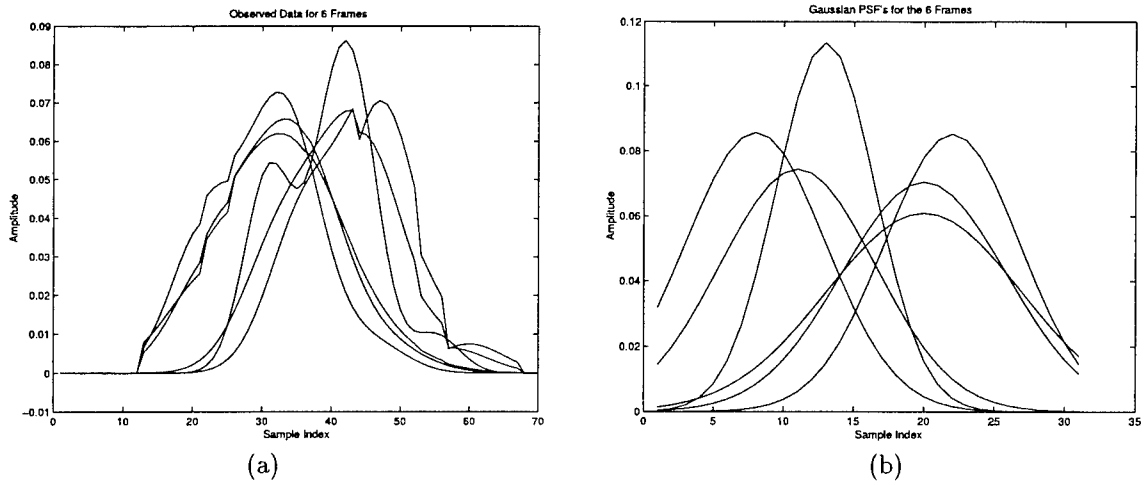


Figure 17: An example of the direct solution method for 1-D multiframe point source image restoration a) The observed data for each of six frames (over-plotted). PSNR is 200 dB. b) Blur point spread functions for the six frames (over-plotted).

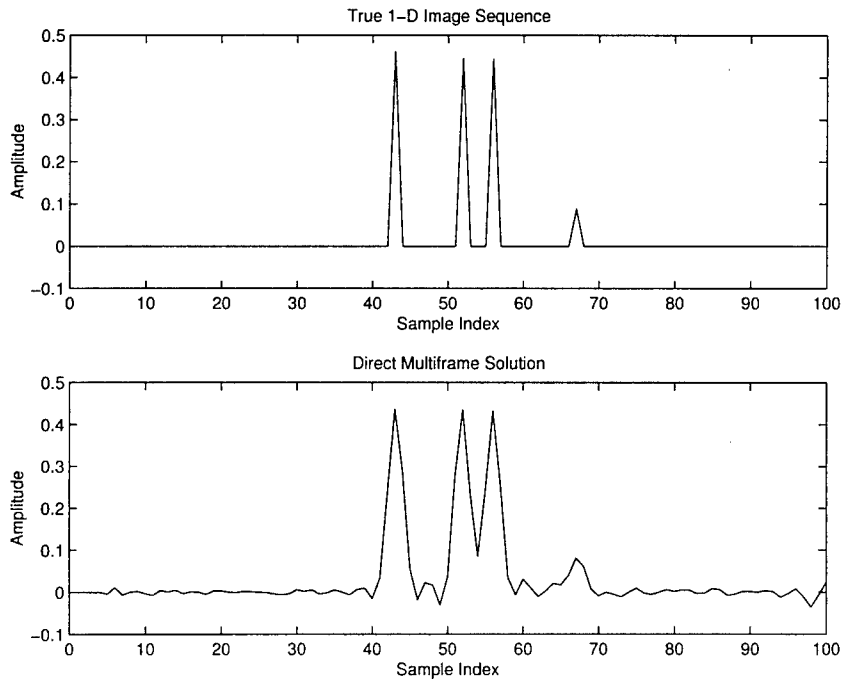


Figure 18: An example of the direct solution method for 1-D multiframe point source image restoration (cont.) a) [top] The true image sequence with four points (stars). b) [bottom] The estimated image sequence.

to 1-D examples due to the large size of $\mathbf{G}_{(k)}$ used in eigenvector computation. In future work we will exploit the prior knowledge that the true image is point-like to simplify computation.

6.3 Cross Relationship Multiframe Blur Estimation

This section reports on studies involving direct estimation of the frame blur psf's, \mathbf{H}_i , without jointly estimating the true image, \mathbf{f} . As with the direct signal (image) estimation method of Section 6.2, the direct blur methods are developed as adaptations of recently published algorithms found in the literature of digital communications, blind channel equalization [20, 21, 18, 19, 22]. By first obtaining high quality estimates of the blurs, it is then possible to use more conventional, well understood non-blind restoration algorithms to recover \mathbf{f} . This sequential approach (estimate \mathbf{H}_i first, then find \mathbf{f}) can yield higher accuracy signal estimates than a joint approach because the degrees of freedom in each estimation stage are reduced.

The cross relationship multiframe blur estimator exploits an algebraic relationship between frames to estimate psf's, \mathbf{H}_i , independent of the object, \mathbf{f} . As shown in [15] and [22], the fact that the true image, \mathbf{f} , is common to every observation frame implies that in the noiseless case the following set of equations must hold

$$G_i = H_i * F \quad (31)$$

$$H_i * G_k - H_k * G_i = 0, \quad \forall i, k, i \neq k. \quad (32)$$

These have been called the "cross relationship" equations because each observed frame is "cross convolved" with another frame's unknown blur function. If the frame blurs have no common factors and \mathbf{f} contains sufficient modes (is persistently exciting) then the \mathbf{H}_i can be uniquely determined from equation (32). There are $(M^2 - M)/2$ equations in (32) when all combinations of i and k are evaluated, which in the absence of noise yields a fully determined system with a unique solution to within an arbitrary scale constant. In [15, 22] a large matrix is formed which expresses all of the relationships of equations (32), and eigen-decomposition methods are then used to find the nullspace of this matrix. This nullspace contains the solution for the \mathbf{H}_i 's. This structure is not well suited to images because of the corresponding huge matrices for which eigen-decompositions must be computed. Additionally, these closed form solutions are not optimal in the presence of noise.

To address these problems, we have developed a computationally efficient iterative least squares algorithm that is suitable for large image sizes. Equation (32) is approximated by

$$\hat{\mathcal{H}} = \arg \min_{\mathcal{H}} \sum_i \sum_{k \neq i}^{i-1} \|H_i * G_k - H_k * G_i\|_F^2, \quad (33)$$

where $\|\cdot\|_F$ indicates the Frobenius norm, and \mathcal{H} represents the set of all blur PSF frames, as in equation (5). For blurs with no common factors, equation (33) gives a unique solution for all H_i if an additional scale constraint is applied, and if F and the H_i are restricted to finite regions of support such that the entire convolution result is seen in G_i without truncation.

It is difficult to solve (33) jointly for all the H_i , so the proposed algorithm iterates by solving for each individual blur successively, while temporarily assuming the current blur estimates for the other frames are accurate. The iteration also cyclically applies region of support and scaling constraints. This approach of sequentially applying a series of constraints is essentially a projection onto convex sets (POCS) method. The solution to equation (33) for the i^{th} blur frame, assuming all other H_k , $k \neq i$ are held fixed is given by

$$\frac{d}{dH_i} \sum_{k \neq i} \|H_i * G_k - H_k * G_i\|_F^2 = 2 \sum_{k \neq i} G_k * (G_k * H_i - G_i * H_k) = 0, \quad (34)$$

where \star indicates the 2-D deterministic correlation operation. In the frequency domain, (34) becomes the easily computed form

$$\tilde{H}_i = \frac{\tilde{G}_i \odot \sum_{k \neq i} \tilde{G}_k^* \odot \tilde{H}_k}{\sum_{k \neq i} \|\tilde{G}_k\|_F^2} \quad (35)$$

where ‘ \sim ’ indicates the 2-D Fourier transform, ‘ * ’ is the complex conjugate, and ‘ \odot ’ is the element-by-element Schur matrix product.

The region of support and scaling constraints are more readily applied in the space domain, i.e. we require that

$$\mathcal{M} \odot H_i = \mathbf{0}, \text{ and} \quad (36)$$

$$\sum_{m,n} H_i(m,n) = 1.0, \quad (37)$$

where \mathcal{M} is a masking matrix with ones corresponding to the finite region of support for H_i , and zero elsewhere. Combining these steps yields the following cross relationship blind blur estimation algorithm:

The Iterative Cross Relationship Blur Estimator

1. Compute the Fourier transform, $\tilde{G}_i = \mathcal{F}\{G_i\}$.
2. Iterate until done.
 - (a) Iterate for each frame, i .
 - i. Compute \tilde{H}_i using equation (eqn:crossfreq).
 - ii. Compute inverse Fourier Transform, $H_i = \mathcal{F}^{-1}\{\tilde{H}_i\}$
 - iii. Apply the region of support constraint, equation (36).
 - iv. Transform back to frequency domain, $\tilde{H}_i = \mathcal{F}\{H_i\}$.
 - (b) Apply the scaling constraint, equation (37).
3. End

Figure 19 illustrates results for this algorithm applied to five frames of synthetic AO star image data. Figure 19a is the original true image, and 19b shows the true blur frames, which are generated with an ellipsoidal Lorentzian function central peak, and a Markov random field mottled texture halo. The Lorentzian peaks have randomly generated major and minor axis length and orientation. This has been shown to be an excellent model for AO residual blur for the SOR telescopes [5, 6]. Figure 19c shows the observed data frames, which have noise added for a 50 dB PSNR level. Figure 19d shows the estimated blur frames. Note that the peak orientations are correctly estimated, however the random halo level is higher than in the true blurs.

6.4 Cross Relationship Metric used in Iterative Bayesian Restoration

In this section we adapt the cross relationship constraint so that it may be incorporated in the blind GGMRF MAP algorithm discussed above. This approach has the advantage that available prior information regarding the object and the blur can be expressed in a natural way in the form of probability density functions (pdf’s). These pdf’s regularize the ill posed inverse problem, and can yield significant restoration performance improvement, particularly with lower SNR data sets. The cross relationship constraint of equation (33) represents additional available prior knowledge regarding the form of the solution. Any algorithm which does not exploit this information gives up potential performance improvement. We will express this information as a term in the blur PSF prior probability density function model used in Bayesian maximum *a posteriori* (MAP) image restoration. This term reduces the probability in the model for any solution which deviates significantly from the cross relationship constraint. The following sections review the development of the GGMRF blind restoration method, and shows how the method is adapted to incorporate the cross relation constraint.

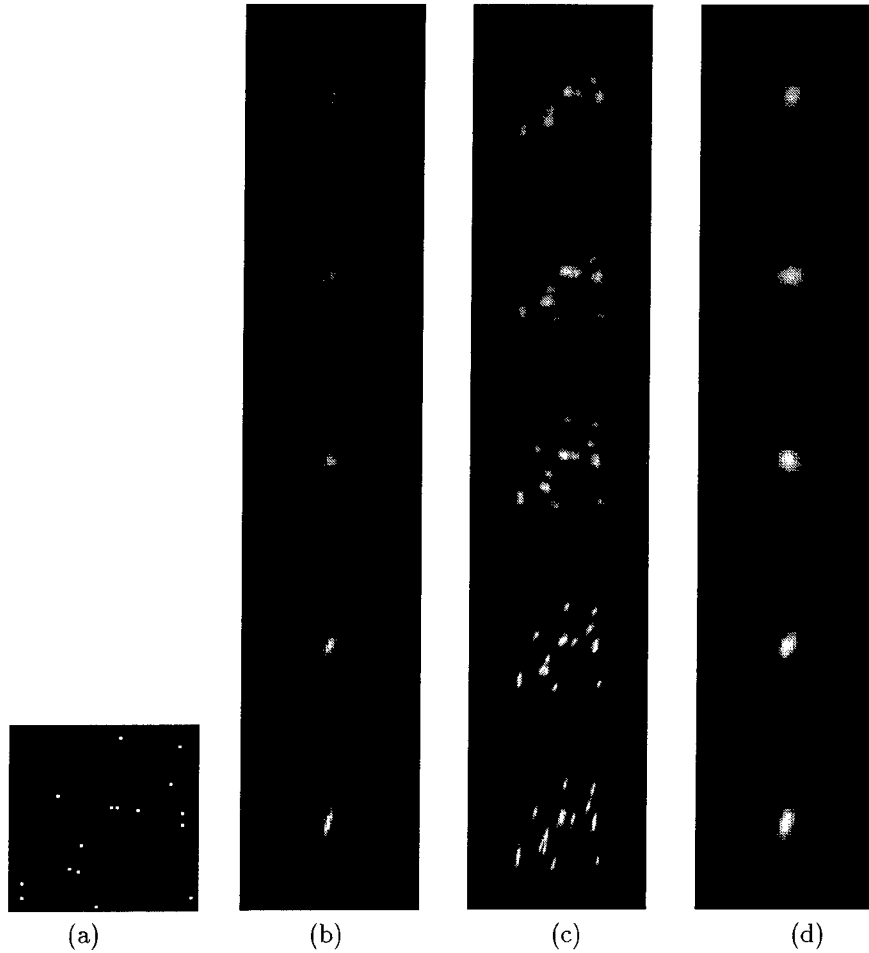


Figure 19: Blind multiframe blur estimation example using cross relationship. a) Original point source image. b) True blur psf's for five frames. c) Observed blurred image frames. d) Estimated blurs.

6.4.1 The Composite GGMRF - Cross Relation Blur Model

The proposed blur pdf model need for blind Bayesian blur estimation is a composite of a GGMRF density and a Gibbs distribution based on the cross relationship of equation (33). The GGMRF is well suited to the task of modeling AO residual blur as well as the space object image because it can be adapted (by changing p) to favor the smoother, band-limited image types usually encountered as blur operators.

Our notions of what a blur field should look like are conveyed by specifying a few neighbor potential weights, the GGMRF shape parameter (q will be used to distinguish it from the object shaper parameter, p) and a mean value, μ_h . This in turn defines a texture class used to penalize the optimization objective function if a candidate blur differs significantly from the model. The composite blur model is given by

$$p_h(\mathcal{H}) = \frac{1}{Z_h} \exp \left\{ -\alpha \left[\sum_{\langle s,t \rangle \in \mathcal{C}_h} c_{s,t} |(h_s - \mu_{h,s}) - (h_t - \mu_{h,t})|^q + \sum_{s \in S_h} d_s |h_s - \mu_{h,s}|^q \right] \right\}$$

$$-\nu \sum_i \sum_{k \neq i}^{i-1} \|\mathbf{G}_i \mathbf{h}_k - \mathbf{G}_k \mathbf{h}_i\|^2 \Big\} \quad (38)$$

where \mathcal{C}_h is the set of all cliques of pixels invoked by the specified neighborhood system, q is the GGMRF shape parameter, S_h is the set of all points in blur the lattice over all frames (set of every pixel in every frame), and $c_{s,t}$ and d_s are potential weights. The first bracketed term of equation (38) represents the GGMRF portion of the blur pdf model. The terms on the second line is the cross relationship term. Under the assumption of white Gaussian noise, independent from frame to frame, the Gibbs distribution associated with the cross relationship term can properly be viewed as an independent Gaussian distribution on the residuals for the exact cross constraint of equation (32). It has been shown that for $1.75 < q < 3.0$ and \mathcal{C}_h corresponding to a first or second order uniformly weighted neighborhood, this model produces a random field with smoothed structures typical of many blur operators [13] [12].

6.4.2 Solution for GGMRF Blur and Object Models

In this section we present the MAP solution expression given the above models. A steepest descent algorithm to compute this solution is given in the following section. Substituting equations (38), (8) and (7) into (5), and performing a little algebra yields

$$\begin{aligned} \hat{\mathbf{f}}, \hat{\mathcal{H}} = & \arg \min_{\mathbf{f}, \mathcal{H}} \sum_{i=1}^M \|\mathbf{g}_i - \mathbf{H}_i \mathbf{f}\|^2 + \gamma \left[\sum_{\langle s,t \rangle \in \mathcal{C}_f} b_{s,t} |f_s - f_t|^p + \sum_{s \in S_f} a_s |f_s|^p \right] \\ & + \lambda \left[\sum_{\langle s,t \rangle \in \mathcal{C}_h} c_{s,t} |(h_s - \mu_{h,s}) - (h_t - \mu_{h,t})|^q + \sum_{s \in S_h} d_s |h_s - \mu_{h,s}|^q \right] \\ & + \vartheta \sum_i \sum_{k \neq i}^{i-1} \|\mathbf{G}_i \mathbf{h}_k - \mathbf{G}_k \mathbf{h}_i\|^2, \end{aligned} \quad (39)$$

where we have taken the logarithm of the r.h.s. (which does not change the maximization due to monotonicity) and have dropped additive constants. γ , λ and ϑ control the relative influence, as regularizing terms, that the image, GGMRF blur, and cross relationship pdf's have respectively on the solution. The theoretically optimum values for γ , λ and ϑ are functions of p , q , and the SNR, though exact expressions for are difficult to derive. Therefor, these parameters are usually manually adjusted for most desirable results. The following proportionality relationships give some guidance on how to set γ and λ

$$\gamma \propto 2\beta\sigma_\eta^2, \quad \lambda \propto 2\alpha\sigma_\eta^2. \quad (40)$$

6.4.3 Steepest Descent Algorithm

In order to simplify gradient computation, the objective function of equation (39) can be expressed as

$$\begin{aligned} J(\mathbf{f}, \mathcal{H}) = & (\bar{\mathbf{g}} - \mathcal{H}\mathbf{f})^T (\bar{\mathbf{g}} - \mathcal{H}\mathbf{f}) + \gamma \text{Trace}\{\text{Diag}\{\sum_{t \in \delta_f} b_t |\mathbf{f} - \mathbf{P}_t \mathbf{f}|^p\}\} \\ & + \lambda \sum_i \text{Trace}\{\text{Diag}\{d |\mathbf{h}_i - \mu_h|^q + \sum_{t \in \delta_h} c_t |(\mathbf{h}_i - \mu_h) - \mathbf{P}_t (\mathbf{h}_i - \mu_h)|^q\}\} \\ & + \vartheta \sum_i \sum_{k \neq i}^{i-1} (\mathbf{G}_i \mathbf{h}_k - \mathbf{G}_k \mathbf{h}_i)^T (\mathbf{G}_i \mathbf{h}_k - \mathbf{G}_k \mathbf{h}_i) \end{aligned} \quad (41)$$

where $|\cdot|^p$ indicates element-wise exponentiation of the magnitude and $\text{Diag}\{\cdot\}$ forms a diagonal matrix from a vector. We have assumed $a_s = 0$ (a common choice [11]), and that $b_{s,t}$, $c_{s,t}$, and d_s are constant

with respect to s . This assumption restricts the model to homogeneous (spatially stationary) random fields. \mathbf{P}_t is the permutation matrix defined in Section 2.4. The corresponding iterative steepest descent algorithm based on the gradient of equation (41) is

$$F^{k+1} = F^k + 2\alpha \sum_{i=1}^M H_i^k \star (G_i - H_i^k \star F^k) - \alpha \gamma p \sum_{t \in \delta_f} b_t Q_t \star |Q_t \star F^k|^{p-1} \odot \text{sign}\{Q_t \star F^k\} \quad (42)$$

$$\begin{aligned} H_i^{k+1} = & H_i^k + 2\alpha F^k \star (G_i - F^k \star H_i^k) - \alpha \lambda q \sum_{t \in \delta_h} c_t Q_t \star |Q_t \star (H_i^k - \mu_h)|^{q-1} \odot \text{sign}\{Q_t \star (H_i^k - \mu_h)\} \\ & - \alpha \lambda d |(H_i^k - \mu_h)|^{q-1} \odot \text{sign}\{H_i^k - \mu_h\} + \alpha 2\vartheta \sum_{k \neq i} G_k \star (G_i \star H_k - G_k \star H_i), \end{aligned} \quad (43)$$

where as in equations (17) and (18), all upper case variables represent 2-D images (rather than the column scanned images), superscripts, k , indicate the iteration number, ' \star ' represents 2-D deterministic correlation, ' \star ' indicates 2-D convolution, and α is the iteration step size.

7 Additional Accomplishments Supported by the SREP Grant

This section summarizes accomplishments resulting from the AFOSR Summer Faculty Research Extension Program support of my research collaboration with Starfire Optical Range at Kirtland Air Force Base. These activities are in addition to the research progress reported above, and include work completed from the end of 1997 until the present.

Accomplishments:

1. Technical Papers Resulting From SOR Work:
 - (a) Brian D. Jeffs and Julian Christou, "Blind Bayesian restoration of adaptive optics images using generalized Gaussian Markov random field models," *Proceedings of the SPIE, Conference 3353, Adaptive Optical System Technologies*, Mar. 23-26, Kona Hawaii.
 - (b) Brian D. Jeffs, Julian Christou and Sheila Hong, "Blind MAP Restoration Of Adaptive Optics Telescope Images Using Estimated Shape Parameters For Generalized Gaussian MRF Models," *Proceedings of the 1998 IEEE DSP Workshop*, Bryce Canyon UT, Aug. 9-12, 1998.
 - (c) Brian D. Jeffs, Sheila Hong, and Julian Christou, "A Generalized Gauss Markov Model for Space Objects in Blind Restoration of Adaptive Optics Telescope Images," 1998 IEEE International Conf. on Image Processing, Chicago IL, Oct. 4-7, 1998.
 - (d) Brian D. Jeffs, Julian Christou, and Sheila Hong, "A Unified Model Based Approach for Blind Bayesian Restoration of Adaptive Optics Images," in preparation, to be submitted to *IEEE Transactions on Image Processing*, November 1998.
2. Master's thesis: Hong Hong, *Blind Bayesian Restoration for Adaptive Optics Telescope Images*, Brigham Young University, Aug. 1998.
3. Developed a data base of satellite images for space object model parameter estimation.
4. Student support: Have supported three graduate students as research assistants to pursue this topic for their theses: Sheila Hong, Brent Chipman and Miguel Apezteguia.
5. Developed an ongoing fruitful collaboration with lab point-of-contact, Julian Christou. Several joint projects are in progress.
6. Estimated GGMRF image prior model shape parameters for a variety of spacecraft. This has validated the approach, and helped improved restoration results.

7. Developed a method for GGMRF neighborhood influence parameter estimation. This also has helped improve restoration results.
8. Developed simulation software to synthesize realistic AO residual Blur Frames. This has simplified the process of evaluating algorithm changes.
9. Ongoing work (in addition to the report above) includes improving parameter settings for the GGMRF model for satellites and blur representation.

8 Conclusions

This report has detailed the progress made under support from 1998 AFOSR Summer Research Extension Program for research in multiframe blind restoration of space objects images from adaptive optics systems. This effort has been very fruitful, and some very promising new technologies have been identified. It is expected that this research effort will lead to higher resolution restorations of AO images with less computational burden than other blind algorithms.

The results presented in Section 3, along with the new methods presented to estimate GGMRF model parameters, suggest that the Bayesian GGMRF approach to blind restoration of adaptive optics data has been successful. This is the first known blind method that permits explicit incorporation of the prior knowledge that space objects are sharp edged and have well defined regions of constant intensity. A particularly attractive aspect of the method is that the same statistical model can be used for both object and blur by judicious choice of model parameters. These two related models then provide sufficiently distinct regularization to separate the image and blur components in the solution. The next step in this effort will be to process much more real AO data with the algorithm to get a better measure of real-world performance.

It is also hoped that the deterministic and composite methods introduced above will enable better satellite structural detail resolution than is currently achievable in typical observing with the SOR 3.5 m AO system. The early work on multiframe blind point source image restoration suggests that this problem will yield a breakthrough solution that will dramatically enhance system performance when computing parameters for binary stars or for dense star fields. The approach is quite different than any previously applied to the problem, and preliminary simulations look good.

This research program has also had a profound effect on three of my graduate students. Sheila Hong has recently graduated with a Master's degree, and a fine thesis reporting her work in AO image post processing. Also, Brent Chipman and Miguel Apezteguia have each recently started their thesis work based on this research program. I expect that my research in this fruitful area and collaboration with Starfire Optical Range will continue for a number of years.

References

- [1] S.M. Jefferies and J.C. Christou, "Restoration of astronomical images by iterative blind deconvolution", *Astrophysical Journal*, vol. 415, pp. 862-874, Oct. 1993.
- [2] J.C. Christou, D. Bonaccini, and Nancy Ageorges, "Deconvolution of adaptive optics near-infrared system images", *Proceedings of the SPIE*, vol. 3126: Conference on Adaptive Optics and Applications, July 1997.
- [3] J.M. Conan, L. Laurent, T. Fusco, V. Michau, and G. Rousset, "Deconvolution of adaptive optics images using the object autocorrelation and positivity", *Proceedings of the SPIE*, vol. 3126: Conference on Adaptive Optics and Applications, July 1997.

- [4] R.B. Paxman, J.H. Seldin, B.J. Thelen, M.F. Reiley, and D.A. Carrarra, "Focused-beam scoring techniques, volume i", Tech. Rep. 278140-9-F(V.I), SOR, Air Force Phillips Laboratory, Kirtland AFB, 1997.
- [5] J.D. Drummond, "Sizes, shapes and rotational poles of ceres and vesta from adaptive optics images", *Bulletin of the American Astronomical Society*, vol. 27, pp. 16, 1996.
- [6] J.D. Drummond, R.Q. Fugate, J.C. Christou, and E.K. Hege, "Full adaptive optics images of asteroids ceres and vesta: Rotational poles and triaxial ellipsoid dimensions", *to appear in ICARUS*, 1998.
- [7] R. L. Lagendijk and J. Biemond, *Iterative Identification and Restoration of Images*, Kluwer, Boston, 1991.
- [8] P.J. Sementilli, M.S. Nadar, and B.R. Hunt, "Poisson map super-resolution estimator with smoothness constraint", *Proceedings of the SPIE*, vol. 2032, July 1993.
- [9] Y. Yang, N.P. Galatsanos, and H. Stark, "Projection-based blind deconvolution", *Journal of the Optical Society of America A*, vol. 11, no. 9, Sept. 1994.
- [10] Z. Mou-yan and R. Unbehauen, "New algorithms of two-dimensional blind deconvolution", *Optical Engineering*, vol. 34, no. 10, pp. 2945-2956, Oct. 1995.
- [11] C. Bouman and K. Sauer, "A generalized Gaussian image model for edge-preserving MAP estimation", *IEEE Trans. on Image Processing*, vol. 2, no. 3, pp. 296-310, July 1993.
- [12] Wai Ho Pun, *Parametric Model-Adaptive Image Restoration*, PhD thesis, Brigham Young University, 1995.
- [13] W. H. Pun and B. D. Jeffs, "Shape parameter estimation for generalized gaussian markov random field models used in map image restoration", in *Conference Record, 29th Asilomar Conf. Signals, Syst., Comp.*, Oct. 1995, pp. 1472-1476.
- [14] H. Liu and G. Xu, "A deterministic approach to blind symbol estimation", *IEEE Signal Processing Letters*, vol. 1, no. 12, pp. 205-207, Dec. 1994.
- [15] M. I. Gurelli and C. L. Nikias, "Evam: An eigenvector-based algorithm for multichannel blind deconvolution of input colored signals", *IEEE Trans. on Signal Processing*, vol. 43, no. 1, pp. 134-149, Jan. 1995.
- [16] L. Tong, G. Xu, B. Hassibi, and T. Kailath, "Blind channel identification based on second-order statistics: A frequency-domain approach", *IEEE Transactions on Information Theory*, vol. 41, no. 1, pp. 329-333, Jan. 1995.
- [17] E. Moulines, P. Duhamel, J. F. Cardoso, and S. Mayrargue, "Subspace methods for the blind identification of multichannel fir filters", *IEEE Trans. on Signal Processing*, vol. 43, no. 2, pp. 516-525, Feb. 1995.
- [18] D. T. M. Slock, "Blind fractionally-spaced equalization, perfect-reconstruction filter banks and multichannel linear prediction", in *IEEE International Conference on Acoustics, Speech, and Signal Processing*, Adelaide, SA, Australia, Apr. 1994, vol. 4, pp. 585-588.
- [19] D. T. M. Slock and C. B. Papadias, "Further results on blind identification and equalization of multiple fir channels", in *IEEE International Conference on Acoustics, Speech, and Signal Processing*, Detroit, MI, May 1995, vol. 3, pp. 1964-1967.

- [20] Y. Hua, "Fast maximum likelihood for blind identification of multiple fir channels", *IEEE Trans. on Signal Processing*, vol. 44, no. 3, pp. 661-672, Mar. 1996.
- [21] H. Liu, G. Xu, and L. Tong, "A deterministic approach to blind identification of multi-channel fir systems", in *IEEE International Conference on Acoustics, Speech, and Signal Processing*, Adelaide, SA, Australia, Apr. 1994, vol. 4, pp. 581-584.
- [22] G. Harikumar and Y. Bresler, "Efficient algorithms for the blind recovery of images blurred by multiple filters", in *Proceedings of ICIP-96, 1996 IEEE Int. Conf. on Image Processing*, Lausanne, Switzerland, Sept. 1996, vol. 3, pp. 97-100.
- [23] A. K. Jain, *Fundamentals of Digital Image Processing*, Prentice Hall, Englewood Cliffs, 1989.
- [24] C. C. Chen, *Markov random field models in image analysis*, PhD thesis, Michigan State University, East Lansing, 1988.
- [25] Hong Hong, "Bind bayesian restoration for adaptive optics telescope images", Master's thesis, Brigham Young University, 1998.
- [26] N.L. Johnson and D.M. Rodvold, "Europe and asia in space, 1993-1994", Tech. Rep., USAF Phillips Laboratory/XPF, Kirtland AFB, NM, 1994.
- [27] R. L. Kashyap and R. Chellappa, "Estimation and choice of neighbors in spatial-interaction models of images", *IEEE Transactions on Information Theory*, vol. 29, pp. 60-72, Jan. 1983.
- [28] J. Besag, "Spatial interaction and the statistical analysis of lattice systems", *Journal of the Royal Statistical Society, Series B*, vol. 36, pp. 192-236, 1974.
- [29] Alan V. Oppenheim and Ronald W. Schaffer, *Discrete-Time Signal Processing*, Prentice Hall, Englewood Cliffs, New Jersey, 1989.
- [30] E. R. Cole, "The removal of unknown image blurs by homomorphic filtering, utec-csc-74-029", Tech. Rep., Department of Computer Science, University of Utah, 1973.
- [31] G. B. Giannakis and R. W. Heath Jr., "Blind identification of multichannel fir blurs and perfect image restortion", in *Proceedings of ICIP-96, 1996 IEEE Int. Conf. on Image Processing*, Lausanne, Switzerland, Sept. 1996, vol. 1, pp. 717-720.

LUMPED PARAMETER MODEL FOR MULTIMODE LASER CUTTING

Aravinda Kar
Associate Professor
Department of Mechanical and Aerospace Engineering
Center for Research and Education in Optics and Lasers

University of Central Florida
P. O. Box 162700
Orlando, FL 32816-2700

Final Report for:
Summer Faculty Research Program
Phillips Laboratory, Applied Laser Technology Branch (PL/LIDB)

Sponsored by:
Air Force Office of Scientific Research
Bolling Air Force Base, DC

and

Phillips Laboratory, Applied Laser Technology Branch (PL/LIDB)

February 2000

LUMPED PARAMETER MODEL FOR MULTIMODE LASER CUTTING

Aravinda Kar
Associate Professor
Department of Mechanical and Aerospace Engineering
Center for Research and Education in Optics and Lasers
University of Central Florida

Abstract

A lumped parameter mathematical model is developed to relate the cut depth to the laser cutting parameters and material properties. The model takes into account the threshold power of the incident laser beam for the initiation of cutting and modifies an earlier cutting model so that it applies to a wide set of process parameters ranging from low to high laser powers and slow to fast cutting speeds. Plain steel is taken as an example to show the effects of various process parameters such as the laser power, spot size and cutting speed on the cut depth. Special emphasis is given to the effect of laser mode structure on its cutting capability.

LUMPED PARAMETER MODEL FOR MULTIMODE LASER CUTTING

Aravinda Kar

1. Introduction

Laser cutting is probably the most widely used laser processing technology. There are still many problems that are not well-understood in laser cutting. Mathematical modeling of laser cutting is essential for improved understanding of the process. A variety of overviews have appeared over the last decade, with guidelines and data for the laser cutting of various types of materials.¹⁻³ Modeling of laser cutting has relied on analysis of a given condition based on energy balance and the solution of a set of heat transfer equations to obtain a detailed temperature field evolution.⁴⁻⁸ Additional modeling endeavors have extended the level of analysis to incorporate secondary factors such as reactions between the assist gas and cutting front,⁹⁻¹¹ and dynamic effects of striation formation.¹² The variation of material absorptivity is also an important factor in laser cutting for which some investigations have been conducted in recent years.^{13,14} The modeling of laser cutting generally attempts to evaluate the cutting quality for given conditions^{15,16} or to estimate the cutting capability for a given laser and material^{17,18}.

Kar et al.¹⁹ developed a model using lumped-parameter technique to relate the kerf width to various process parameters, and obtained an expression similar to the empirical expression presented by Atsuta et al.²⁰ However, the model consists of a few constants that are difficult to measure. Also, the effect of laser beam mode structure on the cut quality is seldom reported. The reason may be that industrial lasers usually have high power output and complex mode structures. However, lower order beam is desirable for high precision cutting, drilling and welding due to better convergence and smaller spot size.²¹ The present paper analyzes the effect of lower order laser modes on the cut quality.

2. Mathematical Model

2.1. Cutting with a Gaussian beam

A lumped parameter approach adopted by Kar et al.¹⁹ is applied and modified here to model cutting with a single Gaussian mode beam under the following two assumptions on the temperature profile:

The temperature in the molten region has a quadratic distribution symmetric to the central line along the laser scanning direction (Fig. 1), that is,

$$T_l(y) = ay^2 + c \quad \text{for} \quad -\frac{w_k}{2} \leq y \leq \frac{w_k}{2} \quad (1)$$

The heat conduction layer consists of four zones, which are the front layer, two side layers, and a bottom layer as indicated by I, II, III and IV respectively in Fig. 1. The temperature distribution normal to the solid-liquid interface is assumed to satisfy the following cubic function in these four regions:

$$T_s(\zeta) = \left(1 - \frac{\zeta}{\delta}\right)^3 (T_m - T_0) + T_0 \quad \text{for} \quad 0 \leq \zeta \leq \delta \quad (2)$$

Here $\delta = \sqrt{4\alpha\tau}$ and ζ is the distance from the solid-liquid interface, that is, $\zeta = x - \frac{l}{2} - \delta$

for region I, $\zeta = y + \frac{w_k}{2} + \delta$ for region II, $\zeta = y - \frac{w_k}{2} - \delta$ for region III and $\zeta = z - d - \delta$ for region IV.

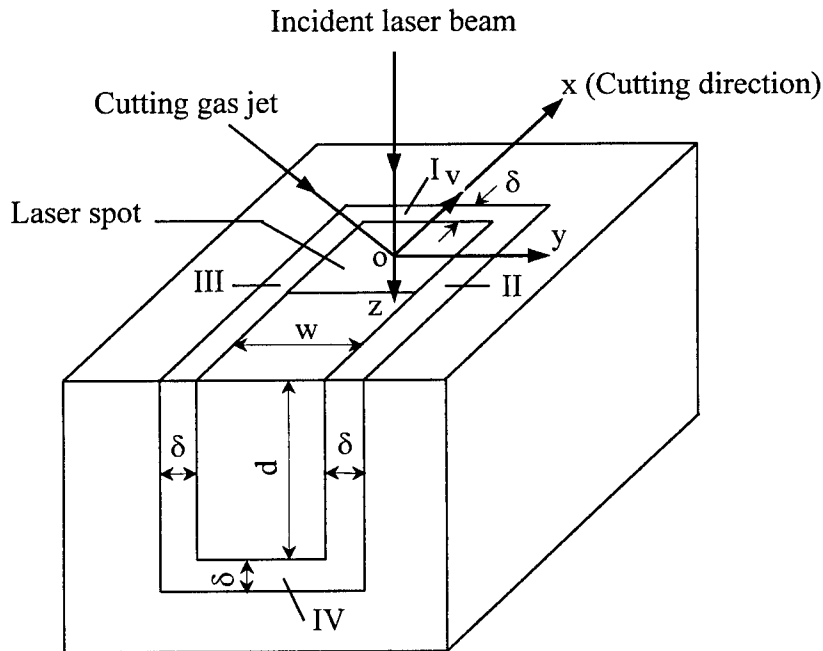


Fig. 1 Geometry of laser cutting model

From Eq. (1), we have

$$T_l\left(\frac{w_k}{2}\right) = a\left(\frac{w_k}{2}\right)^2 + c \quad (3)$$

at $y = w_k/2$. Applying the following Stefan condition at the solid-liquid interface of the kerf wall:

$$q_i'' - q_0'' = \rho v_k L_m$$

where q_i'' and q_0'' represent the heat fluxes in the molten and solid regions, respectively, at the interface and v_k is the velocity of the liquid-solid interface, for which we have

$$q_i'' = -k \frac{dT_l}{dx} \bigg|_{y=\frac{w_k}{2}} = -akw_k \quad (4)$$

$$q_0'' = -k \frac{dT_s(y)}{dy} \bigg|_{y=0} = \frac{3k}{\delta} (T_m - T_0) \quad (5)$$

and $v_k = 0$ at the moment the interface stops developing. From Eqs. (3 - 5), $T_l(y)$ is found to be

$$T_l(y) = -\frac{3}{\delta w_k} (T_m - T_0) y^2 + \frac{3w_k}{4\delta} (T_m - T_0) + T_m \quad (6)$$

The lumped parameter method considers the overall energy balance without accounting for the pointwise distribution of temperature in the substrate. The overall energy balance is

$$E_i = E_{T_m} + E_{L_m} + E_{T_l} + E_{L_h} + E_{loss} \quad (7)$$

where E_{loss} represents the energy loss which is given by $E_{loss} = E_{cond} + E_{conv} + E_{rad}$. E_{cond} is the conduction heat loss in the solid substrate through the front wall perpendicular to the cutting direction, two lateral sides parallel to the cutting direction and a bottom surface beneath the laser spot as indicated by regions I, II, III and IV respectively in Fig. 1. E_{conv} is convection heat loss and E_{rad} is radiative heat loss. E_{rad} is usually very small since the surface area of the localized hot spot is small and its temperature is not very high. E_{conv} is usually small with respect to other terms in Eq. (7) since most of the energy of the incident laser beam absorbed by the substrate is utilized to heat and melt the substrate during laser cutting. By defining the laser-substrate interaction time, $\tau = l/v$, Eq. (7) can be written as

$$AP\tau = \rho w_k dv\tau [c_p (T_m - T_0) + L_m] + E_{T_l} + E_{L_h} + E_{cond} \quad (8)$$

$$E_{T_l} = 2 \int_0^{\frac{w_k}{2}} \rho c_p dv \tau [T_l(y) - T_m] dy = \frac{w_k^2}{2\delta} \rho c_p dv \tau (T_m - T_0) \quad (9)$$

$$E_{cond} = 2 \int_0^\delta \rho c_p [T_s(\zeta) - T_0] d\zeta + \int_0^\delta \rho c_p [T_s(\zeta) - T_0] dw_k d\zeta + \int_0^\delta \rho c_p [T_s(\zeta) - T_0] lw_k d\zeta \\ = \rho c_p (T_m - T_0) d\delta \frac{(2l + w_k)}{4} + \frac{1}{4} \rho c_p (T_m - T_0) lw_k \delta \quad (10)$$

$$E_{L_b} = \beta \rho w_k dv \tau L_b \quad (11)$$

where β is defined as the boiling coefficient which represents the fraction of the kerf volume that is evaporated. The higher the average temperature of the melt pool, the larger would be β . Also the longer the interaction time, the larger would be β . So it is reasonable to assume

$$\beta = \omega \frac{T_a - T_m}{T_m} \tau^n \quad (12)$$

where n is a constant and ω is a proportionality constant which is considered constant in this study.

From Eq. (6), we obtain

$$T_a = \frac{1}{w_k} \int_{-\frac{w_k}{2}}^{\frac{w_k}{2}} T_l(y) dy = T_m + \frac{w_k}{2\delta} (T_m - T_0)$$

$$\text{so } \beta = \omega \frac{w_k}{2\delta} \frac{T_m - T_0}{T_m} \tau^n \approx \omega \frac{w_k}{2\delta} \tau^n \quad \text{for } T_0 \ll T_m$$

$$\text{and } E_{L_b} = \frac{\omega \rho dv \tau^{n+1} L_b w_k^2}{2\delta} \quad (13)$$

Substituting Eqs. (9), (10) and (13) into Eq. (8), the overall energy balance takes the form

$$AP\tau = \rho w_k dv \tau [c_p (T_m - T_0) + L_m] + \frac{\rho dv \tau w_k^2}{2\delta} [c_p (T_m - T_0)] + \frac{\omega \rho dv \tau^{n+1} L_b w_k^2}{2\delta} + \\ \rho c_p (T_m - T_0) d\delta \frac{(2l + w_k)}{4} + \frac{1}{4} \rho c_p (T_m - T_0) lw_k \delta$$

or

$$\frac{AP - \frac{1}{4\tau} \rho c_p (T_m - T_0) lw_k \delta}{d} = \rho w_k v [c_p (T_m - T_0) + L_m] + \frac{\rho v w_k^2}{2\delta} [c_p (T_m - T_0)] + \\ \frac{\omega \rho v \tau^n L_b w_k^2}{2\delta} + \rho c_p (T_m - T_0) \delta \frac{(2l + w_k)}{4} \frac{1}{\tau}$$

which can be rewritten in the form

$$\frac{d}{P - P_{th}} = \frac{A_0}{vw_k + A_1(vw_k)^{1/2} + A_2(vw_k)^{3/2} + A_3(vw_k)^{3/2-n}} \quad (14)$$

where

$$P_{th} = \frac{1}{A} c_1 w_k \sqrt{lv}$$

$$A_0 = \frac{A}{c_0}$$

$$A_1 = \frac{c_1}{c_0} \left(2\sqrt{\frac{l}{w_k}} + \sqrt{\frac{w_k}{l}} \right)$$

$$A_2 = \frac{c_2}{c_0} \sqrt{\frac{w_k}{l}}$$

$$A_3 = \frac{c_3}{c_0} l^{n-1/2} w_k^{n+1/2}$$

$$c_0 = 1.67 \times 10^{-11} \times \rho [c_p (T_m - T_0) + L_m]$$

$$c_1 = 4.08 \times 10^{-9} \times \frac{1}{2} \rho c_p (T_m - T_0) \sqrt{\alpha}$$

$$c_2 = 6.82 \times 10^{-14} \times \frac{\rho c_p (T_m - T_0)}{4\sqrt{\alpha}}$$

$$c_3 = 4.08 \times 10^{-15} \times \frac{\omega \rho L_b}{4\sqrt{\alpha}}$$

Here P is in units of kW; d , w_k and l are in mm; v is in m/min and all other parameters are in SI units. The constants c_0 , c_1 , c_2 and c_3 depend on material properties. The threshold power P_{th} arises due to the conduction heat loss at the bottom surface, region IV in Fig. 1, and its physical meaning is that a minimum amount of laser power is required to heat the substrate surface to its melting temperature in order to initiate the cutting process.

In Eq. (14), when the scanning velocity v goes to zero, the first three terms in the denominator of the right-hand expression also go to zero. Since the cut depth in this case should have a finite value, the last term in the denominator must be a constant independent of v , that is, $\frac{3}{2} - n = 0$ or

$n = \frac{3}{2}$. So Eq. (14) and A_3 are simplified as

$$\frac{d}{P - P_{th}} = \frac{A_0}{vw_k + A_1(vw_k)^{1/2} + A_2(vw_k)^{3/2} + A_3} \quad (15)$$

$$A_3 = \frac{c_3}{c_0} l w_k^2$$

Based on steel cutting experiments, the value of ω is recommended as $1 \text{ s}^{-3/2}$ for steels. Assuming $T_0 = 300 \text{ K}$, and using the typical thermophysical properties of iron given in Table 1, the coefficients c_0 , c_1 , c_2 , and c_3 are found to be $c_0 = 0.126$, $c_1 = 0.0518$, $c_2 = 0.0198$, $c_3 = 0.0105$. Thus, A_1 , A_2 and A_3 become

$$A_0 = 7.94A$$

$$A_1 = 2.64 \sqrt{\frac{l}{w_k}} + 1.32 \sqrt{\frac{w_k}{l}}$$

$$A_2 = 0.132 \sqrt{\frac{w_k}{l}}$$

$$A_3 = 0.204$$

Table 1. Typical values of the thermophysical properties of iron ²².

Thermophysical properties	Values of thermophysical properties
Density, ρ	7870 kg m ⁻³
Melting point, T_m	1809 K
Boiling point, T_b	3133 K
Specific heat, C_p	456 J kg ⁻¹ K ⁻¹
Thermal conductivity, k	78.2 W m ⁻¹ K ⁻¹
Thermal diffusivity, α	2.18 × 10 ⁻⁵ m ² s ⁻¹
Latent heat of melting, L_m	2.72 × 10 ⁵ J kg ⁻¹
Latent heat of boiling, L_b	6.10 × 10 ⁶ J kg ⁻¹

For effective laser cutting, process is controlled such that w_k is very close to the beam width, that is, $wk \approx w \leq l$. Moreover, the beam width for effective cutting in practice is generally less than 1 mm and the cutting speed v is in the order of 1 m/min or less, therefore, the A_2 in the right hand denominator is small with respect to the first and second terms and its effect in Eq. (15) is correspondingly small and can be neglected. The constant term A_3 , though comparatively small, shows dominance in Eq. (15) while vw_k is small so that it must remain. Therefore, Eq. (15) becomes

$$\frac{d}{P - P_{th}} = \frac{A_0}{vw_k + A_1(vw_k)^{1/2} + A_3} \quad (16)$$

Eq. (16) is based on the total power of the laser beam instead of the power in each mode of the beam. This equation is modified below to account for the power distribution in a multimode beam.

2.2. Cutting with a multimode laser beam

The locations of maximum power in various modes of a multimode laser beam are different. This creates localized peaks of energy deposition (hot spots) within the focused laser spot. Suppose the incident laser beam consists of four transverse modes with the highest mode being TEM_{11} and the spatial intensity distribution for every mode ($I_{mn}(x, y)$, $m = 0, 1$ and $n = 0, 1$) satisfies the Hermite-Gaussian function, that is,

$$I_{00}(x, y) = \frac{8}{\pi l_0 w_0} P_{00} \exp\left(-\frac{8x^2}{l_0^2}\right) \exp\left(-\frac{8y^2}{w_0^2}\right)$$

$$I_{01}(x, y) = \frac{4}{\pi l_0 w_0} P_{01} \frac{32y^2}{w_0^2} \exp\left(-\frac{8x^2}{l_0^2}\right) \exp\left(-\frac{8y^2}{w_0^2}\right)$$

$$I_{10}(x, y) = \frac{4}{\pi l_0 w_0} P_{10} \frac{32x^2}{l_0^2} \exp\left(-\frac{8x^2}{l_0^2}\right) \exp\left(-\frac{8y^2}{w_0^2}\right)$$

$$I_{11}(x, y) = \frac{2}{\pi l_0 w_0} P_{11} \frac{32x^2}{l_0^2} \frac{32y^2}{w_0^2} \exp\left(-\frac{8x^2}{l_0^2}\right) \exp\left(-\frac{8y^2}{w_0^2}\right)$$

$$P_{00} = \phi_{00}P \quad P_{01} = \phi_{01}P \quad P_{10} = \phi_{10}P \quad P_{11} = \phi_{11}P$$

Here P is the total incident laser power and ϕ_{mn} ($m, n = 0, 1$) is the fraction of power in each mode, that is,

$$\phi_{00} + \phi_{01} + \phi_{10} + \phi_{11} = 1$$

The Gaussian spot dimensions l_0 and w_0 are related to the length l and width w of the spot for a beam with TEM_{mn} mode by the expressions²², $l = l_0 \sqrt{2m+1}$ and $w = w_0 \sqrt{2n+1}$. Therefore, $l = \sqrt{3}l_0$ and $w = \sqrt{3}w_0$ for the TEM₁₁ mode beam. The effective spot size for each mode is written as follows:

$$\text{TEM}_{00}: l_{00} = l_0 = \frac{\sqrt{3}}{3}l \quad w_{00} = w_0 = \frac{\sqrt{3}}{3}w$$

$$\text{TEM}_{01}: l_{01} = l_0 = \frac{\sqrt{3}}{3}l \quad w_{01} = \sqrt{3}w_0 = w$$

$$\text{TEM}_{10}: l_{10} = l_0 = l \quad w_{10} = w_0 = \frac{\sqrt{3}}{3}w$$

$$\text{TEM}_{11}: l_{11} = \sqrt{3}l_0 = l \quad w_{11} = \sqrt{3}w_0 = w$$

Based on the spatial intensity distribution, the four modes can then be further divided into several domains referred to as the energy deposition regions, which are

$$\text{TEM}_{00}: -\frac{\sqrt{3}}{6}l \leq x \leq \frac{\sqrt{3}}{6}l, -\frac{\sqrt{3}}{6}w \leq y \leq \frac{\sqrt{3}}{6}w$$

$$\text{TEM}_{01}: -\frac{\sqrt{3}}{6}l \leq x \leq \frac{\sqrt{3}}{6}l, -\frac{1}{2}w \leq y \leq 0 \text{ and } -\frac{\sqrt{3}}{3}l \leq x \leq \frac{\sqrt{3}}{3}l, 0 \leq y \leq \frac{1}{2}w$$

$$\text{TEM}_{10}: -\frac{1}{2}l \leq x \leq 0, -\frac{\sqrt{3}}{6}w \leq y \leq \frac{\sqrt{3}}{6}w \text{ and } 0 \leq x \leq \frac{1}{2}l, -\frac{\sqrt{3}}{6}w \leq y \leq \frac{\sqrt{3}}{6}w$$

$$\text{TEM}_{11}: -\frac{1}{2}l \leq x \leq 0, -\frac{1}{2}w \leq y \leq 0; -\frac{1}{2}l \leq x \leq 0, 0 \leq y \leq \frac{1}{2}w; 0 \leq x \leq \frac{1}{2}l, -\frac{1}{2}w \leq y \leq 0$$

$$\text{and } 0 \leq x \leq \frac{1}{2}l, 0 \leq y \leq \frac{1}{2}w.$$

The multimode beam cutting model is based on the principal of equivalent melt volume. An equivalent melt pool of volume equal to the total volume of the material melted by the laser energy of each mode at different energy deposition regions is considered, that is,

$$V_{eq} = \sum_{m=0}^1 \sum_{n=0}^1 \sum_{s=1}^{N_{mn}} V_{mn,s} \quad (17)$$

where V_{eq} is the equivalent melt pool (kerf) volume, N_{mn} is the number of the energy deposition regions due to TEM_{mn} mode and $V_{mn,s}$ is the melt pool volume corresponding to the s -th energy deposition region of the TEM_{mn} mode. For an arbitrary cut length l_a , Eq. (15) can be written as

$$d_{eq} w_{k,eq} l_a = \sum_{m=0}^1 \sum_{n=0}^1 \sum_{s=1}^{N_{mn}} d_{mn,s} w_{k,mn,s} l_a$$

or

$$d_{eq} w_{k,eq} = \sum_{m=0}^1 \sum_{n=0}^1 \sum_{s=1}^{N_{mn}} d_{mn,s} w_{k,mn,s} \quad (18)$$

where d_{eq} and $w_{k,eq}$ are the equivalent kerf depth and width respectively. $d_{mn,s}$ and $w_{k,mn,s}$ are, respectively, the depth and width of the melt pool corresponding to the s -th region of the TEM_{mn} mode. $d_{mn,s}$ is evaluated using Eq. (14) by substituting $w_{k,mn,s}$ for the kerf width w_k , and $w_{k,mn,s}$ is considered to be equal to the width of the s -th region of the TEM_{mn} mode. When Eq. (14) is applied to each individual mode, the threshold power in each mode ($P_{mn,th}$) is taken to be the same fraction of the overall threshold power (P_{th}) as the power fraction of each mode, that is,

$$P_{mn,th} = \phi_{mn} P_{th}.$$

For TEM_{00} , $N_{00} = 1$, $l_{00,s} = l_{00} = \frac{\sqrt{3}}{3} l$, $w_{00,s} = w_{00} = \frac{\sqrt{3}}{3} w$. Substituting into Eq. (16),

we have

$$\frac{d_{00,s} w_{k,00,s}}{P - P_{th}} = \frac{\phi_{00} A_0 w}{vw + A_{00,1} (vw)^{1/2} + A_{00,3}} \quad (19)$$

$$A_{00,1} = \frac{c_1}{c_0} (2.64 \sqrt{\frac{l}{w}} + 1.32 \sqrt{\frac{w}{l}})$$

$$A_{00,3} = 0.333 \frac{c_3}{c_0} l w^2$$

For TEM_{01} , $N_{01} = 2$, $l_{01,s} = l_{01} = \frac{\sqrt{3}}{3} l$, $w_{01,s} = \frac{1}{2} w_{01} = \frac{1}{2} w$. Substituting into Eq. (16),

we have

$$\frac{2d_{01,s}w_{k,01,s}}{P - P_{th}} = \frac{\phi_{01}A_0w}{vw + A_{01,1}(vw)^{1/2} + A_{01,3}} \quad (20)$$

$$A_{01,1} = \frac{c_1}{c_0} (3.03\sqrt{\frac{l}{w}} + 1.32\sqrt{\frac{w}{l}})$$

$$A_{01,3} = 0.289 \frac{c_3}{c_0} lw^2$$

For TEM₁₀, $N_{10} = 2$, $l_{10,m} = \frac{1}{2}l_{10} = \frac{1}{2}l$, $w_{10,m} = w_{10} = \frac{\sqrt{3}}{3}w$. Substituting into Eq. (16),

we have

$$\frac{2d_{10,s}w_{k,10,s}}{P - P_{th}} = \frac{\phi_{10}A_0w}{vw + A_{10,1}(vw)^{1/2} + A_{10,3}} \quad (21)$$

$$A_{10,1} = \frac{c_1}{c_0} (2.46\sqrt{\frac{l}{w}} + 1.41\sqrt{\frac{w}{l}})$$

$$A_{10,3} = 0.289 \frac{c_3}{c_0} lw^2$$

For TEM₁₁, $N_{11} = 4$, $l_{11,s} = \frac{1}{2}l_{11} = \frac{1}{2}l$, $w_{11,s} = \frac{1}{2}w_{11} = \frac{1}{2}w$. Substituting into Eq. (16),

we have

$$\frac{4d_{11,s}w_{k,11,s}}{P - P_{th}} = \frac{\phi_{11}A_0w}{vw + A_{11,1}(vw)^{1/2} + A_{11,3}} \quad (22)$$

$$A_{11,1} = \frac{c_1}{c_0} (2.82\sqrt{\frac{l}{w}} + 1.41\sqrt{\frac{w}{l}})$$

$$A_{11,3} = 0.250 \frac{c_3}{c_0} lw^2$$

Combining Eqs. (15) – (20), we obtain

$$\frac{dw_{k,eq}}{P - P_{th}} = \sum_{m=0}^1 \sum_{n=0}^1 \frac{\phi_{mn}A_0w}{vw + A_{mn,1}(vw)^{1/2} + A_{mn,3}}$$

This expression is rewritten as

$$\frac{d}{P - P_{th}} = \sum_{m=0}^1 \sum_{n=0}^1 \frac{\phi_{mn} A_0}{v w_{k,eq} + A_{mn,1} (v w_{k,eq})^{1/2} \left(\frac{w_{k,eq}}{w} \right)^{1/2} + A_{mn,3} \frac{w_{k,eq}}{w}}$$

Assuming $w = w_{k,eq}$, we obtain

$$\frac{d}{P - P_{th}} = \sum_{m=0}^1 \sum_{n=0}^1 \frac{\phi_{mn} A_0}{v w_{k,eq} + A_{mn,1} (v w_{k,eq})^{1/2} + A_{mn,3}} \quad (23)$$

P_{th} for multimode beam can be determined on the basis of the single Gaussian mode case dealt with above. For TEM_{mn} mode the resulting temperature distribution is limited to a region of width w_{mn} and depth $\delta_{mn} = \sqrt{4\alpha\tau_{mn}}$, $\tau_{mn} = l_{mn}/v$, see Fig. 2. Temperature at $z = 0$ is $T_{mn,s}$ and T_0 at $z = \delta_{mn}$.

From energy balance it is easy to obtain

$$\phi_{mn} P_{th} = c_1 w_{mn} \sqrt{l_{mn} v} \frac{T_{mn,s} - T_0}{T_m - T_0} \quad m, n = 0, 1$$

$$\sum_{m=0}^1 \sum_{n=0}^1 \frac{\phi_{mn} P_{th}}{c_1 w_{mn} \sqrt{l_{mn} v}} = 1$$

$$P_{th} = c_1 \frac{w \sqrt{l v}}{2.28 \phi_{00} + 1.32 \phi_{01} + 1.73 \phi_{10} + \phi_{11}} \quad (24)$$

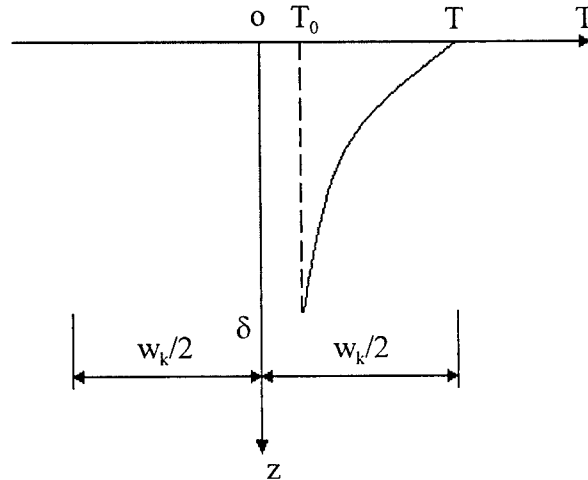


Fig. 2 Schematic of the temperature distribution in the transverse cross section of the cutting front in the case of the threshold power, $T(z) = (1 - \frac{z}{\delta_{mn}})^3 (T_{mn,s} - T_0) + T_0$, $0 \leq z \leq \delta_{mn}$.

3. Results and Discussion

Eqs. (16) and (23) represent scaling laws for laser cutting process. Eq. (23) can be applied to laser cutting with a multimode beam. These equations are used to determine the effects of various parameters on the cut depth. The absorptivity A is taken as 0.55 in all calculations in this study.

First let us investigate the variation of the cut depth with respect to the aspect ratio (ψ) of the rectangular beam. ψ is defined as the ratio of the length, l , which is measured parallel to the cutting direction to the width, w , which is measured perpendicular to the cutting direction, that is, $\Psi = l/w$. From Eq. (16), we can derive, by ignoring P_{th} as it is very small compared to the power practically employed in laser cutting, that the maximum cut depth is achieved when the aspect ratio satisfies:

$$\frac{c_3 w^3}{c_1 (vw)^{1/2}} \psi^{3/2} + \psi = \frac{1}{2} \quad (25)$$

which can be used to optimize the geometry of the beam spot to achieve efficient cutting. Eq. (25) indicates that the aspect ratio for maximum cut depth is independent of the incident laser power. Fig. 3 shows the variation of cut depth with the aspect ratio when the laser power and

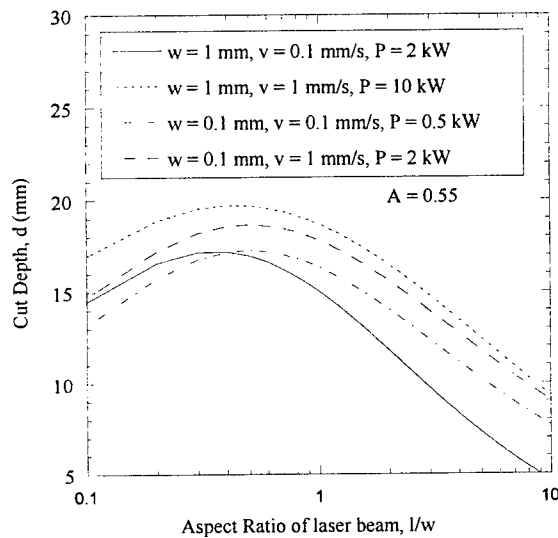


Fig. 3 Cutting depth as function of aspect ratio of the laser beam

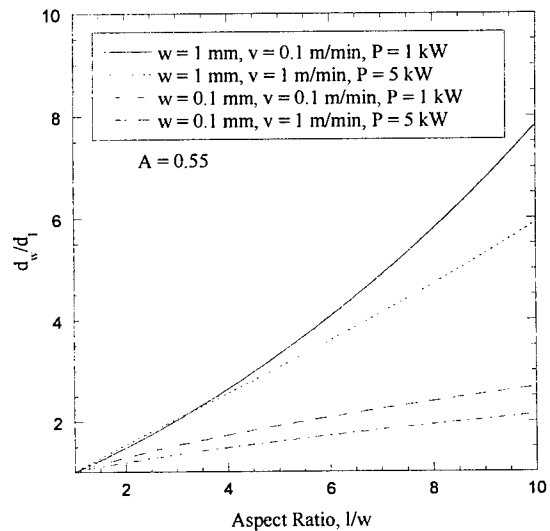


Fig. 4 Ratio of the cut depth corresponding to cutting with the width (d_w) and length (d_l) of the laser beam as function of the aspect ratio

beam width are fixed. It highlights two aspects of the cutting process: (i) the beam length does not affect the cut depth significantly, and (ii) the maximum cut depth occurs always at $l/w = 0.3-0.6$ irrespective of how big or small w is and is almost independent of the cutting speed. Larger w means weaker intensity and therefore a larger threshold power for surface melting as given by Eq. (16). Smaller w means shorter interaction time with the substrate. The ideal value of the aspect ratio appears to be 0.3-0.6 as a result of the interaction between the two effects.

On the other hand, using the shorter side of the laser beam will always give higher cut depth accompanied with smaller kerf width, as can be seen from Fig. 4. It reveals that the effect of the beam width on the cut depth is much more significant than that of the beam length.

Fig. 5 shows the dependence of the cut depth on the laser power distribution in various modes. Laser beams with different modal power distribution but the same spot size and total power have very similar effect on the cut depth. The reason is that in the multimode cutting model the concept of equivalent cut depth is introduced for every mode in such that the equivalent kerf width for each mode is made equal to the virtual kerf width. It is shown in Fig. 5 that the threshold power for cutting is very small relative to the high power used for cutting in practice. Fig. 6 shows the threshold power for laser beams of different modal power

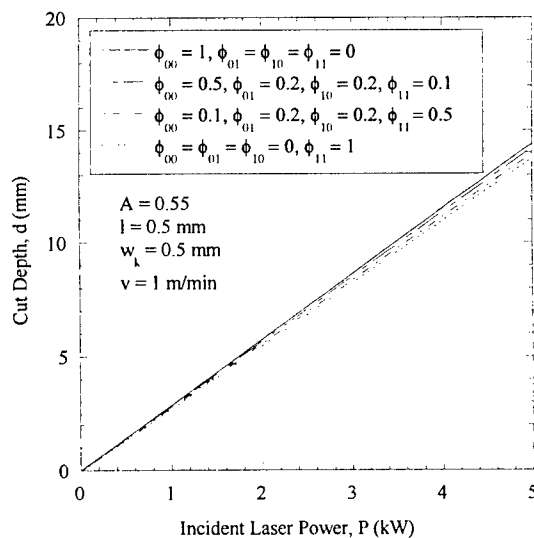


Fig. 5 Variation of kerf area with incident laser power for various mode compositions

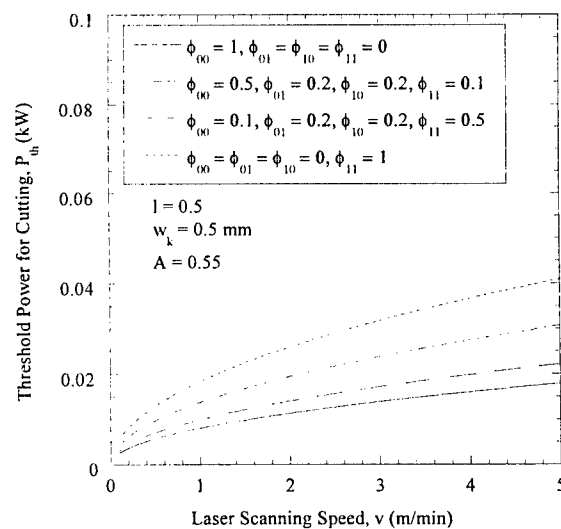


Fig. 6 Threshold laser power required to cause melting as function of cutting speed

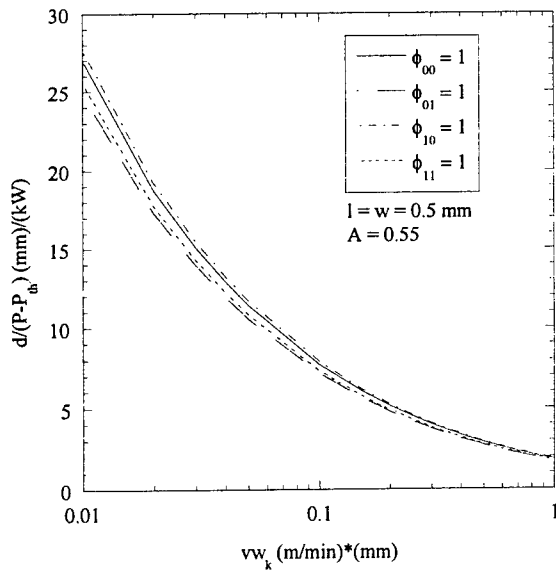


Fig. 7 Comparison of the cutting performance of different modes

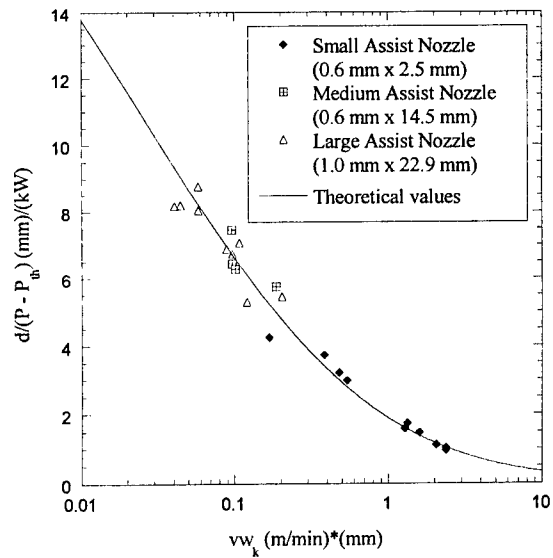


Fig. 8 Comparison of theoretical results with experimental data

distributions. The higher the power fraction for the TEM_{00} mode, the smaller is the threshold power for surface melting.

A more complete comparison of the cutting capability of different mode laser beams is given in Fig. 7. The closely spaced curves in this figure do not mean that different modes will generate nearly the same cut depth under the same cutting condition. It should be noted that the actual kerf width is left as an unknown in Eq. (16) for a single Gaussian beam and in Eq. (23) for a multimode beam. The actual kerf width will change depending on the modal power fraction (ϕ_{mm}) and the spot size.

The experimental data of stainless steel cutting with a COIL laser¹⁹ are compared in Fig. 8 to the results predicted by Eq. (16). The calculation is in good agreement with the experimental data from low to high cutting speeds.

4. Conclusions

An analytic model is presented to describe the cutting capability of a laser beam with rectangular spot. The predictions of the model match the experimental data very well. The model suggests that in order to achieve higher cutting capability, the shorter side of the laser beam

should always be used as the cutting edge, that is, normal to the cutting direction. When the beam width is fixed, reducing the beam length will increase the cut depth, but not to a great extent. The cutting model also accounts for the mode structure and can be used to evaluate the cut depth for cutting with various modal power distributions. However, the kerf width is an undetermined variable in this model. One of the assumptions of the model is that the entire region, where the temperature is at least the melting temperature, is removed by an assist gas jet to generate the kerf. So the model would be valid for cutting with large nozzle outlet for jet gas at high pressures.

Nomenclature

A	Absorptivity of the substrate for incident laser beam
c_p	Specific heat of the substrate
d	Kerf depth
E_{cond}	Heat loss due to conduction
E_{conv}	Heat loss due to convection along free surfaces
E_i	Incident laser energy
E_{L_b}	Latent heat of boiling
E_{L_m}	Latent heat of melting
E_{rad}	Radiation heat loss
E_{th}	Threshold laser energy to cause surface melting
E_{T_l}	Energy required to raise the temperature of the liquid substrate beyond T_m
E_{T_m}	Energy required to raise the solid substrate from T_0 to T_m
k	Thermal conductivity
l	Length of the rectangular laser beam spot
l_0	Length of the Gaussian mode beam
L_b	Latent heat of boiling
L_m	Latent heat of melting

P	Power of the incident laser beam
T_0	Initial temperature of the laser beam
T_a	Average temperature of the melted region
T_b	Boiling temperature of the substrate
T_m	Melting temperature of the substrate
v	Velocity of the scanning laser beam
v_k	Velocity of the liquid-solid interface
w	Width of the rectangular beam spot
w_0	Width of the Gaussian mode beam
w_k	Kerf width

Greek symbols

α	Thermal diffusivity of the substrate
β	Boiling coefficient
δ	Thickness of thermal layer
ϕ_{mn}	Power fraction in TEM_{mn} mode
ρ	Density of the substrate
τ	Laser-substrate interaction time
ω	Proportionality constant
Ψ	Aspect ratio of the laser beam

Reference

1. A. V. Tikhomirov, "State of laser cutting technology and prospects for its development," Bull. Acad. Sci. USSR **47**, 23-28, 1983
2. D. Schuocker, "Laser cutting," The Industrial Laser Annual Handbook (D. Belforte and M. Levitt. Eds.) Tulsa, OK: PennWell Books, 1986, pp. 87-107.
3. J. Powell, "Guidelines and data for laser cutting," The Industrial Laser Annual Handbook (D. Belforte and M. Levitt. Eds.) Tulsa, OK: PennWell Books, 1990, pp. 56-67.

4. D. Schuocker, and W. Abel, "Material removal mechanism of laser cutting," SPIE Proc. Industrial Applications of High Power Lasers, Vol. 455, Bellingham, WA: Society of Photo-optical Instrumentation Engineer – The International Society for Optical Engineering, 1984, pp. 88-95.
5. D. Schuocker, "The physical mechanism and theory of laser cutting," The Industrial Laser Annual Handbook, (D. Belforte and M. Levitt, eds.) Tulsa, OK: Pennwell Books, 1987, pp. 65-79.
6. S. Y. Bang, and M. F. Modest, "Multiple reflection effects on evaporative cutting with a moving CW laser," J. Heat Tran. **113**, 663-669 (1991)
7. M. F. Modest, and H. Abakians, "Evaporative cutting of a semi-infinite body with a moving CW laser," J. Heat Tran. **108**, 602-607 (1986)
8. V. V. Semak, B. Damkroger, and S. Kempka, "Temporal evolution of the temperature field in the beam interaction zone during laser materials processing," J. Phys. D: Appl. Phys. **32** 1819-1825 (1999)
9. M. Vicanek, and G. Simon, "Momentum and heat transfer of an inert gas jet to the melt in laser cutting," J. Phys. D: Appl. Phys. **20** 1191-1196 (1987)
10. G. Chryssolouris, and W. C. Choi, "Gas jet effects on laser cutting," SPIE Proc. CO₂ Lasers and Applications Vol. 1042 (J. D. Evans and E. V. Locke, eds.) Bellingham, WA: Society of Photo-Optical Instrumentation Engineers – The International Society for Optical Engineering, 1989, pp. 86-96.
11. S. L. Chen, "Effects of high-pressure assistant gas flow on high-power laser cutting," J. Mater. Process. Technol. **88** 57-66 (1999)
12. J. D. Chung, J. S. Lee, K.H. Whang, and T. H. Kim, "Analysis of striation formation in laser materials processing," J. Mater. Process. Manuf. Sci. **5** 3-15 (1996)
13. N. R. Pedaneckar, B. Basu, "Mathematical modeling of evaporative removal of materials using high energy laser beam," Proceedings of the 1997 Laser Materials Processing Conference, ICALEO' 97, Part 1 Vol 83 1994 pp. 159-168
14. J. Xie, A. Kar, J. A. Rothenflue, and W. P. Latham, "Temperature-dependent absorptivity and cutting capacity of CO₂, Nd:YAG and chemical oxygen-iodine lasers," J. Laser Appl. **2**, 77-85 (1997)

15. B. S. Yilbas, "Experimental investigation into CO₂ laser cutting parameters," J Mater. Process. Technol. **58** 323-330 (1996)
16. H. Kaebemick, D. Bicleanu, M. Brandt, "Theoretical and experimental investigation of pulsed laser cutting," CIRP Ann. – Manuf. Technol. **48** 163-66 (1999)
17. A. Kar, D. L. Carroll, W P. Latham, and J. A. Rothenflue, "Cutting performance of a chemical oxygen-iodine laser on aerospace and industrial materials," J. Laser Appl. **11** 119-127 (1999)
18. P Sheng, and L. Cai, "Predictive process planning for laser cutting," J. Manuf. Sys. **17** 144-158 (1998)
19. A. Kar, J. E. Scott, and W. P. Latham, "Theoretical and experimental studies of thick-section cutting with a chemical oxygen-iodine (COIL)," J. Laser Appl. **8**, 125-133 (1996)
20. T. Atsuta, K. Yasuda, T. Matsumoto, T. Sakurai, and H. Okado, "COIL and the materials processing," Conference on Lasers and Electro-Optics (CLEO)'94, Vol. 8, 1994 OSA Technical Digest Series (Optical Society of America, Washington, D. C.), 1994, p. 351.
21. G. Chryssolouris, Laser Machining Theory and Practice (Springer, New York, 1991), pp. 42-43, 48, 58-59.
22. A. Kar, J. E. Scott, and W. P. Latham, "Effects of mode structure on three-dimensional laser heating due to single or multiple rectangular laser beams," J. Appl. Phys **80**, 667-674 (1996)
23. E. A. Brandes, (ed.) Smithells Metals Reference Book. 6th edn. London: Butterworth, 1983, pp.8-2 and 14-1.

ADAPTIVE VIBRATION SUPPRESSION
FOR
AUTONOMOUS CONTROL SYSTEMS

Donald J. Leo
Assistant Professor
Mechanical, Industrial, and Manufacturing Engineering Department

The University of Toledo
3210 University Hall
2801 West Bancroft
Toledo, OH 43606

Final Report for:
Summer Extension Research Program
Kirtland AFB

Sponsored by:
Air Force Office of Scientific Research
Bolling AFB, DC

and

Kirtland, AFB
Albuquerque, NM

May 1999

ADAPTIVE VIBRATION SUPPRESSION FOR AUTONOMOUS CONTROL SYSTEMS

Donald J. Leo
Assistant Professor
Mechanical, Industrial, and Manufacturing Engineering Department
The University of Toledo

ABSTRACT

Phase-locked loops are studied as a means of implementing adaptive low-authority control for autonomous vibration suppression. This research has applications in autonomous control of precision spacecraft for remote sensing, surveillance, and telecommunications constellations. A phase-locked loop (PLL) is implemented on a digital signal processor and tested on a closed tube that exhibits multiple acoustic resonances. Simulations indicate that the phase-locked loop can track the resonant frequencies of the tube in the presence of uncorrelated noise and multiple modes within the lock-and-capture range of the PLL. Experimental results support this conclusion in the case when the modal amplitude is dominant compared to noise floor of the external excitation. Future work will concentrate on implementing the PLL on the MACE reflight program and analytically determining the lock-and-capture performance for broadband excitation.

ACKNOWLEDGEMENTS

The author gratefully acknowledges the support of the AFOSR Summer Extension Research Program as administered by Research and Development Laboratories, subcontract 98-0810. Thanks are also due to Dr. Steven Griffin and Dr. Keith Denoyer of the Air Force Research Lab for their support of this research. The author would also like to thank Jiejun Lu and Yimin Yang of the MIME Department at The University of Toledo for performing the research related to this report.

TABLE OF CONTENTS

1. INTRODUCTION	1
2. THEORETICAL DEVELOPMENT	4
PHASE-LOCKED LOOP	4
<i>Operating principles of the Phase-Locked Loop</i>	<i>4</i>
<i>Simple analysis of three functional blocks</i>	<i>5</i>
<i>Lock and Capture</i>	<i>7</i>
<i>Linear Model.....</i>	<i>8</i>
<i>False Lock.....</i>	<i>12</i>
A PARTICULAR PHASE-LOCKED LOOP USED AS THE MODEL PLL	12
<i>VCO section</i>	<i>16</i>
<i>Loop Filter section</i>	<i>16</i>
<i>Phase comparator section.....</i>	<i>18</i>
3. EXPERIMENT DESCRIPTION	22
SIMULATION EXPERIMENTS	22
ACTUAL EXPERIMENT	26
4. EXPERIMENTAL RESULTS	31
5. CONCLUSIONS	36
REFERENCES.....	37

ADAPTIVE VIBRATION SUPPRESSION FOR AUTONOMOUS CONTROL SYSTEMS

Donald J. Leo
Assistant Professor
Mechanical, Industrial, and Manufacturing Engineering Department
The University of Toledo

1. Introduction

Autonomy is becoming increasingly important for suppressing vibrations on precision spacecraft. Remote sensing systems, military surveillance satellites, and communications constellations all require some form of vibration suppression to maintain strict pointing accuracy. Fast, inexpensive digital signal processors provide the computing power necessary for autonomous control, but what is required is the development of robust identification and control algorithms that can sense the disturbance environment of a spacecraft and automatically adapt control parameters to maintain pointing accuracy.

The most advanced systems would be fully autonomous and require no interaction with ground support personnel. Full autonomy would make the control systems more reliable because they could automatically adapt to changes in the disturbance environment. Problems due to inaccuracies in ground test models would not be an issue because the systems would perform on-orbit identification of the system dynamics. Autonomous control systems would be cost effective because they would reduce the need for expensive pre-mission ground testing and eliminate the need for ground support during the early phases of the mission.

Autonomy implies a large degree of adaptation. The focus of this work is the development of a frequency-tracking system that identifies the predominant motion of a resonant structure and automatically adapts itself to the critical frequencies. Frequency identification could then be used to tune low-authority control laws that actively damp the structural resonance. This low-authority control system could be used in conjunction with a high-authority adaptive loop that maintains strict pointing accuracy.

The feasibility of adaptive control algorithms is currently being studied by several research labs, companies, and universities in the Middeck Active Control Experiment (MACE) reflight program. The goal of the MACE reflight program is to test autonomous control systems on a scaled model of a flexible satellite. The control algorithms will perform on-line system identification and pointing control of the MACE test article. This program will be the first demonstration of autonomous control systems for flexible structure control.

One of the control algorithms being tested is the low-authority adaptive system discussed in this research. The goal of the present work is to demonstrate a simple, robust adaptive algorithm for low-authority control of the

flexible dynamics of the MACE test article. It is possible that these simple algorithms will also be combined with more sophisticated algorithms for pointing control of the satellite.

The low-authority control algorithm is based on the classical implementation of the phase-locked loop. The phase-locked loop will provide an accurate estimate of the predominant frequencies of vibration for the purpose of actively suppressing the resonant motion. Active vibration suppression will be maintained in the presence of uncertain or time-varying structural dynamics.

The remainder of this chapter describes the basic operating principles of a phase-locked loop. A review of the operation of the PLL and its component are presented next, along with a specific PLL which is integrated on a single chip and a digital PLL which is based on that specific analog PLL. The test structure (tube) and experiments are then described. Lastly, the experimental results are presented and conclusions are drawn.

A classical phase-locked loop is essentially a servo loop consisting of a phase detector, a loop filter, and a voltage controlled oscillator (see Figure 1). The voltage controlled oscillator (VCO) operates at a set of frequency, f_0 , also known as the free-running frequency or center frequency. When an input is applied to the system, the phase detector compares the phase and frequency of the input signal to the VCO frequency and generates an error voltage related to the phase and frequency difference between the two signals. The feedback provided by the error voltage causes the VCO frequency to vary in such a way that the frequency difference between the input signal and the VCO signal is minimized. When the input frequency and the VCO free-running frequency (center frequency) are sufficiently close, the feedback nature of the PLL synchronizes the two signals and the PLL locks onto the input signal. Once the PLL has obtained a lock, the VCO frequency is identical to the input signal over a defined frequency range about the free running frequency known as the "lock range".

The concept of the phase-locked loop (PLL) was introduced by de Bellescize [15] in 1932, however its application was not wide spread until the advent of television. PLL's were used in television receivers to synchronize the horizontal and vertical sweep oscillators to the transmitted sync pulses. Other applications for PLL's include: frequency scaling, synchronization of digital transmission, frequency synthesis, and frequency demodulation [16]. Today PLL's are constructed as single integrated chips and can be found in virtually every home: in television receivers, radios, and communication equipment.

This research presents a simple and inexpensive analog and digital solution to low-authority control, by developing and testing an electronic PLL circuit used on a test article consisting of a resonant tube. The focus of this work is to track the natural frequency of the tube by using a software-based digital phase locked loop. A excitation is applied to the tube simulate an external disturbance, and its natural frequency is obtained either by theoretical calculation or by experimental test.

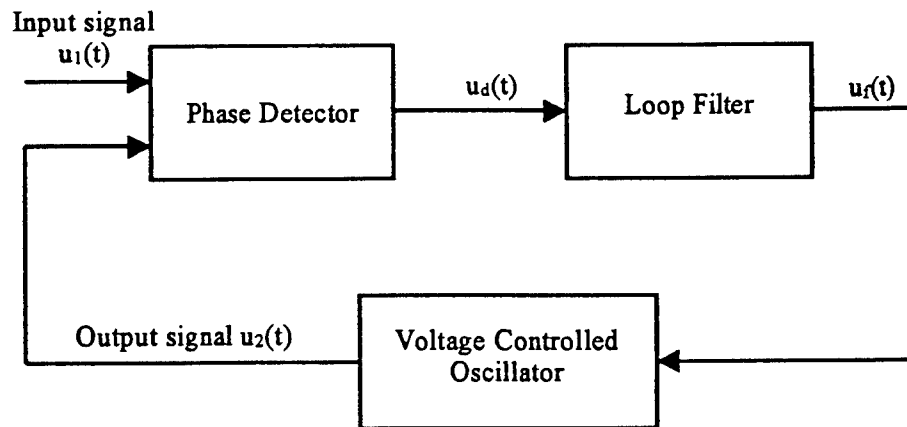


Figure 1. PLL Block Diagram

The application of the PLL to track or control the mechanical structure vibration was first described by Balas [2]. Since then some work has been performed on large space structures using PLL's with residual mode filters to control mechanical vibration [12-14]. Cudney and Niezrecki's work [1] work dealt with the application of an analog phase lock loop to the modal control of mechanical structures. Both researchers used a phase-locked loop to track a single frequency for the purpose controlling vibration. Cudney and Niezrecki used an analog PLL but this paper focuses on the use of a microprocessor-based digital PLL. The other primary difference is that Cudney and Niezrecki used a single frequency sine wave, but this paper concentrates on broadband noise as the excited signal.

2. Theoretical development

Phase-Locked Loop

Phase-locked loops are not linear control systems. An accurate mathematical analysis of the PLL is beyond the scope of this paper. However, the system can be linearized to demonstrate the PLL's tracking ability. The lock-in process can not be linearized and is always governed by non-linear differential equations [17]. The lock and capture process will be described from a qualitative point of view. The problem of PLL's locking onto harmonics and sub-harmonics of the input signal is briefly addressed. The theoretical development is derived from references [17-19].

The PLL is comprised of three basic functional blocks, a phase comparator (phase detector), loop filter, and a voltage controlled oscillator, as shown in Figure 1.

Operating principles of the Phase-Locked Loop

A PLL is a circuit that causes a particular system to track another one. More precisely, a PLL is a circuit synchronizing an output signal (generated by an oscillator) with a reference or input signal in frequency as well as in phase. In the synchronized –often called locked- state the phase error between the oscillator's output signal and the reference signal is zero, or very small.

If a phase error builds up, a control mechanism acts on the oscillator in such a way that the phase error is again reduced to a minimum. In such a control system the phase of the output signal is actually locked to the phase of the reference signal. This is why it is referred to as a phase-locked loop.

It is quite simple to deduce the operating principle of a PLL. Its block diagram is shown in Figure 1. The PLL consists of three basic functional blocks:

A voltage controlled oscillator (VCO)

A phase detector (PD)

A loop filter (LF)

The signals of interest within the PLL circuit are defined as follows:

The reference (or input) signal $u_1(t)$

The angular frequency ω_1 of the reference signal

The output signal $u_2(t)$ of the VCO

The angular frequency ω_2 of the output signal

The output signal $u_d(t)$ of the phase detector

The output signal $u_f(t)$ of the loop filter

The phase error θ_e , defined as the phase difference between signals $u_1(t)$ and $u_2(t)$

First we assume that the angular frequency of the input signal $u_1(t)$ is equal to the center frequency ω_0 . The VCO then operates at its center frequency ω_0 . As we see, the phase error θ_e is zero. If θ_e is zero, the output signal $u_d(t)$ of the PD must also be zero. Consequently the output signal of the loop filter $u_f(t)$ will also be zero. This is the condition that permits the VCO to operate at its center frequency.

If the phase error θ_e were not zero initially, the PD would develop a nonzero output signal u_d . After some delay the loop filter would also produce a finite signal u_f . This would cause the VCO to change its operating frequency in such a way that the phase error finally vanishes.

Assume now that the frequency of the input signal is changed suddenly at time t by the amount $\Delta\omega$. The phase of the input signal then starts leading the phase of the output signal. A phase error is built up and increases with time. The PD develops a signal $u_d(t)$, which also increases with time. With a delay given by the loop filter, $u_f(t)$ will also rise. This causes the VCO to increase its frequency. The phase error becomes smaller now, and after some settling time the VCO will oscillate at a frequency that is exactly the frequency of the input signal. Depending on the type of loop filter used, the final phase error will have been reduced to zero or to a finite value.

Simple analysis of three functional blocks

Phase comparator (phase detector)

The properties of the phase detector circuit have a strong influence on the dynamic performance of the PLL system. The two most common types of phase detectors are linear and digital. The linear types are built from circuits which have previously been applied in the field of analog computation. The digital types, however, are based on logic circuits such as the EXCLUSIVE-OR gate. Moreover, digital PDs operate on binary signals exclusively, which means that both the reference and the output signals should be square waves.

The linear phase comparator is typically a multiplier circuit that mixes the input signal with the VCO signal. Assume for the moment that both input and output signals are sine wave signal and have the same frequency ω_1 , then, the two signals can be defined as:

$$u_1(t) = U_1 \sin(\omega_1 t + \theta_1) \quad (1)$$

$$u_2(t) = U_2 \cos(\omega_1 t + \theta_2)$$

The phase detector output signal $u_d(t)$ is by definition the product of these two signals, expressed as:

$$u_d(t) = k u_1(t) * u_2(t) = \frac{k U_1 U_2}{2} [\sin(\theta_1 - \theta_2) + \sin(2\omega_1 t + \theta_1 + \theta_2)] \quad (2)$$

where U_1 and U_2 are the amplitudes and θ_1 and θ_2 the phase of U_1 and U_2 , respectively, and k is the gain constant.

Equation (2) reveals that $u_d(t)$ is a superposition of a dc and ac component. The ac component is almost completely filtered out by the loop filter. Therefore we will henceforth consider the dc or average component of u_d only, which is given by

$$\overline{u_d} = K_d \sin \theta_e \quad (3)$$

since θ_e is very small, we can assume $\sin \theta_e \approx \theta_e$, then the equation (3) becomes:

$$\overline{u_d} = K_d \theta_e \quad (4)$$

$$\text{where } K_d = k \frac{U_1 U_2}{2}, \theta_e = \theta_1 - \theta_2$$

Loop Filter

The dynamic performance of the PLL is influenced not only by the type of PD chosen, but also by the type of loop filter used in a particular application. The possible loop filter includes passive and active first-order, or second order loop filter. According to the location of the poles and zeroes, they also can represent either a low-pass or a high-pass filter. However, in most cases the loop filter will be given by a passive, first-order, low-pass filter. The most general form of transfer function for a first-order filter is given by:

$$F(j\omega) = \frac{a + b(j\omega)}{c + d(j\omega)} \quad (5)$$

for a passive, low-pass filter, $b=0$.

The loop filter's main function in PLL is to eliminate the sum frequency component produced by the phase detector and only pass the dc or low frequency component. The loop filter characteristics directly affect the capture range, time required to obtain a lock (pull-in time), and the transit response of the system once the PLL has locked.

If u_d is the input signal of loop filter and u_f is the output signal, then we can get:

$$u_f(s) = F(s) u_d(s) \quad (6)$$

Voltage Controlled Oscillator (VCO)

The voltage controlled oscillator initially operating at its center frequency. Let us define the frequency it works at is its output. When VCO get a input signal, the output of it will change according to the voltage of the input signal, it means it will oscillate at another frequency rather than its center frequency. This voltage is called the control voltage of the PLL, and it is equivalent to the output of the loop filter.

In analog circuit, the center frequency ω_0 of VCO has to be determined by one or more external components. The methods vary from one type IC to another, but in most cases the center frequency depends on an RC product.

Since the angular frequency of a signal is defined as the first derivative of its phase with respect to time, the output of the oscillator is related to the control voltage by:

$$\dot{\omega}_2 = \dot{\theta}_2 = K_0 u_f(t) \quad (7)$$

Integrating equation (7), we obtain:

$$\theta_2(t) = K_0 \int_0^t u_f(t) dt \quad (8)$$

where $u_f(t)$ is the filter output and K_0 is the VCO gain constant.

Taking the Laplace transform of Equation (8), we obtain the transfer function of the VCO:

$$\theta_2(s) = \frac{K_0 u_f(s)}{s} \quad (9)$$

The action of the VCO in the feedback loop can be seen to act as an integrator.

Lock and Capture

Consider the case where the loop is not yet in lock. The phase comparator again mixes the input and the VCO signals to produce sum and difference frequency components. Now, however the difference component may fall outside the band edge of the low pass filter and be removed along with the sum frequency components. If this is the case, no information is transmitted around the loop and the VCO remains at its initial free-running frequency. As the input frequency approaches that of the VCO, the frequency of the difference component decreases and approaches the band edge of the low pass filter. Now some of the difference component is passed, which tends to drive the VCO towards the frequency of the input signal. This in turn decreases the frequency of the difference component and allows more information to be transmitted through the low pass filter to the VCO. This is essentially a positive feedback mechanism that causes the VCO to snap into lock with the input signal. With this mechanism in mind, the term capture range can be defined as the frequency range centered about the VCO initial free-running frequency over which the loop can acquire lock with the input signal. The capture range is a measure of how close the input

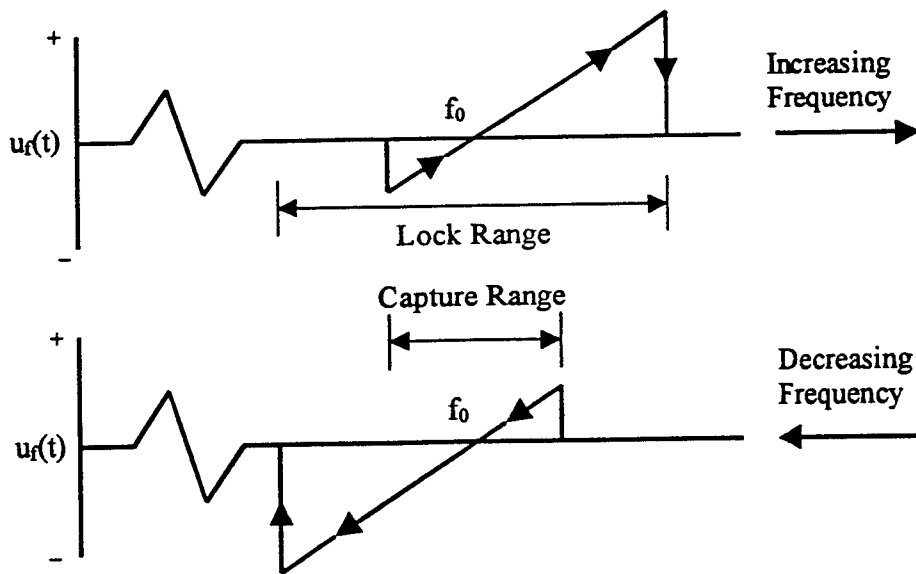


Figure 2. PLL frequency to voltage transfer characteristics

signal must be in frequency to that of the VCO to acquire lock. The capture range can assume any value within the lock range and depends primarily upon the band edge of the low pass filter together with the closed loop gain of the system. It is this signal-capturing phenomenon which gives the loop its frequency selective properties. Then we can understand the strong ability of the PLL to suppress noise superimposed on its input signal. Let us suppose that the input signal of the PLL is buried in noise. The PD tries to measure the phase error between input and output signals. The noise at the input cause the zero crossings of the input signal $u_1(t)$ to be advanced or delayed in a stochastic manner. This cause the PD output signal $u_d(t)$ to jitter around an average value. If the corner frequency of the loop filter is low enough, almost no noise will be noticeable in the signal $u_f(t)$, and the VCO will operate in such a way that the phase of the signal $u_2(t)$ is equal to the average phase of the input signal $u_1(t)$. Therefore we can state that the PLL is able to detect a signal that is buried in noise. These simplified considerations have shown that the PLL is nothing but a servo system which controls the phase of the output signal $u_2(t)$.

When the loop is in lock, the difference frequency components on the output of the phase comparator (error voltage) is DC and will always be passed by the low pass filter. Thus, the lock range is limited by the range of error voltage that can be generated and the corresponding VCO frequency deviation produced. The lock range is essentially a DC parameter and is not affected by the band edge of the low pass filter. [19]. Figure 2 shows the typical PLL frequency to voltage transfer characteristics for increasing decreasing frequencies.

Linear Model

To evaluate the PLL's tracking ability, it is necessary to linearize the model of the PLL. This can be done if the assumption is made that PLL is locked. Figure 3 shows the linear model of the PLL derived from the functional

block diagram of Figure 1. The PLL transfer functions for the phase detector, loop filter, and the VCO are respectively given by:

Phase detector:

$$\frac{u_d(s)}{\theta_e(s)} = K_d \quad (10)$$

Loop filter:

$$\frac{u_f(s)}{u_d(s)} = F(s) \quad (11)$$

VCO:

$$\frac{\theta_2(s)}{u_f(s)} = \frac{K_0}{s} \quad (12)$$

From equation (10), (11), (12) we can calculate either $\theta_2(s)$ as a function of $\theta_1(s)$ or $\theta_e(s)$ as a function of $\theta_1(s)$. For $\theta_2(s)$ and $\theta_e(s)$ we get:

$$\theta_2(s) = \theta_1(s) \frac{K_0 K_d F(s)}{s + K_0 K_d F(s)} \quad (13)$$

$$\theta_e(s) = \theta_1(s) \frac{s}{s + K_0 K_d F(s)} \quad (14)$$

then we get the phase transfer function $H(s)$ and error transfer function $H_e(s)$:

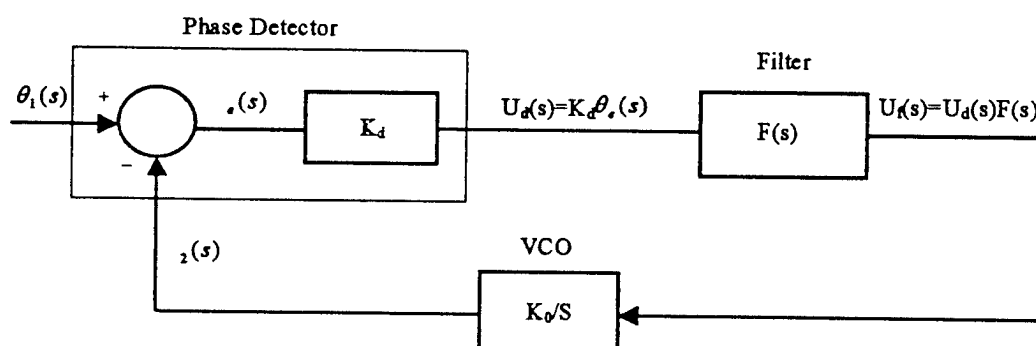


Figure 3. Linearized model of the PLL

$$H(s) = \frac{\theta_2(s)}{\theta_1(s)} = \frac{K_0 K_d F(s)}{s + K_0 K_d F(s)} \quad (15)$$

$$H_e(s) = \frac{\theta_e(s)}{\theta_1(s)} = \frac{s}{s + K_0 K_d F(s)} \quad (16)$$

if we use passive, first-order, low pass filter, then the transfer function of it is given by according to Equation (5):

$$F(s) = \frac{1}{1 + s\tau_1} \quad (17)$$

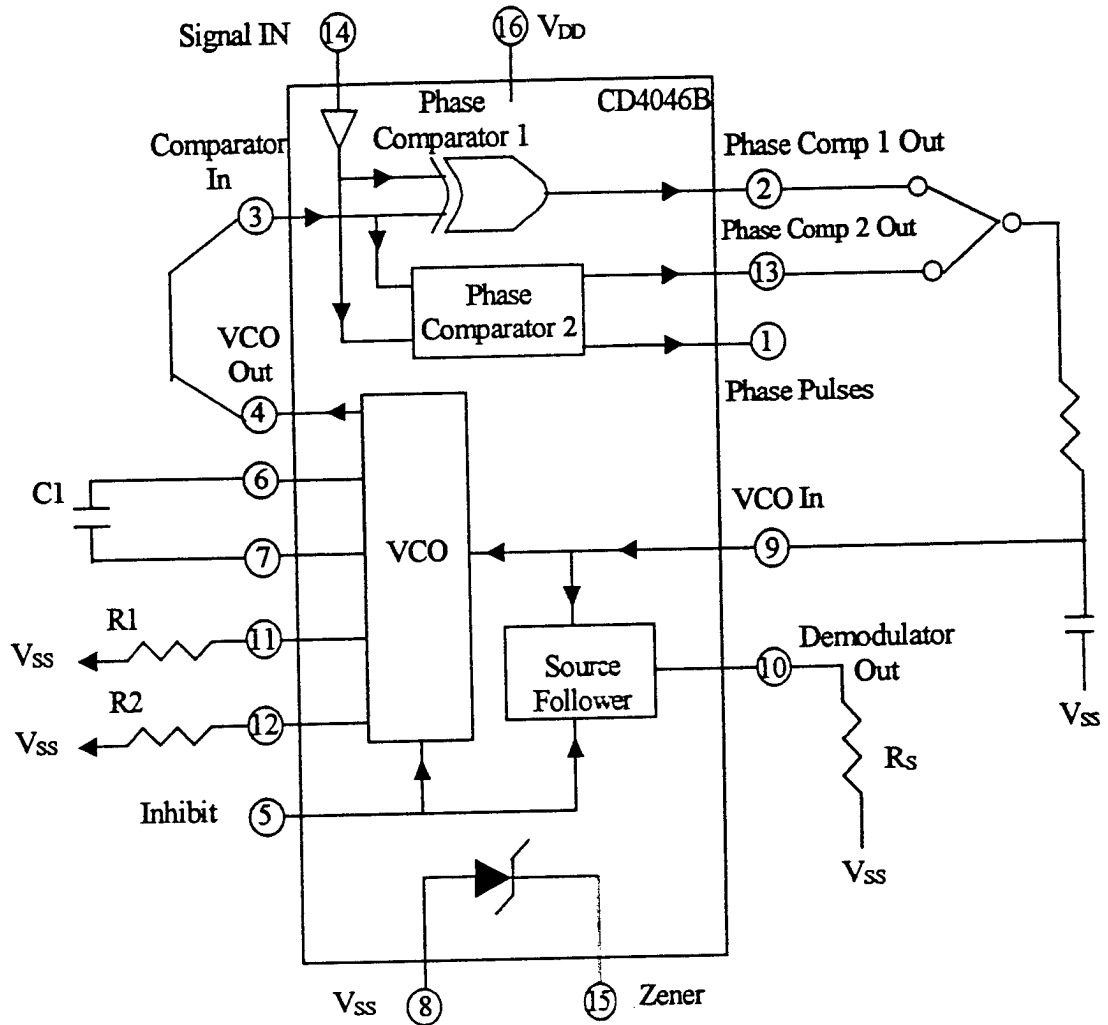


Figure 4. CMOS Phase-Locked Loop block diagram

Where τ_1 is time constant, is equal to the product of the value of the resistor and capacitor in the filter circuit.

Substitute the Equation (17) into the Equation (15) we can get:

$$H(s) = \frac{s\omega_n \left(2\xi - \frac{\omega_n}{K_0 K_d} \right) + \omega_n^2}{s^2 + 2\xi\omega_n s + \omega_n^2} \quad (18)$$

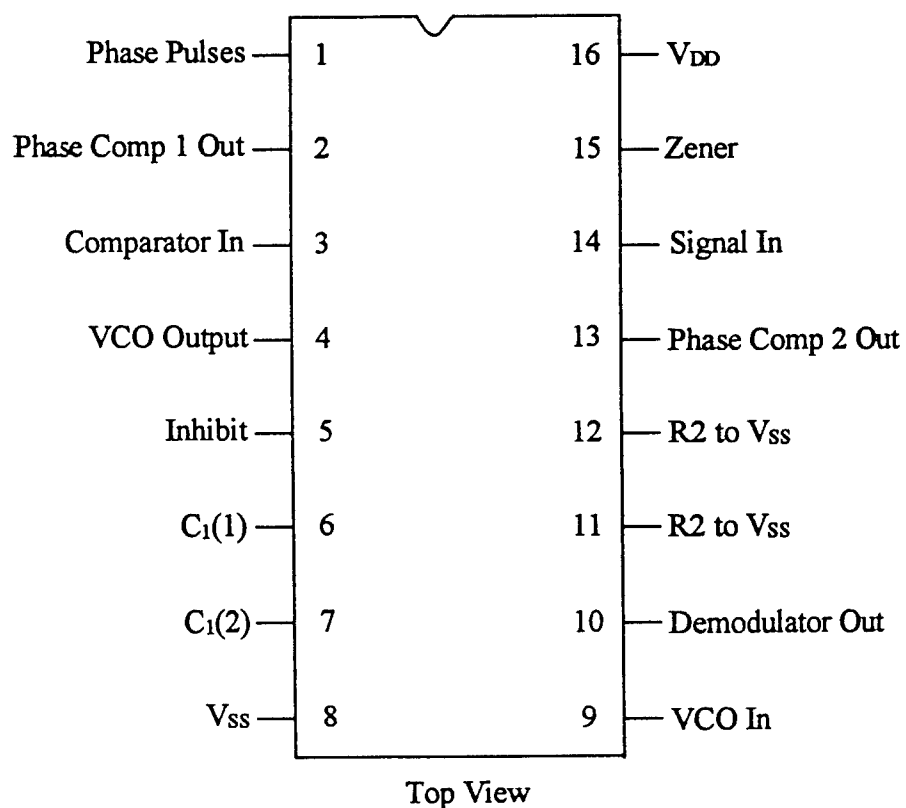


Figure 5. A CMOS Phase-Locked Loop Terminal Assignment

Where

$$\omega_n = \left(\frac{K_0 K_d}{\tau_1} \right)^{1/2} \quad (19)$$

$$\xi = \frac{1}{2} \left(\frac{K_0 K_d}{\tau_1} \right)^{1/2} \quad (20)$$

Equation (18) indicates that the PLL's phase transfer function act like a second order low pass filter for input phase signals, $\theta_1(t)$. This means that the PLL will track phase and frequency changes as long as the modulation frequencies are roughly less than the natural frequency of the phase transfer function, $\omega_n(t)$. [17].

False Lock

If the input signal is a symmetrical square wave, it consists of odd harmonics at $3f_1, 5f_1, \dots$, etc. If the input becomes asymmetrical, even harmonics will also be generated. The same applies to the VCO output. As a result, the PLL may lock onto subharmonics or harmonics of the center frequency. Therefore locking is possible when the reference and output frequencies have a common divider, when the ration of $f_1:f_0$ has the values 1:1, 2:1, 3:1, 1:2, 1:3, 2:3, 3:2, ..., etc. Locking onto harmonics and subharmonics is an unwanted effect and can be suppressed by a proper choice of phase detector, band limiting, or by using a sinusoidal VCO. [17].

A particular Phase-locked Loop used as the model PLL

A digital phase-locked loop realized by Simulink will be used to perform a set of experiments on a specific

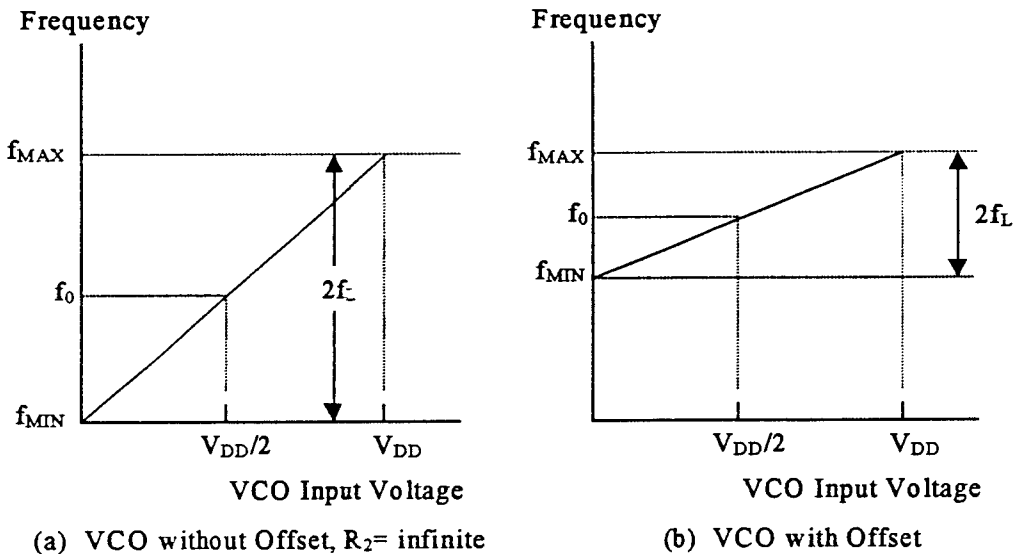


Figure 6. VCO Frequency

mechanical structure: a tube. The length of this tube can be changed, and the natural frequency of it will change along with the change of the length. Figure 16 shows the schematic of the tube. To design this digital-PLL we must have a analog PLL circuit as the base.

A wide variety of ICs for PLL systems or parts thereof are available from semiconductor manufacturers. Many chips contain complete PLL systems, but on others only the functional blocks of PLL (such as a VCO or a PD) are implemented. At present fully integrated PLLs on a single chip operate at frequencies of up to 35 MHz. Higher-frequency ranges are easily obtained by combining various ICs containing functional blocks only. There are two different types of fully integrated PLL systems on single chip. In the first and larger group, all connections between the individual functional blocks are made internally on the chip. Thus the number of external components and connections is reduced, but the user has only limited freedom of individual design. There is a second group of fully integrated PLL ICs in which the individual functional blocks are uncommitted. This enables the designer to build

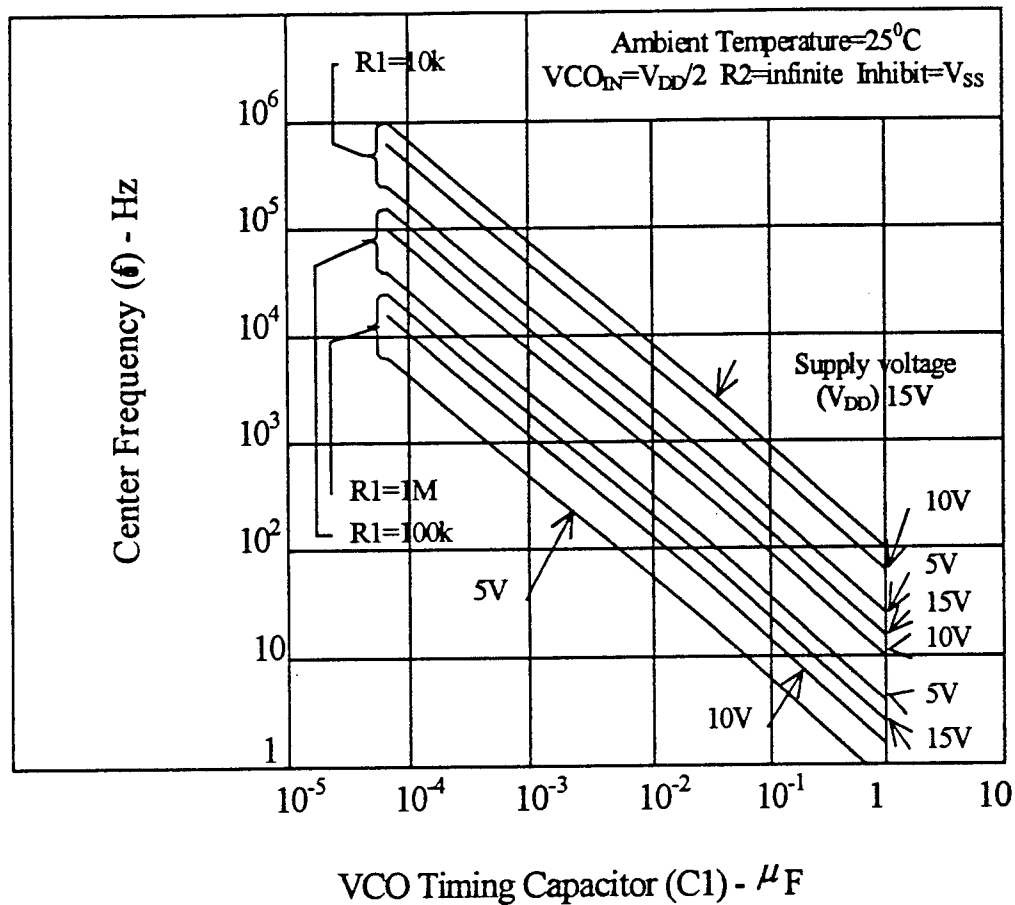


Figure 7. Typical Center Frequency as a Function of C_1 and R_1 at V_{DD} =5V, 10V and 15V.

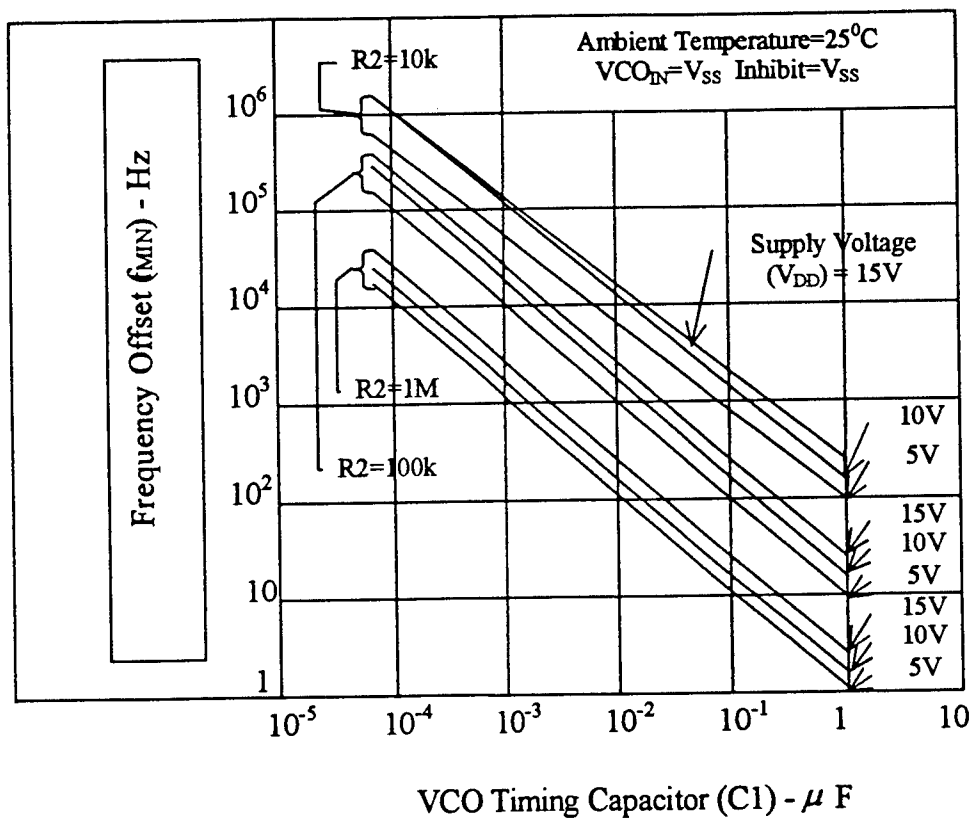


Figure 8. Typical Frequency Offset as a Function of C₁ and R₂ for V_{DD}=5V, 10V, and 15V

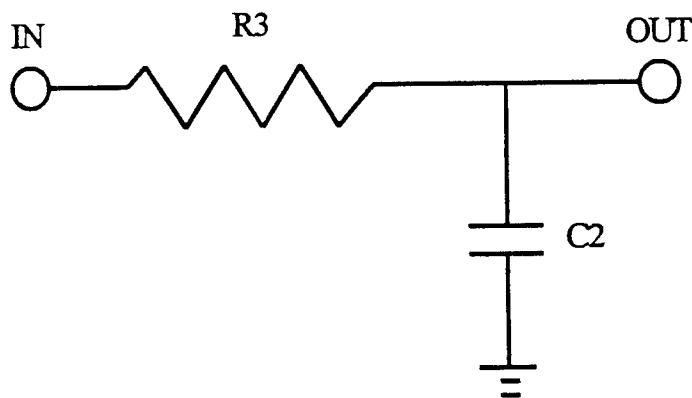


Figure 9. PLL passive first-order filter

individually tailored systems.

We selected Harris company's CD4046B CMOS Micropower Phase-locked Loop as our model PLL. This PLL consists of a low power, linear voltage controlled oscillator(VCO), and two different phase comparators having a common signal input amplifier and a common comparator input. A 5.2 V zener diode is provided for supply regulation if necessary. Figure 4 is its block diagram, and Figure 5 is its terminal assignment.

VCO section

The VCO in this chip requires one external capture capacitor C_1 and one or more external resistors (R_1 or R_1 and R_2). Resistor R_1 and capacitor C_1 determine the frequency range (lock range) of the VCO and resistor R_2 enables the VCO to have a frequency offset if required. VCO can work on some low supply voltage, such as 5-V, 10-V, 15-V, the supply voltage will determine its center frequency. If there is no signal input, VCO will adjust to center frequency, f_0 . The VCO frequency is shown in Figure 6. Figure 6 shows clearly that the VCO will have a offset if R_2 is nonzero, consequently, it will change the center frequency of the VCO.

The relationship between R_1 , C_1 , R_2 , power supply and the center frequency, lock range and frequency offset is displayed in Figures 7 and 8. Figure 7 shows clearly that if the value of R_1 and C_1 become smaller, then the center frequency of the VCO will decrease. Figure 8 shows clearly the relationship between R_2 , C_1 and f_0 , if decrease the value of R_2 and C_1 , center frequency of the VCO will be decreased.

Loop Filter section

Between the output of the phase detector and the input of the VCO, we can build a loop filter of the PLL. The loop filter used is a passive, first order, low pass filter, as shown in Figure 9.

The capture range of this PLL is:

$$2f_C = \frac{1}{\pi} \sqrt{\frac{2\pi f_L}{\tau_1}}, \quad \tau_1 = R_3 C_2 \quad (21)$$

the time required to obtain a lock (pull-in time) is:

$$T_P = \frac{\Delta\omega_0^2}{2\xi\omega_n} \quad (22)$$

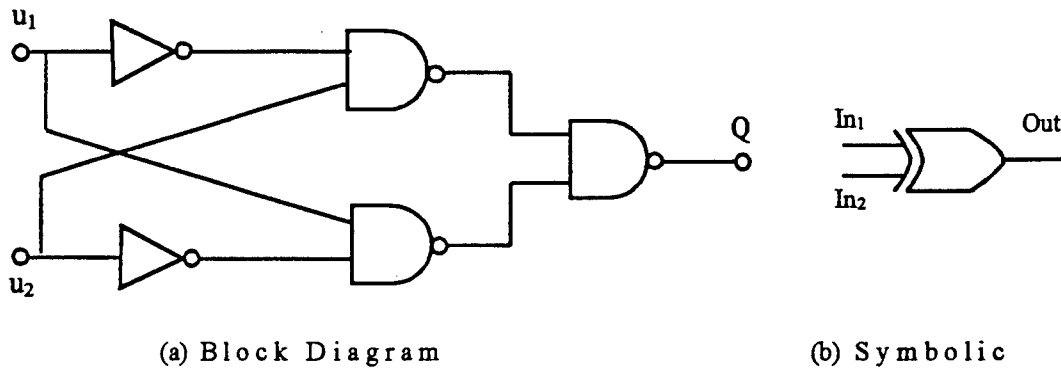


Figure 10. Exclusive OR gate

Where, $\Delta\omega_0$ is the initial frequency offset $\omega_1 - \omega_2$ for $t=0$; ω_n and ξ are the same as described in the Equation (19) and (20).

From equations (21) and (22), we can see that the loop filter characteristics (R_3 , C_2) directly affect the capture range and pull-in time. At the same time, from Equation (22), we can observe that beside R_3 and C_2 , $\Delta\omega_0$ also influence the pull-in time of the PLL. The capture range is \leq the lock range, however, we can select the value of the R_3 and C_1 to make f_c as large as f_L , please see the seventh column of Table 1.

Table 1. The relationship between f_c and f_L for certain value of τ_1

$2f_L = 18.9K$						
Time Constant τ_1 ($\Omega * \mu F$)	375	189	57.8	40.8	29.1	17.2
$2f_c$ (KHz) Theoretical value	4.01	5.64	10.2	12.15	14.38	18.7
$2f_c$ (KHz) Experimental value	3.81	5.32	9.48	11.24	13.29	17.24
Percentage Error	4.98	6.01	0.73	7.5	7.6	7.8

The percentage error are all below 10%, it is acceptable.

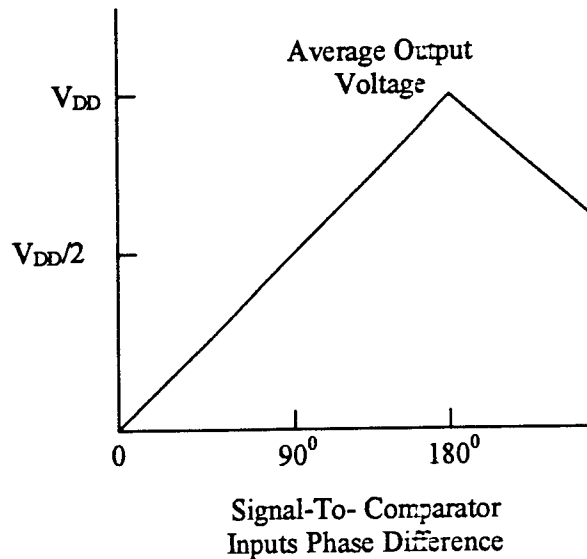


Figure 11. Phase comparator I characteristics at low pass filter output

It has been mentioned in previous sections that the lock range of this analog PLL is decided by the value of the external capacitor C_1 , external resistor R_1 and R_2 . And the capture range is decided by the lock range and the parameter of the loop filter, their relationship is described in equation (21). An experiment is designed to verify this relationship, for a certain value of $2f_L$ (the values of R_1 , R_2 and C_1 are fixed), input a square wave and try to find the capture ranges of the PLL under different time constant τ_1 , which is equal to $R_3 * C_2$. Table 1 shows the test result.

Phase comparator section

The phase comparator signal input (terminal 14) can be direct-coupled provided the signal swing is within CMOS logic level [logic "0" $\leq 30\%(V_{DD}-V_{SS})$, logic "1" $\geq 70\%(V_{DD}-V_{SS})$]. For small swings the signal must be capacitively coupled to the self-biasing amplifier at the signal input.

In this chip there are two phase comparators. Phase comparator I is an EXCLUSIVE-OR gate, as shown in Figure 10. Phase comparator II is an edge controlled digital memory network. We are interested in phase comparator I. It operates analogously to an over-driven balanced mixer. To maximize the lock range, the signal and comparator input frequencies must have a 50% duty cycle. With no signal or noise on the signal input, this phase comparator has an average output voltage equal to $V_{DD}/2$. The low pass filter connected to the output of phase comparator I supplies the averaged voltage to the VCO input, and causes the VCO to oscillate at the center frequency f_0 . One characteristic of this type of phase comparator is that it may lock onto input frequencies that are close to harmonics of the VCO center frequency. A second characteristic is that the phase angle between the signal and the comparator input varies between 0° and 180° , and is 90° at the center frequency. Figure 11 shows the typical, triangular, phase-to-output

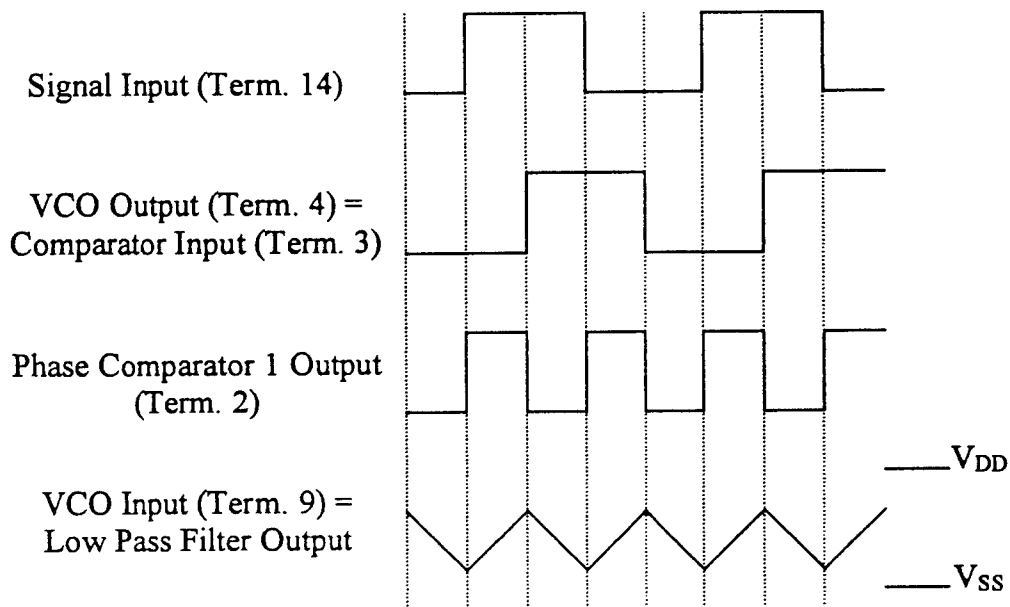


Figure 12. Typical waveforms for CMOS Phase-Locked Loop employing phase comparator I in locked condition

response characteristic of phase comparator I. Typical waveforms for a CMOS phase-locked loop employing phase comparator in locked condition of f_0 is shown in Figure 12.

The digital PLL is implemented by using Simulink that contains the functional blocks which will be used. Figure 13 shows the functional block diagram of the digital phase-locked loop. The whole idea of it is to input a signal into the digital PLL, then get the output of the PLL, this output is a square and with the same frequency of the input signal. In the experiment the amplitude of the input signal will be restricted between -0.5 and 0.5 , then add it a constant 0.5 , its becomes between 0 and 1 , they satisfied the requirement of the logic calculation of the phase detector.

Figure 14 shows the block diagram of phase detect (exclusive OR gate)and loop filter. In functional block of loop filter, we put the transfer function of first order, low pass loop filter in it, it is $\frac{b}{1+as}$, constant a is similar the product of R_3C_2 (time constant τ_1) in analog PLL, and constant b is the gain of the loop filter. Constants a and b act together to affect the capture range and pull-in time of the PLL.

Figure 15 shows the block diagram of voltage controlled oscillator.

A sine function is in F_{cn} block, it is: $F_{cn} = \sin(cu_f + \omega_0)$, u_f is the output of loop filter, ω_0 is the center

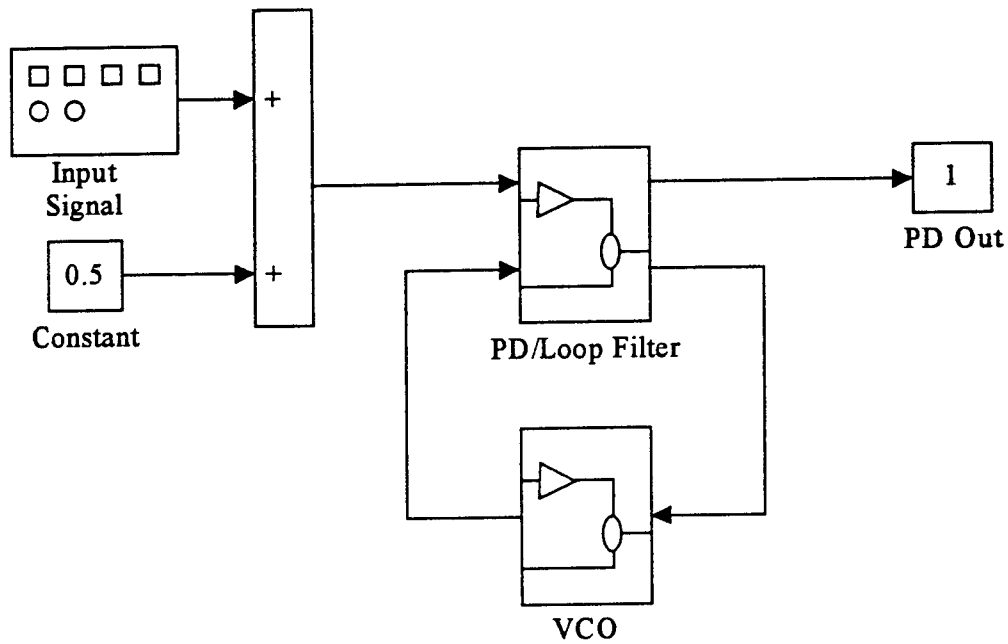


Figure 13. Block diagram of digital Phase-Locked Loop

frequency of VCO. Constant c is a coefficient of VCO, it can amplify or limit the value of u_f which is put into the VCO to adjust the lock range of the PLL, so its function is equal to the function of R_1 and C_1 in analog PLL.

Above is only a general concept of digital PLL, a more detailed description of the digital PLL implementation is given in Reference [20].

So far, the digital phase-locked loop has been implemented. Next work is to investigate its performance in simulation and actual experiments.

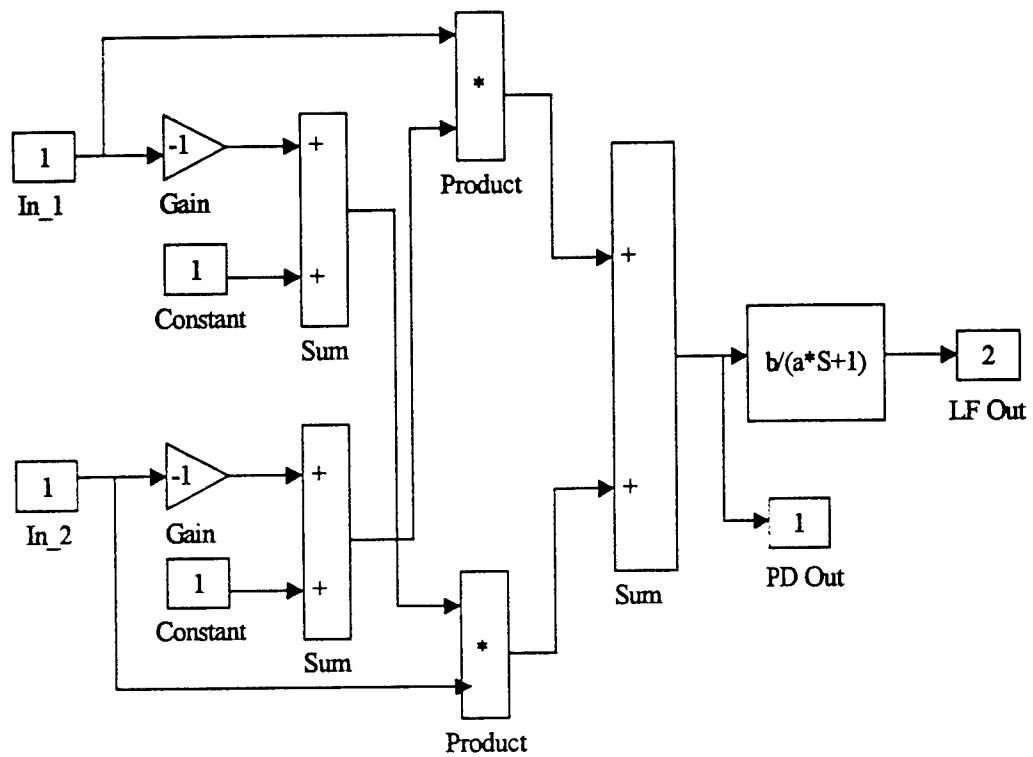


Figure 14. Block diagram of phase detector and loop filter

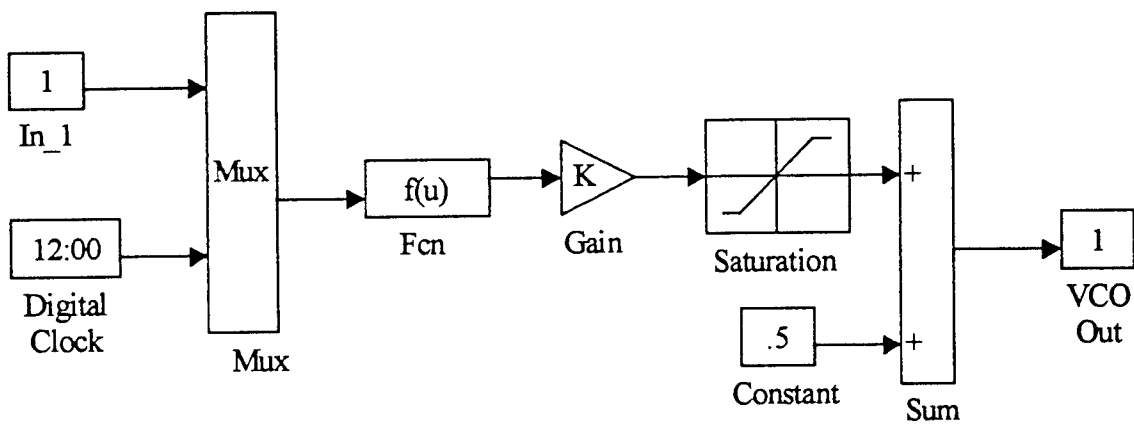


Figure 15. Block diagram of VCO

3. Experiment Description

In order to realize the broadband noise reduction using digital phase-locked loop, a digital PLL is interfaced to a tube via two sensors, a speaker and a microphone. The maximum length of the tube is 153 cm and its diameter is 12 cm. A sensor, a speaker and a microphone are located at one end of the tube. Another sensor is located at the other end of the tube, this end is free and a handle is installed inside the tube. The handle can be moved to change the effective length of the tube, thus changing the natural frequencies. Figure 16 is the schematic of the tube.

Simulation Experiments

Before performing experiments directly on the tube, three simulation experiments have been conducted to verify the performance of the PLL tracker.

The first experiment is completed by using Simulink. Simulink is an application of Matlab that is installed in a Personal Computer. The whole digital PLL circuit is implemented by Simulink, the input signal is a single frequency Square wave. The block diagram of this simulation is shown in Figure 17.

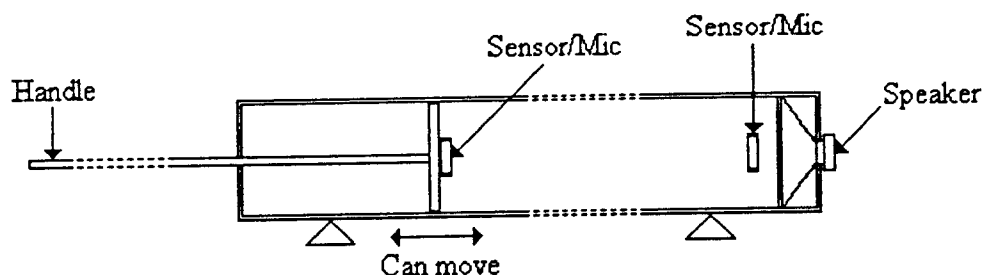


Figure 16. Schematic of the tube

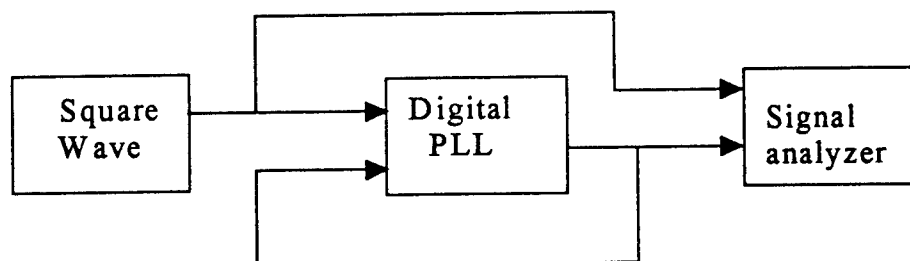


Figure 17. Block diagram of the PLL simulation.

This experiment is designed to demonstrate the narrow band tracking ability of the digital PLL circuit and to get the proper parameters of this PLL when varying the center frequency. Figure 18 shows the transient waveforms of input signal, VCO, Phase Detector and Loop Filter before lock. Figure 19 shows the waveforms of the same four signals in lock condition. The frequency of the input signal is 40 Hz and the center frequency of the VCO is set on 50 Hz. At first the PLL is in the unlocked condition and the VCO oscillates at its center frequency which is different from that of the input signal. The PD detects this difference and LF filters out the high-frequency component of the difference. This difference then causes the VCO to change and it gives it some adjustment value to make it oscillate at the frequency that is approximately equal to the input signal. After some while, the digital PLL locks on the input signal and the VCO oscillates at the frequency that is the same as that of the input signal.

Figure 20 shows the output of Loop Filter during a period of time that is from unlocked condition to locked condition. This figure describes the basic operating procedure of the PLL. In Figures 18, 19 and 20, the center frequency of VCO is 50 Hz. Similar results are obtained if the center frequency is changed.

In the second experiment also applied a single frequency square wave, but now it is generated by function generator out of PC instead of by Simulink that installed in PC. The digital PLL circuit is downloaded into microprocessor [20], then observe the output of VCO by an oscilloscope. The whole system is shown in Figure 21.

The purpose of this experiment is to verify the digital PLL that is accomplished by PC can be downloaded properly into microprocessor and the microprocessor can work properly. This system works properly, according to different center frequency of VCO and corresponding parameters of the circuit, the PLL can track the input signal within the lock range. Table 2 summarizes the parameters and performance of this PLL.

Table 2. Parameters of the digital PLL under different center frequencies

Transfer function of LF	Function of VCO	Sample time	Center frequency of VCO (Hz)	Lock range (Hz)	Pull in time (Min)
$\frac{2}{\frac{2}{2\pi}S + 1}$	$\sin((20u_f + 1000)t)$	0.001	16	0-50	1
$\frac{2}{\frac{2}{2\pi}S + 1}$	$\sin((10u_f + 1000)t)$	0.001	16	0-50	1
$\frac{1}{\frac{2}{2\pi}S + 1}$	$\sin((5u_f + 1000)t)$	0.001	16	0-50	3
$\frac{1}{\frac{2}{2\pi}S + 1}$	$\sin((10u_f + 1570)t)$	0.0005	50	30-80	More than 10
$\frac{1}{\frac{0.5}{2\pi}S + 1}$	$\sin((10u_f + 1570)t)$	0.0005	50	30-80	10
$\frac{1}{\frac{1}{2\pi}S + 1}$	$\sin((10u_f + 1570)t)$	0.0005	50	30-80	4
$\frac{1}{\frac{1}{2\pi}S + 1}$	$\sin((5u_f + 1570)t)$	0.0005	50	30-80	3
$\frac{0.5}{\frac{0.5}{2\pi}S + 1}$	$\sin((10u_f + 3140)t)$	0.0005	100	70-130	More than 10
$\frac{1}{\frac{0.5}{2\pi}S + 1}$	$\sin((5u_f + 3140)t)$	0.0005	100	70-130	10
$\frac{0.5}{\frac{0.5}{2\pi}S + 1}$	$\sin((5u_f + 3140)t)$	0.0005	100	70-130	3
$\frac{0.5}{\frac{0.5}{2\pi}S + 1}$	$\sin((2u_f + 3140)t)$	0.0005	100	70-130	12

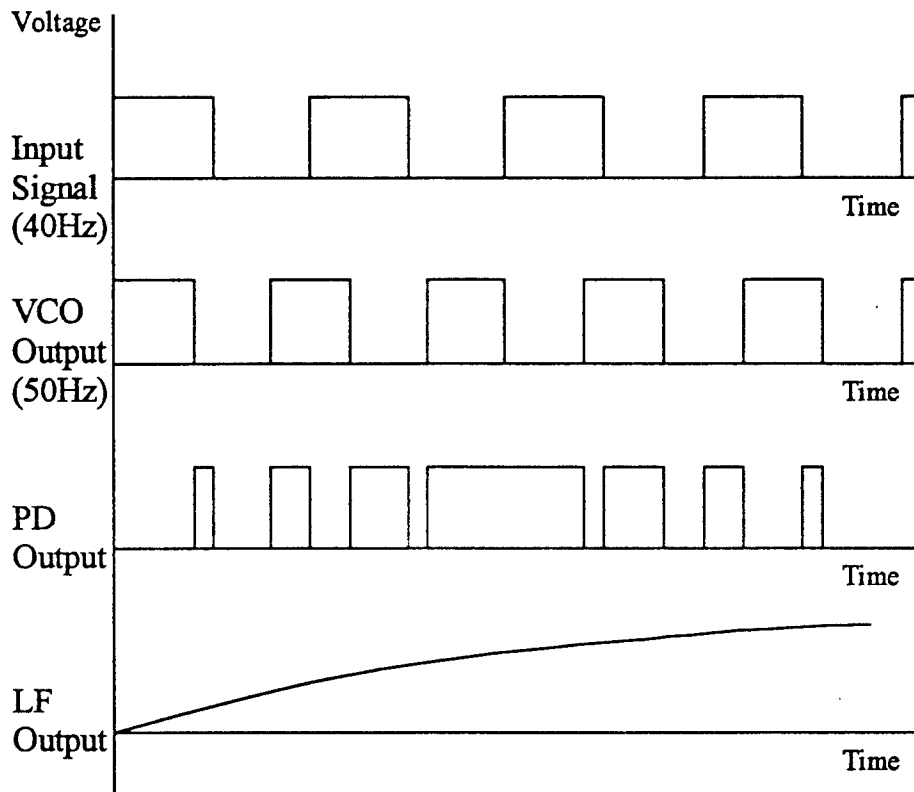


Figure 18. Transient waveform of digital PLL in unlock condition

The third experiment is very similar to the first one, but the input signal is a noise signal instead of a single frequency sine wave. This experiment is designed to see if PLL can distinguish some frequency components from the noise. Because the bandwidth of the noise signal is too broad, it is necessary to add a second order filter to filter some frequency before it goes into the PLL the block diagram of this experiment is shown in Figure 22. This second-order filter models the resonant dynamics of a mechanical structure. The transfer function of second-order

filter is: $\frac{A}{S^2 + 2\xi\omega_n + \omega_n^2}$,

where, constant A is the gain of this filter and ω_n, ξ is natural frequency and damping ratio, respectively. When the bandwidth of the noise signal is narrow enough, the PLL can track the frequency components that are around the center frequency of the VCO and within the lock range of the PLL. The center frequency and lock range are easily changed for tracking different frequency component of the input noise signal.

Actual Experiment

In order to verify the frequency selective properties of the PLL to mechanical structures, some experiments have been done directly using the tube. In this part, two experiments are conducted.

The first one is designed to get the natural frequencies of the tube at different points at which the lengths of the tube are different. The first step is to calculate the theoretical values of natural frequencies at four different points. These four points are arbitrarily chosen, they locate as the following:

A: $L_A=40$ cm; B: $L_B=80$ cm; C: $L_C=40$ cm; D: $L_D=40$ cm.

By theory, $f_i = \frac{ic}{2L}$, $C \approx 340m/s$

A: $L_A = 40$ cm

$$f_1 = (1) (340)/(2)(0.4) = 425 \text{ Hz}$$

$$f_2 = (2) (340)/(2)(0.4) = 850 \text{ Hz}$$

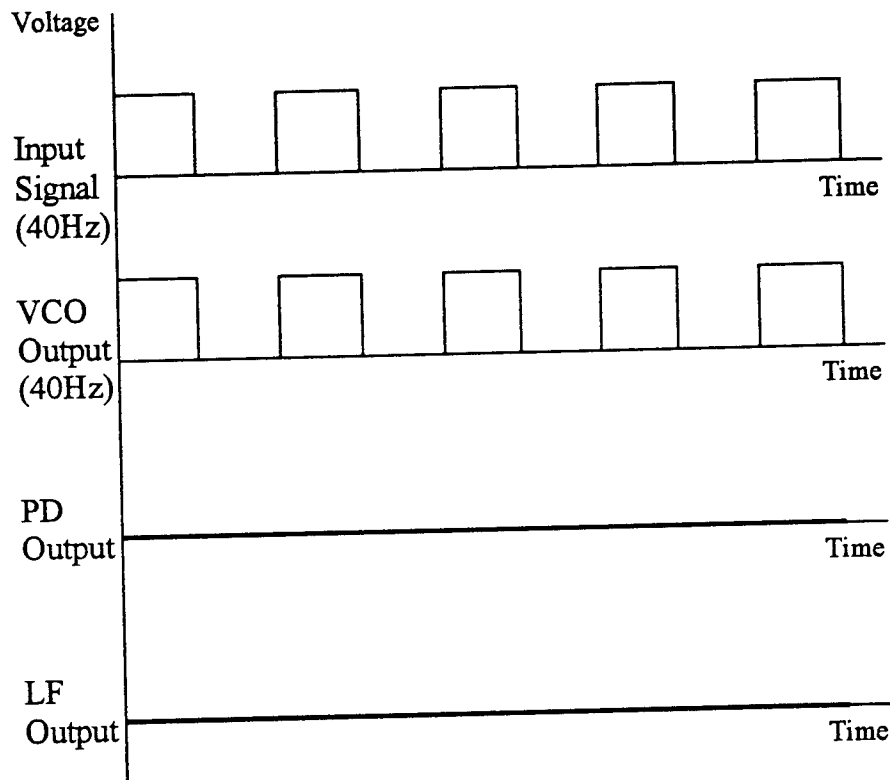


Figure 19. Waveform of digital PLL in locked condition

B: $L_B = 80 \text{ cm}$

$$f_1 = (1) (340)/(2)(0.8) = 212.5 \text{ Hz}$$

$$f_2 = (2) (340)/(2)(0.8) = 425 \text{ Hz}$$

C: $L_C = 120 \text{ cm}$

$$f_1 = (1) (340)/(2)(1.2) = 141.67 \text{ Hz}$$

$$f_2 = (2) (340)/(2)(1.2) = 283.33 \text{ Hz}$$

D: $L_D = 150 \text{ cm}$

$$f_1 = (1) (340)/(2)(1.5) = 113.33 \text{ Hz}$$

$$f_2 = (2) (340)/(2)(1.5) = 226.67 \text{ Hz}$$

The first natural frequency is the most important frequency in our analysis, so the theoretical natural frequencies of A, B, C and D are 425, 212.5, 141.67 and 113.33 Hz respectively.

The second step is to get the actual natural frequencies at these points according to the theoretical values using sine wave excitation. Input a single frequency sine wave, then the response of the tube at a point is different when the frequency of this sine wave is different. It may be the combination of several frequencies or a single frequency

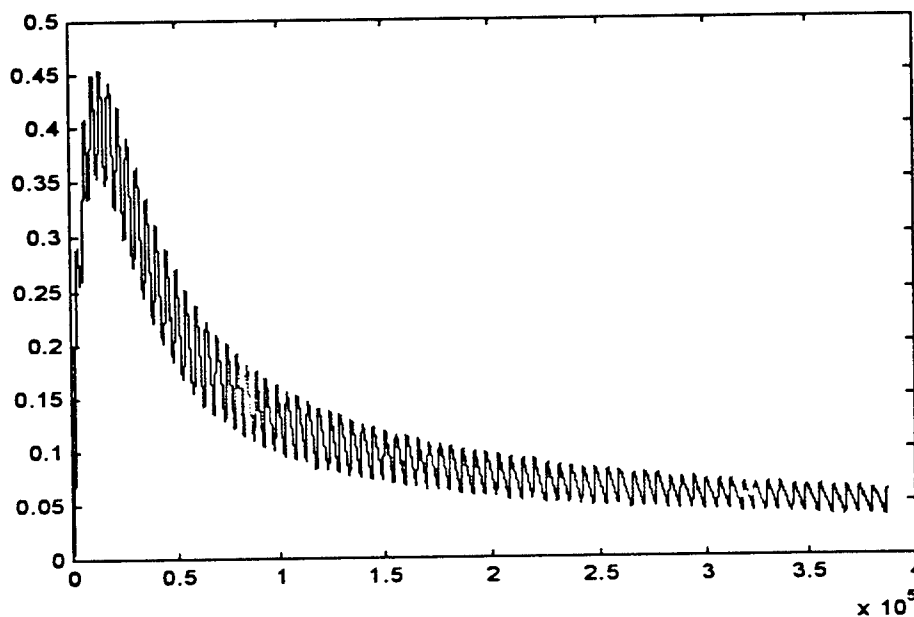


Figure 20. Output of LF vs. Time

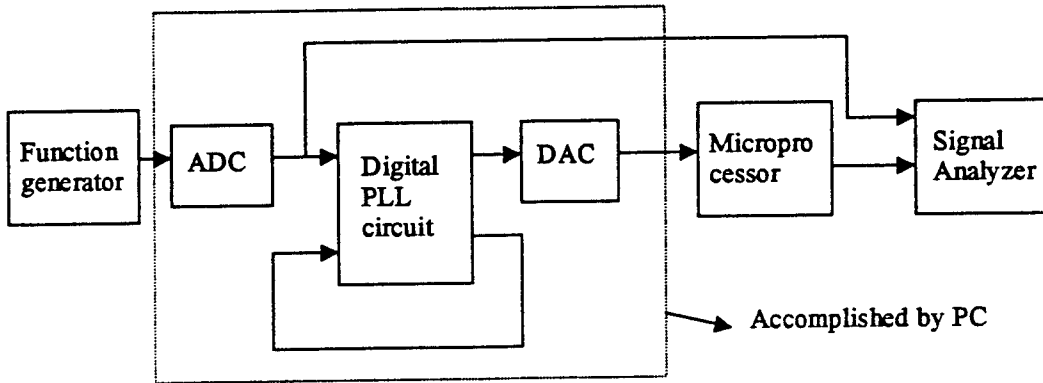


Figure 21. System block diagram of experiment II

different from the input signal and the amplitude is very small. But there always exists a frequency which excited the tube to have the largest response which have the same frequency as the input signal and its amplitude is relatively high, this frequency is the natural frequency of the tube at this point.

Table 3. Natural Frequencies of different lengths of the tube

Point	Length (cm)	Theoretical Natural Frequency (Hz)	Experimental Natural Frequency (Hz)	Experimental Error (%)
A	40	425.0	443.3	4.3
B	80	212.5	229.1	7.8
	90	188.9	200.3	6.0
	100	170.0	182.5	7.4
	110	154.5	162.5	5.2
C	120	141.7	151.2	6.6
	130	130.8	138.1	5.5
	140	121.4	129.5	6.7
D	150	113.3	119.4	5.4

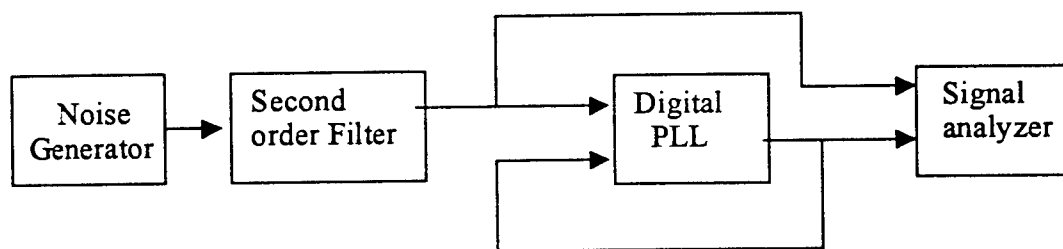


Figure 22. Block diagram of experiment III

According to the above describe to do the experiments to get the actual natural frequencies at points A, B, C and D, they are 443.3, 229.1, 151.2, 119.4 Hz, respectively. The results of both theoretical and experimental values of natural frequencies are summarized in Table 3. In order to get more information, more points have been tested in the experiment, they are located from point B to Point D and the increment of the length is 10 centimeter. The experimental error is a little larger than expected, but it is acceptable.

The second experiment is designed to input a noise signal into the tube, the tube will be excited by this signal and have different responses when it has different lengths. The peak response when it has certain length should be the natural frequency of this length. The response of the tube is then be transferred into the digital PLL, this digital PLL should track on the natural frequency.

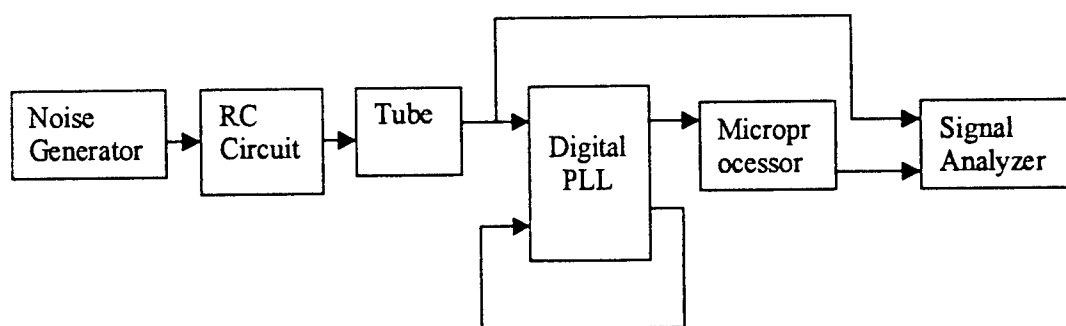


Figure 23. System block diagram of experiment II

Figure 23 shows the system block diagram of this experiment. Because the bandwidth of the noise signal is too broad, so the response's bandwidth it excited also too broad, then uses a simple RC circuit to filter out some high frequency. This system works properly, the PLL can distinguish the natural frequency of the tube of different lengths from the noise.

4. Experimental Results

One of the most intriguing capabilities of the PLL is its ability to suppress noise superimposed on its input signal. Now suppose that the input signal of the PLL is buried in noise. The PD tries to measure the phase error between input and output signals. The noise at the input causes the zero crossings of the input signal $u_1(t)$ to be advanced or delayed in a stochastic manner. This causes the PD output signal $u_d(t)$ to jitter around an average value. If the corner frequency of the loop filter is low enough, almost no noise will be noticeable in the signal $u_d(t)$, and the VCO will operate in such a way that the phase of the signal $u_2(t)$ is equal to the average phase of the input signal $u_1(t)$. Therefore we can state that the PLL is able to detect a signal that is buried in noise. Actually, the theory of noise in PLLs is very cumbersome. Exact solutions for noise performance have been derived for first-order PLLs only; for second-order PLLs, computer simulations have been made which provided approximately results. They are all beyond this paper's research scope, here only cites the final results of the noise theory.

As a rule of thumb, for $SNR \geq 4$, stable operation is generally possible. Where, SNR is signal-to-noise ratio,

$SNR = \frac{P_s}{P_n} = \frac{U_s^2(rms)}{U_n^2(rms)}$, where P_s and P_n are the power of signal and noise respectively, U_s and U_n are the rms value of voltage of signal and noise respectively.

In the first experiment the input of the tube is broadband white noise. According to FFT analysis there exists a peak response which corresponds to the natural frequency of the tube of fixed length. Although the peak response of the tube is at the natural frequency, the signal-to-noise ratio is too low for the PLL to accurately track the natural frequency. The PLL cannot distinguish this weak signal from the noise because the SNR criterion is not satisfied.

To remedy this situation a second set of experiments was performed in which the input signal was equal to broadband white noise plus a sine wave of a single frequency. When we put such a signal into the tube, the peak response of the tube is very distinguished. The amplitude of the peak response which corresponds to the natural frequency of the tube is much higher than the amplitude of the broadband noise signal. The purpose of the experiment is just to deal with this kind of situation, separate the peak response from the noise and provide it to the control system for being used in the next step. Now the SNR condition is satisfied and the PLL operates properly.

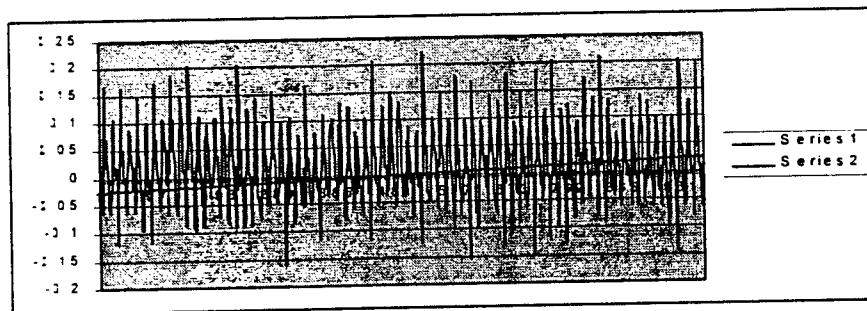
Figures 24 through 27 show the response of the tube at different length from $L = 80\text{cm}$ to $L = 150\text{cm}$, the increment of two adjacent points are 10cm . Figure A is the input of the tube, Figure B is the output of the tube, it is also the input of the digital PLL, and Figure C is the output of the digital PLL.

$L = 80\text{cm}$

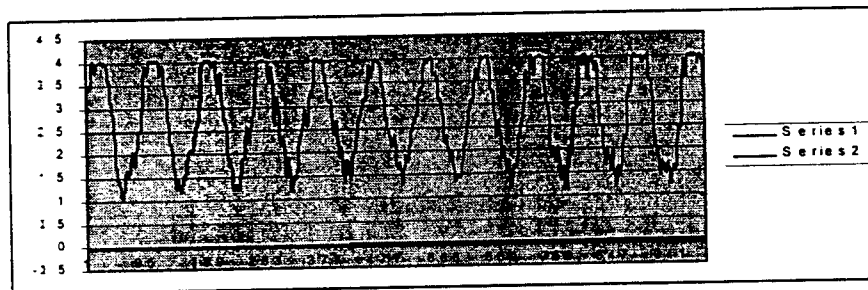
Figure A is the input of the tube, it is a sine wave + noise

Amplitude of the sine wave: 0.01v(rms) ; Frequency of the sine wave: 229Hz

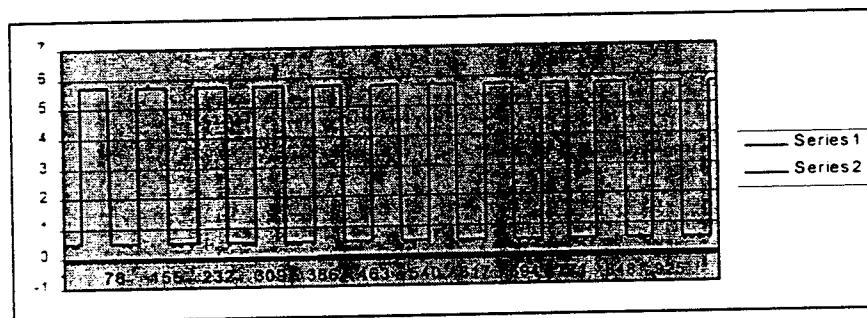
Amplitude of the noise: 0.1v(rms) .



A. Input of the tube



B. Output of the tube/Input of the PLL



C. Output of the PLL

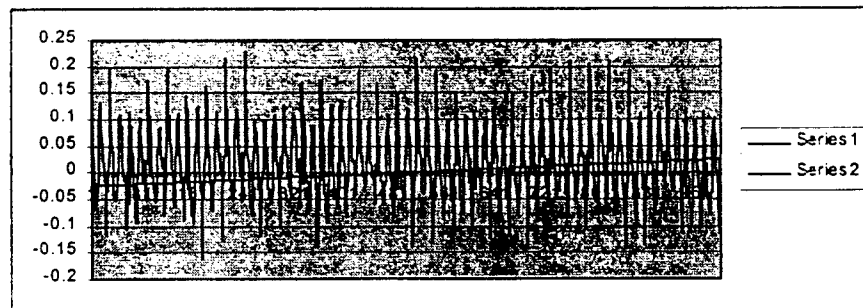
Figure 24. Waveform at Tube Length = 80 cm

$L = 90\text{cm}$

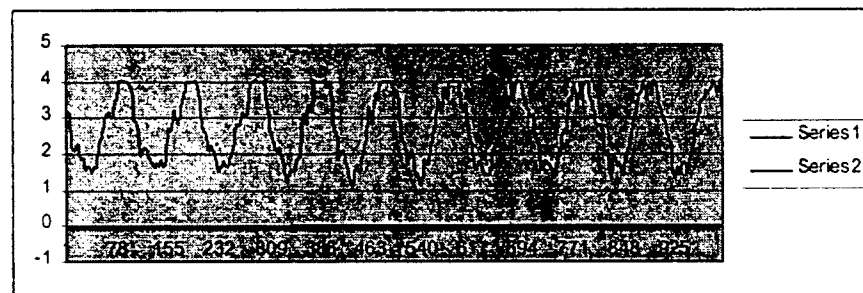
Figure A is the input of the tube, it is a sine wave + noise

Amplitude of the sine wave: 0.01v(rms) ; Frequency of the sine wave: 200Hz

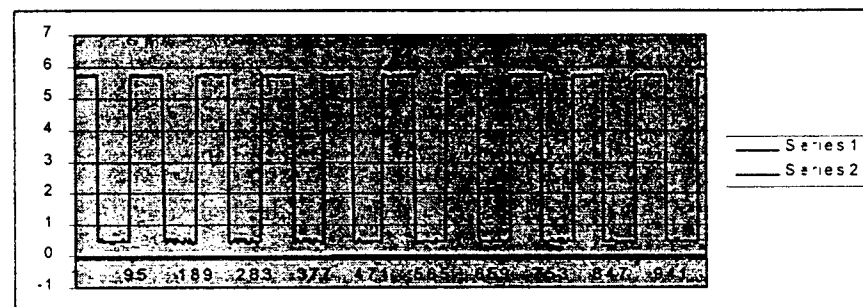
Amplitude of the noise: 0.1v(rms) .



A. Input of the tube



B. Output of the tube/Input of the PLL



C. Output of the PLL

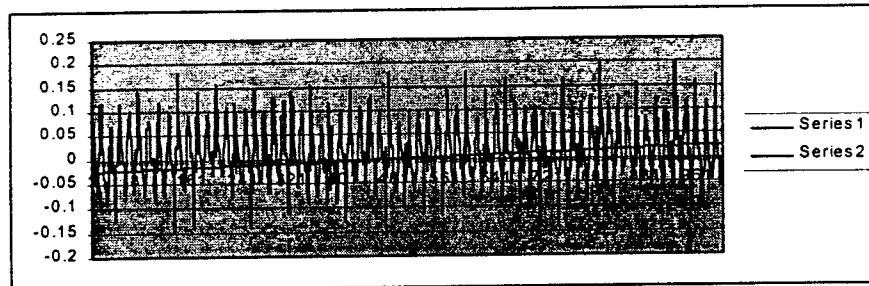
Figure 25. Waveform at Tube Length = 90 cm

$L = 110\text{cm}$

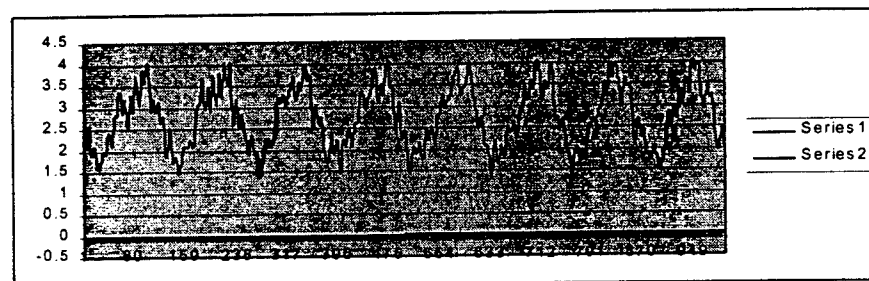
Figure A is the input of the tube, it is a sine wave + noise

Amplitude of the sine wave: 0.01v(rms) ; Frequency of the sine wave: 162Hz

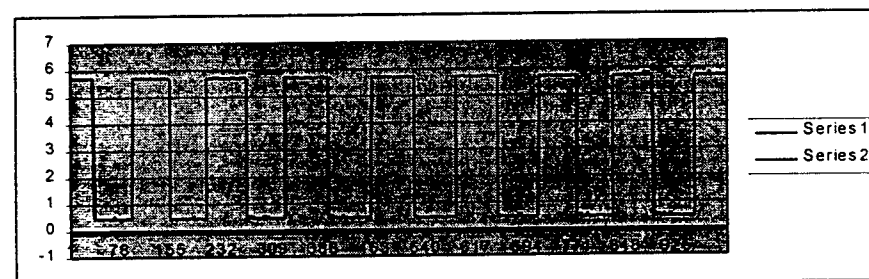
Amplitude of the noise: 0.1v(rms) .



A. Input of the tube



B. Output of the tube/Input of the PLL



C. Output of the PLL

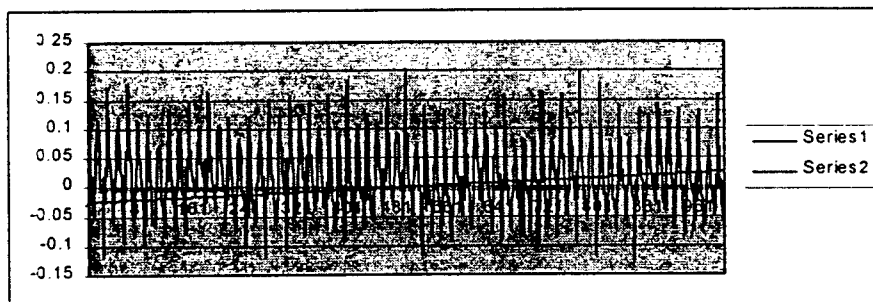
Figure 26. Waveform at Tube Length = 110 cm

L = 130cm

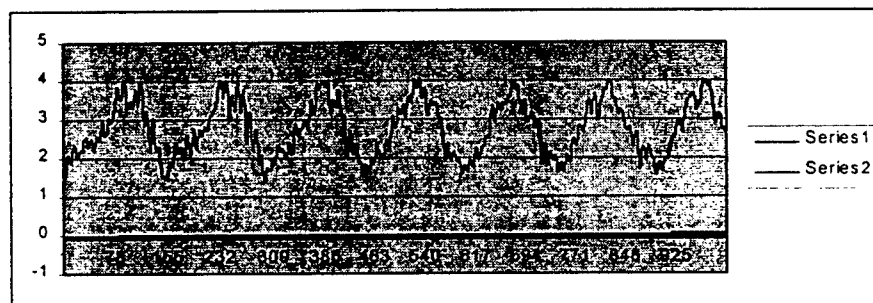
Figure A is the input of the tube, it is a sine wave + noise

Amplitude of the sine wave: 0.01v(rms); Frequency of the sine wave: 138Hz

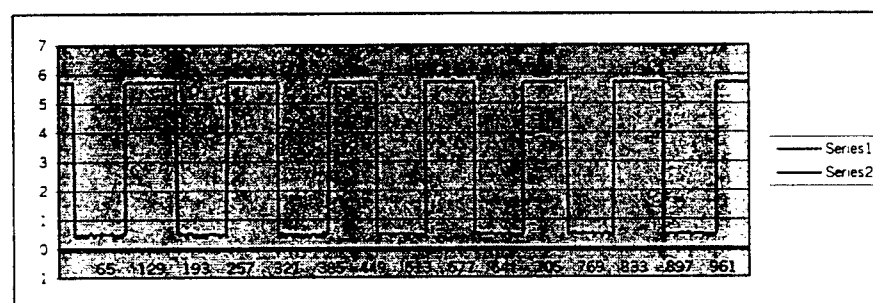
Amplitude of the noise: 0.1v(rms).



A. Input of the tube



B. Output of tube/Input of the PLL



C. Output of the PLL

Figure 27. Waveform at Tube Length = 130 cm

5. Conclusions

The PLL tracker has been experimentally shown to be effective in tracking a single natural frequency of tube at a point and tracking the resonant frequency in the presence of broadband excitation. The tracker is simple, inexpensive, and also has other practical applications and benefits. The PLL tracker's capture range and center frequency are easily changed for different natural frequency of the tube when it has the different lengths. For tracking the several natural frequencies, a paralleled set of PLL trackers can be applied. The PLL is also capable of extracting the main response of a sensor even when the sensor signal is heavily buried in noise, producing a smooth square wave output.

The software based digital PLL tracker does have some drawbacks with respect to the analog one. The pull in time is longer than expected due to the processing speed of the microprocessor. The other drawback is that accumulated error causes the PLL to fail after certain finite time. This is a problem attributed to the software implementation of the PLL. These drawbacks don't necessarily cause serious error because they can be overcome using high speed CPU and optimizing the source code. Despite these drawbacks, the PLL tracker remains a simple and effective way to track the natural frequency of a mechanical structure.

TECHNICAL REPORT
(FOR AFOSR SUMMER RESEARCH EXTENSION PROGRAM)

**A CONTINUOUS-WAVE APPROACH TO 3-D IMAGING THROUGH TURBID MEDIA
WITH A SINGLE PLANAR MEASUREMENT**

DR. HANLI LIU
BIOMEDICAL ENGINEERING
P.O. BOX 19138
UNIVERSITY OF TEXAS AT ARLINGTON
ARLINGTON, TEXAS 76019
OFFICE: (817) 272-2054 HOME: (817) 461-9910
FAX: (817) 272-2251
E-Mail Address: hanli@utarlg.uta.edu

GRANT AMOUNT: \$25,000

INSTITUTION COST-SHARING AMOUNT: \$17,500
\$12,500 (indirect cost)+\$5,000 (equipment).

START/END DATE:

June 1998 -- May 1999

AIR FORCE LAB FOCAL POINT:

DR. CHARLES L. MATSON
Air Force Research Laboratory
KIRTLAND AFB, NM 87117-5776
(505) 846-2049
E-Mail Address: matson@plk.af.mil

UNIVERSITY CONTRACT OFFICIAL:

MS. Laura L. Wade
DIRECTOR OF SPONSORED PROJECTS
UNIVERSITY OF TEXAS AT ARLINGTON
350 DAVIS HALL, BOX 19145
ARLINGTON, TEXAS 76019
OFFICE: (817) 272-2105 FAX: (817) 272-5808
E-Mail Address: wyatt@uta.edu

January 2000

A. Research Objective

The general objective for this summer extension program proposal was to continue in validating, applying, and extending new theory developed by the Air Force Research Laboratory (AFRL) to imaging through various types of turbid media including clouds and biological tissue. By the end of summer 1997, preliminary experimental validation on the theory had been succeeded using breast phantoms and a frequency-domain approach in a frequency range of a few tens of MHz. Further investigations on the feasibility of applying the theory and technology to both military and biomedical applications were very desirable, particularly, with a continuous-wave (CW) approach. If this approach is successful, it can provide novel, economic, and fast imaging methodologies for both the Department of Defense and medical community.

The modified specific aims of this research proposal included:

- 1) to modify the MHz frequency-domain system by using low modulation frequencies in kHz ranges to validate the idea of utilizing CW light for 3-dimensional breast localization.
- 2) to characterize optical properties of the tumor imbedded inside the breast phantom so as to assist identifying/quantifying the tumor.
- 3) to assist the AFRL collaborator in conducting laboratory tests for rapid imaging of airplanes through clouds and in studying conditions to optimize the reconstruction algorithm based on the laboratory data.

B. Background and 1997 Summer Research Conclusions

Near infrared radiation for imaging inhomogenieties in turbid media has been recently explored and investigated.^{1,2,3,4} Benefits of using this technique include both imaging breast tumors in the breast tissue and imaging objects through clouds. The Air Force Research Laboratory (AFRL) at Kirtland has been developing a new theory,⁵ i.e., turbid media version of the Fourier diffraction theorem⁶, significantly different from existing theory.^{1,2} This theory provides new insight into fundamental limitations in our ability to image objects imbedded in turbid media, and has led to a significant new reconstruction algorithm that permits 3-D imaging of objects in turbid media using a single planar measurement. In addition, to validate this algorithm experimentally, the principle investigator (PI) of this proposal and one of her graduate students from the University of Texas at Arlington spent the summer of 1997 doing initial laboratory testing sponsored by the Air Force Office of Scientific Research (AFOSR) Summer Research Program. The validation research was performed using realistic breast-tissue phantoms⁷ with finite sizes. This kind of laboratory validation was necessary since the new theory was derived using highly-idealized conditions and tested only by highly-idealized computer simulations⁸.

Specifically, the PI with her graduate student performed experiments on tissue phantoms using a frequency-domain photon migration system that was provided by Air Force Research Laboratory. The system included an amplitude-modulated laser diode, two radio frequency (RF) signal generators, an avalanche photo detector, and a lock-in amplifier. The tissue phantoms were made with inhomogeneities imbedded and were then scanned with the system at various RF frequencies (10-100 MHz). The data obtained from the amplitude and phase measurements were analyzed using the new reconstruction algorithm. The reconstructed data at 20-40 MHz showed clear validation of the new algorithm and afforded to localize inhomogeneities hidden in turbid media in three dimensions in a frequency range of 20-60 MHz. In addition, preliminary analysis of the results allowed us to conduct investigation on optimization of experimental parameters to obtain high-quality, reconstructed images. In summary, the results from the 1997

summer research were very satisfactory and promising, leading to a mutual desire to extend this research for another year at the PI's home institution with equipment support and theoretical consult from Air Force Research Laboratory.

C. Budget Justification and Institution Cost-Sharing

The PI borrowed the previously existing frequency-domain system from Air Force Research Laboratory for two years (November 1997-November 1999) in order to continue the investigation at the PI's home institution. In addition, both parties of the collaboration realized the importance of validating a continuous wave approach to 3-dimensional imaging through turbid media and the potential of such an approach for practical applications. Validation of this approach was rather straightforward by modifying the existing Air Force Research Laboratory's frequency-domain system. Therefore, the major budget of the AFOSR summer research extension program was to hire two graduate students to perform experiments and to conduct validation and feasibility tests using both MHz and KHz modulation frequencies.

The PI's institution had an amount of \$11,000 for institution cost-sharing: \$5,000 for existing equipment in the PI's laboratory that was participated in the project, and \$6,000 for 10% of the faculty time spent on the project.

D. Research Methodology and Results

For specific aim 1): to modify the current system by using low modulation frequencies in kHz ranges to validate the idea of utilizing D.C. light for 3-dimensional inhomogeneity imaging in turbid media.

D 1.1 Methodology

For this aim, the instrument was modified from the previously existing frequency-domain system: the two signal generators was still utilized to generate signals in the range of 9 KHz to a few hundred KHz, and all of the power splitters, amplifiers, and mixers were switched to those with the corresponding frequency range accordingly. Then we measured similar inhomogeneous phantoms that we used before with the MHz signals to compare the two different cases. We started the measurements with relatively low absorption samples first and then scanned higher absorption/scattering samples, and eventually, we also took measurements on the phantoms containing multiple imbedded objects. Then resolutions and optimum experimental parameters were studied by taking measurements under various conditions. Also the experimental and theoretical comparisons were performed to validate the theory for such a D.C. approach. In brief, this part of studies included three components: 1) instrument completion, 2) system testing and refining, and 3) inhomogeneous phantom studies. It took a graduate student two semesters to complete this aim.

All of the scans used for this report were performed on areas of 8 cm x 8 cm having 64x64, 32x32, or 16x16 grids of pixels. In the case of MHz measurements, all the data shown in this report were at 20 MHz. In the case of kHz measurements, 10 kHz modulation frequency was used. The software package called Interactive Data Language (IDL) was used to process the measured data and to perform the reconstruction process.

In the following, we will use the XYZ coordinate system shown in Figure 1 to refer to the positions of the imbedded tumors in the phantoms. The XY plane is in parallel with the detection plane, the origin is set at the light source (i.e., $z_1=0$), and the Z axis is pointing from the source plane into the phantom. If a bead is placed in the center of a phantom, its coordinate will be (0, 0, $d/2$ cm), where d is the thickness of the phantom. In the case of multiple hidden

tumors, two beads (the same or different kind) were normally imbedded at $(0, -2 \text{ cm}, d/2 \text{ cm})$ and $(0, 2 \text{ cm}, d/2 \text{ cm})$ inside of a phantom. In making tumor-containing phantoms, we positioned the object(s) on top of a semi-dried, background material which had been cast earlier, and then added an equal amount of ready-to-cast resin on top of the first part to complete the phantom. In this way, we implanted the objects inside the phantoms with good 3D coordinate references, and X-ray measurements confirmed the positions of some imbedded objects.

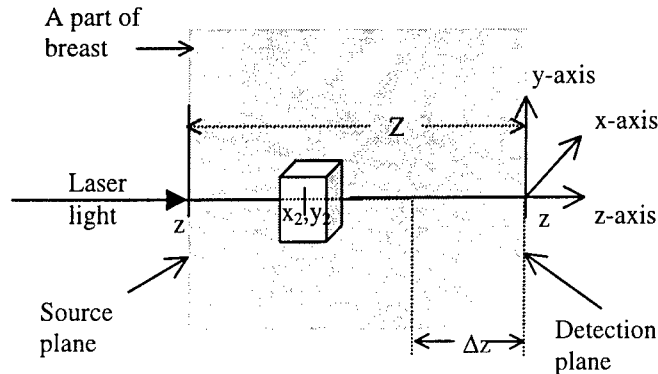


Figure 1. Schematic diagram showing the geometry for the backpropagation algorithm. The illumination source is located at $(0, 0, z_1)$, the center of the inhomogeneity/tumor is represented by the cube located at (x_2, y_2, z_2) , and the detection plane is located at z_0 . The gray area represents the homogenous background. Coordinate z is used for selected backpropagation planes, and it will vary to cover the entire volume of the breast phantom.

D 1.2 Experimental Results and Reconstructed Images

In this section, we show a few examples of reconstructed images and 3D tumor localization for several breast phantoms containing a) one single high-absorbing tumor, b) one high-absorbing and one high-scattering tumor, and c) two low-contrast tumors. A reconstructed Diffuse Photon Density Wave (DPDW) can be displayed at any chosen z plane in the phantom. One particular choice is to display the reconstructed DPDW at the detection plane. In this plane, the reconstruction process consists only of subtraction of the homogeneous wave and low-pass filtering of the resulting scattered wave since no backpropagation is necessary. From this portion of the reconstructed DPDW, the tumor/tumors can be localized in the X and Y dimensions so that plots in the Z -direction can be made from the locations of the transverse center of the tumors. In all the results presented here, the images reconstructed at the detection plane were used to determine the x and y positions of the tumor, while the z plots to be were used for localization in the z direction. The origin of the coordinate system is set at the light source, i.e., $z_0=0$. The reconstructed amplitude images shown in this section use gray scales with darker levels corresponding to larger amplitudes and lighter levels corresponding to lower amplitudes.

a) one high-absorbing tumor in the breast phantom

Figures 2 and 3 show amplitude images of reconstructed DPDW's with 20 MHz and 10 kHz modulation frequencies, respectively. The measured data were obtained with a 780 nm laser scanned on a 8 cm x 8 cm area of a phantom containing one black bead. The phantom was 4.7 cm thick, and the black bead had a diameter of 9 mm and was imbedded in the middle of the phantom, i.e., 2.35 cm behind the detection plane. The illumination spot on the phantom was -1.5 cm off-centered in the x -axis direction with respect to the center of the phantom. The absorption and reduced scattering coefficients of the background medium were 0.04 ± 0.01 and $9.6 \pm 0.9 \text{ cm}^{-1}$, respectively, which were determined using a homogeneous sample. Obtained with 20 MHz modulation, Figure 2(a) displays a 2D amplitude image of DPDW's reconstructed at the detection plane with a dark circular spot. This spot results from a large intensity change in the scattered DPDW's caused by the hidden object, indicating the XY location of the hidden

object. Thus, this figure shows that the hidden object is located at (1.4 cm, -0.3 cm) with respect to the center of the detection plane. Figure 2(b) is an amplitude plot in z direction with a peak at 2.2 cm, which implies that the hidden object is 2.5 cm behind the detection plane. The deviations between these values and the true ones are within 2 mm. Next, Figure 3 shows the results of another measurement obtained with 10 kHz modulation for the same phantom; the XY image and z plot in this case are presented in the same format/style as those used in Figure 2. In this case, the illumination spot on the phantom was -1.0 cm off-centered in the x-axis direction with respect to the center of the phantom. Figure 3 shows that the hidden object is located at (1.1 cm, 0.2 cm, 2.7 cm) with respect to the light source, having the object 2.0 cm behind the detection plane. The maximum deviation in x and y directions between the reconstructed values and the actual location is 2 mm. The maximum deviation in z direction between the reconstructed value and the actual location is 3.5 mm. This could be improved by choosing smaller Δz values.

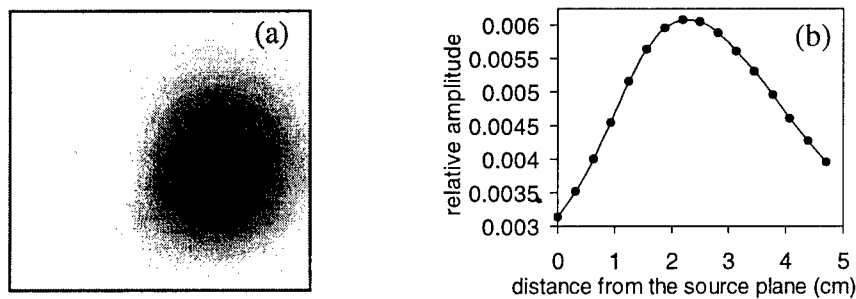


Figure 2. Modulation frequency is 20 MHz. (a) Reconstructed amplitude image at the detection plane of the scattered DPDW through a tissue phantom containing one 9-mm black bead. (b) The corresponding plot of the reconstructed amplitudes along a line containing the inhomogeneity center and perpendicular to the detection plane.

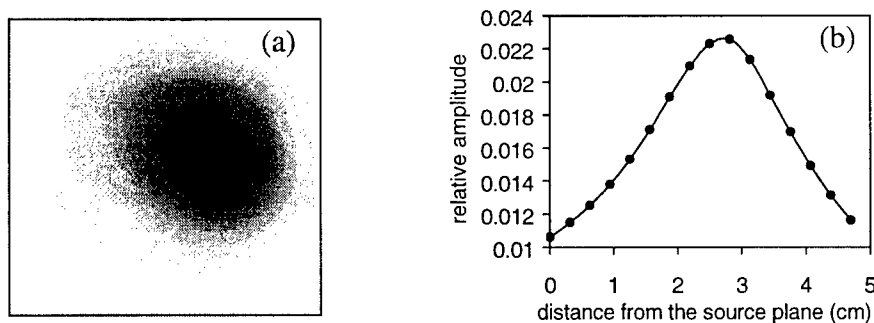


Figure 3. Modulation frequency is 10 kHz. (a) Reconstructed amplitude image at the detection plane of the scattered DPDW through a tissue phantom containing one 9-mm black bead. The image size is 8 cm x 8 cm. (b) The corresponding plot of the reconstructed amplitude along the line containing the inhomogeneity center and perpendicular to the detection plane.

We learned a few important features from these two figures: 1) we can obtain similar results and localization information from the measurements with either MHz or kHz modulation frequencies, and 2) the relative amplitudes of the reconstructed DPDW's with kHz modulation are 3-4 times larger than those with MHz modulation. This means that a kHz photon migration system may be capable of localizing a tumor in 3D as accurately as a MHz photon migration system with easier-to-detect signals since light with lower modulation frequencies attenuates

less and thus penetrates more in tissue than light with higher modulation frequencies. This agrees with a theoretical prediction conducted for signal-to-noise analysis by the authors;⁹ they showed that our ability to both detect and characterize inhomogeneities decreases as the modulation frequency increases.

b) two non-identical tumors in the breast phantom

Figure 4 shows the results with another set of imbedded objects: one 13-mm black marble and 12-mm clear bead. These two objects were imbedded in the middle of a 5-cm thick phantom and 4 cm apart vertically symmetric to the center of the phantom. A 32x32 grid of pixels with a modulation frequency of 20 MHz was chosen to scan an 8cm x 8cm area. The background medium had absorption and reduced scattering coefficients of $0.016 \pm 0.00 \text{ cm}^{-1}$ and $10.0 \pm 0.7 \text{ cm}^{-1}$. Similarly, Figures 4(a) and 4(b) are the amplitude image and z plot, respectively. It can be seen that the black marble results in a dark spot, whereas the clear bead produces in a much lighter spot in the image plane. This indicates that the black marble scatters the light much more strongly than the clear bead. Notice the presence of a white ring in the image surrounding the location of the clear bead. Because we are employing a reverse gray scale to display the images, the white ring is just a region of low intensity (i.e., low scattering) in the image. The separation between the dark spot produced by the black marble and the lighter spot produced by the clear bead is 4.2 cm. Furthermore, Figure 4(b) shows that both the black marble and clear bead are located 2.3 cm behind the detection plane, in good agreement with the expected values.

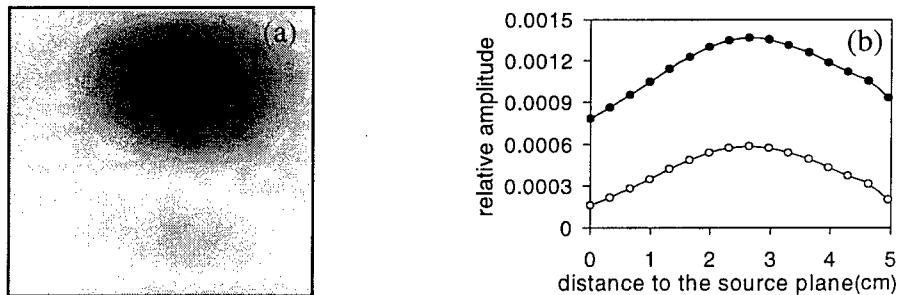


Figure 4. Modulation frequency is 20 MHz. (a) Reconstructed amplitude image at the detection plane of the scattered DPDW through a tissue phantom containing one 12 mm black marble and one 12 mm clear bead. The image size is 8 cm x 8 cm. (b) The corresponding plot of the reconstructed amplitude along the lines containing the tumor centers and perpendicular to the detection plane. The solid circles correspond to the top dark spot; the open circles correspond to the bottom light spot.

c) two low-contrast tumors in the breast phantom

All of the inhomogeneous phantoms mentioned above have a very large contrast in absorption or scattering between the simulated tumors (i.e., black and white marbles/beads) and the background medium. The ratio of absorption (or scattering) coefficients between the simulated tumors and the background medium can be 1000 or larger, which is not realistic for human breasts and breast tumors. Thus, we created a phantom with low contrast between the background tissue and the tumors. The imbedded objects had similar scattering properties to that of the background medium but had an absorption coefficient 5-6 times larger than that of the background medium. This was accomplished by adding a small amount of NIR dye into the simulated tumors. The uniform scattering coefficient was 15 cm^{-1} , whereas the absorption coefficients were 0.02 cm^{-1} and 0.12 cm^{-1} for the background and the simulated tumors,

respectively. The sample thickness in this case was 4.5 cm, and the imbedded objects were $0.8 \times 0.8 \times 0.8 \text{ cm}^3$ cubes and placed 2.3 cm below the detection plane. In this case, only the 10 kHz modulation frequency was used. Since the contrast was low, a 680 nm laser with a stronger output power was used to increase the signal to noise ratio. Shown in Figures 5(a) and 5(b), respectively, are the reconstructed amplitude image at the detection plane and the z plot for the two hidden objects. Figure 5(a) demonstrates that the two imbedded objects are located at (-0.6 cm, -2.0 cm) and (-0.6 cm, 2.6 cm) with respect to the center of the detection plane. Figure 5(b) reveals that the imbedded objects are both located at 2.5 cm behind the detection plane, being 2 mm deeper than the expected value.

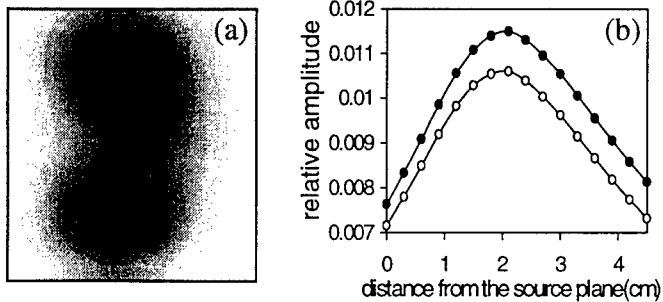


Figure 5. Modulation frequency is 10 kHz. (a) Reconstructed amplitude image at the detection plane of the scattered DPDW through a tissue phantom containing two low-contrast simulated tumors. The image size is 8 cm x 8 cm. (b) The corresponding plot of the reconstructed amplitude along the lines containing the tumor centers and perpendicular to the detection plane. The solid circles correspond to the top spot; the open circles correspond to the bottom spot.

D 1.3 Discussion

Through laboratory measurements with real instrument noise, we have validated the backpropagation algorithm by demonstrating that with either a MHz or kHz amplitude-modulated laser, we are able to localize a variety of hidden simulated tumors in breast phantoms three dimensionally. We showed that with a single planar measurement and finite-size (14 cm x 14 cm x 4 cm) phantoms, the algorithm still allows us to localize imbedded objects within a deviation of 2-3 mm. We demonstrated that for localization, kHz modulation actually gives better signal to noise ratio than MHz modulation, as predicted by theory. In general, the advantage of using MHz modulation frequencies is the ability to obtain phase information, which permits quantitative calculations for optical properties of the inhomogeneities.^{10,11} However, a MHz frequency-domain system is much more complex and costly than a kHz frequency-domain system. Therefore, a kHz or even a DC system is preferred to a MHz system if localization is a major application.

All of the amplitude images shown are of the reconstructed DPDW's at the detection plan in order to obtain the X and Y locations of the hidden tumor/tumors so that the appropriate z plot can be obtained. Once the Z location for the embedded tumor plane is determined, another XY amplitude image can be displayed at the tumor plane, where the optimal resolution can be achieved for the reconstructed image. If multiple measurements are taken at different angles with respect to the center of the phantom, it is possible to reconstruct the shape of the hidden tumor.

We believe that our current work shows the feasibility and explores the possibility and potential of developing low-cost optical tomographic instruments. The existing imaging modalities for breast cancer imaging, such as X-ray mammography and sonography, can localize abnormal masses in the breast quite accurately. However, those images are structural, not functional. It would be very desirable if the optical method/optical tomography can show functional as well as structural information. This is the basis for Specific Aim 2.

For specific aim 2): to characterize optical properties of the tumor imbedded inside the breast phantom so as to assist identifying/quantifying the tumor.

D 2.1 Algorithm for Tumor Characterization

Based on the newly developed turbid media version of diffraction tomography theory,¹² we can characterize the optical properties of a hidden tumor after we localize it. Briefly, the reconstructed, two-dimensional Fourier transform of the scattered wave, $U_{rec, pw}(\omega_x, \omega_y; z_0)$, is given by¹²

$$U_{rec, pw}(\omega_x, \omega_y; z_3) = \frac{F(\omega_x, \omega_y)}{K_1(z_3)} \frac{\exp(-iz_3\gamma_{\omega i})}{2\gamma_{\omega}} \times \exp[-(z_3 - z_1)k_i] \exp(-iz_1k_r) \\ \times \iiint o(x', y', z') \exp[-(z_3 - z')(\gamma_{\omega r} - k_i)] \times \exp[-i[k'_x\omega_x + y'\omega_y + z'(-\gamma_{\omega i} - k_r)]] dx' dy' dz' \quad (1)$$

where $F(\omega_x, \omega_y)$ is a regularizing filter and $K_1(z_3)$ is a normalizing factor. Based on our experience, we wish to emphasize that filter type and cutoff frequency are very important factors, affecting the resolution of the reconstructed images. Furthermore,

$$\gamma_{\omega} \equiv \gamma_{\omega r} + i \gamma_{\omega i} \\ = \text{Re} \left(\sqrt{\omega_x^2 + \omega_y^2 - k^2} \right) + i \text{Im} \left(\sqrt{\omega_x^2 + \omega_y^2 - k^2} \right), \\ k \equiv k_r + i k_i = \text{Re} \left(\sqrt{\frac{-\mu_a + i2\pi f/c}{D}} \right) + i \text{Im} \left(\sqrt{\frac{-\mu_a + i2\pi f/c}{D}} \right), \\ o(x, y, z) = o_a(x, y, z) + o_s(x, y, z), \text{ where} \\ o_a(x, y, z) = -3\mu_s' \delta\mu_a(x, y, z) \quad o_s(x, y, z) = \frac{-\delta\mu_s'(x, y, z)}{\mu_s' + \delta\mu_s'(x, y, z)}.$$

When the light source is constant or modulated at very low frequency, such as a few kHz, we can simplify the above equations as

$$\gamma_{\omega r} = 0; \quad \gamma_{\omega i} = \sqrt{\omega_x^2 + \omega_y^2 + 3\mu_a\mu_s'}; \\ k_r = 0; \quad k_i = \sqrt{3\mu_a\mu_s'}.$$

This leads eq. (1) to the following expression:

$$U_{rec, pw}(\omega_x, \omega_y, z_3 = z_2) = \exp(-z_2 k_i) \iiint \left[\frac{3\mu_s' \delta\mu_a}{\sqrt{\omega_x^2 + \omega_y^2 + 3\mu_a\mu_s'}} + \frac{\sqrt{3\mu_a\mu_s'} \delta\mu_s'}{(\mu_s' + \delta\mu_s')} \right] \times \exp[i(\omega_x x' + \omega_y y')] dx' dy' dz'. \quad (2)$$

Assuming the tumor to be in cubic shape and homogeneous, then eq. (2) can be further simplified as

$$U_{rec, pw}(\omega_x, \omega_y, z_3 = z_2) = 2 \exp(-z_2 \sqrt{3\mu_a\mu_s'}) \frac{\sin(\frac{\omega_x a}{2})}{\omega_x} \frac{\sin(\frac{\omega_y a}{2})}{\omega_y} a \times \left[\frac{3\mu_s' \delta\mu_a}{\sqrt{\omega_x^2 + \omega_y^2 + 3\mu_a\mu_s'}} + \frac{\sqrt{3\mu_a\mu_s'} \delta\mu_s'}{(\mu_s' + \delta\mu_s')} \right], \quad (3)$$

where a is the dimension of the tumor. Eq. (3) is 2-D Fourier transform of the backpropagated scattered wave at the plane, $z=z_2$, containing the tumor center in z direction, $U_{rec}(\omega_x, \omega_y, z_2)$. By using non-linear Marquardt fitting method¹³, we can obtain the tumor size, a , and optical properties of the tumor, i.e., μ_a and μ_s' .

D 2.2 Fitting Results

Based on the algorithm mentioned above, we can Fourier transform the scattered wave into spatial frequency domain, and then obtain the best fitted parameters, a , μ_a , and μ_s' , for tumor characterization. Figure 6 shows an example of such a fitting curve with the solid curve being the best fit to the experimental data.

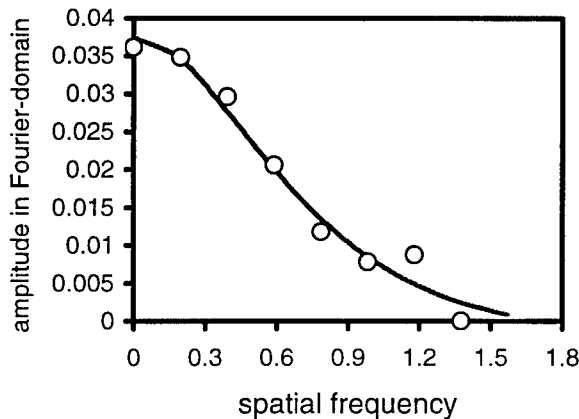


Figure 6. An example of fitting theory (eq. 3) to the experimental data (open circles) in the Fourier spatial frequency domain.

However, the study shows that the initial guess for the fitting procedure is very crucial in this non-linear fitting process. It can lead to large errors if the initial guess is far from the expected value, as shown in Table 1. This may result from an intrinsic issue of using DC light, as discussed in Refs. 10 and 11. If this is true, a MHz frequency-domain system seems necessary if one desires to quantify the tumor. Further study and search for solutions, such as using multiple wavelengths, are underway. However, if 3D localization and imaging is the primary goal, then the DC approach is adequate enough to use.

Table 1. Error Comparison between a Good and Bad Initial Guess

	With a good initial guess	With a bad initial guess
a	10%	20%
$\delta\mu_a$	<10%	50%
$\delta\mu_s'$	<10%	50%

For specific aim 3): to assist the AFRL collaborator in conducting laboratory tests for rapid imaging of airplanes through clouds and in studying the conditions to optimize the reconstruction algorithm based on the laboratory data.

D 3.1 Laboratory Models for Imaging Airplanes through Clouds

We imbedded an airplane model, shown in Figure 7, in a tissue phantom with transverse dimensions of 25 cm and 10 cm, a depth of 5.5 cm, and absorption and scattering coefficients of 0.01 cm^{-1} and 18 cm^{-1} , respectively. These values resulted in an optical depth of 100. The airplane's fuselage was 7.5 cm in length. Our kHz laboratory setup was used to generate the data. A notable difference was the fact that the 780 nm laser diode, modulated at 20 kHz, was used to provide illumination. Because the modulation frequency was so low, only amplitude information was obtained, so the reconstruction process was the same as one used for breast tumor data. However, the laser diode was not expanded spatially prior to entering the medium,

so the illumination was a point. Because light decays so quickly in the transverse dimension relative to the transverse extent of the airplane model, we took four sets of data before reconstructing an image in order to adequately illuminate all parts of the airplane. For each set of data, the laser light spot was moved to a new position. The four positions of the laser diode were as follows: centered on the forward portion of the fuselage, centered on the aft portion of the fuselage, centered on the left wing, and centered on the right wing. The four datasets were added together and then the backpropagation algorithm was implemented on this combined image.

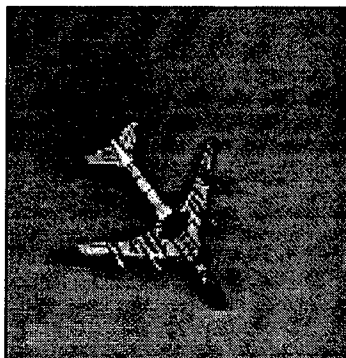


Figure 7. Airplane models used for laboratory data collection.

D 3.2 Results

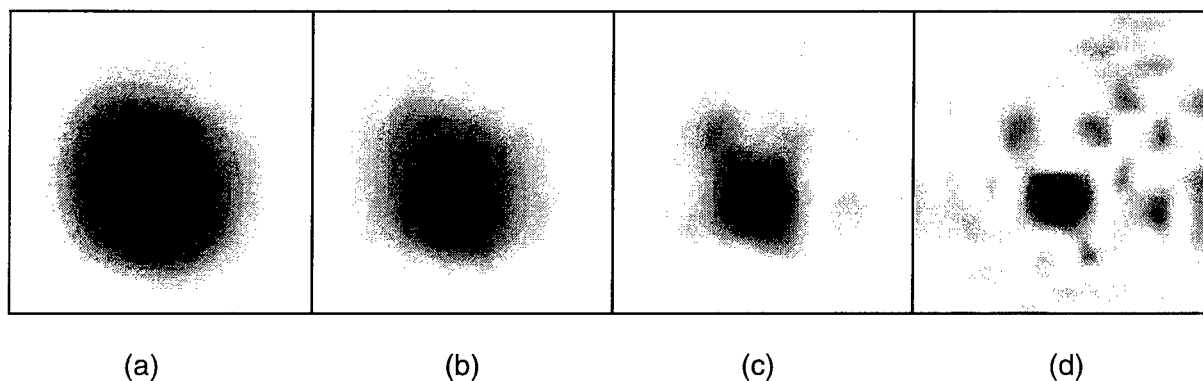


Figure 8. Reconstructed images of the airplane model shown in Figure 2(b) at several depths in the turbid medium using laboratory data: (a) in the detection plane, (2) at an optical depth of 22, (3) at an optical depth of 43 (the actual location of the airplane), and (4) at an optical depth of 65.

Our image reconstructions are shown above in Figure 8. In Figure 8(a) we had the reconstruction of the scattered wave in the detection plane, for which no backpropagation has occurred. The reconstruction was basically an unresolved blur of light. The lack of detail in the detector-plane reconstruction for laboratory data is probably due to the imperfect homogeneous wave subtraction. In Figure 8(b) we show the image reconstruction in the plane halfway between the detection plane and the plane that the airplane resides in. We can start to see elongations in the image that correspond to the wings and the tail, but the reconstruction is still essentially a single blur spot. Next, in Figure 8(c) we see the reconstruction of the airplane in the plane where it resides. Here we can clearly see the wings and the tail along with an indication of the forward portion of the fuselage. Finally, in Figure 8(d) we show a reconstruction a distance beyond the location of the airplane. As for the simulated data, we see

that the reconstruction has dissolved into a collection of points of light. Thus, the results in Figure 8 show that the backpropagation algorithm was successful at reconstructing image detail from data that had no detail. In addition, the image that has the best image quality is the image that was reconstructed using a backpropagation filter that corresponds to the true depth of the object. This shows that, even with laboratory data, we can locate an object in 3D using only measured CW data and information about the turbid medium in which the object resides.

D 3.3 Discussion

We have learned that a finer pixel grid does not improve significantly the resolution or quality of the reconstructed images. This is because a low-pass filter in the spatial-frequency domain has been used in the algorithm to achieve stability. This low-pass filter cuts off high spatial frequency components and makes images with finer pixels equivalent to images with larger pixels. According to our previous and current studies¹², choosing both the right filter and optimum cutoff spatial frequencies is very crucial to accurate 3D tumor localization, particularly for localization in the z-axis direction. The cutoff spatial frequency is inversely proportional with the spatial resolution. A too high cutoff frequency would generate significant noise in the reconstructed image, whereas a too low cutoff frequency would result in an image with very low resolution. Thus, an optimum cutoff spatial frequency should be chosen such that it is low enough to allow us to achieve a good stability for backpropagation but high enough to give good spatial resolution. According to the forward problem analysis⁹, we determined our cutoff spatial frequency at the frequency where the Fourier transform of the scattered DPDW's becomes dominated by noise. Further studies and understanding of resolution limits are underway.

The current backpropagation algorithm, like some other reconstruction algorithms used in optical tomography, requires having accurate optical properties of the background medium. In our previous experiments, we made and measured identical background phantoms to obtain scattered DPDWs. However, in clinical situations, the breast under tests can be only either "tumor-free" or "tumor-containing". There exists no "homogeneous" background available for tumor detection. Thus, we need to eliminate the measurement for the homogenous sample in the future; instead, we either refer to pre-known optical parameters of healthy human breasts or extrapolate mean optical properties of a tumor-containing phantom/breast from its measurement. The latter step is possible since the amplitude of the scattered DPDWs is much smaller than that of the primary, unscattered DPDWs.

Our future work includes to explore the possibility to obtain the background information from single measurement, to modify and improve the fitting algorithm to optimize the fitted tumor properties, and to test whether multiple views are necessary to improve the accuracy for tumor characterization.

E. Benefit to Both the PI and Air Force Research Laboratory

Both parties in this collaboration have benefited from the joined study. Benefits to the PI included understanding how the new theory and algorithm can be used to detect and characterize breast cancer using nonionizing radiation. More specifically, the university as well as the medical community can benefit if the proposed work leads to cheaper, safer, and more effective methods for detecting breast cancer. Benefits to Air Force Research Laboratory include understanding the role that scattering media such as clouds and smoke play in interfering with the capabilities of optical surveillance systems. This can lead to methods for mitigating such deleterious effects as well as providing new insight into how to build optical systems which have the capability to see through turbid media in order to meet Air Force needs that cannot be accomplished now by existing optical systems.

F. Publications and Presentations Resulting from this Collaboration

1. **Hanli Liu**, Charles L. Matson, and Kelly Lau, "Experimental Validation of a Backpropagation Algorithm for Three-dimensional Breast Tumor Localization," IEEE J. of Selected Topics in Quantum Electronics: Lasers in Medicine and Biology, **5**(4), 1049-1057 (1999).
2. Charles L. Matson and **Hanli Liu**, "Backpropagation in turbid media," Journal of the Optical Society of America A, **16**(6), 1254-1265 (1999).
3. Charles L. Matson and **Hanli Liu**, "Analysis of the Forward Problem with Diffuse Photon Density Waves in Turbid Media Using a Diffraction Tomographic Model," Journal of the Optical Society of America A, **16**(3), 455-466 (1999).
4. **Hanli Liu** and C. L. Matson, "3-D Localization and Characterization of Breast Tumors Using Diffraction Tomography," SPIE Biomedical Optics'99, San Jose, CA, 23-29 January 1999.
5. **Hanli Liu**, R. R. Mapakshi, K. Lau, and C. L. Matson, "3-D Tumor Localization in Breast Phantoms," 16th Annual Houston Conference on Biomedical Engineering Research, Univ. of Houston, Houston, TX, April 2-3, 1998.
6. **Hanli Liu**, Kelly Lau, and Charles L. Matson "Experimental Validation of an Algorithm for 3-Dimensional Tumor Localization in Turbid Media with a 2-Dimensional Frequency-Domain Measurement," OSA Proc. on Advances in Optical Imaging and Photon Migration **21**, 171-173 (1998).

G. References

- ¹ M. A. O'Leary, D. A. Boas, B. Chance, and A. G. Yodh, "Simultaneous Scattering and Absorption Images of Heterogeneous Media Using Diffusive Waves within the Rytov Approximation," SPIE, **2389**, p.328-339 (1995).
- ² Brain W. Pogue, Michael S. Patterson, and Tom J. Farrell, "Forward and Inverse Calculations for 3-D Frequency-Domain Diffuse Optical Tomography," SPIE, **2389**, p.328-339 (1995).
- ³ M. S. Patterson, B. Chance, and B. C. Wilson, "Time resolved reflectance and transmittance for the non-invasive measurement of tissue optical properties," Appl. Opt. **28**, 2331-2336 (1989).
- ⁴ J. B. Fishkin and E. Gratton, "Propagation of photon-density waves in strongly scattering media containing an absorbing semi-infinite plane bounded by a straight edge," J. Opt. Soc. Am. A **10**, 127-140 (1993).
- ⁵ C. L. Matson, N. Clark, L. McMackin, and J. S. Fender, "Three-dimensional tumor localization in thick tissue with the use of diffuse photon-density waves," Appl. Opt. **36**, 214-220 (1997).
- ⁶ C.L. Matson, "A diffraction tomographic model of the forward problem using diffuse photon density waves," Optics Express **1**, 6-11 (1997).
- ⁷ M. Firbank, M. Hiraoka, and D. T. Delpy, "Development of a stable and reproducible tissue equivalent phantom for use in infrared spectroscopy and imaging," SPIE, **1888**, 264-274 (1993).

⁸ See the PMI (Photon Migration Imaging) Code Home Page: <http://www.osa.org/homes/BIOOPTIC/Resource/softwar.htm>

⁹ Charles L. Matson and Hanli Liu "Analysis of the forward problem with diffuse photon density waves in turbid media using a diffraction tomographic model," J. of Opt. Soc. Amer. A **16**, 455-466 (1999).

¹⁰ Simon R. Arridge and William R. B. Lionheart, "Nonuniqueness in diffusion-based optical tomography," Opt. Lett. **23**, 882-884 (1998).

¹¹ J. C. Ye, R. P. Millane, K. J. Webb, and T. J. Downar, "Importance of the ∇D term in frequency-resolved optical diffusion imaging," Opt. Lett. **23**, 1423-1425 (1998).

¹² Charles L. Matson and Hanli Liu, "Backpropagation in turbid media," J. of Opt. Soc. Amer. A **16**(6), 1254-1265 (1999).

¹³ Philip R. Bevington, Data Reduction and Error Analysis for the Physical Sciences, (McGraw-Hill Book Company, New York, 1969).

Associate did not participate in the program.

OPTIMIZATION AND ANALYSIS OF A WAVERIDER VEHICLE FOR GLOBAL SPACEPLANE TRAJECTORIES

Eric Paulson
Graduate Research Assistant
Department of Aerospace Engineering Sciences

Prof. Brian Argrow
Faculty Advisor
Department of Aerospace Engineering Sciences

University of Colorado at Boulder
Campus Box 429
Boulder, Colorado 80309-0429

Final Report for:
Summer Research Extension Program
Phillips Laboratory-Edwards AFB

Sponsored by:
Air Force Office of Scientific Research
Bolling Air Force Base, DC

and

Phillips Laboratory-Edwards AFB

December 1998

OPTIMIZATION AND ANALYSIS OF A WAVERIDER VEHICLE FOR GLOBAL SPACEPLANE TRAJECTORIES

Eric Paulson
Graduate Research Assistant
Department of Aerospace Engineering Sciences
University of Colorado at Boulder

Abstract

A study of the performance of an osculating cones derived waverider was conducted, comparing its performance to that of the Boeing Reusable Aero Space Vehicle (RASV) for a skipping trajectory once around the world. The purpose of the study was to evaluate the design with tools in use at the Propulsion Analysis Branch of the Propulsion Directorate at the Air Force Research Laboratory-Edwards Air Force Base for the 1997 Graduate Student Summer Research Program. Preliminary trajectory simulations indicate that the waverider's higher aerodynamic efficiency will allow a smaller scale vehicle than RASV to achieve the skipping mission constraints.

OPTIMIZATION AND ANALYSIS OF A WAVERIDER VEHICLE FOR GLOBAL SPACEPLANE TRAJECTORIES

Introduction

Recent interest in Access to Space has renewed research in ways to get payloads to orbit reliably while reducing the cost of doing so. One such method is to make the payload delivery vehicle suborbital and reusable, with a popup stage to take the payload to its final orbit while the delivery vehicle returns to base. This requires less structure on the delivery vehicle since deorbit capabilities are no longer necessary. Another variation on this idea is using a skipping trajectory upon reentry, to extend the range of the vehicle by skipping into the upper atmosphere, reducing drag and radiating heat into space during the peaks of these skips.

A study of a winged body, the Boeing RASV, was made during the AFOSR 1997 Graduate Summer Research Program at the Analysis Branch of the AFRL Propulsion Directorate at Edwards AFB, CA. In the summer study, a trajectory using the RASV aerodynamic data was optimized to maximize the payload weight carried on a polar route from Vandenberg AFB south, reaching a popup separation condition of 340,000 ft altitude, 24,500 fps velocity, and zero degrees relative flight path angle at main engine cutoff. The vehicle then had to return to Edwards AFB for landing with the payload still onboard, simulating the limiting case for the maximum allowable payload. The premise of this study was that a waverider vehicle, designed using the method of osculating cones,¹ could better optimize the mission parameters, since waveriders are vehicles designed for maximum aerodynamic efficiency. The purpose of this study was to:

1. Obtain waverider configurations using the Waverider Interactive Parameter Adjustment Routine (WIPAR) developed at the University of Colorado by Dr. Kenneth Center.² WIPAR is a workstation tool that designs and optimizes osculating cones derived waveriders
2. Evaluate the vehicle configurations at off-design points to provide aerodynamic data necessary for the trajectory optimization code.
3. Optimize the vehicle's trajectories to maximize payload, while meeting the popup launch constraints from the study at Edwards AFB in 1997, mentioned above.
4. Compare the performances of the waverider vehicles to that of the winged body RASV.

5. Use the results of the comparison to further refine the vehicle configurations, maximizing performance in the skipping trajectories studied.
6. Report the findings of the study.

To date, the following has been accomplished:

1. Several possible candidate configurations have been examined. The vehicles have been designed using WIPAR. One particular classic waverider shape, nearly cone-derived with a freestream upper surface, was selected to be the test case to test the remaining steps in the evaluation process.
2. The vehicle's off-design aerodynamics were evaluated using a CFD code, CFL3D, obtained from NASA-Langley. The vehicle's size and weights were calculated using a spreadsheet setup by the author, using assumptions elaborated later.
3. The data was input into the Program to Optimize Simulated Trajectories (POST) for the evaluation of the vehicle's performance for the skipping trajectory studied during the summer of 1997 at Edwards AFB.
4. The trajectory results have been compared to RASV's results yielding some interesting results to date.
5. An evaluation of the results points toward vehicle changes that would enhance the waverider's performance.
6. The final report is hereby submitted with these preliminary results and suggestions for further study.

Methods

A number of parts are required to evaluate a vehicle design. Since the focus of this study was the aerodynamics of the configurations, several simplifications were required for the ancillary matters of vehicle's structural and thermal protection system (TPS) weights, propulsion system size and mass, and usability of the vehicle's available volume for tankage. As for structural and TPS weights, the original vehicle studied was the Boeing RASV from the 1980's, shown in figures 1-3. This vehicle was designed

with integral fuel tanks, which combine the support structure of the vehicle, the thermal protection, and the propellant tankage into a single interrelated system. A study funded by the Air Force, Have Region, validated the overall concept and the mass assumptions, to within 3% of such a system. The original RASV design used this concept, therefore the waverider vehicles designed were assumed to use the same concept. Since the original study was classified, an assumption of the weight of such a system was made of 4.5 lbs. per square foot of vehicle wetted area.

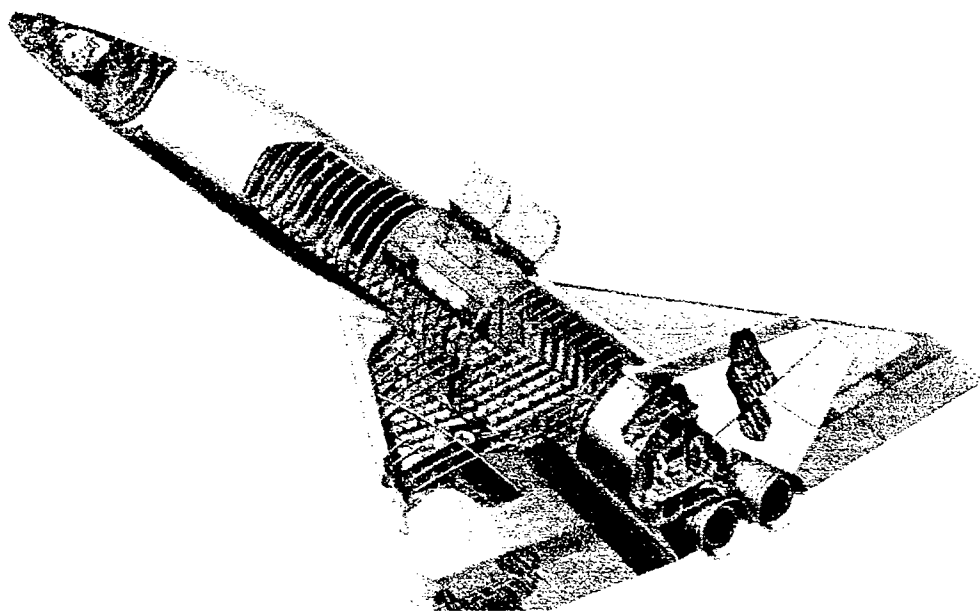


Figure 1. Boeing RASV configuration cutaway.

Boeing assumed, based on historical data, that a majority of the time and money in developing a new rocket system is spent in the engine development. Therefore by using an already developed engine (SSME) with only evolutionary changes to improve deep throttling characteristics, the overall vehicle design timetable would be shortened. The design also assumed horizontal launch, with a sled assist up to 600 feet-per-second (fps) at liftoff to partially negate the effects of having to size the wings for takeoff, rather than for the lighter landing condition.

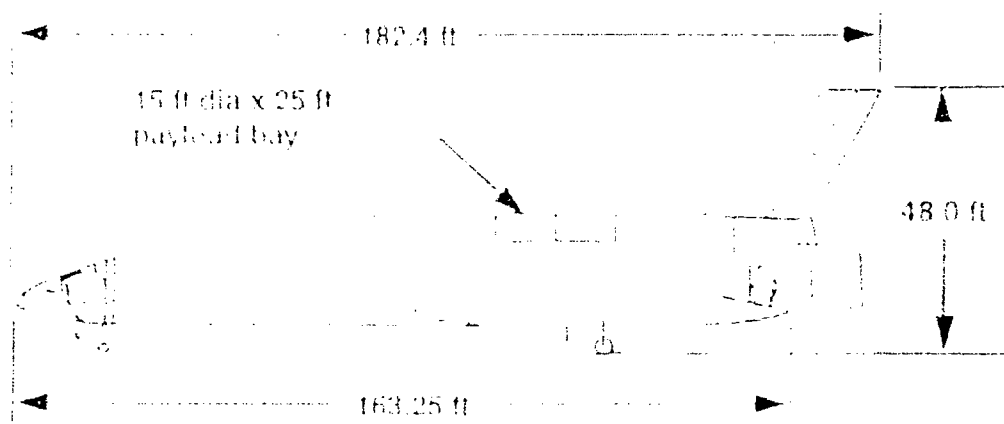


Figure 2. RASV side view.

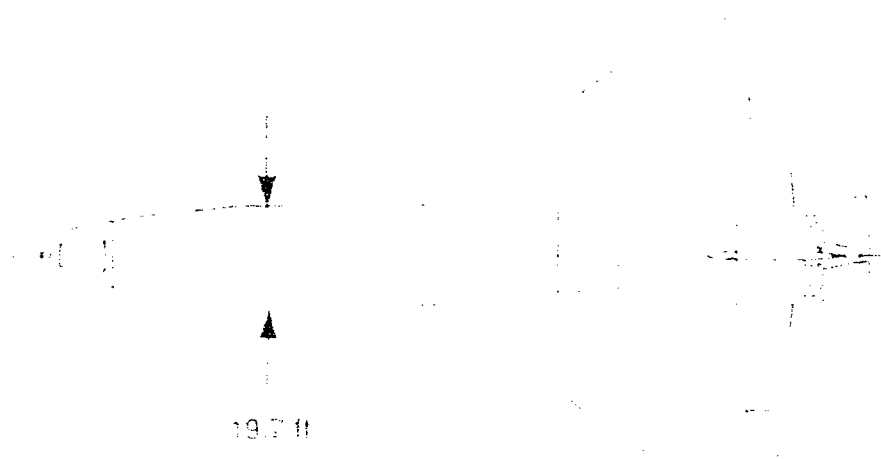


Figure 3. RASV top view.

Therefore this study assumes the use of the same SSME-derived engine package for the waverider vehicle's propulsion. The two advanced SSME's with extendible nozzles increase the engine efficiency of the engines above sea level, with the weight of the engines assumed to be the same as the current SSME engine. Additionally, the landing gear weight of the vehicles was assumed to be a percentage of the vehicle's maximum landing weight. The weight assumptions are summarized in table 1.

Weighting & Scaling Parameters

Config Name	M-10 Freestream WR12GEXP	
Reference Length (ft)	180	180
Max Volume (ft ³)	75233	72900
Planform Area (ft ²)	10552	11988
Wetted Area (ft ²)	21568	26572
Tank Volume (ft ³)	52663	51030
Max Propellant Weight	1158585	1122660
Engine Weight (lb)	14960	14960
Engine Volume (ft ³)	88	88
Weight:TPS+Structure	97056	119574
Weight:Landing Gear	4110	4786
Liftoff Weight (lb)	1274711	1261980
Weight Payload	25000	25000

Notes:	10 degree cone angle	7 degree cone angle
---------------	-------------------------	------------------------

Assumptions:

Wgt.:Struct.+TPS (lb/ft ² wetted area)	4.5
Wgt.:Landing Gear (% Landing Wgt.)	3
Propellant % (of Max Volume)	70

TABLE 1. Scale and mass assumptions.

The payload weights are the final optimized values achieved during the RASV study. The engine weight and volume is derived from published Space Shuttle reference data. The usability of a vehicle's volume for propellant tanks depends on the type of tanks and the vehicle shape.

Several assumptions were made in the CFD modeling. The Reynolds number for the full-scale vehicle modeled was set to 10 million. This was admittedly arbitrary considering the wide range of flows encountered during a full skipping trajectory, however, Reynolds number independence of aerodynamic coefficients has been discussed in other references. The grid size was set at (idim,jdim,kdim) = 41 x 61 x 51 for the half body modeled. A study of grid fineness effects on convergence is planned for a later date. The criteria for convergence was reduction of the total residual to $< 10^{-8}$, with visible convergence of the C_L and C_D . The base pressure was assumed to be equal to freestream pressure, giving base drag a zero

The author used two waverider designs in this stage of the study. The first was a Mach 12 waverider developed and studied at the German DLR.³ The configuration was created using WIPAR, and has been evaluated numerically and in the wind tunnel. It has mainly been studied for use in a two-stage-to-orbit (TSTO) concept after the model of the Sanger aerospace plane.⁴ This body has a classic waverider planform, with an upper surface that concentrates the usable volume along the vehicle's centerline. The vehicle is illustrated in figure 4. As one moves spanwise away from the center body, the wing area is an expansion surface to minimize the base drag associated with a boattail vehicle. This also creates an area at the wing's trailing edge suitable for control devices. This makes for a vehicle with lower usable volume than a conventional winged body, but a structurally realizable shape.

The second configuration is a Mach 10 waverider with a freestream upper surface, shown in figure 5. This geometry is nearly a cone-derived shape, accomplished with the WIPAR code. This waverider shape was chosen as one of the first configurations compared to RASV for a couple of reasons. First it is a much-studied shape with a large body of work published examining the various aerodynamic characteristics of such shapes. Second, the simple shape of the body makes assumptions about scaling and weight fairly easy to modify.

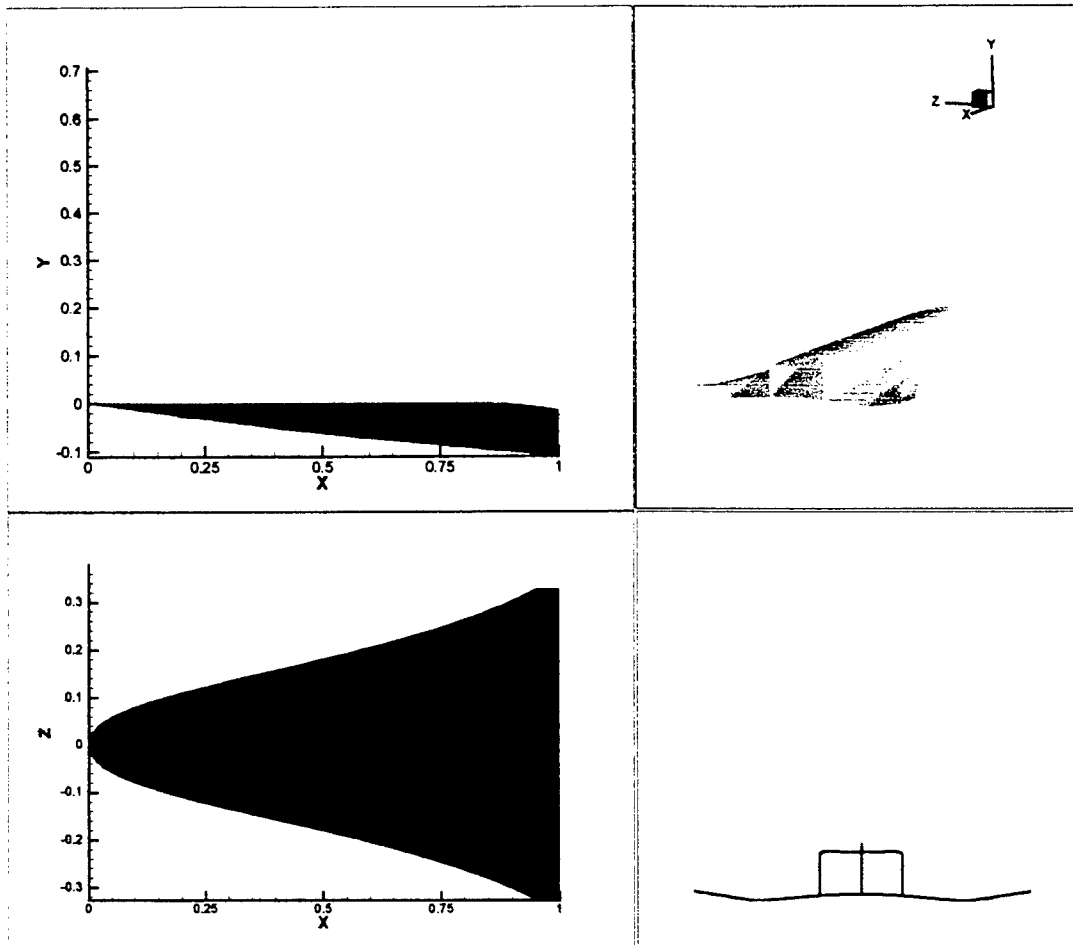


Figure 4. DLR Waverider WR12GEXP

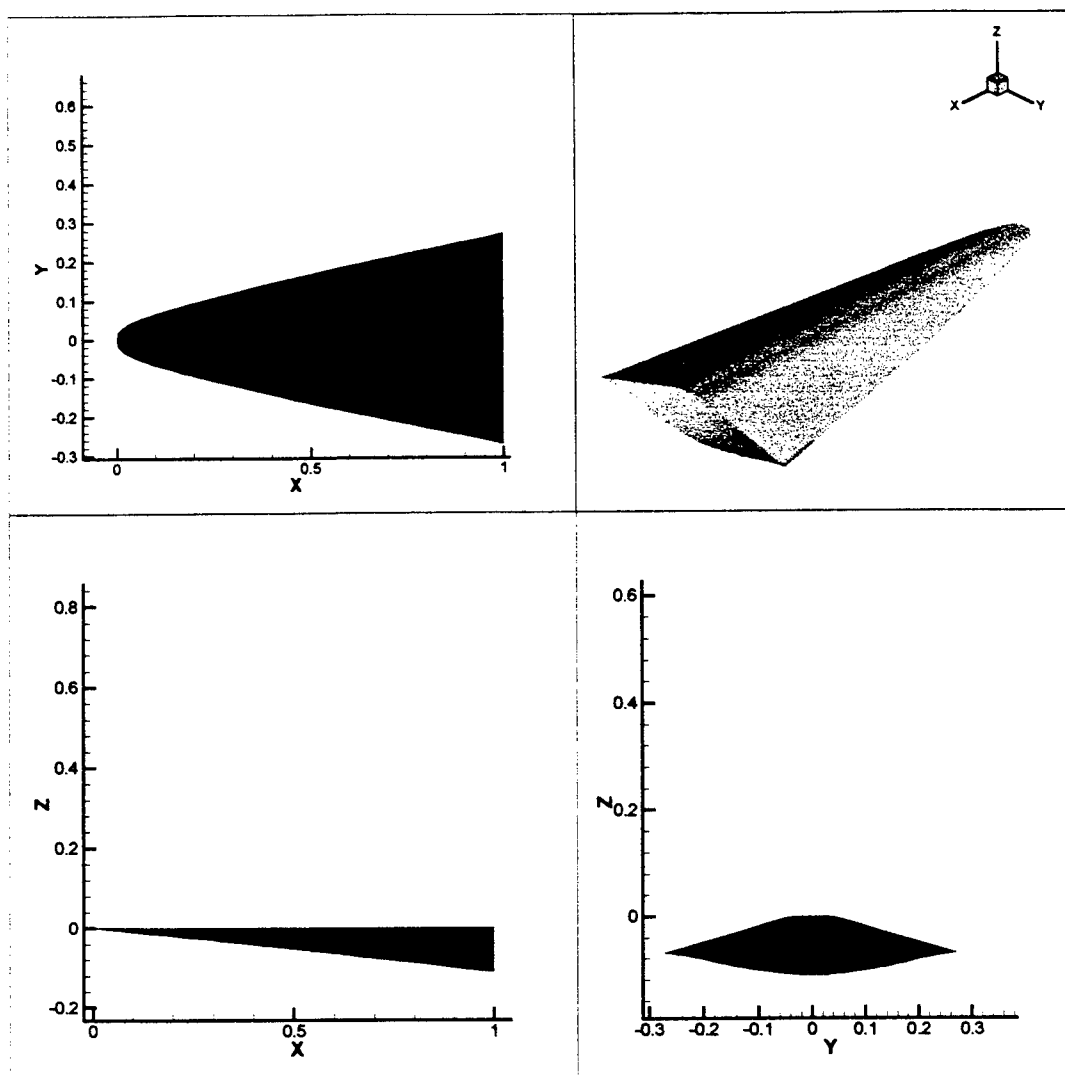


Figure 5. Mach 10 Freestream Upper Surface Waverider

Tools

Several tools were required for the design and evaluation of the considered. The vehicle design starts with the use of the WIPAR design code. This code allows the design and modification of Method Of Osculating Cones (MOOC) waveriders, and evaluates the waverider's geometric and on-design aerodynamic characteristics. WIPAR outputs a vehicle surface grid file in PLOT3D format. The grids for use in the CFD code were generated using a grid generator code, HYGRID, written by Kevin Jones at the University of

Colorado. HYGRID was modified to accommodate sharp leading edge vehicles such as waveriders.

Tecplot⁵ was used to visually check the grids, as well as examine the flow solutions.

The CFD code used to evaluate the configuration aerodynamics was CFL3D, Version 5.0⁶. CFL3D is a NASA-Langley Reynolds-Averaged thin-layer Navier-Stokes flow solver for structured grids. CFL3D uses upwind biasing for the convective and pressure terms, and central-differencing for the shear stress and heat transfer terms. Several turbulence models are available, though in this study only the Baldwin-Lomax algebraic model was utilized. A majority of the CFD problems were run using a Silicon Graphics Octane workstation with dual R10000 processors, at the AFRL-Edwards AFB. After producing the off-design aerodynamic data, the configuration was evaluated using POST-3D, Program to Optimize Simulated Trajectories⁷.

Results

CFL3D and Tecplot provide a great deal of information about the flowfield of configurations such as the two studied. The location of the shock wave developed by the vehicle, streamlines on the vehicle surface, and pressure contours along the body can be extracted from the solution file generated by the CFD code. With these analysis tools, general features of the flow can be examined for their importance in the overall design. Figures 6 & 7 illustrate the flowfield data from the Mach 10 Freestream waverider.

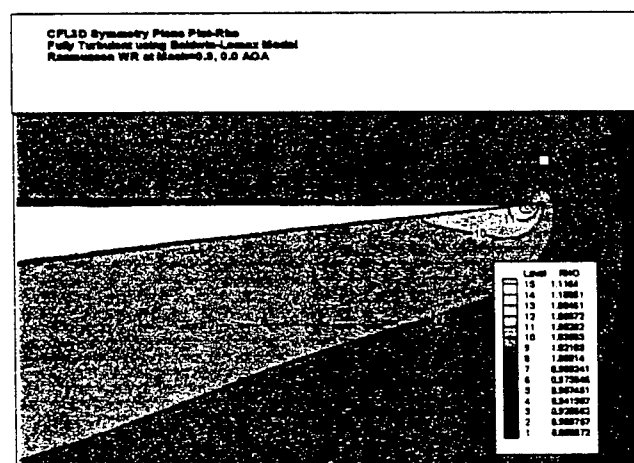


Figure 6. Symmetry Plane Nondimensional Density for Mach 10 Freestream WR.

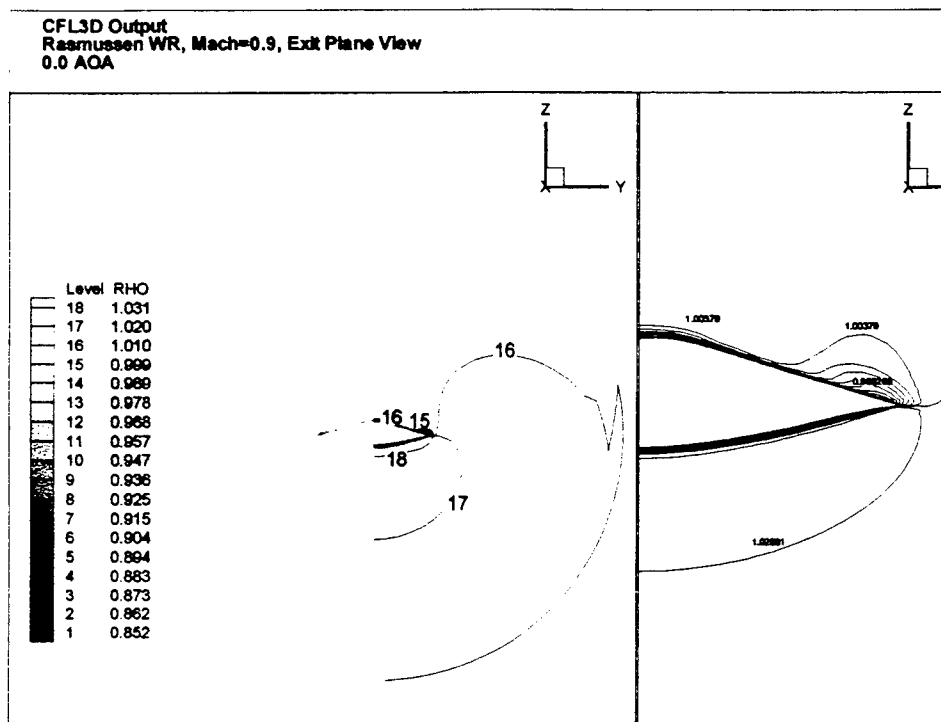


Figure 7. Exit Plane $\text{Rho}/\text{Rho}_{\text{inf}}$ for Mach 10 Freestream WR.

One application of the flowfield characteristics that can be exploited, is modification of a configuration's planform. By modifying the waverider's planform away from the classic planform to a delta wing planform, vortices are created in subsonic and transonic flight, even for low angles of attack. These improve the vehicle's lift coefficient by lowering the pressure on the upper surface, and shift the vehicle's center of pressure. This shift varies throughout the subsonic to hypersonic flight regime, limiting the degree to which the planform can be modified to delta wing planform, without incurring excessive trim losses.⁸

An interesting trend developed from the POST runs conducted with the DLR vehicle configuration and to a lesser degree the Mach 10 Freestream waverider. Both the DLR WR12GEXP and the WR10 Freestream waverider were initially sized as 180-foot vehicles in length, about the length of the RASV. Using the 25,000-lb. payload weight maximized for the RASV, the WR12GEXP achieved orbit velocity. As the

starting solutions for the angle-of-attack were modified to force the simulation to achieve the popup launch constraints mentioned earlier, the trajectory code created a pre-popup skip into the atmosphere shown in figure 8, wasting energy before the popup stage. The control events of the trajectory code were changed several times to attempt to modify the problem to achieve the popup launch constraints, with no success. Only when the payload weight was increased 1.5 times, could a trajectory somewhat resembling that evaluated with RASV be achieved. This leads one to the conclusion that the waverider configurations, as scaled, are oversized for the mission.

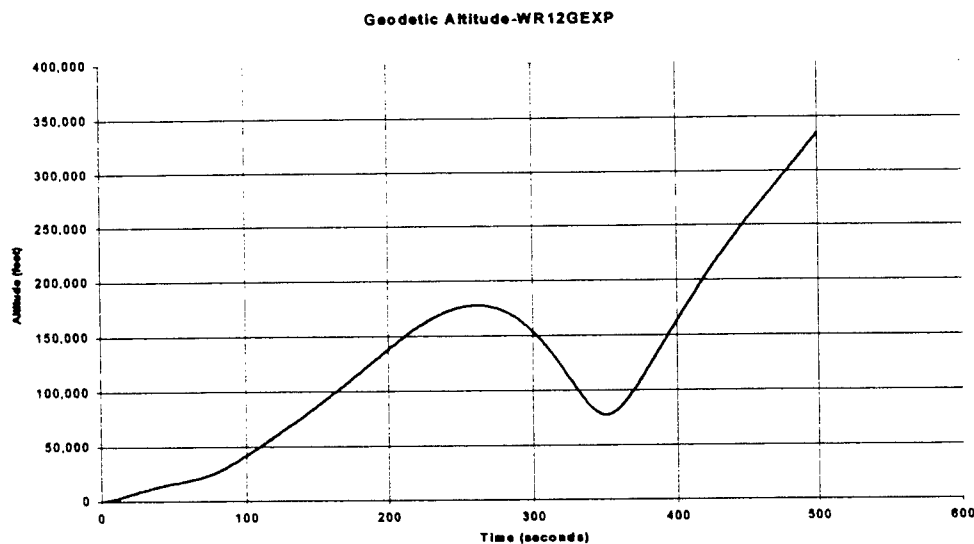


Figure 8. Waverider pre-popup skip in POST trajectory simulations.

The problem has proven extremely sensitive to the angles-of-attack during the first 100 seconds of the trajectory. After this time, the vehicle is out of the sensible atmosphere, in a predominately ballistic trajectory, for the launch phase of the trajectory. Because the vehicle was oversized, the latter trajectory phase, the skipping reentry, was not simulated. However, it seems reasonable again to assume that the waverider in this phase would be oversized, yielding larger excursions than are necessary to reach the final landing site. The current plan is to modify the configuration scaling until the popup launch constraints can be met.

Conclusions

A great deal of work remains to be accomplished. The next logical step of the study is to modify the vehicle's sizing assumptions until a smaller vehicle that accomplishes the mission's constraints is achieved, allowing a direct comparison between RASV and the waverider configurations. Time precluded the completion of a resizing iteration before this report was due.

For the tool set to be used to evaluate several configurations for a given mission, the off-design data must be evaluated using a method other than full CFD simulations. Though the individual CFD solutions may be run fairly quickly on powerful workstations, the steps necessary to setup the off-design problems remain a time consuming process. Since a wide range of flight conditions must be simulated, from subsonic to hypersonic, multiple approximation methods must be incorporated to get reasonable aerodynamic coefficients. This first step using CFD was necessary, however, to get a database from which to evaluate future approximation's relative accuracy.

Several configurations should then be evaluated using the streamlined procedure, to quantify the effect of varying parameters, such as the degree of progression from gothic planform to delta wing planform. Additionally, sensitivity analyses should be performed on optimized configurations to get a feeling for the waverider weight and sizing assumptions.

Acknowledgements

The author would like to acknowledge the following organizations and people for their contributions to this effort. The U. S. Air Force Office of Scientific Research is acknowledged for their financial support of this of this research grant. Dr. Richard Seebass provided technical advice and support. Dr. Ray Moszee, Terry Galati, and Francis McDougall of the AFRL Propulsion Directorate-Analysis Branch provided technical guidance and support for the research, as well as computer time. The University of Colorado Aerospace Engineering Department provided financial support, and research facilities. Dr. Ken Center and Rick Graves provided helpful technical advice and information.

References

- ¹ Sobieczky, H., Dougherty, F. C., and Jones, K. D., "Hypersonic Waverider Design for Given Shock Waves," *Proceedings of the First International Hypersonic Waverider Symposium*, University of Maryland, College Park, MD, 1990.
- ² Center, K. B., "Interactive Waverider Design and Optimization," Ph.D. Thesis, Univ. of Colorado, Boulder, CO, 1993.
- ³ Eggers, T., Strohmeyer, D., Nickel, H., and Radespiel, R., "Aerodynamic Off-Design Behavior of Integrated Waveriders from Take-Off up to Hypersonic Flight," AIAA Paper 95-6091, April 1995.
- ⁴ Weingartner, S., "SANGER-The Reference Concept of the German Hypersonic Technology Program," AIAA Paper 93-5161, Dec. 1993.
- ⁵ Amtec Engineering, Inc., *Tecplot Version 7 User's Manual*, Amtec Engineering Inc., Bellevue, WA, 1996.
- ⁶ Krist, S., Biedron, R., Rumsey, C., *CFL3D Version 5.0 User's Manual*, NASA Langley Research Center, Hampton, VA, Sept. 1997.
- ⁷ Brauer, G. L., et al., *Program to Optimize Simulated Trajectories (POST), VOL. II*, Martin Marietta Corp., Denver, CO, 1989.
- ⁸ Strohmeyer, D., Eggers, T., and Haupt, M., "Waverider Aerodynamics and Preliminary Design for Two-Stage-to-Orbit Missions, Part 1," *Journal of Spacecraft and Rockets*, Vol. 35, No. 4, 1998, pp. 450-458.

BOUNDARY CONDITIONS FOR THE AIR FORCE COMPUTER SIMULATION PROGRAM,
MACH

Kenny F. Stephens II
Doctoral Candidate
Department of Physics

University of North Texas
Denton, TX 76203

Final Report for:
Summer Research Extension Program
Phillips Laboratory

Sponsored by:
Air Force Office of Scientific Research
Bolling Air Force Base, Washington DC
and
University of North Texas
Denton, TX

February 1999

BOUNDARY CONDITIONS FOR THE AIR FORCE COMPUTER SIMULATION PROGRAM,
MACH

Kenny F. Stephens II
Doctoral Candidate
Department of Physics
University of North Texas

Abstract

An extended set of boundary conditions for the interface between a plasma and a material surface have been developed for the Air Force magneto-hydrodynamic simulation program, MACH. The original model (see Ref. [1]) describes the plasma sheath, using a fully-kinetic self-consistent theory, when space-charge saturation is present and the material surface is electrically floating. The extension allows a net electric current to the surface, thus permitting anode, cathode and electrically floating plasma-facing surfaces to be modelled. Considering a planar source of plasma ions and electrons, as well as secondary electrons, the phase-space distribution functions are evaluated for a monotonically decreasing electric potential profile and a single minimum profile, with a negatively biased surface. With the distribution functions, the particle density and flux are found for each species. Boundary conditions are then imposed on these quantities to develop a system of nonlinear equations describing the electric potential at the sheath/presheath interface and the potential at the surface, as well as the potential minimum. Approximate expressions are then found for these quantities.

BOUNDARY CONDITIONS FOR THE AIR FORCE COMPUTER SIMULATION PROGRAM, MACH

Kenny F. Stephens II

I Introduction

Whenever a plasma is in contact with a solid surface, a plasma sheath develops near the surface to slow the loss of plasma electrons to the solid. The sheath is a region of high electric field that greatly affects particle and energy fluxes between the bulk plasma and the surface. Being only a few Debye lengths in extent, the sheath is not accurately considered in many plasma simulation programs. The present work is a review of current research to develop particle and energy transport relations suitable for use in plasma simulation codes, such as MACH.[2]

This work is an extension of a fully kinetic approach to describing the sheath.[1] The previous work considered an electrically floating surface, while including the effects of secondary or thermionic emission from the plasma-facing surface. The extension allows for a current carrying sheath. Using the planar-source model, the bulk plasma is replaced by a planar source of plasma ions and electrons, described by half-maxwellian distributions. Constructing the phase-space distribution function for three particle species (plasma ions, plasma electrons and surface-emitted electrons), boundary conditions are imposed that lead to a system of nonlinear equations governing the sheath and presheath potentials. These nonlinear equations are replaced by approximations, accurate within 7% of the numerically determined results, over a range of plasma parameters.

Two electric potential profiles are examined. These are shown in Fig. 1. The first, Fig. 1(a), monotonically decreases from the edge plasma, x_p . This profile occurs for no space-charge saturation and small electron emission coefficients. The electron emission coefficient, δ , is defined as the ratio of surface-emitted electron flux to incident electron flux. If δ exceeds a critical value, the potential is no longer monotonically decreasing. Rather, a minimum occurs within the sheath, as shown in Fig. 1(b). Note that both profiles illustrated in Fig. 1 consider plasma-facing surfaces that are

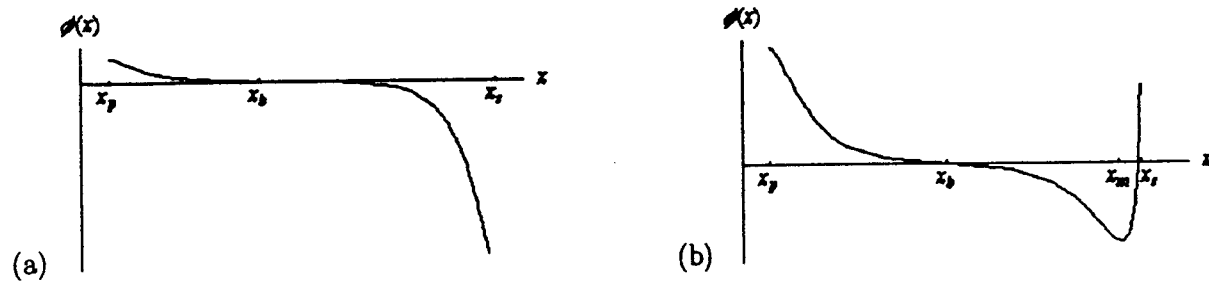


Figure 1: Possible electric potential profiles in the presheath and sheath: (a) monotonically decreasing potential with no space-charge saturation; and (b) single-minimum potential, negatively-biased surface, with space-charge saturation. These profiles correspond to a thermal hydrogen plasma adjacent to an anode surface: $\zeta = 1$, $\xi = \sqrt{1836}$, $\tau_\delta = 0.2$ and $\gamma_i = -0.01$. The electron emission coefficient is (a) $\delta = 0.2$ and (b) $\delta = 20$.

negatively biased with respect to the plasma. Ref. [1] found that extremely large values of δ are required for the surface to become positively biased. For this reason, only negatively biased surfaces are discussed. The equations for a positively biased surface are presented in order to determine the transition from a negative surface to a positive surface.

A review of the fully-kinetic sheath theory is presented in Sect. II. Detailed evaluation of the sheath and presheath potentials is given in Sect. III. The approximate expressions are provided in Sect. IV, followed by concluding remarks in Sect. V. Historical reviews of fully kinetic sheath theory can be found in Refs. [3] and [4]. The basis for the planar-source model is contained in Ref. [5].

II Theory Review

This section reviews the underlying theory presented in Ref. [1]. The electric potential profiles considered in the present work are shown in Fig. 1. For each profile, the phase-space distribution function (DF) for each species (plasma ions, plasma electrons and surface-emitted electrons) is derived by considering those regions in phase-space that are kinematically forbidden. For example, all plasma electrons with velocity $v_x > 0$ entering the electric potential of Fig. 1(a) are allowed. However, those with velocity $v_x < -\sqrt{2e[\phi(x) - \phi(x_s)]/T_{pe}}$ are forbidden since such electrons would

have to originate from the surface. Thus, the DF for plasma electrons, of charge $-e$ and mass m_e , in the electric potential of Fig. 1(a) is

$$f_e(x, v) = n_{pe} \left(\frac{\beta_e}{\pi} \right)^{3/2} e^{-\beta_e v^2 + e[\phi(x) - \phi(x_p)]/T_{pe}} \Theta \left(v_x + \sqrt{\frac{2e}{m_e}} [\phi(x) - \phi(x_s)] \right),$$

where $\Theta(x)$ is the Heaviside step function, n_{pe} and T_{pe} are the edge plasma electron density and temperature and $\beta_e = m_e/(2T_{pe})$. With the DF for each species, the particle density, $n = \int f d^3v$, and particle flux, $F = \int v_x f d^3v$, are determined. Boundary conditions are then applied to these quantities to yield a system of equations for the presheath and sheath potentials.

In constructing each system of equations, some variables always occur in certain combinations. Each of these combinations is replaced by a single parameter. The ion charge state, Z , always appears as a ratio with the normalized ion temperature, $\tau_i = T_{pi}/T_{pe}$, where T_{pi} is the edge plasma ion temperature. This ratio is represented by $\zeta \equiv Z/\tau_i$. Similarly, the ion-to-electron mass ratio, $\eta \equiv m_i/m_e$, also occurs as a ratio with τ_i ; thus $\xi \equiv \sqrt{\eta/\tau_i}$. Other parameters are the normalized surface-emitted electron temperature, $\tau_\delta \equiv T_{s\delta}/T_{pe}$, where $T_{s\delta}$ is the secondary electron temperature. The normalized current density is defined as

$$\gamma_i \equiv \frac{ZeF_i - e(F_e - F_\delta)}{Zen_{pi}/2\sqrt{\pi}\beta_i}, \quad (1)$$

where n_{pi} is the edge plasma ion density and $\beta_i = m_i/2T_{pi}$. Also, F_i and F_e are the plasma ion and electrons fluxes (taken positive for flux into the surface) and F_δ is the surface-emitted electron flux (taken positive for flux out of the surface).

To simplify notation, positions are represented by the following subscripts: p — edge plasma and presheath interface; b — presheath/sheath interface; m — electric potential minimum when space-charge saturation is not present; x — arbitrary position; and s — sheath/surface interface. Symbols with two position subscripts represent a location difference, e.g., $\phi_{ms} = \phi(x_m) - \phi(x_s)$. The subscripts i , e and δ represent species quantities. The electric potential is not used directly, but rather a ratio to particle potential energy to temperature is used, e.g., $\psi_i = Ze\phi/T_{pi}$, $\psi_e = -e\phi/T_{pe}$ and $\psi_\delta = -e\phi/T_{s\delta}$. As an example, the normalized plasma electron potential energy difference between an arbitrary position and the sheath/surface interface in the current notation is represented as $\psi_{xse} = -e[\phi(x) - \phi(x_s)]/T_{pe}$.

III Evaluation of the sheath and presheath potentials

Three boundary conditions are required to determine the sheath and presheath potentials:

Condition 1: The charge density at the presheath/sheath interface is zero.

Condition 2: The presheath is globally neutral.

Condition 3: The electric field at the electric potential minimum is zero.

The first condition is a matching condition between the presheath and the sheath. Forcing the integral of the charge density in the presheath to be zero satisfies Condition 2. This is equivalent to requiring zero electric field at the edge plasma/presheath interface and the presheath/sheath interface. Condition 3 is relevant only when space-charge saturation is present. Without space-charge saturation, the electric potential minimum occurs at the surface, along with a finite electric field.

To develop the equations describing the presheath and sheath potentials, the particle densities and fluxes are required for each species. These quantities are provided as Eqs. (1)–(62) and (77)–(91) in Ref. [1]. Using these, along with the normalized current density definition, Eq. (1), the neutralization factor, [3] $\alpha = Z n_{pi}/n_{pe}$ is given by

$$\alpha = \frac{1 - \delta}{1 - \gamma_i} \xi e^{-\psi_{spe}}, \quad (2)$$

$$\alpha = \frac{1 - \delta e^{-\psi_{ms\delta}}}{1 - \gamma_i} \xi e^{\psi_{mpe}}, \quad (3)$$

$$\alpha = \frac{1 - \delta e^{-\psi_{ms\delta}}}{1 - \gamma_i e^{-\psi_{spi}}} \xi e^{-\psi_{mpe}} e^{-\psi_{spi}}. \quad (4)$$

Eq. (2) applies if space-charge saturation is absent [Fig. ??(a)]. When space-charge saturation is present, Eq. (3) should be used for a negatively-biased surface [Fig. 1(b)] and eq. (4) for a positively-biased surface [Not shown in Fig. 1]. Hereafter, each occurrence of α is assumed to be replaced by the appropriate expression from Eqs. (2)–(4). It should also be noted that these expressions for α do not apply at the ion saturation current, $\gamma_i = 1$.

In order to enforce Conditions 1-3, the charge density is required. Defined by $\rho = e[Zn_i - n_e - n_s]$, it is given, for the three cases mentioned above, by

$$\frac{2e^{\psi_{spe}}}{en_{pe}}\rho(x) = \alpha e^{\psi_{spe}}G_1(\psi_{pxi}) - G_2(\psi_{sxe}) - \frac{\delta}{\sqrt{\tau_\delta}}G_1(\psi_{sxd}), \quad (5)$$

$$\frac{2e^{\psi_{mpe}}}{en_{pe}}\rho(x) = \alpha e^{\psi_{mpe}}G_1(\psi_{pxi}) - G_2(\psi_{mxe}) - \frac{\delta}{\sqrt{\tau_\delta}}e^{-\psi_{ms\delta}}G_1(\psi_{mxd}), \quad (6)$$

$$\frac{2e^{\psi_{mpe}}}{en_{pe}}\rho(x) = \alpha e^{\psi_{mpe}} \left[2e^{\psi_{spi}}G_1(\psi_{pxi}) - G_1(\psi_{sxi}) \right] - G_2(\psi_{mxe}) - \frac{\delta}{\sqrt{\tau_\delta}}e^{-\psi_{ms\delta}}G_1(\psi_{mxd}), \quad (7)$$

where $G_1(z) = e^z \operatorname{erfc}(\sqrt{z})$ and $G_2(z) = e^z \operatorname{erfc}(-\sqrt{z})$. Equations (6) and (7) only apply for $x_p \leq x \leq x_m$. The charge density between x_m and x_s is not required to determine the presheath and sheath potentials.

Equations (5)-(7) are set equal to zero at x_b in order to satisfy Condition 1, producing

$$\alpha e^{\psi_{spe}}G_1(\psi_{pbi}) = G_2(\psi_{sbe}) - \frac{\delta}{\sqrt{\tau_\delta}}G_1(\psi_{sbd}), \quad (8)$$

$$\alpha e^{\psi_{mpe}}G_1(\psi_{pbi}) = G_2(\psi_{mbe}) - \frac{\delta}{\sqrt{\tau_\delta}}e^{-\psi_{ms\delta}}G_1(\psi_{mbd}), \quad (9)$$

$$\alpha e^{\psi_{mpe}} \left[2e^{\psi_{spi}}G_1(\psi_{pbi}) - G_1(\psi_{sbi}) \right] = G_2(\psi_{mbe}) - \frac{\delta}{\sqrt{\tau_\delta}}e^{-\psi_{ms\delta}}G_1(\psi_{mbd}). \quad (10)$$

Condition 2, requiring a globally quasineutral presheath, can be satisfied by $\int_{\psi_{pe}}^{\psi_{be}} \rho(\psi_{xe}) d\psi_{xe} = 0$.

[6] Using Eqs. (5)-(7), this yields

$$-\frac{\alpha}{\zeta}e^{\psi_{spe}} \int_0^{\psi_{pbi}} G_1(z) dz = \int_{\psi_{spe}}^{\psi_{sbe}} G_2(z) dz + \delta\sqrt{\tau_\delta} \int_{\psi_{spe}}^{\psi_{sbd}} G_1(z) dz, \quad (11)$$

$$-\frac{\alpha}{\zeta}e^{\psi_{mpe}} \int_0^{\psi_{pbi}} G_1(z) dz = \int_{\psi_{mpe}}^{\psi_{mbe}} G_2(z) dz + \delta\sqrt{\tau_\delta}e^{-\psi_{ms\delta}} \int_{\psi_{spe}}^{\psi_{sbd}} G_1(z) dz, \quad (12)$$

$$\begin{aligned} & -\frac{\alpha}{\zeta}e^{\psi_{mpe}} \left\{ 2e^{\psi_{spi}} \int_0^{\psi_{pbi}} G_1(z) dz - \int_{\psi_{spi}}^{\psi_{sbi}} G_1(z) dz \right\} \\ & = \int_{\psi_{mpe}}^{\psi_{mbe}} G_2(z) dz + \delta\sqrt{\tau_\delta}e^{-\psi_{ms\delta}} \int_{\psi_{mpe}}^{\psi_{mbd}} G_1(z) dz. \end{aligned} \quad (13)$$

Condition 3, applied only to those cases in which the electric potential minimum is not coincident with the surface, requires a zero electric field at the potential minimum. Since, by Condition 2, the electric field is also zero at the presheath/sheath interface, the charge density between two

locations of zero electric field must be zero, i.e., $\int_{\psi_{be}}^{\psi_{me}} \rho \, d\psi_{ze} = 0$. From Eqs. (6) and (7), this condition produces the following equations:

$$-\frac{\alpha}{\zeta} e^{\psi_{mpe}} \int_{\psi_{pi}}^{\psi_{pmi}} G_1(z) \, dz = \int_{\psi_0}^{\psi_{mbe}} G_2(z) \, dz + \delta \sqrt{\tau_\delta} e^{-\psi_{mas}} \int_{\psi_0}^{\psi_{mbd}} G_1(z) \, dz, \quad (14)$$

$$\begin{aligned} & -\frac{\alpha}{\zeta} e^{\psi_{mpe}} \left\{ 2e^{\psi_{spi}} \int_{\psi_{pi}}^{\psi_{pmi}} G_1(z) \, dz - \int_{\psi_{bi}}^{\psi_{smi}} G_1(z) \, dz \right\} \\ & = \int_{\psi_0}^{\psi_{mbe}} G_2(z) \, dz + \delta \sqrt{\tau_\delta} e^{-\psi_{mas}} \int_{\psi_0}^{\psi_{mbd}} G_1(z) \, dz. \end{aligned} \quad (15)$$

Equations (11)–(15) can be evaluated by using the relations $\int G_1(z) \, dz = G_1(z) + 2\sqrt{z/\pi}$ and $\int G_2(z) \, dz = G_2(z) - 2\sqrt{z/\pi}$.

A reference point for the electric potential needs to be defined in order to use the above equations. This position is taken at the presheath/sheath interface, i.e., $\phi(x_b) = 0$. With this choice, ψ_{pe} gives the potential drop across the presheath and ψ_{se} the drop across the sheath. Equations (8) and (11) can now be simultaneously solved to determine ψ_{pe} and ψ_{se} for a monotonically decreasing potential. Likewise, the solution of Eqs. (9), (12) and (14) [(10), (13) and (15)] yields ψ_{pe} , ψ_{me} and ψ_{se} under conditions of space-charge saturation for a negatively-biased [positively-biased] surface. Once the necessary normalized electric potential values have been determined, the electric potential profile across the presheath and sheath can be found by integrating Poisson's equations:

$$\frac{x}{\lambda_D} = \int_{\psi_{pe}}^{\psi_{se}} \left[\int_{\psi_{pe}}^{\psi'_{ze}} \frac{2\rho(\psi''_{ze})}{en_{pe}} \, d\psi'_{ze} \right]^{-1/2} d\psi'_{ze}, \quad (16)$$

where λ_D is the Debye length. If space-charge saturation is present, Eq. (16) only applies between x_p and x_m since Eqs. (12), (13), (14) and (15) are not defined for $x_m < x < x_s$. Ref. [1] contains the necessary particle densities to calculate ρ for $x_m < x < x_s$.

IV Simple expressions

This section presents approximations to the solutions to the equations developed in Sect. III. Expressions for the plasma presheath and sheath potentials, along with the electron emission coefficient at the onset of space-charge saturation, are given. These were determined by solving each system of equations for several parameter values [See Table 1] and finding a suitable fit to these values.

$\zeta = \frac{Z}{\tau_i} = \frac{ZT_{pe}}{T_{pi}}$	0.2, 1, 5
$\xi = \sqrt{\frac{\eta}{\tau_i}} = \sqrt{\frac{m_i T_{pi}}{m_e T_{pe}}}$	20, 50, 100, 500, 1000
$\gamma_i = \frac{eZF_i - e(F_e - F_\delta)}{Zen_{pi}/\sqrt{2\pi m_i/T_{pi}}}$	-0.5, 0, +0.5
$\tau_\delta = \frac{T_{s\delta}}{T_{pe}}$	0.01

Table 1: Parameter values used for obtaining fits.

The approximations considered all possible combinations of the parameters given in Table 1 with $\tau_\delta = 0.1$. This value for the normalized secondary electron temperature was chosen because the potential is essentially independent of τ_δ for values $\tau_\delta < 0.1$.

The onset of space-charge saturation occurs when the electric field is zero at the surface. Recall that the electric field is positive at the surface for a monotonically decreasing potential. Increasing the electron emission coefficient increases the space-charge in front of the surface. When δ exceeds a critical value, δ_c , the electric field at the surface becomes negative. This field limits the number of secondary electrons that can reach the edge plasma by reflecting them back to the surface. An expression that describes this critical electron emission coefficient value is

$$\delta_c = 1 - 2.9\zeta^{0.28} (1 - \gamma_i)^{0.7} \xi^{-0.79} \quad (17)$$

$$(0.2 \leq \zeta \leq 5, 20 \leq \xi \leq 1000, |\gamma_i| \leq 0.5)$$

and agrees within 4% of the numerical solutions of Eqs. (9), (12) and (14) with $\psi_{me} = \psi_{se}$. Beneath Eq. (17) is the parameter range over which it is expected to be suitable.

When space-charge saturation is absent, $\delta < \delta_c$, the electric potential monotonically decreases from the edge plasma. The following two expressions describe the presheath and sheath potential drop when $\delta < \delta_c$:

$$\psi_{pe} = -0.288 \ln(1 + 2.07\zeta) \left[1 + \frac{0.45\zeta\gamma_i}{\xi} \right] \left[1 + \frac{0.19\delta^{1.4}}{\zeta^{0.3}} \right], \quad (18)$$

$$\psi_{se} = \ln \left(0.4715\xi \frac{1-\delta}{1-\gamma_i} \right) - 0.5 \ln(1 + 1.61\zeta) \left[1 + \frac{1.3\gamma_i}{\zeta^{0.56}\xi} \right] \left[1 + 0.208\zeta^{0.041}\delta^{1.3} \right] \quad (19)$$

$$(0.2 \leq \zeta \leq 5, 20 \leq \xi \leq 1000, |\gamma_i| \leq 0.5, \delta \leq \delta_c)$$

These expressions are each within 7% of the numerically determined solutions of Eqs. (8) and (11). The values of δ used to obtain these were 0 and δ_c .

Once the electron emission coefficient exceeds that critical value, $\delta > \delta_c$, space-charge saturation occurs. For this case, the potential at the edge plasma/presheath, electric potential minimum and presheath/sheath interface are given respectively by:

$$\psi_{pe} = -0.271 \ln(1 + 3\zeta) \left[1 + \frac{0.57\zeta\gamma_i}{\xi} \right], \quad (20)$$

$$\begin{aligned} \psi_{me} = & 0.0864 - 0.0101\zeta + (0.626 + 0.121\zeta - 0.0181\zeta^2) \delta_c \\ & + (-0.128 - 0.0416\zeta + 0.00549\zeta^2) \delta_c^2, \end{aligned} \quad (21)$$

$$\begin{aligned} \psi_{se} = & \psi_{me} - 0.00693(1 - 0.074\delta)\delta \\ & (0.2 \leq \zeta \leq 5, 20 \leq \xi \leq 1000, |\gamma_i| \leq 0.5, \delta_c \leq \delta \leq 6) \end{aligned} \quad (22)$$

These expressions are within 7%, 3.5% and 3%, respectively, of the numerical solutions of Eqs. (9), (12) and (14). Eq. (17) is used in Eq. (21). The parameter values used to obtain these expressions were all possible combinations of those shown in Table 1 and $\delta = \delta_c, 1.5, 3.0, 6.0$.

An electrically floating surface can maintain a positive bias with respect to the plasma, $\phi_p < \phi_s$ ($\psi_{pe} > \psi_{se}$). [7] However, there must exist a large thermionic current density for a floating surface to reach this state, or a large current density for an anode surface to be positively-biased. Eqs. (17)–(22) apply only when $\phi_p > \phi_s$ ($\psi_{pe} < \psi_{se}$), i.e., negatively-biased surfaces.

V Concluding Remarks

The present theory considers a single ion species plasma, with no restriction on the ion temperature. Electron emission from the plasma-facing surface is accounted for, even when space-charge saturation is present. This work represents an extension to fully-kinetic sheath theory by allowing the plasma-facing surface to be an anode or cathode. However, the theory is limited to either a

monotonically decreasing or a single-minimum potential. Expressions for the potential drop across the presheath and sheath are provided, along with the electron emission coefficient value at which space-charge saturation begins, to preclude the need for solving a nonlinear set of equations.

Several further extensions are still required. Perhaps the most significant is for a magnetic field whose field lines intercept the surface at an arbitrary angle. Other extensions include multiple ion species and non-planar surface geometries.

References

- [1] C. A. Ordonez, Phys. Rev. E **55**, 1858 (1997). $\rho^{\#}$
- [2] K. F. Stephens II, J. Appl. Phys. **85**, no. 5 (1999).
- [3] L. A. Schwager and C. K. Birdsall, Phys. Fluids B **2**, 1057 (1990).
- [4] L. A. Schwager, Phys. Fluids B **5**, 631 (1993).
- [5] G. A. Emmert, R. M. Wieland, A. T. Mense and J. N. Davidson, Phys. Fluids **5**, 803 (1980).
- [6] C. A. Ordonez, Phys. Fluids B **4**, 778 (1992).
- [7] T. Intrator, M. H. Cho, E. Y. Wang, H. Hershkowitz, D. Diebold and J. DeKock, *et al*, J. Appl. Phys. **64**, 2927 (1988).